MECHANISMS OF STRAIN LOCALIZATION IN ULTRAFINE-GRAINED TUNGSTEN

by

Brady G. Butler

A dissertation submitted to Johns Hopkins University in conformity with the requirements for the degree of Doctor of Philosophy

Baltimore, Maryland

December, 2017

Abstract

The material properties of tungsten are described in a long list of extremes. It has an extraordinarily high strength, density, stiffness, thermal conductivity, and melting-point. This remarkable combination of properties allows tungsten to push the envelope of possibilities in the fields of energy, aerospace and defense. Within the defense industry, there is a considerable effort to take advantage of these properties in ballistic applications. The high strength and density of tungsten make it particularly suitable for anti-armor, kinetic energy penetrator munitions.

The key performance metrics for a kinetic energy penetrator are the ability to withstand the harsh conditions of launch, and efficiently perforate heavily armored targets. However, these basic requirements are actually at odds with each other. An ideal material shows highly stable plasticity during launch, while plastic instabilities, in the form of shear banding, improve ballistic efficiencies down range (i.e. terminal ballistics). Unfortunately, commercial tungsten tends to perform poorly in both instances. The strong tensile loads experienced during launch generally result in brittle failures, while tungsten actually shows a high degree of plastic stability under the pressures and strain rates of terminal ballistics. By contrast, ultrafine-grained tungsten (100-1000 nm) has shown significant promise for achieving ductility or strain localization based on the novel microstructures enabled by the processing conditions; however, the specific mechanisms of these disparate behaviors remain unclear.

The goal of this study was to investigate the conditions for stable plastic flow, brittle fracture, and strain localization in sintered ultrafine-grained tungsten, and tungsten alloys,

for the purpose of improving performance in ordnance applications. In particular, the mechanisms of plastic instability and strain localization were investigated to control the initiation of shear bands. Powder metallurgical processing and alloy development were effective in mediating issues related to plasticity. Mechanical testing was performed to understand the initiation and development of shear bands during deformation. Finally, these ultrafine-grained materials were characterized extensively in order to identify the mechanisms of deformation.

Over the course of this research, it was discovered that commonly accepted models of strain localization in ultrafine grained metals were unsuccessful in describing the physical processes that lead to shear banding in these materials. In particular, it was determined that strain softening mechanisms, based on texture and temperature, were insufficient for describing the initiation of shear bands in ultrafine grained metals. However, these instabilities can be described based on traditional concepts of dislocation mediated plasticity, as long as the relationships between grain size, dislocation density, and deformation are accounted for properly. These discoveries have significant implications for the viability of tungsten in ballistic applications, and extreme engineering environments in general.

Advisor: Kevin J. Hemker

Readers: En Ma, Jonah Erlebacher, James K. Guest, Suveen N. Mathaudhu

Acknowledgements

I would like to thank a number of colleagues at the US Army Research Laboratory. First, and foremost, thank you to James Paramore, Jonathan Ligda, and Anthony Roberts for friendship, and unyielding support in my academic pursuits. Thank you to Eric Klier, Larry Dougherty, and Heidi Maupin for the encouragement to pursue my Ph.D. Thank you to a number of people who supported this research, and assisted in the processing, mechanical testing, and characterization of materials over the past decade: Micah Gallagher, Judy Hays, David Runk, Frank Kellogg, Bradley Klotz, Andrew Jamieson, Scott Middlemas, Paul Moy, and David Gray. Thank you to Brian Schuster, Lee Magness, Suveen Mathaudhu, and Richard Becker for many critical discussions on ballistic mechanisms, and shear banding in tungsten.

Thank you to all of the Hemker Research group for many fruitful discussions on microscopy, mechanical testing, and for the friendships that we've had over the past several years.

Thank you to Kinshuk Srivastava, Zak Fang, Chai Ren, Zi-kui Liu, Yong-Jie Hu, David Foley, and Zach Levin, for helping me to understand deformation, processing, and the role of dislocations in the plastic behavior of tungsten.

I would also like to thank K.T. Ramesh, En Ma, Qiuming Wei, Shailendra Joshi, and D. Jia, for their contributions to this field. These have provided a foundation for my own studies. I am truly standing on the shoulders of giants.

Thank you to my committee members for the time, consideration, and for helpful discussions related to this dissertation. In particular, thank you to my advisor, Kevin

Hemker, for all of your support and for pushing me to think bigger (and smaller) when describing the physical mechanisms of deformation.

Most importantly, thank you to my wife, Megan. You have always been my “rock” when I’ve needed it. Thank *you* for everything.

Dedication

This thesis is dedicated to my daughter, Portia, and my wife, Megan.

Table of Contents

List of Tables

List of Figures

CHAPTER 1. INTRODUCTION

Tungsten is stubborn, intractable and unaccommodating. It tends to be brittle, difficult to form and machine, and it is nearly impossible to cast [1]. Tungsten is the most refractory of all metals.

The word refractory actually stems from the word meaning obstinate, or resistant to change [2]. Although the current scientific consensus of refractory is only based on melting point [3, 4], the colloquial definition provides a fair understanding of this material. Tungsten is thermally refractory; it has a low coefficient of thermal expansion, and a melting point in excess of 3400 °C, the highest of any metal. Tungsten is mechanically refractory, demonstrating an extremely high tensile strength, hardness, wear resistance, and elastic modulus compared to other metals [5]. Tungsten is even refractory in a chemical sense, having a very high cohesive energy [5] and being resistant to attack by most acids [6]. Tungsten is the epitome of refractory, which is exactly what makes it so appealing for extreme engineering environments.

The unaccommodating nature of this material is particularly apparent in terms of plasticity. Tungsten tends to be brittle at room temperature [7, 8], and is highly sensitive to notches, and pre-existing defects [8-10]. Materials science has been working to address these issues for at least a century [11]; however, the plastic properties of tungsten are not just refractory, they are perplexing.

In general, the basic material processes that reduce ductility in other materials tend to improve ductility in tungsten. Sintered tungsten is brittle at room temperature, but cold

working (deforming extensively below the recrystallization temperature) actually increases the ductility [12, 13]. In fact, extreme deformation (i.e. wire drawing, and sheet rolling) is one of the few methods to make tungsten ductile at room temperature. Furthermore, annealing the heavily deformed microstructure actually reduces ductility [14-16]. Alloying with another highly refractory metal, rhenium, leads to great improvements in ductility [17]. Solid solutions tend to harden materials by impeding dislocation mobility, but rhenium additions actually lead to softening [18-21]. Tungsten does not even follow the basic rules that materials science has outlined to describe how a material should deform (i.e. Schmid's law) [22-24].

Although the plastic behavior of tungsten is often confusing, and counterintuitive, the behavior can be explained based on the crystal structure, and dislocation processes that control plasticity. With few notable exceptions, the plastic behavior of all metals is effectively mediated by dislocation activity that allows for deformation at stresses that are orders of magnitude below the theoretical yield strength [25]. In body centered cubic (BCC) metals, dislocation mobility is highly sensitive to temperature [26, 27]. Therefore, a brittle to ductile transition temperature (BDTT) is commonly observed for materials with this crystal structure, and other crystal structures that exhibit a strong temperature dependence on dislocation mobility [28, 29]. Reducing the BDTT may be accomplished by improving dislocation mobility, by alloying [18, 21, 30] or modifying the microstructure [31].

Length scales also play a critical role in the ductility of tungsten, as a polycrystalline sample will show brittle behavior at room temperature, but carefully prepared single crystals exhibit significant ductility [32], and even necking at temperatures below -196°C

[33]. Ductility is also observed at the opposite end of the length-scale spectrum. Microstructural modifications that reduce grain size to the ultrafine-grained (ufg) regime, with a grain size less than 1 μm have been shown to improve the fracture resistance, and reduce the BDTT of tungsten [34, 35]. This presents another confusing situation, because other research has shown that severe microstructural refinement (smaller than ~400 nm) makes the material more susceptible to plastic instabilities [36, 37]. These instabilities effectively limit ductility by localizing strain, which can lead to the formation of shear bands.

These plasticity phenomena play an important role in several extreme engineering environments, specifically in the energy [38, 39], aerospace [40, 41], and manufacturing [42, 43] sectors, where strain localization could result in dangerous, catastrophic failures. In ballistic applications, the same considerations apply during launch of a tungsten projectile; however, strain localization has been shown to improve penetration performance during target interactions [44, 45]. Although this research has implications for improving the ductility of tungsten in general, there is particular focus on understanding plastic instabilities in tungsten to make it more suitable for anti-armor, kinetic energy penetrator applications.

1.1. Significance of the problem

Kinetic energy munitions are designed to perforate heavy armor by imparting large amounts of kinetic energy into a very narrow region of the target. These munitions are typically built in a “long-rod” geometry, with length to diameter ratios greater than 10:1 in order to minimize the volume of interaction with the target. At a given projectile

velocity, the key performance metrics for imparting the maximum kinetic energy on a target are strength, and density, where depleted uranium (DU) and tungsten alloys outperform other engineering materials [44]. Although these two alloy classes exhibit similar strengths and densities, DU alloys tend to strain localize, based on adiabatic shear banding mechanisms, during penetrator-target interactions [46]. Shear banding results in deeper and narrower penetration channels, effectively creating a performance gap between DU and tungsten-based alloys. However, there are concerns regarding health effects associated with DU munitions [47].

Density constraints effectively limit the number of viable materials for this application. This puts the problem squarely in the field of materials science, where the processing-microstructure-property-performance paradigm may be utilized to modify deformation behavior without relying on significant changes to composition. To this end, there have been a variety of microstructure-based methods utilized to improve the penetration performance of tungsten-based penetrators based on modification, including: highly oriented columnar microstructures [48, 49], single crystals [50, 51], bulk metallic glass composites [52], and ufg metals [37, 53-57]. Unfortunately, there still remains a significant performance gap between tungsten and DU alloys [58].

In recent years, several advanced processing methods that have been developed to manufacture these ufg metals [59-65]. There have been several examples where ufg tungsten demonstrates strain localization [36, 37, 53, 66-68], effectively narrowing the gap between DU and tungsten based munitions. Despite these significant advancements, there are still many unanswered questions regarding the mechanisms of strain localization in tungsten and BCC metals in general.

Understanding the mechanics of strain localization in ufg metals holds significant promise for improving the ballistic properties of tungsten-based materials. An accurate description of what initiates localization will help to design new materials that will close the performance gap between DU and tungsten. Furthermore, this knowledge may help to improve the low temperature ductility of BCC metals in general and help to describe the effective limits to the useful application of grain refinement for ufg metals. The implications for microstructural length-scales, and their influence on strain localization and other plasticity phenomena has drastic implications for developing new materials to improve our capabilities in a variety of extreme and demanding engineering environments.

1.2. Problem statement and research hypotheses

Shear banding describes a very general phenomenon where strains localized into intense planar regions of shear, often resulting in catastrophic failure [69]. Although the physical causes of this plastic instability can vary, localization occurs when local hardening is not sufficient to distribute strains throughout a body. While there have been several mechanisms for strain localization that have been described for ufg metals, shear banding mechanisms and terminologies are often incorrectly applied and/or do not adequately describe the physical impetus for strain localization. The two most commonly cited mechanisms of shear band formation in ufg metals are: (1) adiabatic shear banding, and (2) geometric shear banding. Each of these mechanisms has significant merit in predicting the phenomenological response of tungsten when it is deformed at (1) dynamic rates, or (2) ultrafine grain sizes. However, these have specific shortcomings in

adequately describing shear banding that is observed in ultrafine microstructures at quasi-static rates.

Adiabatic shear banding is an established mechanism that accounts for strain-induced softening that develops based on the thermoviscoplastic response of a material. Thermal effects become particularly important at high strain rates, when there is not sufficient time to conduct the heat associated with plasticity away from the area of deformation (hence the term adiabatic) [70]. The susceptibility of materials mechanism provides a description of the time-scale of mechanical testing methods and the thermoplastic response of a material. These features are useful for describing the dynamic behavior of materials, but are not effective for describing the initiation of shear bands in ufg metals, which occurs at quasi-static rates.

Geometric shear banding provides a plausible mechanism for shear banding in ufg materials, which accounts for localization at quasi-static rates. In the most general sense, geometric shear bands are the result of softening that is induced by local reorientation and texture development. A specific model, developed by Joshi and Ramesh [71-73], has shown promise for predicting localization in ufg metals. However, the underlying mechanisms for this model have not been tested adequately, and cannot account for many of the features of strain localization observed in ufg tungsten.

Adiabatic and geometric effects will certainly influence the structure and the propagation of shear bands in all materials. However, these mechanisms do not describe the specific features that *initiate* the plastic instability of ufg materials, and ultimately result in shear band formation. Furthermore, these models do not generally account for the importance

of dislocation activity in accommodating plastic flow, and mediating plastic instabilities. The role of dislocations is particularly important for describing the development of textures, which have a significant influence on the mechanical behavior of these materials even at ultrafine grain sizes. In light of these limitations in existing shear banding theories, an alternative description for shear band formation in ufg metals has been developed. This model is based on the concept of *strain gradient plasticity* (SGP), originally established by Ashby to understand the increased hardening behavior that is observed based on non-homogeneous plasticity [74]. The basic premise relies on a general relation between confined plasticity, lattice curvatures, and dislocation storage; this combination implies a natural length-scale to the deformation behavior of materials that is not captured by traditional mechanics. These intrinsic length-scales provide an improved explanation of several phenomena that are associated with dislocation-mediated plasticity, and they can also provide guidance on the deformation behavior and failure of ufg metals. A simple mathematical description of strain gradient plasticity is shown in Equations (1) and (2).

$$\kappa \propto \rho_G \tag{1}$$

$$\rho_G \propto \frac{\gamma}{\lambda_G} \tag{2}$$

which show that (1) the curvature of the lattice (κ) is directly proportional to the density of geometrically necessary dislocations (ρ_G), and (2) this dislocation content may also be predicted based on the shear strain (γ), and a length scale parameter (λ_G). The first relation creates an interesting opportunity to account for dislocations stored in the lattice based on modern techniques in orientation imaging microscopy. The second relation

provides insight into the enhanced dislocation activity that is required according to the geometrical confinement of grain boundaries. It is the author's hope that a more thorough understanding of dislocations, and the role that they play in describing plastic instabilities will result in a more comprehensive description of strain localization and shear banding in ufg metals.

Tungsten serves as an ideal material to test the specific characteristics of SGP theory. First, tungsten is an excellent material for dislocation analysis, having a high elastic modulus and the highest melting point of any metal means it should have a stable dislocation structure that is less susceptible to changes during sample preparation. Second, the high density and large atomic number of tungsten results in a short extinction distance for electrons that are used to interrogate structure by scanning and transmission electron microscopy methods. Although this is a detriment for transmission electron microscopy, requiring very thin samples (~40nm) in order to allow for electron transparency at conventional imaging acceleration voltages (200 kV), it actually improves the resolution of EBSD orientation measurements by limiting the beam interaction volumes for a given spot size and acceleration voltage. This is particularly critical when performing EBSD on heavily deformed microstructures, as it allows for less distortion and improved image quality for Kikuchi patterns. Additionally, the high melting point, and high thermal conductivity of tungsten [6] help to distinguish non-adiabatic causes of shear band formation. Furthermore, the well-studied plastic behavior of tungsten [24, 75, 76] provides an ideal candidate to test the influence of grain rotation mechanisms that are critical to the Joshi and Ramesh model for geometric shear banding [71-73].

Ultrafine and nano-grained metals are providing new frontiers in materials science [77]. Advanced processing technologies have enabled the production of bulk structural materials with extremely fine microstructural length scales, resulting in incredibly high strengths. In tungsten-based alloys, grain refinement has also shown promise for improving ductility and fracture toughness, which may create new opportunities for utilizing this refractory metal in extreme engineering environments.

The plastic instability and strain localization behavior of ufg metals is a critical issue that has been studied for decades. Although several models have been developed to understand the material parameters that lead to strain localization, many of these models are not founded on the physical observations of dislocation-mediated plasticity. The theory of SGP provides a reasonable framework to understand the influence of grain size in terms of a microstructural confinement on the plastic behavior of metals. This theory provides a robust method, both for predicting [78], and experimentally verifying [79-81] the quantity of dislocations that are geometrically necessary for deformation. The details of this theory may help to elucidate the effects of grain size on plastic instabilities, and provide insight on the methods that can be used to induce, or prevent failures associated with strain localization.

CHAPTER 2. BACKGROUND

The unique and refractory properties of tungsten are already suited for use in a variety of extreme engineering environments. However, it has been shown that the exceptional strength of tungsten may be further improved by refining the grain size into the ufg regime. Furthermore, recent studies have also shown that reducing the grain size also reduces the brittle to ductile transition temperature [31, 82], which is critical for a number of applications. These results raise a question regarding the limits of grain size refinement for promoting ductility. Bulk ufg metals have also demonstrated a propensity for plastic instability in the form of shear bands, especially as the grain size is pushed toward the nanocrystalline regime [36, 68, 83, 84]. The viability of tungsten as a structural material for extreme environments depends on understanding and describing these transitions to unstable plastic behavior. This is particularly true for structural applications, where stable plastic deformation can provide an additional factor of safety in the design of heat shields of nuclear reactors and hypersonic vehicles. However, this research will focus on a unique case where plastic instabilities and shear band formation help to improve the performance of tungsten alloys in anti-armor ballistic applications.

2.1. Ballistic environment of kinetic energy penetrators

Kinetic energy munitions provide a powerful and economical means for destroying heavily armored targets on the battlefield. These munitions are gun launched, line of sight projectiles that impart an overwhelming amount of kinetic energy (>10 MJ for large caliber projectiles) into a small region of the armored target. Although the concept is simple, these projectiles are highly effective and reliable on the battlefield. Kinetic

energy projectiles operate in a ballistic environment with extreme conditions of stress, temperature, strain and strain-rate during launch and especially during target interactions [85, 86]. The materials used in these applications must have exceptional material properties in order to: (1) withstand gun launch and (2) effectively penetrate armor targets [87]. The specific material properties that influence these performance metrics are: density, strength, and plastic behavior (both at high strain rates and under quasi-static conditions). Unfortunately, the material requirements related to plasticity, are at odds during different times of the ballistic event. For internal ballistics (i.e. during gun-launch), plastic stability is essential for surviving the loads imposed during launch. In terminal ballistics (i.e. projectile-target interaction), plastic instabilities promote efficient penetration mechanisms.

The underlying concept of a kinetic energy projectile is fairly simple; efficient perforation of armor occurs by maximizing the kinetic energy density during penetrator-target interactions. In a simple formulation, this occurs by maximizing the overall kinetic energy of the projectile and minimizing the volume of interaction with the target. The total kinetic energy (E_K) of a projectile may be described as a function of mass (m) and velocity (v), but the launch system and flight dynamics effectively limit the volume (V), geometry and maximum velocity that can be achieved for a given projectile in a particular gun system. The only remaining criterion for increasing the kinetic energy of a projectile is to maximize the density (ρ) of the projectile as described by Equation 3.

$$E_K = \frac{1}{2} m v^2 = \frac{1}{2} \rho V v^2 \tag{3}$$

The volume of interaction is predominantly controlled by the geometry of the projectile. A "long rod" projectile configuration, described by a high length to diameter aspect ratio (L/D), is designed to minimize target interaction and maximize the depth of penetration. The length of a kinetic energy penetrator is commonly designed to be 10-30 times the diameter of the projectile. Increasing the L/D can help to improve the penetration performance considerably, but there are limitations imposed by launch dynamics and flight stability. With these geometric limitations in place, much of the materials selection criteria for reduced interaction volume are based on the overall strength of the penetrator and the plastic flow mechanisms at high strain rates.

2.1.1. Internal ballistics (gun launch)

Penetration mechanics are not the only deciding factor in developing kinetic energy projectiles; it is also necessary for a material to survive the extreme conditions of the gun system launch. Most modern gun systems utilize a sabot to accelerate the penetrator out of smooth bore gun tube as described by Figure 1. Large caliber, kinetic energy munitions achieve velocities of over 1500 m/s in less than one hundredth of a second and acceleration rates may approach 42,000 times the force of gravity [88, 89].

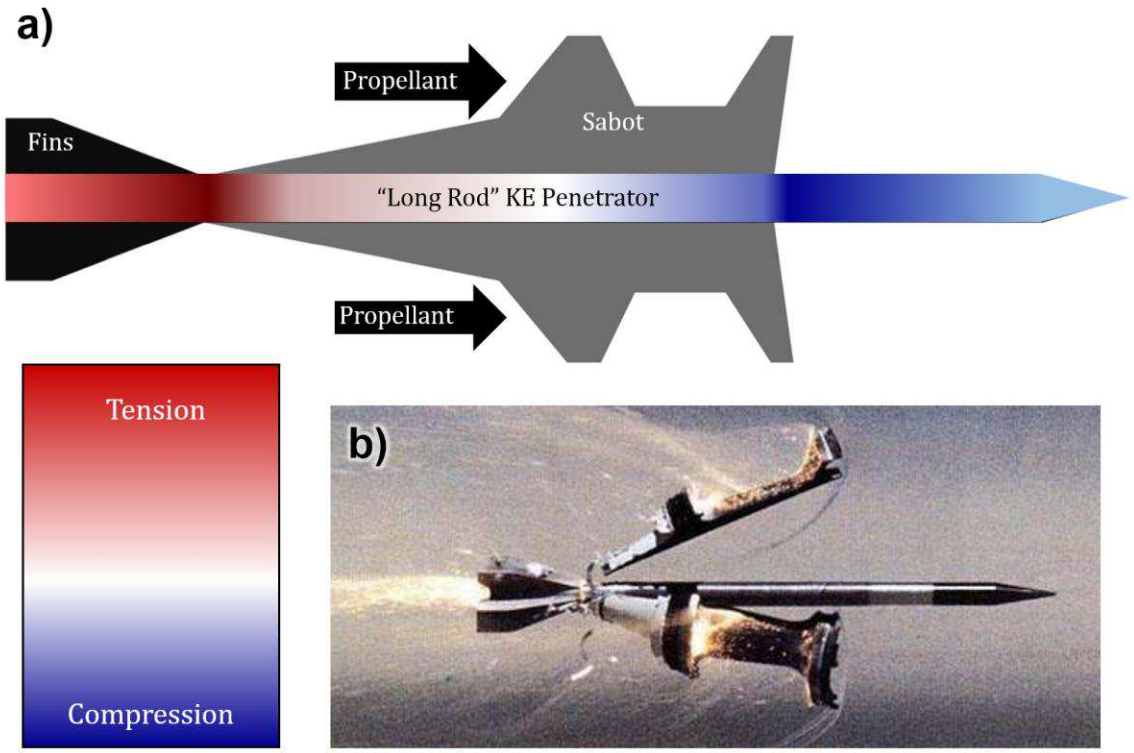

Figure 1 – Long-rod kinetic energy penetrator and sabot. a) Schematic of kinetic energy penetrator munition. The sabot allows the penetrator to be launched from a smooth bore gun and fins stabilize the flight dynamics of the penetrator. The large tensile forces observed at the tail of the penetrator may cause premature failure of materials that do not exhibit tensile ductility at quasi-static strain rates. Schematic does not account for the transient hydrostatic compressive loads that are experienced as a result of propellant ignition. b) Image of the sabot detaching from the penetrator in flight, image from US Army.

The sabot launched projectiles experience strong compressive loads at the head of the projectile and large tensile loads at the tail with shearing forces encountered where the sabot attaches to grooves in the projectile body. The severe loading conditions require significant consideration to prevent in-bore failure, particularly for brittle materials where tensile loads and tensile loads facilitate fracture.

2.1.2. Terminal ballistics (target interaction)

The loading conditions and penetrator-target interactions are severe and highly complex, resulting in stringent requirements for toughness beyond those experienced during

launch. During terminal ballistics, the penetrator may experience pressures exceeding 15 GPa and strain rates as high as 10^5/s [90]. In the 1950s Alekseevski [91] and Tate [92] independently derived a modified hydrodynamic performance equation for long-rod kinetic energy projectiles as described by Equation (4).

$$\frac{\rho_p}{2}(v-u)^2 + R_P = \frac{\rho_t}{2}u^2 + R_t \tag{4}$$

Where R_P, and R_t, are the "resistance" of the projectile and target respectively, which are a function of the yield strengths of each material and the geometry of interaction. Other salient terms include the densities of the penetrator (ρ_p), and target (ρ_t) to describe the relation between the striking velocity (v) and penetration velocity (u) of the projectile as shown in Equation 4. The equation implies that the penetrator and target density terms dominate ballistic penetration results at higher velocities, whereas the strength terms ($R_p \; and \; R_t$) become important at ordnance velocities (below 2000 m/s).

2.1.3. Materials for ballistic applications

Kinetic energy penetrators are generally made from either depleted uranium (DU) or tungsten alloys because of the high strength and density that are critical for performance in these applications. One of the most common kinetic energy penetrator compositions is DU with an addition of 0.75 wt% titanium (U-¾Ti) to improve strength and corrosion resistance. At room temperature, DU has an orthorhombic crystal structure that is fairly soft and exhibits limited ductility. However, alloy additions and metallurgical processing can drastically improve the strength and tune the ductility over a wide range (2-19% tensile elongation) [93]. The high ductility that can be achieved allows DU alloy

penetrators to survive the harsh tensile and shear loadings (and plastic deformations) that occur during launch. Furthermore, DU based penetrators have exceptional properties for efficiently perforating armor targets during terminal ballistics. Although DU is particularly effective in anti-armor kinetic energy projectile applications, there are many concerns over the long-term health and safety effects of these materials [94, 95] and there has been a strong desire to replace DU, specifically in ballistic applications.

Tungsten alloys are also used in a number of kinetic energy-based ballistic applications. It is common to alloy tungsten with significant quantities (8-10 wt%) of nickel, iron and/or cobalt in order to improve the mechanical properties and achieve reasonable ductility in bulk polycrystalline form. Unfortunately, these additions also reduce the overall density of the material and affect the overall kinetic energy of the projectile. The tungsten alloyed in this fashion is colloquially referred to as tungsten heavy alloy (WHA), but the poor solubility of most transition metals in tungsten results in a two phase composite microstructure where the body-centered-cubic (BCC) tungsten particles are surrounded by a contiguous and ductile face-centered-cubic (FCC) phase, which allows for elongation similar to that observed in DU alloys [96].

Although pure tungsten, with an equivalent density to DU, is an ideal candidate for ballistic applications, there are significant issues related to launch survivability of tungsten. Tungsten, owing to its extremely high melting point, is almost always processed by powder metallurgical (PM) means. PM processes are inherently susceptible to impurities and residual porosity, which can be detrimental to ductility. Even high purity, melt-processed tungsten generally experiences a BDTT above 200°C [97] leading to poor tensile ductility under ambient conditions. The addition of 5-25 wt% rhenium can

lead to significant improvements in ductility, in addition to increasing the density. However the cost and availability of rhenium [98], effectively limit usage in these applications and there are currently no known alternatives to rhenium for improving the low temperature ductility of tungsten[99, 100]. A description of the alloys and mechanical properties of KE penetrators is shown in Table 1.

Table 1 – Densities and Mechanical Properties of Common Kinetic Energy Penetrator Alloys

Alloy	Crystal Structure	Density	Processing Condition	Hardness	Yield strength	Tensile strength	Elongation
		[g/cm^3]		[Vickers]	[MPa]	[MPa]	[%]
U (Unalloyed) [*]	orthorhombic	19.1	As cast	200 (g)	205	450	6
U (Unalloyed) [*]	orthorhombic	19.1	Cast, b-quenched(a), H-outgassed(b)	200 (g)	295	700	22
U-0.75Ti [*]	orthorhombic	18.6	γ-quenched(c), aged at 380 °C (d)	412 (g)	965	1656	19
U-0.75Ti [*]	orthorhombic	18.6	γ-quenched(c), aged at 450 °C (d)	544 (g)	1215	1660	<2
W (Unalloyed) [**]	bcc	19.293	Sintered, Hot Work, Anneal (e)	360	550	620	2
W (Unalloyed) [**]	bcc	19.293	Sintered, Cold Worked	500		1862	0
W-6.3Ni-2.7Fe [*]	bcc and fcc	17.34 (f)		294 (g)		940	35
W-7Ni-3Fe [**]	bcc and fcc	16.995		266-318 (g)	615	895	10
W-5.25Ni-2.25Fe [**]	bcc and fcc	17.494		272-327 (g)	579	786	7
W-3.5Ni-1.5Fe [**]	bcc and fcc	17.992		279-327 (g)	621	827	7
W-5Re [**]	bcc	19.57				1380-2208	10
W-25Re [**]	bcc	19.8				1370-1551	10-20

[*]- ASM Handbook [101], [**] – Cardarelli [102],
(a) Quenched from 720 °C, reheated to 600 °C, slow cooled; this sequence is often done twice.
(b) Vacuum heat treated in high-α region; time depends on section thickness.
(c) Heat treated for 1 h at 800 °C in vacuum (longer if required for removing hydrogen from thick sections), quenched in water or oil (rate depends on section thickness).
(d) Age 5 h in vacuum or dry argon.
(e) Swaged, Annealed at 1590 °C
(f) Calculated, volume weighted average
(g) Calculated from Rockwell (B or C) using conversion chart [103]

Tungsten is the only non-radioactive, non-precious metal with a density equivalent to DU (Figure 2). Based on the physical and mechanical properties of tungsten and tungsten alloys in comparison to DU, there should be similar ballistic performance so long as the density, strength, geometry and striking velocity of the penetrator is consistent. However, the plastic behavior of the penetrator has been shown to have a strong influence on the penetration efficiency.

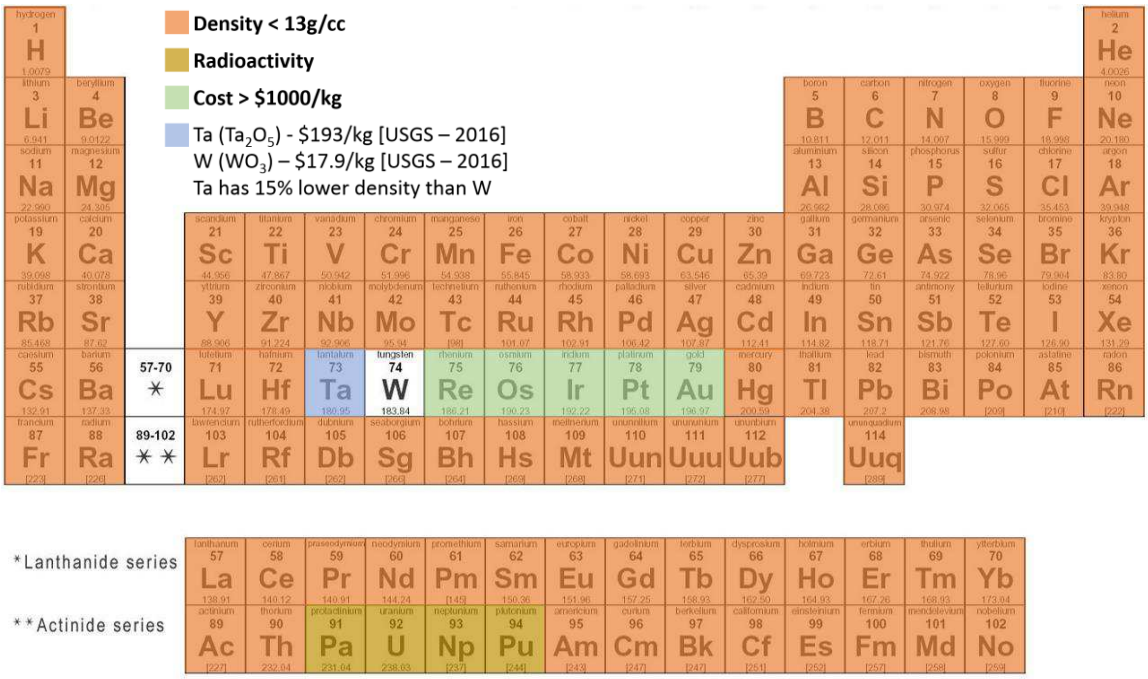

Figure 2 – Viable base materials for DU replacement in kinetic energy penetrator applications. Elements are disqualified based on density, radioactivity and cost in that order (e.g. thorium demonstrates radioactivity, but was previously eliminated based on density constraint). Cost data from [104]. Note: Radioactivity is described by a lack of stable isotopes.

The strength of DU and tungsten alloys is similar, and according to Equation (4), the performance of DU should be equivalent to tungsten alloys of equivalent density [58]. However, experimental evidence shows a considerable difference in the penetration efficiency of DU and tungsten based rounds. For DU, the deformation behavior highly dependent on the strain-rate experienced during specific ballistic events. At lower strain-

rates, DU exhibits stable plastic flow as a result of a high work-hardening ability and strong strain-rate-sensitivity, allowing the material to survive the harsh conditions of gun launch. At high strain-rates (on the order of 10^5/s), plastic flow localization improves the penetration efficiency and provides a reliable mechanism for efficient armor penetration.

2.1.4. Shear banding and ballistic efficiency

Magness provided the first fundamental insight to the mechanisms behind the highly efficient penetration behavior observed for DU-based kinetic energy projectiles [45]. DU experiences plastic instabilities at high strain rates, which result in flow localization, or more specifically shear banding, during terminal ballistics. This deformation mechanism allows the penetrator head to efficiently slough-off in the areas of highest shear leading to what Magness refers to as a "self-sharpening" behavior [46]. By contrast, polycrystalline tungsten and tungsten alloys exhibit stable plastic flow, even at the extremely high strain rates observed during this ballistic event. This stable flow causes more difficulty in shedding the tip of the penetrator causing the penetrator to "mushroom" during target perforation. The difference in projectile geometries after perforating a hardened steel target is shown in the x-ray radiographs of Figure 3.

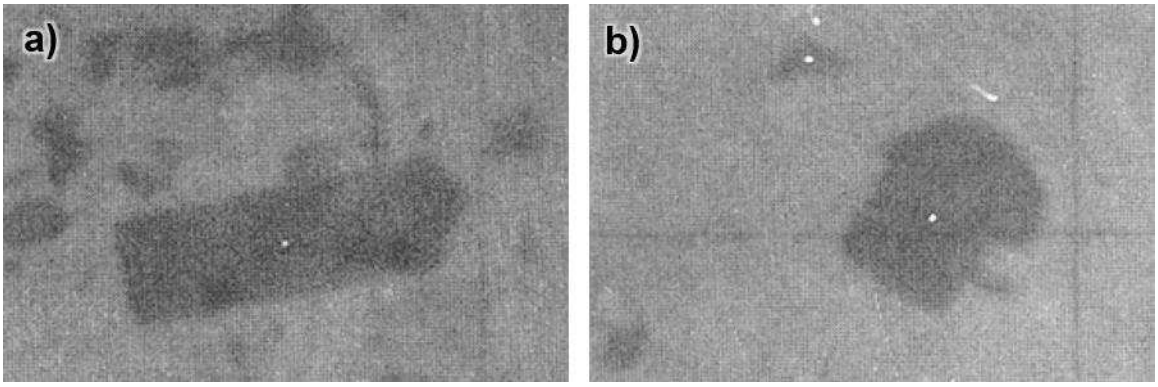

Figure 3 – X-ray radiographs of penetrator materials after perforating rolled homogeneous armor targets. a) Residual penetrator geometry of a "self-sharpened" material indicative of a shear banding mechanisms. b) Residual geometry of a non-shear-banding penetrator showing the "mushroomed" head that is characteristic of stable plastic flow. Modified with permission from [105].

The "self-sharpening" deformation behavior of DU results in a deeper, narrower and more efficient penetration channel when compared to tungsten and tungsten heavy alloy penetrators. The deeper penetration channels are observed over a large range of impact velocities and account for the improved performance of DU in comparison to tungsten-based penetrators. A measurement of the penetration channels and observed deformation mechanisms for DU and WHA penetrators is shown in Figure 4. The shear banding mechanism leads to a significant improvement in penetration efficiency even at equivalent penetrator densities; the DU projectiles may experience up to a 30% improvement in performance at the velocities of interest for kinetic energy rounds [106]

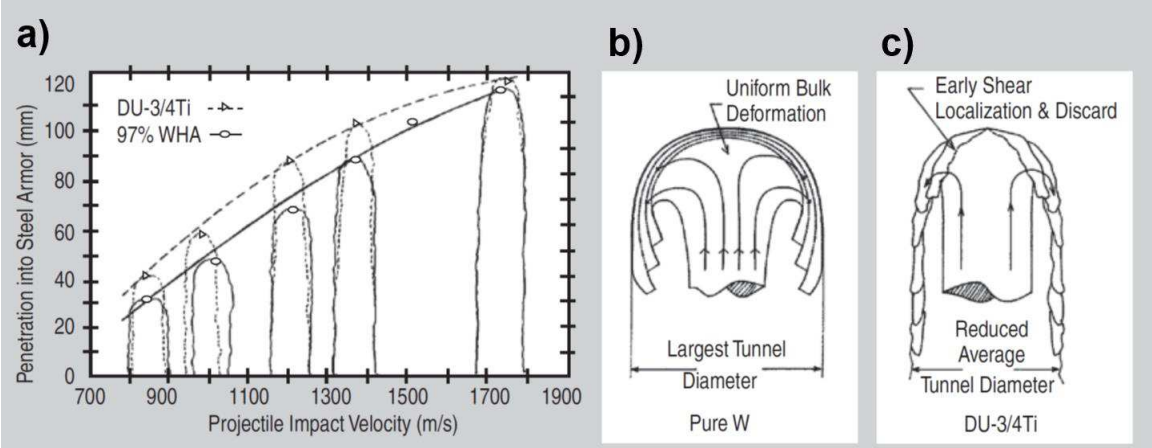

Figure 4 - (a) Comparison of the depth of penetration between DU and WHA into Steel Armor. Both materials had equivalent densities (18.6g/cc) and penetrator geometries (L/D=10) (b) Illustration of the plastic flow behavior of a WHA kinetic energy penetrator. (c) Illustration of the adiabatic shear band deformation of a DU kinetic energy penetrator. [58] These figures have been adapted from [106].

DU demonstrates exceptional ballistic performance by exhibiting the precise plastic behavior required under different conditions of a ballistic event. The viability of tungsten alloys for replacing DU hinges on our ability to manipulate tungsten to show the plastic behavior that occurs naturally in DU kinetic energy alloys. A brief summary of the requirements and the current state of the art for U-¾Ti and various tungsten alloys is shown in Table 2.

Table 2 – Requirements for Kinetic Energy Penetrator Alloys

	Depleted Uranium (U ¾ Ti)	Tungsten Heavy Alloy (W-xNi-yFe) (x+y~10wt%)	Tungsten (nominally pure)	Ultrafine Grained Tungsten (ufg-W)
Radioactivity	Moderate	No	No	No
High Density	Yes	Lower than DU	Yes	Yes
High Strength	Yes	Lower than DU	Yes	Yes
Self-Sharpening Behavior	Yes	No	No	Yes (a), but the mechanism is not clear.
Room Temperature Ductility	**Yes**	**Yes (Matrix Phase)**	**No… Exceptions: Alloy Additions (b), Single Crystals (c), Heavily Worked Wire (c)**	**No… Exceptions: Alloy Additions (b), Deformation Processing(d)**

(a) – [37], (b) – [20], (c) – [8], (d) – [31]

2.2. Fundamental descriptions of deformation and plastic stability

From a mechanics standpoint, plastic instabilities are described by a discontinuity in the homogeneous solution describing the plastic strain of a material. These instabilities may result when local deformations exceed a threshold value and the system transitions from uniform, and controlled behavior to localized, and chaotic behavior. The instability may

present itself as brittle fracture (when local stresses exceed the threshold fracture stress in a material), or strain localization (when the resistance to sustained deformation decreases to the extent that strains concentrate within certain regions, potentially forming shear bands). These types of problems are by no means unique to material deformation, but occur in a number of non-linear and stochastic systems throughout engineering practice [107]. This behavior is often described as a bifurcation at a critical point where a stable and homogeneous elliptical solution of the strain state transitions to an unstable hyperbolic result.

2.2.1. Strain localization

The ductility of a material is not an intrinsic property. There is a strong dependence on the conditions of the test specimen (size, shape, microstructure, dislocation structure, crystal structure, etc.) and the test methods (three-dimensional (3D) stress state, strain rate, etc.) employed during mechanical testing. While it is common to quantify ductility based on the measured elongation during a standardized tensile test [108], this property is rooted in the material's ability to accommodate imposed conditions of stress and strain rate. Ductility is typically high in materials that undergo large amounts of uniform deformation (i.e. before necking). Under most conditions, plastic instabilities will eventually develop over the course of straining, even in highly ductile materials, leading to localized deformation and eventually failure. In a tensile test of a ductile metal, the localized plasticity is observed as "necking", which ultimately leads to rupture within the reduced cross section of the sample.

As discussed previously, plastic instabilities and the localization of strain are not specific to shear band formation and help to describe the onset of failure in a number of critical processes from fracture to fatigue to the common tension test [109]. In 1885, Considère [110] developed a criterion for plastic stability that is worth reviewing in the context of evaluating instabilities in general. For a rate insensitive material under quasi-static, tensile loading conditions (i.e. the true stress (σ) is defined as a function of the true strain (ε) of a material as shown in Equation (5).

$$\sigma = f(\varepsilon) \tag{5}$$

Considère defined the onset of instability as the maximum load in a tension test. The material is considered stable as long as the derivative of load with respect to strain remains positive.

$$\frac{dP}{d\varepsilon} > 0 \tag{6}$$

where P is the applied tensile load. Since the strain is positive over the duration of the test, the onset of instability occurs when the change in load reaches zero. This can be explicitly related to the stress according to Equation (7).

$$dP = 0 = Ad\sigma + \sigma dA \tag{7}$$

where A is the cross-sectional area of the specimen. Given the condition of constant volume during a tension test, the infinitesimal strain ($d\varepsilon$), defined as the increased length of the specimen, normalized by the instantaneous length (dL/L), must be accompanied by a proportional change in cross sectional area of the sample.

$$\frac{dA}{A} = -\frac{dL}{L} = -d\varepsilon \tag{8}$$

Combining equations (7) and (8) provides a description of the critical stress as the derivative of stress with respect to strain.

$$f'(\varepsilon) = \frac{d\sigma}{d\varepsilon} = \sigma \tag{9}$$

Applying a power law model [111] to describe the constitutive relationship between stress and strain for a material that experiences constant strain hardening results in Equation (10)

$$\sigma = f(\varepsilon) = \alpha\varepsilon^n \tag{10}$$

where α is a combined term representing the initial stress and strain of the material and n is the strain (or work) hardening exponent. Differentiating the constitutive model with respect to strain and combining with the results of Equation (10) provides a direct relationship between the critical strain at the onset of instability (ε_c) and the strain hardening behavior.

$$\varepsilon_c = n \tag{11}$$

From this relation, it is clear that materials that exhibit strong strain hardening behavior also tend to demonstrate larger strains to necking during a traditional tension test (i.e. before strain localization sets in).

The Considère criterion is based on the implicit assumptions that the strength of a material is insensitive to strain rate and temperature. In real materials, these assumptions cannot be taken for granted; however, they may be reasonable for specific conditions of a quasi-static test (i.e. $\dot{\varepsilon} < 10^{-3}\ s^{-1}$) in metals. At the point of necking, even in a quasi-static test, the local strain rate increases and rate sensitivity must be considered. The stability criterion for a rate sensitive material (i.e. $\sigma = f(\varepsilon, \dot{\varepsilon})$) was considered using

linear analysis by Hart [112] resulting in a condition for stable plasticity described by Equation (12) [113].

$$\gamma > 1 - m \tag{12}$$

where γ is a work hardening coefficient, and m is the strain rate sensitivity; these variables can be described according to Equations (13) and (14) respectively.

$$\gamma = \frac{1}{\sigma_0} \frac{\partial f}{\partial \varepsilon}\Big|_0 \tag{13}$$

$$m = \frac{\varepsilon_0}{\sigma_0} \frac{\partial f}{\partial \dot{\varepsilon}}\Big|_0 \tag{14}$$

where the subscript 0, indicates the deformation behavior far away from the localization event. The Hart criterion shows that a high strain rate sensitivity also improves the plastic stability of a material by allowing for more strain before a localization (e.g. necking) is triggered.

Modern assessments of plastic instabilities utilize perturbation theory to describe the onset plastic instability in a material [114, 115]. In this process, the onset of instability is described as the situation where a small local deviation of a specific parameter (usually strain), grows with time [69, 109, 115, 116]. If the deformation is stable, the perturbations will decay with time and the solution is termed elliptical. When the perturbations of a given wavelength grow with time, the solution will not converge at extended time-scales and the system is described as hyperbolic. These models give rise to specific criteria for instability in a similar sense to the Considère criterion (Equation (6)); however, the condition for instability does not need to be described *a priori*. Instead, it appears, based on the boundary conditions, and the governing equations for deformation.

The detailed description of plastic instability is highly sensitive the underlying constitutive models employed in defining the instability, both in terms of the controlling variables for deformation (e.g. $\sigma = \sigma(\varepsilon, \dot{\varepsilon}, T)$) and the specific form of the constitutive model (e.g. power law, Johnson-Cook, etc.).

These variations have led to at least a dozen independent models to describe the onset of instability in terms of a critical plastic strain [69] in a fashion similar to Equation (11). However, it is clear that two material parameters, strain hardening (n), and strain rate sensitivity (m), delay plastic instabilities by local perturbations in strain to distribute to the surrounding material. These parameters are helpful for describing the resistance to strain localization in metals. A qualitative description of the influence of these parameters within the context of a standard tensile test is described in Figure 5.

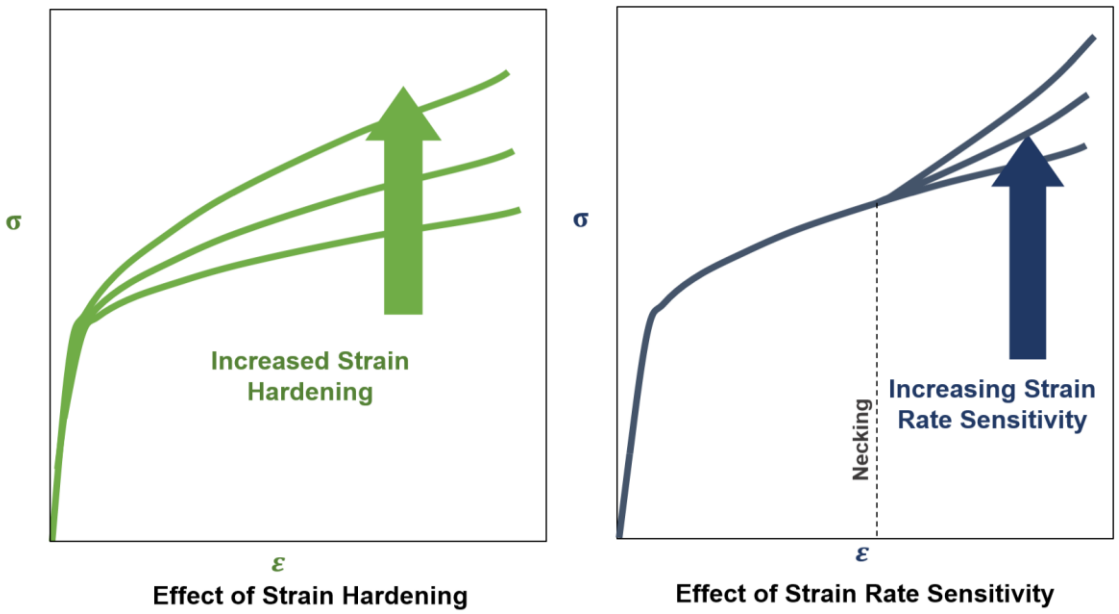

Figure 5 – Qualitative description showing the effects of strain hardening and strain rate sensitivity during a tension test at a constant imposed strain rate. Increased strain hardening (left) and strain rate sensitivity (right) generally improve the plastic flow stability and ductility of metals.

The descriptions of strain localization provided so far, are predicated on the condition that the material exhibits ductile, plastic behavior in the first place. When metals are tested under conditions of limited plastic flow (i.e. based on the poor mobility of dislocations), it is common to observe another type of plastic instability in the form of fracture. The mechanics of fracture, particularly for ductile and semi-ductile materials can be highly complex [117] and the details are generally beyond the scope of this discussion. However, it is important to note that fracture may preclude plastic instabilities in the form of strain localization.

2.2.2. Shear banding

Shear banding describes a very general condition where, strain localization concentrates into intense planar bands of shear. Shear bands prevalent in a number of different materials including: polymers [118], rocks [119], granular materials [120], bulk metallic glasses [121] and of course metals [69]. These highly concentrated localizations in strain can help to describe various phenomena ranging from earthquakes [122], to shock sensitivity in explosives [119], to the basic flow behavior of non-Newtonian fluids [123]. The phenomenon of shear banding is actually fairly uncharacteristic of metals, where dislocation activity tends to cause extensive strain hardening at moderate strains and strain rates. However, the study of shear banding in metals has become much more prevalent, as processes and microstructures that lead to stronger materials tend to limit their resistance to shear band formation.

Although, strain localization is a very general phenomenon, the specific causes of these plastic instabilities can vary significantly. For example, adiabatic shear bands develop under conditions where heat transfer from the system is negligible and the thermoviscoplastic response of a material leads to intense strain localization. Adiabatic shear bands can form with local strains in excess of 100 [69] and a temperature rise that can exceed 1000°C [124]. In other cases, shear bands may form based on crystallographic texture, which can be initially present in a material [125], or develop over the course of straining [126, 127]. In polycrystalline metals, the strain inside of the shear band depends on the dynamic evolution of texture. In the case of bulk metallic glasses, a shear band can form based on free volume within the material [69], the strains inside of the band can exceed 35, and propagate at a velocity of 100m/s.

Shear banding tends to result in catastrophic failure by fracturing along the band [113]. However, shear banding does not always end catastrophically, particularly if the deformation becomes stable once more, based on work hardening after the band has formed. If the plastic behavior stabilizes inside of the band, this forces the shear band to grow laterally and propagate across the entire specimen. This is commonly observed in Lüders bands [128], which resulting from an upper yield point phenomenon common to mild steels. This is also observed based on the Portevin-Le Chatelier (PLC) effect [129], caused by dynamic strain aging that is common to precipitation hardened aluminum alloys tested under the appropriate conditions of temperature and strain rate. These two types of propagative shear bands are distinguished by the mechanism that leads to instability: Lüders bands correspond to a deficiency in the local strain hardening behavior ($n \leq 0$), while PLC bands result from a deficiency in strain-rate-sensitivity ($m \leq 0$) [130].

There are also a number of shear bands that form based on a *Lüders-like* phenomenon. Irradiated metals are also prone to shear banding as dislocations moving through the microstructure clear out the unstable defects induced by radiation damage [131, 132]. Although this mechanism is slightly different from the unpinning of dislocations from solute atmospheres [133]. They show similar behavior, and are often classified as Lüders bands [134].

The susceptibility of a material to shear banding depends on the specific mechanisms that lead to plastic instabilities in the first place. Since dislocation activity describes deformation behavior in most of these materials, dislocations play an important role in describing what leads to the instabilities in the first place. For instance, Lüders bands

form when straining causes a significant increase in the number of mobile dislocations, and materials with annealed microstructures or unstable radiation induced defects are more susceptible to this plastic instability. The PLC effect occurs based on repeated pinning and unpinning of dislocations by solute atoms. For this case, the mobility of dislocations and solutes must be considered and the susceptibility becomes inherently sensitive to temperature and strain rate. This is not to say that twinning or other mechanisms (e.g. free volume in granular materials and possibly metallic glasses [69]) cannot lead to a shear banding, but when deformation is controlled by dislocation activity, dislocation activity will also determine the strain hardening ability and strain rate sensitivity of a material.

Adiabatic shear banding, may also be understood based on dislocation behavior. Materials that exhibit a strong thermal softening behavior are more susceptible to adiabatic shear bands. This type of behavior is generally associated with thermally activated dislocation mobility, which explains the general observation that HCP and BCC materials are more susceptible to shear band formation. Other factors will certainly play a role (thermal conductivity, heat capacity, etc.), but dislocations are critical. Describing the physical mechanisms that lead to shear banding is essential for understanding the initiation event so that shear bands can be resisted or induced, depending on the specific application of the material.

2.2.2.1. Adiabatic shear banding

Some of the first descriptions of shear banding were reported by Tresca as early as 1878 [135] where highly localized shear was observed during high strain rate deformations as

shown in Figure 6, which may have been the first record of strain localization in the context of what we now understand to be shear bands [136]. Zener and Holloman, further recognized the influence of thermoviscoplastic softening and dubbed the conditions for localization resulting from high-rate deformation as “adiabatic” in 1944 [70]. The term adiabatic is fitting, as the time scales of testing (on the order of milliseconds to seconds) do not allow for significant heat transfer from the deformed region to the surrounding material [137]. In contrast, quasi-static testing usually allows sufficient time for the temperature to equilibrate (particularly in metals with a high thermal conductivity) and the conditions are largely isothermal. Over the past few decades, considerable research has been carried out to understand adiabatic shear banding based on the material properties and the mechanics of strain localization [69, 115, 138-140].

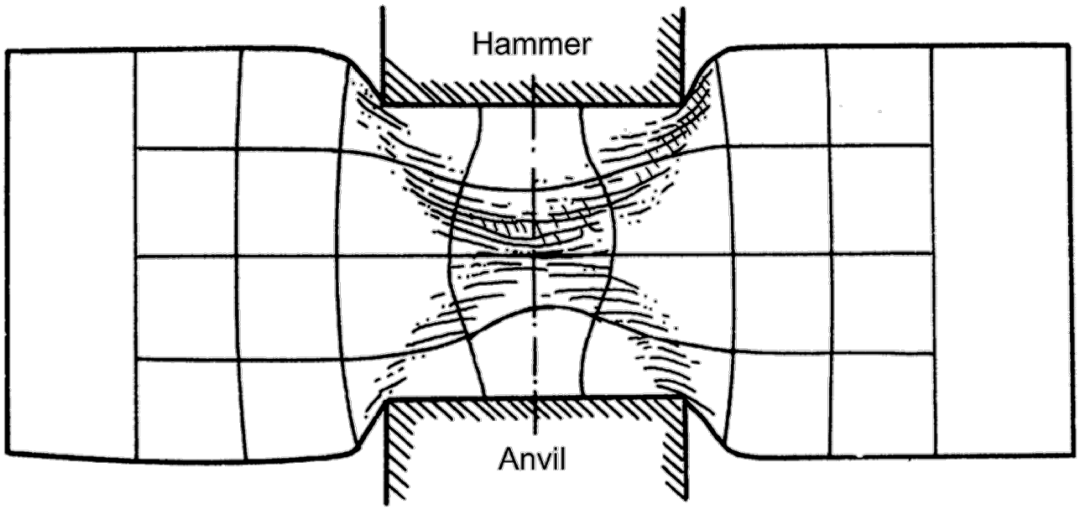

Figure 6 – Plastic distortion of lead stamped with a hammer. The initially uniform grid was drawn into a wax coating on the front surface of the lead bar. It was shown that significant heat was generated and melting of the wax occurred in an ‘X’ shaped region, which Tresca described as the direction of maximum “sliding” [109, 135].

For DU based penetrators, the "self-sharpening" behavior that promotes a high ballistic efficiency is the result of an "adiabatic" shear banding mechanism based on the research of Magness and coworkers [45, 106]. In the case of adiabatic shear banding, the plastic instability develops because there is a positive feedback loop where deformation, temperature rise, and the associated reduction in flow stress are linked to localize plastic flow into small bands of deformation as described by the schematic in Figure 7. There is a critical point (in terms of strain and strain rate) when the constructive feedback from these intimately connected processes reaches a tipping point and a small perturbation in strain will grow and continue to localize.

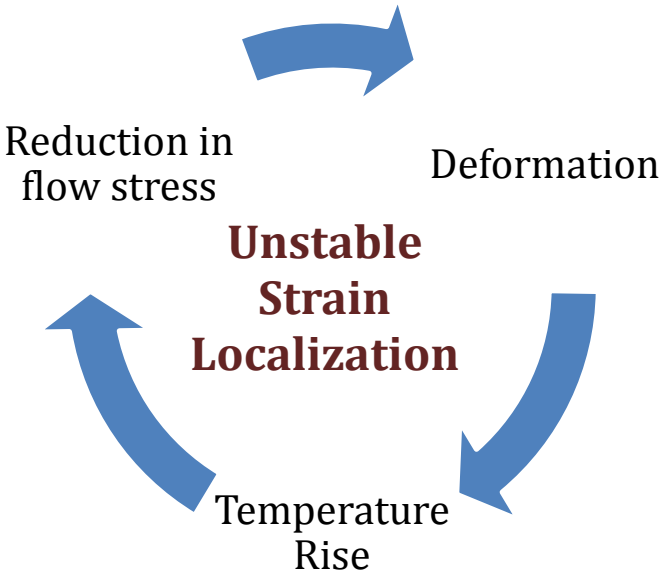

Figure 7 *– Schematic of the positive feedback loop responsible for "adiabatic" shear banding*

Adiabatic shear bands tend to develop in stages where homogeneous deformation develops to localized strain, finally becoming a shear band. In general, adiabatic shear bands have a thickness in the range of 10-100μm [141]. The actual thickness is a

characteristic of the material (thermal conductivity, strength, melting point) and generally independent of the external testing conditions [142], though these testing conditions may determine whether the band will form in the first place.

The generation of adiabatic shear bands is usually undesired. In metal forming and rolling operations, shear bands lead to inconsistencies in material properties and surface finish. In machining operations, shear banding can lead to “tool chatter” and cause additional wear or fracture of the tool-piece. For ballistic applications, adiabatic shear bands in the armor or the penetrator tend to increase the efficiency of armor penetration. In general, their desirability depends on whether the goals are to provide improved lethality or protection. A graphical description for each of these specific adiabatic shear banding events is shown in Figure 8.

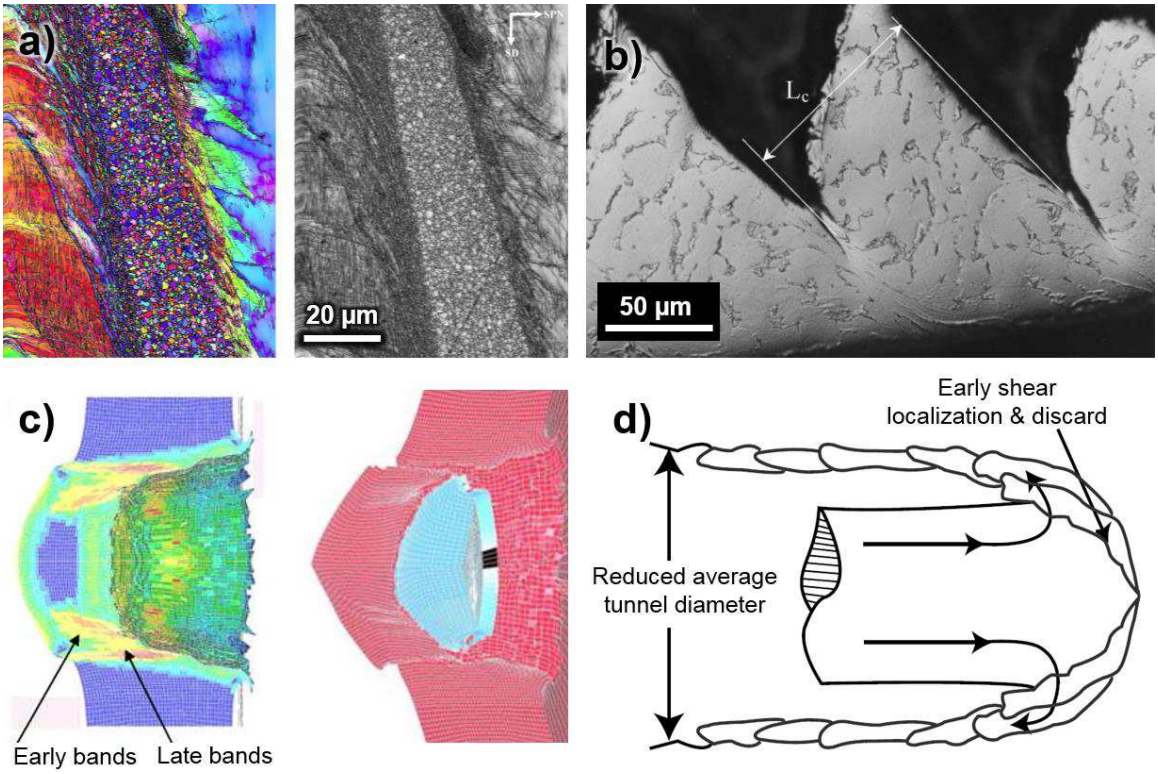

Figure 8 – Examples of adiabatic shear bands in several different materials and applications. a) deformed interstitial steel exhibiting a temperature rise sufficient to recrystallize the microstructure inside of the band [143], b)shear bands in machining chips from Ti-6Al-4V [144], Numerical simulation of shear band formation in armor during penetration by a fragment simulating projectile [145]. This "plugging" phenomenon limits the performance of metallic armors. d) Schematic of how adiabatic shear banding of a DU based kinetic energy penetrator, effectively improves ballistic penetration efficiencies [44].

The mathematics for understanding various adiabatic shear banding phenomena have been described in reviews by Wright [115] and Dodd and Bai [69]. Wright developed a model to describe the propensity of shear band formation (X_{ASB}) as a function of material parameters including: strain rate sensitivity (m), strain hardening exponent (n), and a thermal softening parameter (a) shown in Equation 15. The thermal softening parameter is a function of the flow stress (σ_f), temperature (T), density (ρ) and specific heat capacity of the material (C_p) described in Equation 16.

$$X_{ASB} = \frac{a}{m}\min\left\{1, \frac{1}{\left(\frac{n}{m}\right) + \sqrt{\frac{n}{m}}}\right\} \tag{15}$$

$$a = -\frac{\partial \sigma_f}{\partial T}\left(\frac{1}{\rho C_p}\right) \tag{16}$$

Similar to previous assessments of plastic instabilities, high strain hardening (n) and strain rate sensitivity (m) help to resist shear band formation, though there is also a considerable dependence on the thermal softening behavior of the material. The high degree of strain hardening and strain rate hardening of tungsten demonstrate a poor susceptibility for shear band formation [146] except in cases where the specimen geometry is designed to promote shearing (e.g. top hat specimens [147]). Considerable research has been carried out to destabilize plastic flow and promote shear banding [48, 105, 148].

2.2.2.2. Geometric shear banding

The glide of dislocations is inherently limited based on crystal structure. Even in cubic systems, which have a high degree of symmetry, there is always an orientation dependence on the strength of a material and the plastic behavior in general. Geometric shear bands were originally described based on the observation that orientation can lead to strain softening and shear banding based on the loading conditions, and without requiring the material to actually soften in any physical sense [127]. This observation was made for the case of single crystal aluminum with a shear band shown in Figure 9 [127].

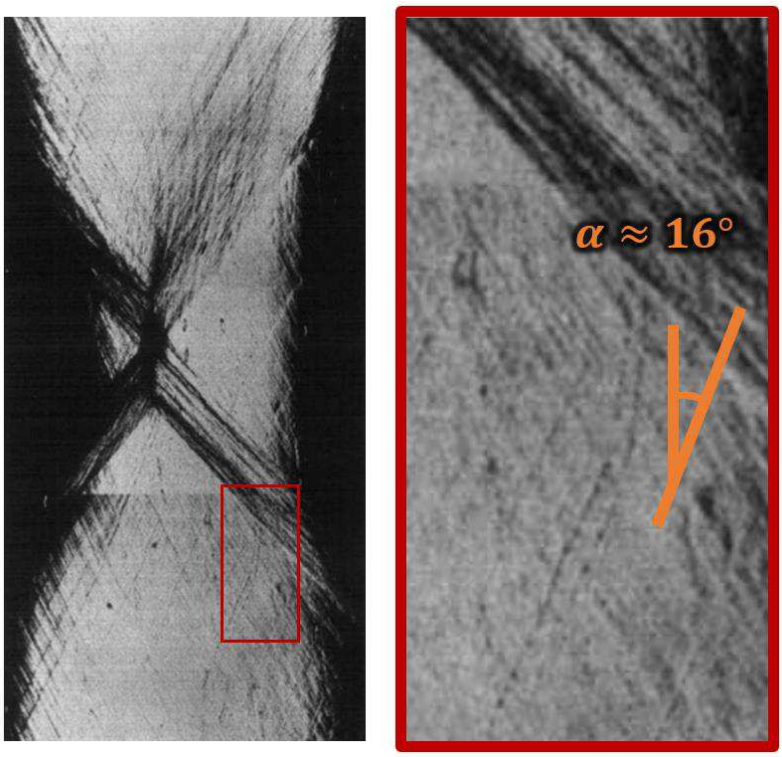

Figure 9 – Geometric shear band observed in Al-3Cu single crystal. The shear band was formed based on reorientation of the crystal during straining. A magnified image of the region near the shear band (right) shows the degree of strain-induced reorientation before the geometry was favorable for the shear band to form. Modified from [127].

It is important to note that a certain degree of strain was required for the crystal to rotate to a soft orientation in the case of the aluminum single crystal because softening is observed with respect to the original orientation of the crystal. Geometric softening may also result in transformation of single crystals to polycrystalline materials based on the development of soft orientations via texturing.

2.3. Plastic behavior of ultrafine grained metals

Bulk ufg and nanocrystalline materials are commonly classified by having a grain size below 1,000 and 100 nm respectively. These materials have been researched heavily over the past several decades because of their promise to make drastic improvements to the

physical and mechanical properties of a material [77, 149]. These studies are particularly important to the field of materials science, where the relationship between processing, structure, properties and performance has been a long-standing paradigm of materials development. In particular, the development of new processing technologies, specifically for controlling grain size while maintaining a high degree of purity, are enabling a new level of understanding and control in the development of new materials.

The Hall-Petch [150, 151] relationship describes the increase in flow stress (σ_y) associated with a reduction in grain size (D) to the power of -0.5 as shown in Equation 17. While this formulation has been described based on several specific mechanisms including: dislocation pile-ups at grain boundaries [152], or the boundaries acting as dislocation sources [153, 154], or the overall dislocation density [74] these are specialized theories and do not account for the broad applicability of this largely empirical Hall-Petch relationship.

$$\sigma_y = \sigma_0 + kD^{-\frac{1}{2}} \tag{17}$$

As the grain size of a metal is reduced beyond a certain critical limit, the Hall-Petch relationship begins to deviate from the relation shown in Equation 17 as a result of "different deformation mechanisms" in the material [155, 156]. In FCC materials at very small grain sizes (on order of 10nm) it has been proposed that novel mechanisms of plasticity may become possible, dislocations still play a role in plasticity at fine grain sizes [149]. The precise grain size where breakdown occurs is material specific, a change in deformation mechanisms has been observed in many different systems. In BCC metals like iron, the deviation from ideal Hall-Petch behavior is particularly apparent when grain

sizes approach 400 nm and below [155]. These grain sizes coincide with reports of plastic instabilities, but these grain sizes appear to be well within the range of deformation that is mediated by conventional dislocation theory. The extended Hall-Petch behavior of iron is shown in Figure 10.

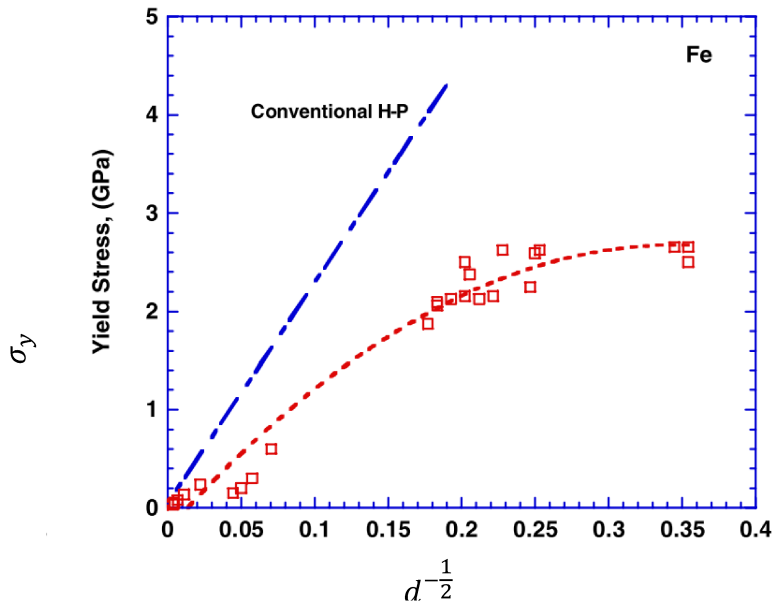

Figure 10 - Deviations from ideal Hall-Petch behavior reported in BCC iron. From Meyers et al. [155].

The development of plastic instabilities in terms of strain hardening (n) and strain rate sensitivity (m) is particularly useful for describing the limitations to the ductility of ufg metals [116]. While there are a few notable exceptions [157], ufg metals exhibit higher strength and much lower ductility than their coarse-grained counterparts as a result of the limited strain hardening ability of these materials [158, 159]. The influence of grain size on the strain rate sensitivity is less intuitive. Wei et al. [57, 160, 161] have shown that the strain rate sensitivity is a strong function of the grain size; however, the observed trend is a function of the crystal structure of the material as shown in Figure 11. FCC metals tend

to have a low strain rate sensitivity [162], which increases as grain size decreases. Coarse grained BCC metals show a fairly high strain rate sensitivity, which decreases with decreasing grain size.

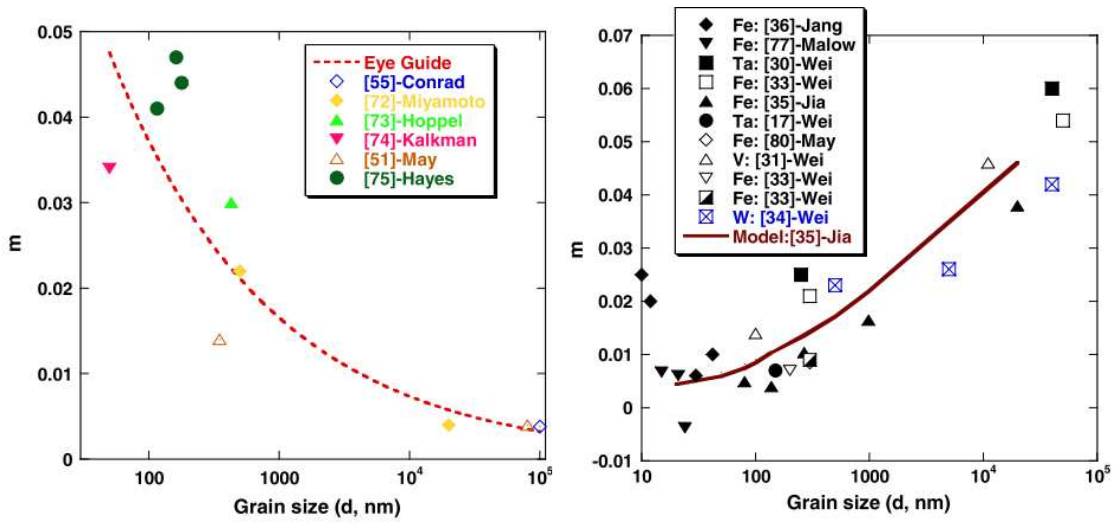

Figure 11 – Strain rate sensitivity of FCC (Aluminum) and BCC alloys as a function of the reported grain size. The primary author is reported next to each symbol and reference numbers correspond to the original manuscript by Wei. Reprinted from [160].

The trends observed in Figure 11 provide significant insight to the susceptibility of ufg materials to shear banding. While both FCC and BCC materials demonstrate limited strain hardening ability (n), shear bands have not been observed in ufg FCC alloys subjected to quasi-static compression [113]. In contrast, several BCC alloys have been shown to shear band once the grain size reaches a critical value within the ufg regime [58, 163-166]. In short, increasing the strain rate sensitivity (m) can deter development of plastic instabilities that result in shear band formation.

2.3.1. Shear banding in ultrafine grained metals

The assessment and plastic instabilities and strain localization relies on the underlying assumption that the material's ductility is sufficient to promote yield and plastic flow instead of brittle failure. The deformation behavior of tungsten and resistance to fracture is ultimately the result of processing, properties, microstructure and composition. Controlling these variables can lead to drastic changes in the plasticity mechanisms of tungsten and promote stable flow, localized flow or brittle fracture as shown in Figure 12. Each of the deformation mechanisms are not mutually exclusive and play an integral role in the performance of kinetic energy penetrators. For example, DU exhibits stable plasticity at moderate strains and strain rates, high rate deformation leads to early shear banding and catastrophic failure results from fracture within the shear band. Each of these processes are critical for effective launch and penetration mechanisms.

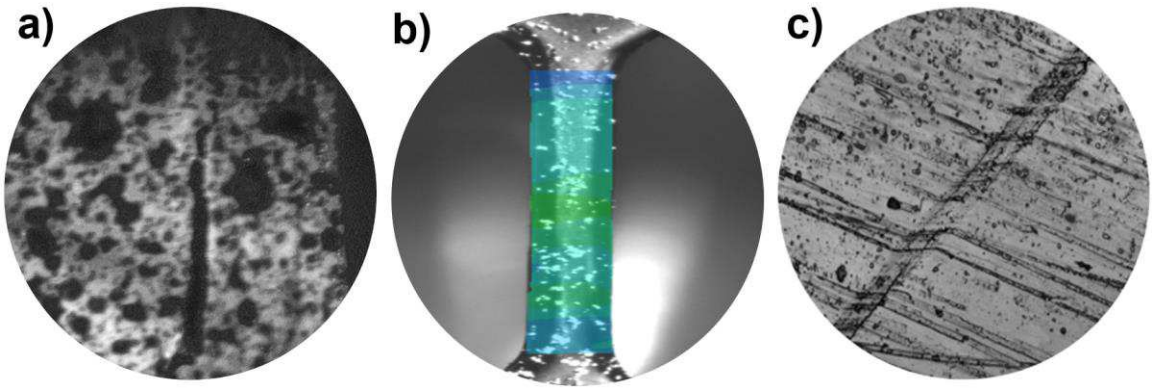

Figure 12 – Various deformation mechanisms observed in tungsten and the factors that affect plasticity and plastic instabilities. a) Brittle fracture in polycrystalline tungsten with cracks parallel to the loading direction. b) Stable plasticity in tungsten single crystals resulting from strong work hardening behavior. c) Shear banding observed in ufg tungsten-5 wt% rhenium at quasi-static rates. Mechanisms of strain localization in ufg metals are not adequately described by existing strain localization mechanisms.

2.3.1.1. Shear banding in ultrafine grained iron

Refining grain size has significant implications for the plastic stability [158] and shear band susceptibility of ufg metals. As discussed previously, plastic instabilities are

generally a detriment to most engineering applications, but the observation that ufg iron may demonstrate shear banding at a grain size of several hundred nanometers [165] sparked a series of investigations to promote shear banding in tungsten and tungsten alloys using similar methods [53, 55, 57, 67, 68, 163, 167-169]. Pure iron, like tungsten, shows a strong work hardening behavior in most instances, and shear banding is generally not observed, even at dynamic strain rates. The influence of grain size on plastic instability and the formation of shear bands at quasi-static rates has been observed by several research groups [165, 170-173], but the detailed mechanisms for this localization behavior is still under debate.

The strain localization observed by Jia et al and Wei et al. in ufg iron from powder metallurgical processing routes [166, 174], formed at quasi-static rates and had a distinctly different character from the adiabatic shear bands that were previously reported for iron alloys tested at high strain rates. In particular, shear bands initiate at very low macroscopic strains and there does not appear to be a regime of stable deformation developing into localized deformation and ultimately resulting in shear band formation as shown for adiabatic shear bands Figure 13.

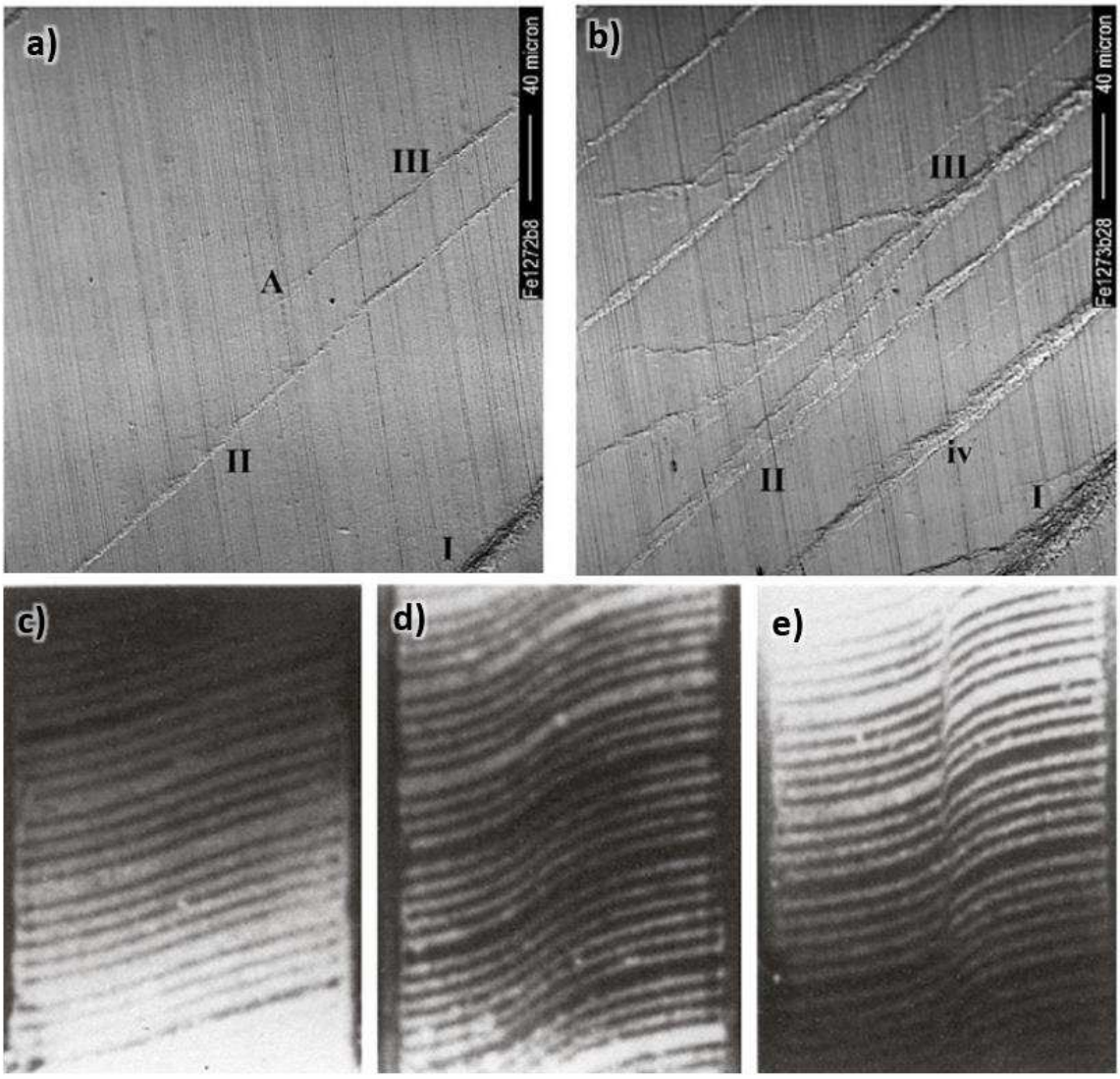

Figure 13 – Shear bands observed at successive levels of deformation. Hot pressed iron (top), with an ultrafine grain size (268 nm) tested in compression under quasi-static strain rates from [165]. HY100 steel tested under torsion at high strain rates. Fiducial markers, running horizontally across the specimen surface show three distinct deformation conditions (c) uniform deformation, (d) localized deformation, and (e) intense shear banding, from [175].

Wei et al. [169], conducted a follow-up study on iron with a similar grain size (~300 nm), but processed by ECAE. This material showed limited strain hardening at quasi-static rates, and failed by shear-banding at dynamic rates; however, shear banding was not reported for the quasi-static tests. The difference in the stability of deformation processed

and consolidated iron was attributed to impurities and porosity that result from powder metallurgical processing.

2.3.1.2. Shear banding in ultrafine grained tungsten

Similar investigations into shear band formation in ufg tungsten were met with varied success. Processing ufg by equal channel angular extrusion showed that brittle fracture, observed parallel to the loading axis, may preclude shear band formation in ufg tungsten [68] as shown in Figure 14. The suppression of brittle fracture is critical for assessing the plastic deformation behavior and shear band susceptibility of tungsten.

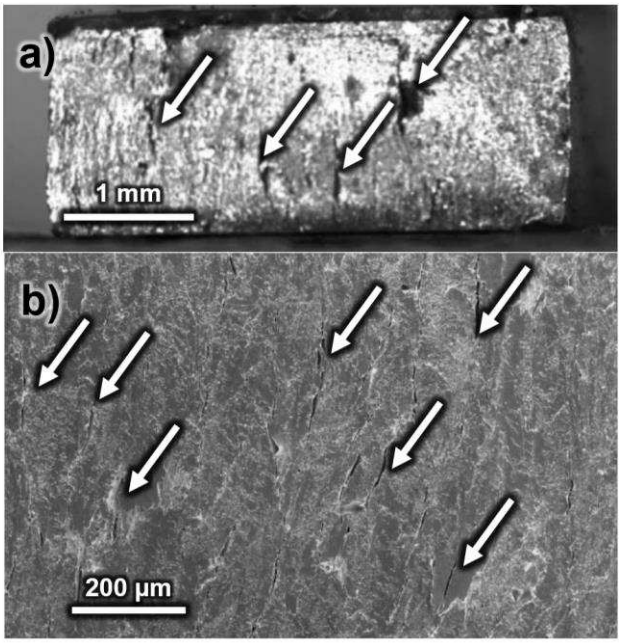

Figure 14 – Brittle Fracture in ECAE Tungsten, loading direction is vertical. a) macroscopic and b) microscopic cracking along the loading direction [68].

The first demonstrations of shear banding in ufg tungsten were observed by Wei et al. in material processed by equal channel angular extrusion with subsequent cold rolling[68]. However, the grain size of ~500nm was considerably larger than the previous iron

samples that demonstrated shear banding and shear banding was observed only at high strain rates. Additional studies showed that that shear banding could occur in severe plastic deformation samples processed by high pressure torsion [36, 37] or cold rolling [176], as shown in Figure 15. These severe plastic deformation processes result in highly textured materials with highly anisotropic properties. Unfortunately, shear banding was only reported for specific orientations that are not conducive to producing long rod penetrators.

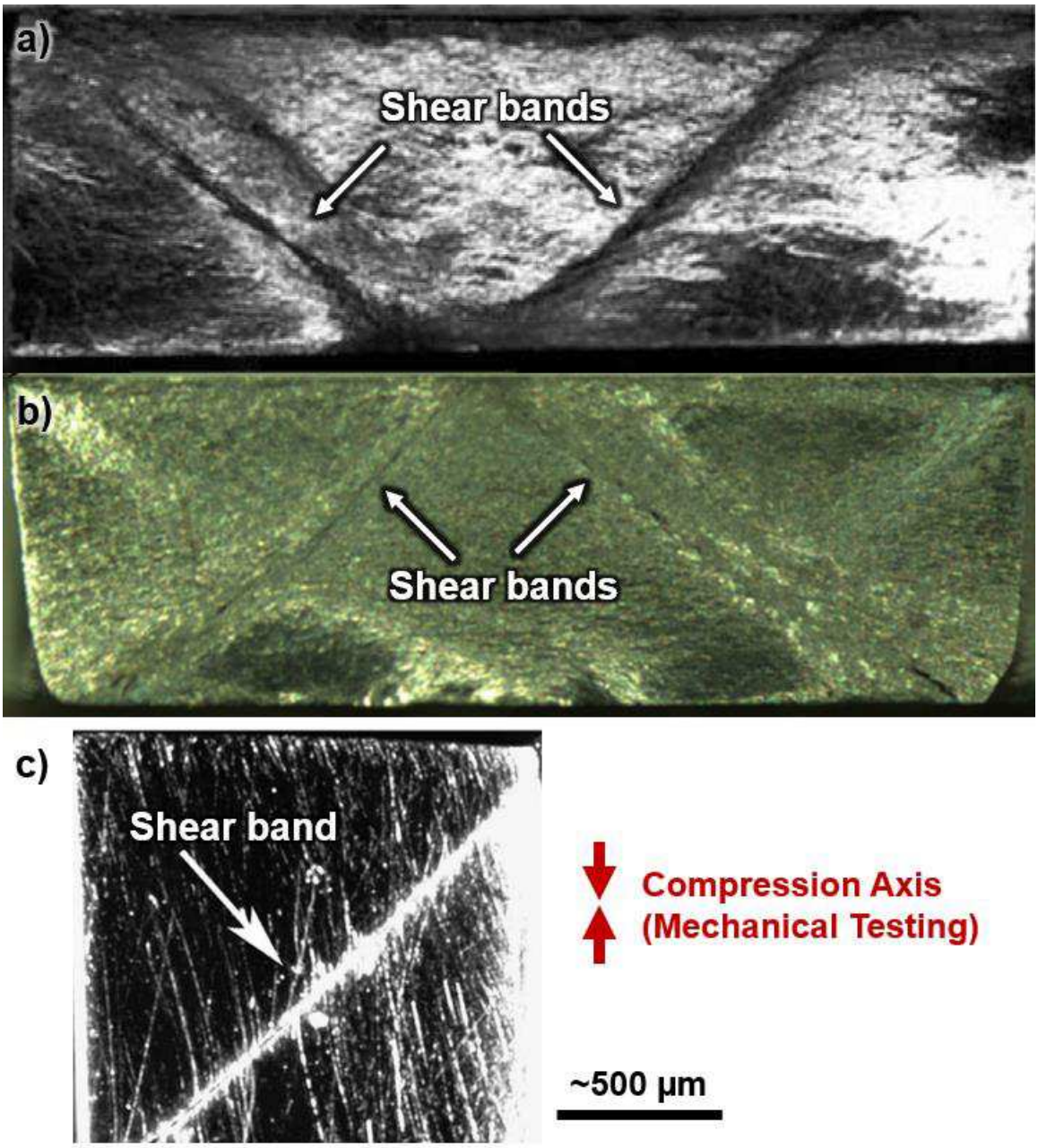

Figure 15 – Shear banding observed in ufg tungsten processed by severe plastic deformation. Samples are loaded in compression along the vertical axis of each image. a) equal channel angular extrusion followed by cold rolling [68], b) conventional cold rolling [176], and c) high pressure torsion [37].

2.3.2. Adiabatic shear banding in ultrafine grained metals

The strain localizations observed in ufg tungsten were described to be adiabatic based on the mathematical description provided by Wei et al. [68]. In essence, Wei applied the

concept of a thermal conduction length-scale (X) to see whether the thermal diffusivity (α) and duration of the test (Δt) could account for a distance larger than the observed shear band as shown in Equation (18) and the thermal diffusivity is described by the thermal conductivity (k), the density (ρ) and the specific heat capacity (C_p) of the shear banding material as shown in Equation (19). Equation 18 is a simplified estimate, but if the thermal conduction length scale is the same size or smaller than the width of the shear band (δ_{SB}), then the band is considered adiabatic.

$$X = \sqrt{\alpha\, \Delta t} \tag{18}$$

$$\alpha = \frac{k}{\rho C_p} \tag{19}$$

According to Wei et al. [68], if the thermal conduction length-scale is smaller than the shear band, the band is adiabatic. Actually, this method only provides a good technique to definitively show that the shear band is **not** adiabatic. If the thermal length scale is much larger than the width of the shear band ($X \gg \delta_{SB}$), then it is clear that there has been sufficient time to diffuse heat away from the local perturbations in deformation that ultimately lead to shear banding and the instability can be approximated using isothermal conditions. In fact, the thermal diffusivity for all metals varies by approximately two orders of magnitude, generally between 10^{-6}-10^{-4} m^2/s [5] (with the exception of selenium, which has an unusually low thermal conductivity). Shear bands tend to have widths in the 10-100 μm range [141]; however shear bands in ufg metals and bulk metallic glasses can be much finer. Accounting for the maximum shear band width and the minimum thermal diffusivity, any test for any metal that takes more than 0.1 seconds to complete shouldn't be suspected of shear banding by an adiabatic mechanism.

The shear banding as a result of high rate testing conducted by Wei et al. [36, 68, 176] showed distinct characteristics of thermoplastic softening and the conditions of testing were certainly fast enough to be considered adiabatic. However, the shear banding would not be likely to occur without specific microstructural features that impeded strain hardening and strain rate hardening in these ufg tungsten samples. The blanket description of adiabatic shear banding ignores the grain size and texture effects that could promote the localization of strain even under non-adiabatic conditions.

2.3.3. Geometric shear banding in ultrafine grained metals

The original observations of shear banding in ufg BCC iron, noted that once a critical grain size is reached, shear banding is observed, even at quasi-static rates [165, 166, 170]. Wei et al. [177] stated that this unusual behavior could not be explained by adiabatic mechanisms and provided an explanation based on ultrafine grain sizes making it "possible for a large group of grains to quickly develop the texturing favorable for slip propagation in a cooperative manner." This phenomenon was termed "geometric" shear banding after a similar description provided by Asaro [127] to explain a specific condition where soft orientations develop over the course of straining single crystals. The geometric softening, which is essentially described by negative strain hardening as the result of texture that develops during plastic straining.

The mechanisms of geometric shear banding were investigated more thoroughly by Joshi and Ramesh [71-73] and a mathematical description of the grain reorientation and softening process was created that could account for differences in stability based on the mechanical characteristics of specific systems as described by Figure 16.

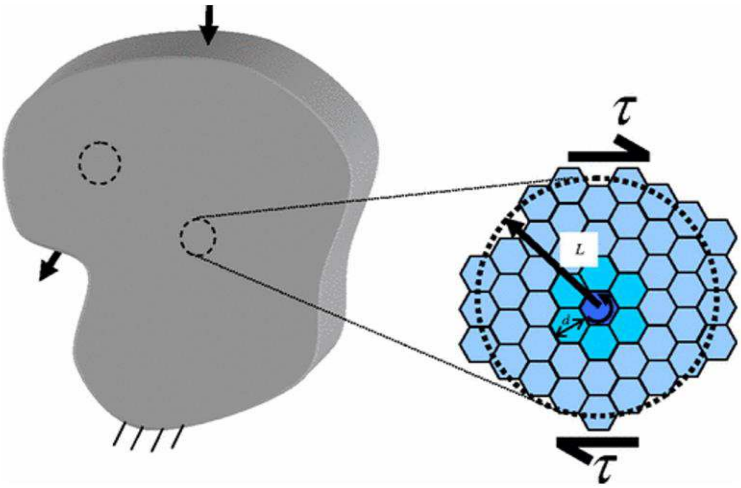

Figure 16 – Geometric shear banding model describing the localization of ufg materials based on collaborative rotation of grains to orientations with reduced flow stresses [71].

The geometric shear banding model uses a "first-order perturbation analysis of a nonlocal continuum model for the grain rotation driven shear instability." Ultimately, the model is based on the assessing the fraction of grains that have rotated to the "soft" orientation (ϕ) based a coefficient for rotational diffusion (D_r), initial texture and grain size effects (ψ), and the local plastic shear strain rate ($\dot{\gamma_p}$) as described by Equation 20.

$$\dot{\phi} = \psi\dot{\gamma_p} + D_r\frac{\partial^2\phi}{\partial X^2} \tag{20}$$

The backbone of this model is the formulation of a critical length-scale (λ_{crit}), which is the critical wavelength, derived from perturbation theory, where localization is prevalent. When the grain size (D) approaches this critical wavelength, based on a strength index ($\boldsymbol{\mathcal{M}}$), shown in Equation 21, the material becomes inherently unstable. The strength index described by the measurable and tabulated values of material properties including: the shear modulus (μ), strain rate sensitivity (m), and a parameter ($\overline{c}$), which accounts for a difference between hard and soft orientations (τ_{h0} and τ_{s0} respectively) as described by

Equation 22. (Note: Equation 22 was modified from Joshi's original formulation [71], because a typo resulted in negative and non-realistic values for the strength index.) The strength index can be calculated based on the material parameters describing

$$\lambda_{crit} = \left(\frac{\boldsymbol{\mathcal{M}}}{(2-\nu)\psi\hat{\gamma}_p^h} \left(\frac{d^2}{j}\right) \left(\frac{\eta_{bulk}}{\eta_{eff}}\right) \right)^{\frac{1}{2}} \tag{21}$$

$$\bar{c} = 1 - \frac{\tau_{h0}}{\tau_{s0}} \tag{22}$$

$$\boldsymbol{\mathcal{M}} = \frac{\tau_{s0}\bar{c}}{\mu m} \tag{23}$$

A more detailed description of the variables in Equation 21 can be found in the reference [71]. For a given material (e.g. tungsten) this formulation allows the strength index ($\boldsymbol{\mathcal{M}}$) to be calculated based on only on the measured strain rate sensitivity. This value may be plotted versus grain size to describe the stability of the system as shown is Figure 16.

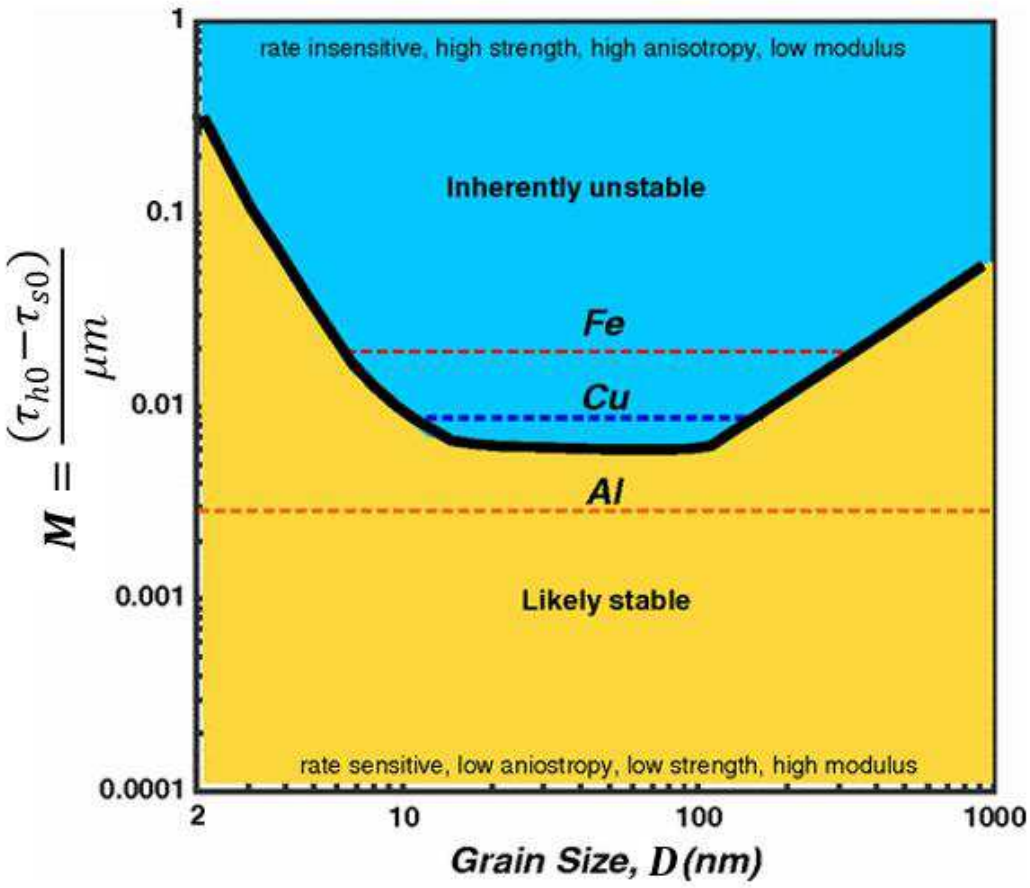

Figure 17 – Stability of various tungsten-based microstructures as a function of the strength index (M), and grain size (D), from [71].

Much of the effort to describe shear band formation in ufg materials has concentrated on the effect of grain size on the strain rate sensitivity (SRS) (m) of the system as opposed to the strain hardening behavior (n). These efforts focusing on strain rate sensitivity of ufg metals are critical because they effectively distinguish between the stability of BCC and FCC metals as a function of grain size. The strain rate sensitivity of FCC metals tends to increase as grain size is reduced beyond a critical limit; in contrast, BCC metals show a decrease in strain rate sensitivity, which has significant implications for plastic stability during deformation. While these trends are generally accepted, the basic causes for these differences in terms of dislocation mediated plasticity is still an active area of research.

2.4. Strain gradient plasticity

The strain rate sensitivity of ufg BCC metals show a significant decrease in the strain hardening exponents compared to coarse grained material [178]. From a continuum mechanics standpoint, these two conditions could promote plastic instability without requiring any consideration of thermal- or texture-based softening. Unfortunately, the continuum analysis does not elucidate the fundamental mechanisms that lead to these changes in flow and strain rate dependent behavior. In an early evaluation of the shear instabilities for ufg metals, Ma [158] cited dislocation activity to account for the changes strain rate sensitivity and strain hardening behavior that contribute to plastic instabilities (and shear band formation) in ufg metals. In recent years, a discussion of strain gradient plasticity has emerged to explain the additional dislocations that are geometrically necessary to account for the straining of heterogeneous and/or confined microstructures.

2.4.1. Describing physical phenomena with strain gradient plasticity

This basic mechanism of strain gradient plasticity accounts for several fundamental descriptions of the mechanics of materials, particularly in ufg materials. These mechanisms are not accounted for by traditional continuum plasticity theory, which does not have an internal length scale and considers infinitesimal segments of material to have the same properties as the bulk [179]. Furthermore, these classical plasticity theories rely on the assumption that the stress of an individual point is a function only of the strain at that point [180]. When these models approach a spatial resolution approaching the micrometer scale, lattice curvature, or strain gradients become critical. Experimentally, the ability to strain harden is not isolated to a single point, but instead relies on the

dislocation density (and by relation, the curvature) of the surrounding lattice [78, 181-184]. Furthermore, these observations are intrinsically linked to the dislocation content in a material, which provides a physical description of the hardening phenomenon.

Ashby [74] developed the concept of strain gradient plasticity to account for the increased work hardening rate of heterogeneous materials. The past few decades have been filled with several experimental observations of strain gradient plasticity to describe the general "smaller is stronger" [77, 185-188] phenomena in materials. Specifically, Fleck et al [78] used strain gradient plasticity to describe a threefold increase in the specific torque required to deform a copper wire as the diameter decreases from 170 μm to 12 μm. Nix and Gao [184] utilize strain gradient plasticity to describe indentation size effects observed in nanoindentation experiments, which may increase the strength by a factor of two as the indentation depth decreases from 10 μm to 1 μm. Finally, a recent critical review by Cordero et al. [189] shows that this mechanism provides the most consistent explanation of the "constants" associated with the Hall-Petch relationship between grain size and yield strength (Equation (17)).

Dislocations describe much of the key phenomenological behavior of crystalline materials undergoing plastic deformation. Conventional work hardening occurs because dislocations become stored in the lattice during straining and require additional stress to overcome the barriers imposed by stored dislocations. The shear stress required for a material to yield (τ_y) may be calculated as a function of the total density of stored dislocations (ρ_T) according to the Taylor formula shown in Equation (24).

$$\tau_y = \alpha \mu b \sqrt{\rho_T} \tag{24}$$

where α represents a material constant, μ is the shear modulus, and b is the Burgers vector assocated with the dislocation.

Following the descriptions of Ashby [74], from a macroscopic viewpoint, the dislocations may be of the form where they are required to maintain continuity in a curved lattice, referred to as geometrically necessary dislocations (GNDs). Otherwise, the stored dislocations trapped by "random" events in the lattice and are described as statistically stored dislocations (SSDs). At this macroscopic scale, SSDs may not contribute to the macroscopic curvature, but nevertheless contribute to the overall dislocation density and the work hardening of the material. The total dislocation density may be described as the summation of GNDs and SSDs per unit volume of material as shown in Equation (25)

$$\rho_T = \frac{(n_{SSD} + n_{GND})}{V} = \rho_S + \rho_G \tag{25}$$

where n_{SSD} and n_{GND} are the number of SSDs and GNDs respectively per unit volume (V), which may be descibed in terms of the individual dislocation densities.

The strengthening behavior occurs naturally by accounting for the density of SSDs and GNDs content according to Equation (24) and Equation (25):

$$\tau = \alpha\mu b\sqrt{\rho_T} = \alpha\mu b\sqrt{\rho_S + \rho_G} \tag{26}$$

The description of strain gradient plasticity can be summed up with a simple description of how to account for the dislocations associated with lattice curvature in a simple beam bending experiment. A two-dimensional (2D) schematic of non-uniform shear strain during a beam bending experiment and the induced dislocation density is shown in Figure 18.

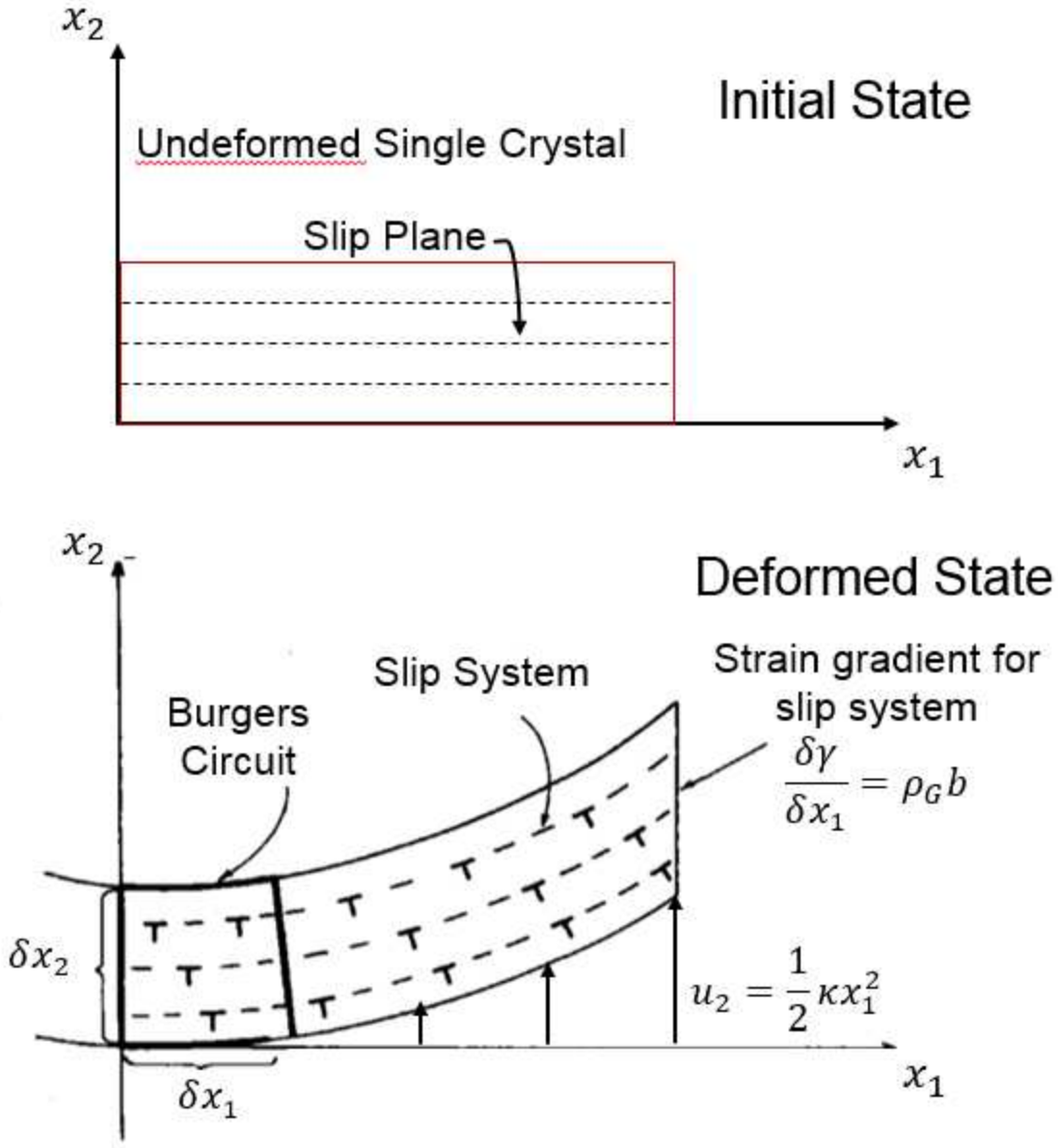

Figure 18 – Beam bending schematic demonstrating the effective dislocation density induced by non-uniform strain, which leads to a curvature of the lattice. Note: there is an underlying assumption that the elastic strain is small in comparison to plastic strain. Modified from Fleck et al. [78]

Following the derivation of Ashby [74], and Fleck et al. [78], and neglecting elastic strains, a small, fully plastic displacement field in the bent beam, shown in Figure 18, may be described according to Equation (27)

$$u_1 = 0, u_2 = \frac{1}{2}\kappa_3 x_1^2, u_3 = 0 \tag{27}$$

where u_1, u_2, and u_3 are the respective displacements for the Cartesian coordinate system of x_1, x_2, and x_3; k is a constant. Since the displacements are fully plastic and assumed to result from the dislocations on glide planes normal to the axis of deformation, the minimum number of dislocations to account for the lattice curvature can be described according to the Figure 16d, which may be described in terms of the shear strain gradient according to

$$\Delta nb = \delta\gamma\delta x_2 = \frac{\partial\gamma}{\partial x_1}\delta x_1\delta x_2 \tag{28}$$

The density of geometrically necessary dislocations may be described by as:

$$\rho_G = \frac{1}{b}\frac{\partial\gamma}{\partial x_1} \tag{29}$$

where b is the magnitude of the Burgers vector for the active slip system. Alternatively, each cell could be described by an infinitesimal lattice rotation about x_3 ($\delta\phi_3$), such that:

$$\delta\phi_3 = \delta\gamma = \rho_G b\delta x_1 \tag{30}$$

The plastic bending of a crystal to a lattice curvature $\boldsymbol{\kappa}$, where $\kappa_{31} = \delta\phi_3/\delta x_1$, requires a specific density of geometrically necessary dislocations. Rearranging Equation (30), and applying the definition of lattice curvature results in a useful, albeit simple description of the dislocation density:

$$\rho_G = \frac{\delta \phi_3}{b \delta x_1} = \frac{\kappa_{31}}{b} \tag{31}$$

The accumulation of GNDs based on lattice curvature is further complicated by the possibility of multiple dislocation types for a given crystal structure, each of which are described by a unique Burgers vector ($\boldsymbol{b}$) and sense vector ($\boldsymbol{\xi}$) (i.e. the dislocation line direction). Furthermore, the prescribed lattice curvature in Equation (31) was the result of a prescribed strain gradient along a single direction (x_1), with the prescribed rotational axis normal to that direction. A more rigorous description of lattice curvature is discussed later according to the dislocation tensor ($\boldsymbol{\alpha}$), also referred to as the Nye tensor [190] when elastic contributions are deemed to be negligible.

2.4.2. Assessment of the length-scale parameter

One of the most critical issues regarding mathematical formulations of strain gradient plasticity lies in the physical meaning of the length scale parameter which is the basis for many of the observed phenomena of SGP. As discussed previously, Ashby [74] describes the length scale parameter λ_G based on the average distance that a dislocation moves before coming to a final resting point. As with other formulations [191, 192], this length scale was assumed to be constant during the deformation process. However, it is clear that the microstructure (and the effective slip distance λ_G) evolves as a function of deformation in many situations [193-195]. Using nanoindentation experiments Abu al-Rub and Voyiadjis [196] showed that the length scale is a function of temperature and strain rate ($l = l(T, \dot{\varepsilon})$), while formulations by [197] showed that the details of strain

gradient plasticity does not require a scalar length scale if the interactions between dislocations can be accounted for explicitly. However, the complexities of coupling dislocation flux to each individual slip system create many difficulties in implementing the model to polycrystals at a scale that is useful in engineering practice.

For coarse grained materials, it is undoubtedly true that the length scales of phenomena salient to deformation (and grain sizes) change during deformation. This concept has been used for centuries, and is critical for deformation processing. In ufg materials, the degree of grain refinement that can be achieved by deformation is highly limited in comparison to bulk materials. In this study, we define the length-scale based on the grain size of the material, and do not consider this length-scale to change significantly during the deformation process. This simplified description is modeled after the original concept provided by Ashby [74], and serves as a reasonable approximation.

2.4.3. Practical models of strain gradient plasticity

Observations of strain gradient plasticity have been used to describe strain gradients and the associated GNDs are the result of: (1) the geometry of deformation, (2) boundary conditions for mechanical testing, or (3) the microstructure itself. A graphical depiction of several examples of strain gradient plasticity are shown in Figure 19 [78].

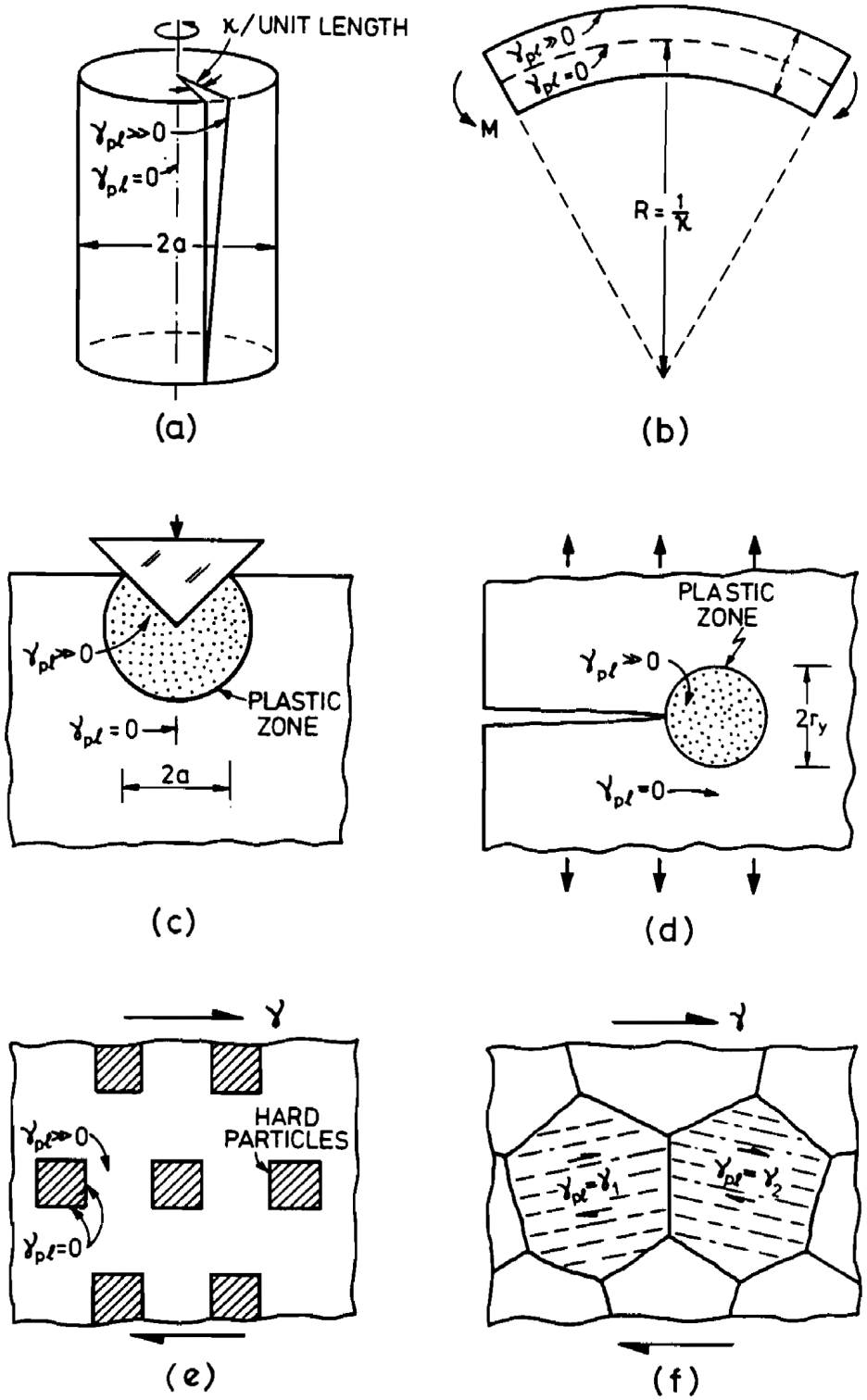

Figure 19 – Strain gradient plasticity and geometrically necessary dislocations, which account for an increase in strength based on: the geometry of deformation (a, b), local boundary conditions (c, d), and the microstructure of the material (e, f). Used with permission from Fleck et al. [78].

Strain gradient plasticity may also be used to describe the increase in strength associated with decreasing grain size in a polycrystal according to the methods of Ashby [74]. In essence, grain boundaries confine slip, causing non-uniform plasticity, even for pure metals. For small deformations, the grain deforms predominantly by single slip resulting in gradients in the shear strain, which cause rotation of the lattice. This lattice rotation may ultimately lead to slip on a secondary slip system, but a basic assessment of the strain gradient plasticity can be inferred from the initial and final structure in a similar thought experiment to that described in Figure 18. In uniaxial tension, displacement of the grains can be described with and without the confining influence of grain boundaries. A 2D depiction of this thought experiment is shown in Figure 20. Dislocations may be added en masse to accommodate the overlaps and voids that occur without the confining influence of grain boundaries.

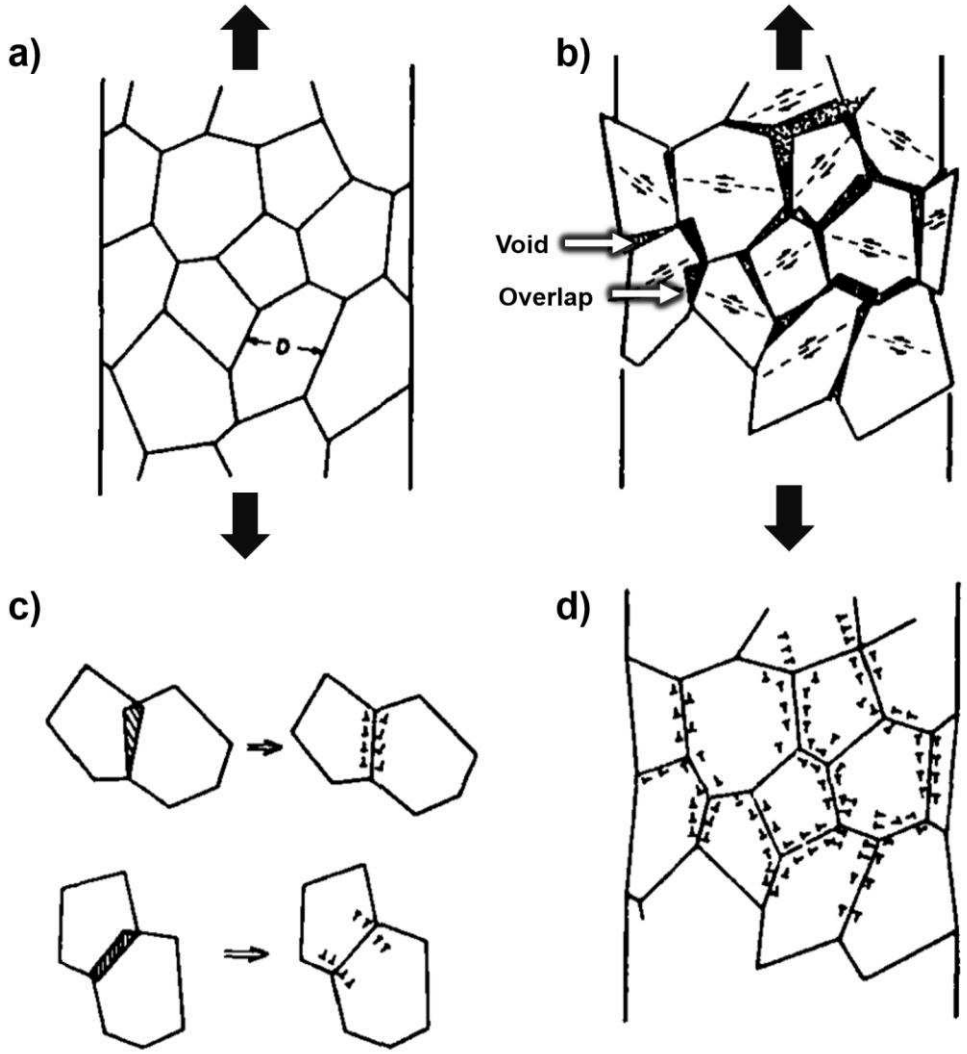

Figure 20 – Determination of strain gradient plasticity and the geometrically necessary dislocations observed in a tension test of a polycrystalline sample. A material deforms in tension (a), resulting in overlap and voids between grains (b). Geometrically necessary dislocations are added to correct for individual voids and overlaps (c), resulting in a uniform sample with dislocations to account for the geometric aspects of deformation [74]

The analytical approximation for the density of GNDs (ρ_G) as a function of the grain diameter (D) and the macroscopic tensile strain ($\bar{\epsilon}$) is described by Ashby as:

$$\rho_G \cong \frac{\bar{\epsilon}}{4bD} \tag{32}$$

In a more general sense, ρ_G, may be described in terms of the geometric slip distance, λ_G, which is generally described by the boundary conditions that describe strain gradient

plasticity. While this slip distance is generally approximated as the grain diameter (i.e. $\lambda_G \cong D$), it is useful to describe GNDs in terms of the slip distance so that the relation may be applied to additional conditions described in Figure 19. The slip distance is considered to be effectively constant with respect to strain, resulting in a logarithmic increase in ρ_G as a function of strain. ρ_S on the other hand, is the result of dislocation multiplication interactions and the rate of increase changes depending on the microstructure and the extent of strain. A graphical description of the evolution of GND and SSD densities is shown for copper in Figure 21.

$$\rho_G = \frac{1}{\lambda_G}\frac{4\gamma}{b} \tag{33}$$

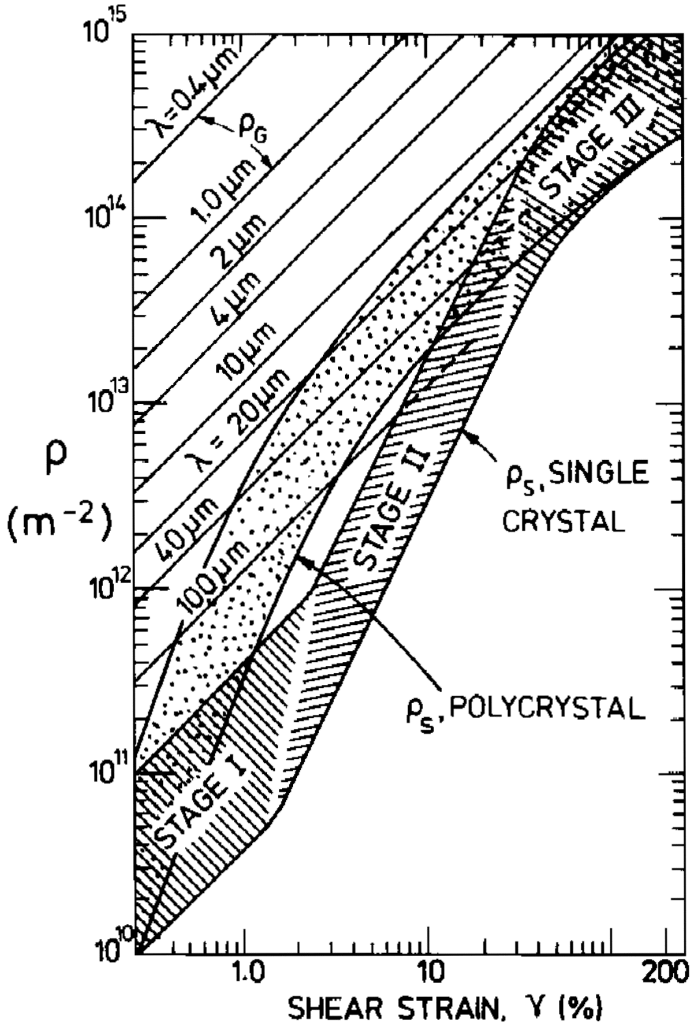

Figure 21 - Plot of the density of statistically stored dislocations (SSDs) in a copper single crystal (hatched) and polycrystal (dotted). Geometrically necessary dislocations (GNDs) show a series of parallel lines that is dependent on an assumed microstructural length scale, λ_G, determined from Equation (33). Used with permission from [74]. Single crystal copper data from Basinski and Basinski [198]

There is great difficulty in predicting dislocation density as a function of strain, in part, because of the stochastic nature of accumulating SSDs in the microstructure. However, the number of GNDs quickly engulfs the total dislocation content as the geometric slip distance, λ_G, decreases, especially in the sub-micrometer range.

The versatility of strain gradient plasticity theory in describing physical phenomena associated with length scales and constrained plasticity has become apparent over the last several decades. As a result, several mathematical models have been developed to impose strain gradient plasticity onto traditional continuum plasticity models. An effective review of many of the mathematical advancements in this theory has been provided by Zhang and K. E. Aifantis [195] and some of the highlights will be covered here. Several years after the Ashby description of strain gradients in non-homogeneous plasticity, a mechanics-based description was independently formalized by E.C. Aifantis [199]. This theory also accounts for several important deviations from continuum mechanics that are observed in real world materials. Interestingly, the models developed by Aifantis, were originally intended to describe shear banding phenomena [191]. Additional formulations were provided to give a thermodynamic framework for strain gradient plasticity theory [200-202] and the principle of work include higher order terms to the account for hardening imposed by pre-existing lattice curvature (i.e. dislocations) without having the requirement to generate curvature and hardening effects directly through the accumulation of strain [203]. These advancements help to tune the accuracy of strain gradient plasticity to fit more detailed problems, but the original theories of Ashby and later phenomenological models [78, 184] provide a sound framework for assessing the interactions between length scale, strain, and dislocations.

CHAPTER 3. METHODS

Grain refinement is critical to developing the instabilities that promote plastic instabilities in ufg BCC metals. There are numerous ways of reducing grain size, but it is important to realize that the processes used to achieve a particular grain size in bulk ufg metals have significant implications for the microstructure and dislocation structure that is achieved in the final product. For unknown reasons, ufg BCC metals that were produce by powder consolidation routes showed a higher propensity for shear band formation at a given grain size. The focus of this research was to understand the criteria for shear band development in ufg tungsten produced from bottom-up, powder metallurgical processes.

Mechanical testing was performed using a variety of methods to investigate the plastic behavior of ufg tungsten. Compression testing was performed at quasi-static and dynamic rates to investigate the susceptibility of powder metallurgical materials to shear band formation. In certain cases, 2D digital image correlation (DIC) was used to map strains during shear band formation. Additional mechanical characterization was carried out using nanoindentation (AKA instrumented indentation) to assess the strain rate sensitivity and local plastic behavior of materials. Finally, materials were analyzed "*post-mortem"* using transmission electron microscopy (TEM), scanning electron microscopy (SEM) and electron backscatter diffraction (EBSD) to investigate the microstructure and dislocation structure after mechanical testing**.**

3.1. Synthesis of ultrafine grained tungsten and tungsten alloys

The microstructure and properties of ufg metals can vary significantly based on the processes used to form them. While the grain size alone can provide a very general

description of microstructure, material behavior ultimately depends on the detailed relationships between processing, microstructure and properties. This is particularly true in the realm of ultrafine and nanograined materials because far-from-equilibrium processing techniques offer plenty of opportunities to corrupt the microstructure or composition of a material. For example, early work in the field of nanocrystalline materials suggested that the modulus was significantly lower than bulk specimens [204]; however, later studies verified that residual porosity was the culprit for these deceptive results [205]. Some of these challenges in ultrafine and nanomaterial production can be avoided with careful control of processes, but many of these fundamental details of microstructure are inherent to the processing techniques employed in their production. The processing route is particularly critical to understanding the development of plastic instabilities and shear bands.

The production methods employed for ultrafine and nanograined materials generally fall into two broad categories: bottom-up and top-down approaches. Bottom-up approaches generally rely on powder technologies and tend to have a lower purity as a result of the methods employed to produce nanocrystalline powders and consolidate them to full density. These bulk ufg materials may also contain significant residual porosity, which can have significant implications for the fracture and plastic instability. However, these powder metallurgical approaches allow for bulk production, and also offer significant opportunities for alloying to improve ductility.

Top-down methods generally rely on severe plastic deformation to produce materials in the ufg regime. These methods have the significant benefit of being carried out in bulk and tend to result in higher purity, higher density materials. However, deformation

processing of metals develops texture because of the inherently anisotropic behavior of dislocation mediated plasticity. Severe plastic deformation generally leads to heavily textured materials with non-uniform grain morphologies.

For this study, ufg metals were primarily produced using powder metallurgical processing routes. These bottom-up, powder metallurgical routes relied on a scalable, mill, press and sinter approach that is common to high-throughput manufacturing. Although top-down, severe plastic deformation is highly effective for producing ufg materials, the focus of this study was on ufg materials produced from powder metallurgical methods in order to provide a direct comparison to the quasi-static localization phenomenon reported by Jia et al. [165] and test the viability of geometric shear banding theories.

3.1.1. Powder metallurgical processing

The first essential component of this study was to provide a reliable process for synthesizing bulk ufg tungsten that demonstrates the shear banding at quasi-static rates. The main hurdle was to produce a material with sufficient plastic stability for avoiding perfectly brittle fracture during room temperature compression testing. Polycrystalline tungsten is reported to have a brittle-to-ductile transition temperature above 500K [8, 97]. Furthermore, tungsten is notoriously notch sensitive [96], and the residual porosity that is associated with powder metallurgical processing is likely to increase the susceptibility to fracture.

Bulk ufg tungsten was produced from commercially available nanocrystalline powders with a crystallite size of 20 nm (measured by x-ray diffraction). As received powders

were in the form of hard aggregates with a particle size of ~5-20 µm (measured by SEM)). Samples were milled in a Netzsch Mini-Cer bead mill in an organic medium and spray dried to achieve loosely agglomerated nanoparticles with an aggregated particle size of 1-20 µm. These powders were compacted by cold isostatic pressing and sintered to produce bulk ufg tungsten [53]. The process, described pictographically in Figure 22, is easily modified to incorporate dopants and alloy additions to improve the plastic behavior of tungsten and influence the mechanisms of flow and fracture in these materials.

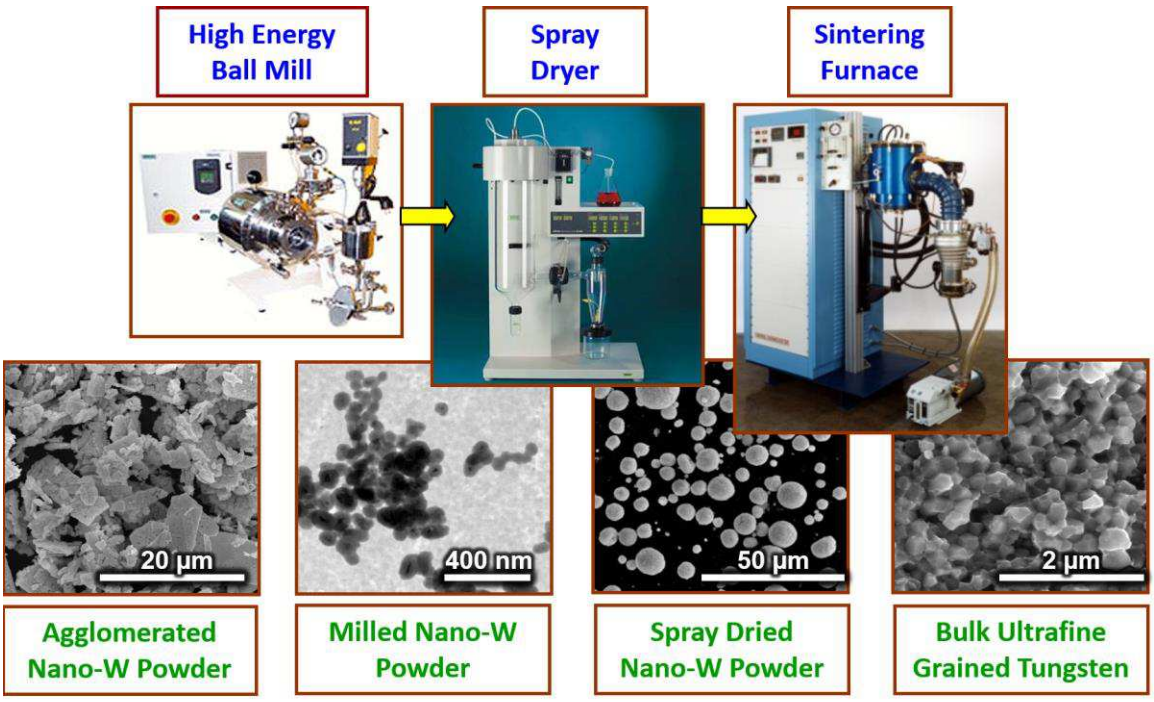

Figure 22 – Flow chart describing the basic processes for producing bulk ufg tungsten.

Milling, drying and compaction processes were optimized to produce uniform densities and minimal defects prior to sintering. The reduction kinetics of residual tungsten oxides

were studied in great detail in order to improve the density and purity of the final product [53]. Finally the kinetics of grain growth and densification were investigated to optimize the microstructure of sintered ufg tungsten [206]. These processing methodologies are well suited for producing tungsten with a grain size of 100-500 nanometers and densities that range from 90-99% of the theoretical density. Higher sintering temperatures led to higher density materials, but also resulted in larger grain sizes.

Several ufg alloys were formulated with dopants to improve grain boundary cohesion (Boron) [207, 208] and alloy additions to improve dislocation mobility at room temperature (Rhenium) [19-21, 209] in order to identify the critical causes of brittle fracture in polycrystalline tungsten. Rhenium (-325 mesh, 99% purity, Rhenium Alloys) and amorphous boron (-325 mesh, 98% purity, Alpha Aesar) powders were used as feedstock additions.

Careful control of the microstructure to eliminate processing defects and minimize residual porosity, allowed for the first reported demonstration of shear banding in a tungsten-rhenium alloy tested at quasi-static rates [53]. More recent efforts, carried out over the course of this current research study, demonstrated that reliable shear banding may be observed in unalloyed tungsten as well. This is further validation of the susceptibility of ufg metals to shear banding, which was originally reported by Jia et al. [165] for pure iron. The materials produced for this study, to investigate these mechanisms of shear banding behavior, were engineered to have a grain size of approximately 250 nm and densities exceeding 95% of the theoretical density of tungsten based on sintering at a temperature of 1400 °C for 30 minutes.

3.2. Mechanical testing of ultrafine grained tungsten

In an effort to identify the causes of shear band formation, several mechanical testing methods were employed to provide a detailed view of the mechanical behavior and plastic instabilities of ufg tungsten. Compression testing under quasi-static conditions was performed in conjunction with digital image correlation (DIC) techniques [210-212] to map the strain fields associated with testing. Instrumented indentation [213-215] was used to and assess local mechanical properties of ufg tungsten before and after shear banding, and strain rate sensitivity was assessed according to the methods of Maier et. al [216]. High strain rate mechanical testing was performed in collaboration with colleagues at the US Army Research Laboratory using an instrumented split Hopkinson compression bar [217].

3.2.1. Compression testing

Mechanical test samples consisted of cubes that were approximately 2mm in length. Later tests were slightly elongated (0.1-0.2mm) along the compression axis in order to minimize the effects of confinement during shear banding. Samples were cut to the prescribed geometry by electrical discharge machining and most samples were mechanically polished on successively finer silicon carbide papers to 1200 grit, and finished with diamond lapping compound down to a 1μm finish. However, several samples were prepared with a 1200 grit finish to allow for strain mapping by digital image correlation (DIC) of the native sample surface.

Quasi-static mechanical testing was performed using MTS or Instron servohydraulic load frames with 5,000 lb. load cells. Highly polished tungsten carbide platens were lubricated

with MoS_2 in order to minimize friction during testing. In some cases, strain was calculated from displacement based on a linear variable differential transformer to minimize issues with machine compliance. Other strain measurements utilized digital image correlation (DIC) in order to observe the strain behavior throughout the surface of the specimen.

The fine length scales and high propagation velocities of shear bands create some difficulty in finding suitable measurement techniques to measure the temporal and spatial distribution of strain within a material, but 2D DIC [210-212, 218] provides an effective method for investigating the strain evolution in shear banding materials during mechanical testing. Images were acquired using a 2.0-megapixel camera at a resolution of 2.0-2.5 μm per pixel, and at a frame rate ranging from 1-10 frames per second (FPS). Higher frame rates (~100FPS) were used to investigate shear band initiation, and propagation velocities. DIC of local displacements and strains were performed using a MATLAB based code developed by Christoph Eberl [210], or VIC 2D (Correlated Solutions, Inc.). The Eberl code appeared to be less sensitive to issues with image contrast, and proved useful for preparing stress-strain curves for samples with a native surface finish. VIC 2D was used for all of the strain mapping, which was carried out with a subset size of 57 pixels and a step size of two. The critical variables for correlating and mapping strains in 2D DIC include: camera resolution, frame rate, size, contrast, and distribution of the optical pattern on the sample surface, and computational details used in tracking of displacement based on cross correlation methods and the conversion to strain based on the various 2D strain descriptors. DIC is capable of achieving sub-pixel

resolution [219] in the measurement of strain and reasonably accurate strain maps may be captured using macroscopic imaging techniques.

High rate compression tests were conducted at the US Army Research Laboratory [53] using a 9.5mm diameter maraging steel (Vascomax C350) split Hopkinson bar with copper pulse shapers to provide better resolution during the linear elastic region and early yield point. Tungsten carbide platens and MoS_2 lubricants were employed in a fashion similar to quasi-static testing. Images were taken during a few of the tests using a DRS Hadland Imacon 200 high-speed digital camera; however, the resolution was not sufficient for DIC analysis of strain.

3.2.2. Nanoindentation

Indentation tests were performed on an Agilent Technologies G200 Nanoindenter system using a three-sided, Berkovich diamond indenter. Indentation was performed using the continuous stiffness method developed by Oliver and Pharr [220] for depth-sensing indentation machines. The indenter tip contact area was approximated based on indentation into a fused silica standard, which is amorphous and displays no considerable depth effect to the measured hardness [187]. Machine compliance was also accounted for based on stiffness measurements of the silica standard. Properties were analyzed at depths greater than 200 nm in order to minimize the errors associated with tip area calibrations. Indentation depths were generally limited to less than 2000 nm because of the high strength of ufg tungsten and load limitations of the nanoindentation apparatus.

Strain rate sensitivity was measured using indentation jump tests according to the methods described by Maier et al. [216, 221]. The jump tests show significant

improvement over constant strain rate measurements by reducing thermal drift associated with long indentation times [222]. The measurement of strain rate sensitivity has a fundamental underlying assumption that the microstructure and dislocation structure is the same for each strain rate. Jump tests are particularly useful for minimizing the influence of dislocation structure accumulated over the course of indentation. Hardness was measured at an effective strain rate from 0.025 – 0.0025/s.

3.3. Assessment of shear banding mechanisms

In order to assess the physical mechanisms for shear band formation, it necessary to assess critical features related to shear band formation. In particular, the temperature, strain, strain-rate and texture inside of the band are important for distinguishing the potential causes of strain localization. In several instances, shear bands have a characteristic amount of strain before the plastic instability develops, or a characteristic width that describes the rate dependent behavior of the materials [69].

3.3.1. Microstructural analysis

Before testing, microstructural analysis is a critical component for assessing the susceptibility to shear band formation. Polycrystalline tungsten tends to be extremely brittle at room temperature, and the presence of macroscopic processing defects ultimately leads to brittle fracture before shear banding can occur. To assess the uniformity of microstructure, and identify the presence of processing defects, metallographically polished, and intentionally fractured specimens were examined by SEM. Metallographic specimens were prepared by mechanically polishing on

successively finer silicon carbide papers to 1200 grit, followed by successive lapping with 9, 3, and 1μm diamond suspension applied to a lapping pad. To highlight grains, the traditional Murakami solution [223] for etching tungsten proved too aggressive, and superior results were achieved by finish polishing with a ChemoMet, colloidal silica based attack polish (Buehler North America). As an additional measure, specifically to look for macroscopic processing defects, samples were intentionally fractured and the fracture surfaces were characterized with a scanning electron microscope. Microstructural analyses were performed on a Hitachi 4700, or FEI Nano600, high resolution scanning electron microscope (SEM).

3.3.2. Microscopic evaluation of strain inside of shear bands

Shear bands were analyzed predominantly in the as-tested condition, as surface preparation generally obscures the details of the shear band. Analysis was performed on an Olympus LEXT OLS 3100 scanning confocal microscope. Additional microstructural analyses were also performed by scanning electron microscopy (SEM) using Hitachi 4700 and FEI Nano600 high resolution scanning electron microscopes. Image analysis was performed using Image J v1.5n image analysis software [224, 225].

One of the most descriptive features of a shear band is the shearing strain that accumulated during propagation of the band. If preexisting scratches intersect a shear band, they will be displaced by an angle that is indicative of the relative amount of shearing inside of the band. If the region outside of the band is undeformed, this provides an indication of the total shear strain within the band. The shear strain may be calculated

based on the angle a scratch is displaced entering and exiting the shear band as described by Equation (34)

$$\gamma_{SB} = \tan(\alpha_{SB} + \theta_s) - \tan(\theta_s) \tag{34}$$

where γ_{SB} is the engineering shear strain inside of the deformation band, α_{SB} is the angle describing the deflection of the scratch, and θ_s is the angle of the scratch with respect to the shear band normal. The strain can be measured directly from where the shear band intersects the surface of the sample as shown in Figure 23.

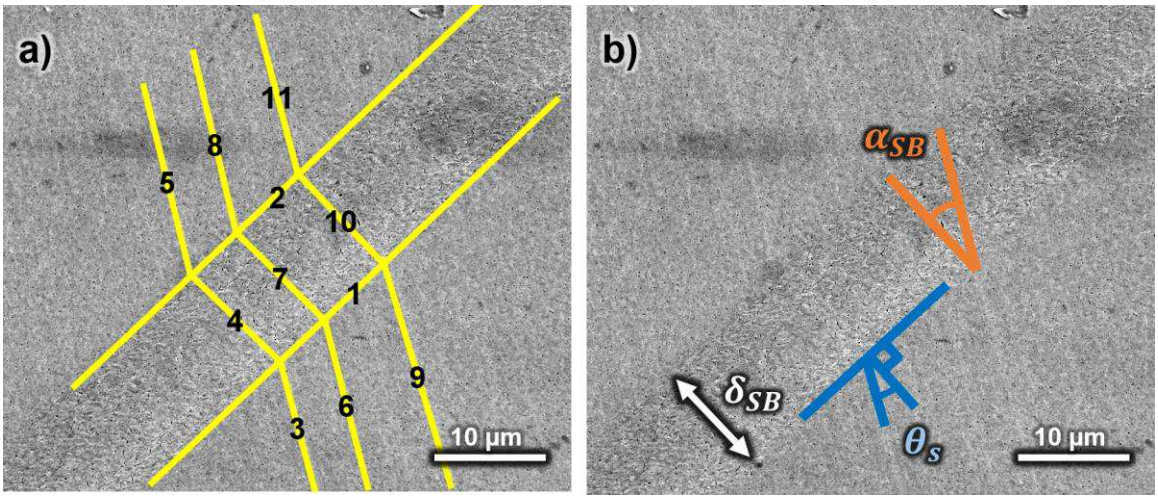

Figure 23 – Measurement of shear band width, and measurement of strain based on preexisting scratches that traverse the band; a) raw data collected by ImageJ, and b) the estimated angle of deflection (α_{SB}), shear strain (γ_{SB}), and width (δ_{SB}) of a shear band.

3.3.3. Temperature of shear bands

Knowing the temperature rise associated with strain localization is critical to understanding the formation and propagation of shear bands [226-228]. An interesting method for assessing the temperature rise at the surface of a shear band was utilized by Lewandowski and Greer [228] to determine the temperature rise associated with shear band formation in bulk metallic glasses. Samples were deposited with a fusible tin coating on the surface. When the surface temperature exceeds the melting point of the

coating, local melting is observed. Microscopic analysis after deformation can provide a description of temperature contours with very high spatial resolution, exceeding the capabilities of IR imaging techniques. An example of the fusible coating technique, and the local melt pools that are formed as a result of deformation are shown in Figure 24.

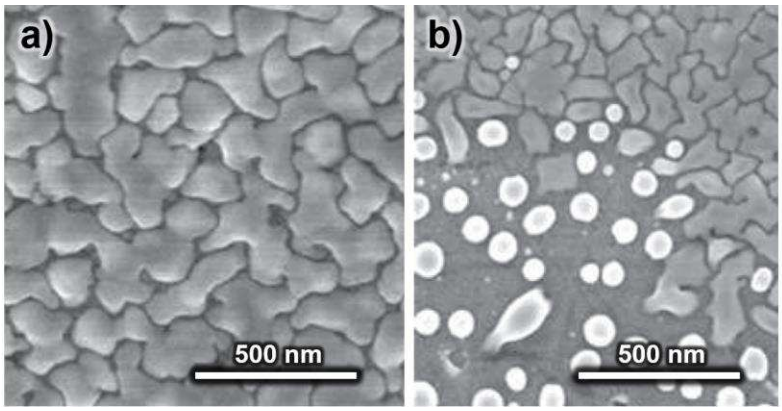

Figure 24 – Fusible tin coating on the surface of a bulk metallic glass a) as deposited and b) after local melting, from [228].

A preliminary estimate on the temperature rise of a shear band in ufg tungsten shows that the temperature may not exceed 225 °C, even under perfectly adiabatic conditions. This temperature rise is not high enough to definitively melt tin (Melting Point (MP) = 232°C), so an indium coating (MP = 157°C) was applied to determine the temperature and temperature profile around shear bands.

The temperature of the shear band may also be estimated based on the strain, and strain rate inside of the band. The shear banding process is highly dynamic with strain and strain rate continually changing throughout the deformation process. Digital image correlation provides a reliable method for *in-situ* measurement of the strain field development inside of shear bands during mechanical testing. These methods can help to identify the local strain rates to determine whether adiabatic mechanisms play a role in

shear band development. The small size and highly dynamic nature of shear banding creates some challenges in acquiring reliable strain information from localized features, but comparing high speed DIC measurements to *post-mortem* microscopic evaluation of shear bands can provide an effective method for determining the local plastic behavior of ufg tungsten.

3.4. Texture and microstructure inside of shear bands.

Measuring texture development is critical to understanding shear band formation, particularly as it relates to the "geometric" shear banding mechanisms. Orientation imaging microscopy by electron backscatter diffraction (EBSD) provides a unique tool for investigating the local textures, such as those developed inside of shear bands. Furthermore, this method may be used to assess dislocation structure based on the assessment of GNDs from measured local lattice curvatures. TEM may also be used to analyze changes in microstructure and texture associated with the formation and propagation of shear bands. The length-scales associated with plastic instabilities and shear banding are actually quite large in comparison to the regions imaged during TEM studies. EBSD was used as the predominant method for characterizing texture and deformation structure, and TEM played a supporting role in validating the observations from EBSD.

3.4.1. Electron backscatter diffraction (EBSD)

Sample preparation for EBSD consisted of electropolishing with a Struers Lectropol-5 electropolishing system. The electrolyte was composed of 2 wt% NaOH in water 10 wt%

glycerol added as a thickening agent for improved film formation. Electropolishing was carried out at a voltage of 10V and a moderate level of electrolyte flow, resulting in a uniform polishing rate of approximately 10 μm per minute. Pattern acquisition was performed in a FEA Nano600 SEM with an EDAX Hikari camera. An acceleration voltage of 20 kV and a probe current of 2.1 nA was used for all acquisition. A square mapping grid, with a step size of 20 nm was employed for pattern acquisitions in order to provide approximately 10 linear data points of orientation information for each grain in these ufg samples.

EBSD is a technique for mapping crystallographic orientation of materials within a scanning electron microscope. The method utilizes Kikuchi diffraction patterns, generated by coherent backscattered electrons, to determine the orientation of a crystalline material [229, 230]. In general, EBSD requires the sample to be inclined with respect to the electron beam (typically at 70°) in order to increase the yield of backscattered electrons that are captured on a phosphor screen that is placed a few centimeters away from the sample. The phosphor screen is imaged with a low light CCD camera. A schematic of the common experimental conditions for capturing EBSD is shown in Figure 25.

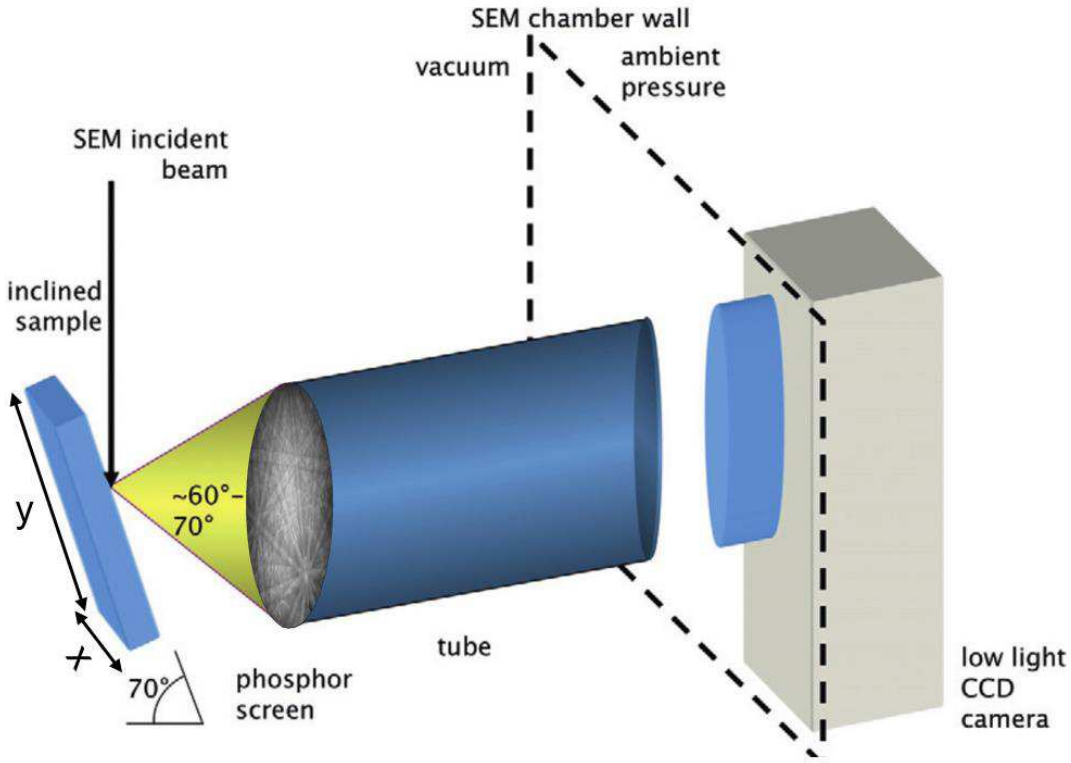

Figure 25 – Experimental setup for electron backscatter diffraction measurements. Modified from Wilkinson [80].

The spatial resolution of EBSD, defined by the physical volume that provides backscattered electron signal, is generally considered to be less than 100 nm [230]. This signal is a function of the acceleration voltage and diameter of the electron beam, and the electron interactions within the sample itself. In general, the physical resolution is actually larger than the effective resolution, which can be described as the ability to distinguish between neighboring points of unique orientation. The effective resolution is actually a function of the software algorithms used to solve for the orientation [231]. The effective resolution on a copper sample at 20 kV using a field emission gun is approximately 20 nm [229]. The tilted sample geometry may also result in a factor of three decrease in spatial resolution in the y-direction (described in Figure 25).

EBSD maps were processed and presented without employing orientation filtering (e.g. Kuwahara filtering, confidence index filtering, etc.) in order to preserve the fidelity of the data. Traditional EBSD mapping algorithms were used for analyzing data. In particular, kernel average misorientation (KAM) (first nearest neighbor, five-degree maximum threshold) was used to estimate misorientation within grains. The grain tolerance angle was measured using the grain orientation spread (GOS) technique to highlight regions of large deformations (i.e. shear bands). Details of these techniques have been reported by Wright et al. [81].

The angular resolution of the EBSD method is also highly sensitive to the computational algorithms used to index orientation (or differences in orientation). The traditional, automated, EBSD acquisition and indexing methods, involving the Hough transform, have a reported resolution limit around 0.009 radians (~0.5 degrees) [229]. Cross correlation analysis methods has been reported to improve the angular resolution to better than 10^{-4} radians (~0.006 degrees) [232], which is helpful for reducing the background noise for calculation of geometrically necessary dislocations.

The speed of acquisition and indexing is an important, but often overlooked factor that has an indirect influence on both the spatial and angular resolution of EBSD. Long dwell times can lead to surface contamination and drift, leading to systematic errors in the angular and spatial resolution respectively. This is of particular concern at fine step sizes, approaching the theoretical limits to EBSD spatial resolution.

3.4.1.1. **Assessment of the dislocation tensor**

The basis lattice curvature as a description of geometrically necessary dislocations has been established in continuum mechanics since the 1950s [190, 233, 234]. Using the method of El Dasher et al. [235] The *fundamental equation for continuum dislocation theory* relates the dislocation tensor ($\boldsymbol{\alpha}$) to the elastic distortion tensor ($\boldsymbol{\beta}^e$) [234].

$$\boldsymbol{\alpha} = curl(\boldsymbol{\beta}^e) \tag{35}$$

This relation may be simplified to describe the dislocation tensor in terms of the infinitesimal gradients in elastic strain ($\varepsilon^e_{jl,k}$) and lattice orientation ($g_{jl,k}$) [236], allowing the dislocation tensor to be written as:

$$\alpha_{ij} = e_{ikl}(\varepsilon^e_{jl,k} + g_{jl,k}) \tag{36}$$

where e_{ikl} is the permutation tensor.

A critical assumption for Nye's original formulation of the dislocation tensor [190] is that plastic components, leading to reorientation of the lattice (i.e. $g_{jl,k}$) are large in comparison to the elastic strains ($\varepsilon^e_{jl,k}$), a criterion that should hold true in the absence of long range elastic stress fields (an assumption that was also applied in Ashby's description in Figure 18). Applying this assumption results in Equation (37), a foundation for describing the geometrically necessary dislocation content of a material.

$$\alpha_{ij} = e_{ikl}g_{jl,k} \tag{37}$$

The dislocation tensor may be used to describe a network of dislocations of specific types by explicitly accounting for the Burgers vector ($\boldsymbol{b}^{(s)}$) and the sense vector ($\boldsymbol{\xi}^{(s)}$) for each

independent dislocation character (s). The dislocation tensor may then be described as a summation of all dislocation types (S) that are present to describe the local lattice curvature, according to Equation (38).

$$\alpha_{ij} = \sum_{s}^{S} \rho_G^{(s)} \boldsymbol{b}^{(s)} \otimes \boldsymbol{\xi}^{(s)} \tag{38}$$

3.4.1.2. Geometrically necessary dislocations by EBSD

One significant issue with measuring dislocations by EBSD lies in the simple fact that the Nye tensor (Equation (38)) is inherently three dimensional, while the EBSD is a surface measurement technique. This feature results in the fact that only five of the nine components of the Nye tensor can be accessed by mapping orientations in a 2D space. The accessible components of the Nye tensor are described in Figure 26 [237]. Furthermore, dislocations may relax during sample preparation and migrate to the free surface and annihilate. This artifact has been modeled by dislocation dynamics simulations to show a significant reduction in the dislocation density of copper at a range of 50nm from the surface [238], the region contributing to the bulk of the backscattered electron signal. Finally, there is a possibility that some of the dislocations will not contribute to the overall lattice curvature (i.e. statistically stored dislocations), and therefore not contribute to the measured content. All of these features tend to reduce the measured density of dislocations compared to the measured density. Therefore, the Nye tensor, as measured by EBSD, provides the lower bound estimate for dislocation content in the system (at least until errors associated with angular resolution are taken into account.)

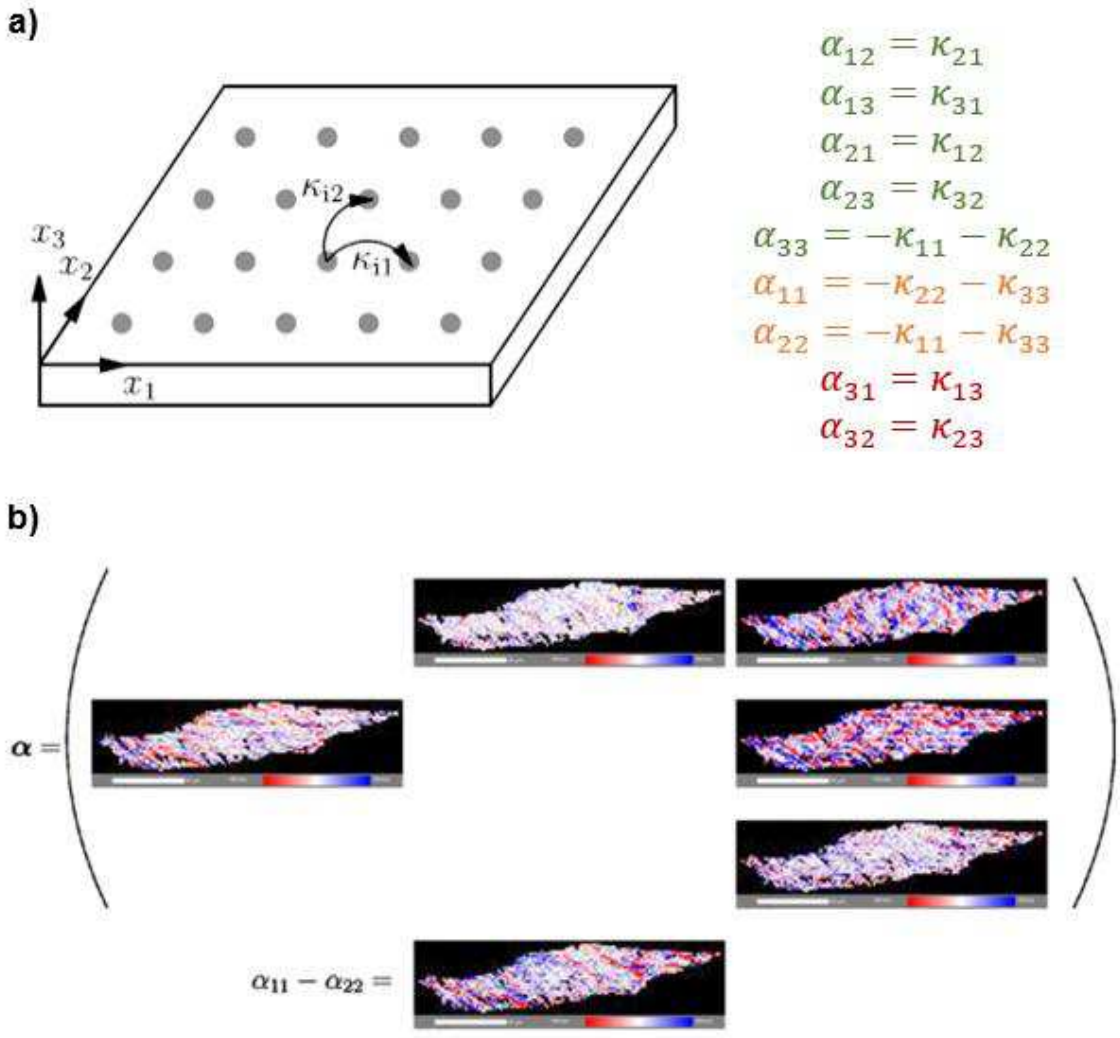

Figure 26 – Schematic describing the measurable components of lattice curvature by EBSD and correlation of curvature to specific components of the Nye tensor. b) Mapped components of the Nye tensor in a deformed aluminum alloy. [237]

The density of GNDs is highly sensitive to the step size in a number of ways [239]. First, the total number of dislocations that are lead to lattice curvature and are considered geometrically necessary depend on the actual step size because dislocation dipoles will not result in a change in lattice curvature if they lie between two successive steps. In essence, all dislocations would become geometrically necessary if we could probe

misorientations at a fine enough scale. This concept is presented very clearly in the work of Arsenlis and Parks [240].

This basic description of the dislocation tensor allows a specific lattice curvature to be ascribed to a specific dislocation content. However, there is no unique solution for the types of dislocations, and their respective densities, to account for any specific curvature [240]. This is particularly apparent for high symmetry crystal structures where there is an abundance of dislocation types to choose from to describe the observed lattice rotations [235]. A minimization scheme (e.g. based on the total length or energy of dislocations) must be employed to provide an estimate for the specific dislocation content associated with a prescribed curvature [240, 241].

There are several methods in the literature for approximating the density of geometrically necessary dislocations based on EBSD measurements [79, 232, 235, 237]. From a practical applications standpoint, the dislocation density may be acquired using two distinct techniques that will be described as the KAM GND, and Nye GND methods. Both of these approaches are based on assessing local misorientations and attributing those orientations to the scalar value of dislocation density. The KAM GND method provides a rough estimate of the dislocation density without consideration of the specific crystal system (only the Burgers vector). The Nye GND provides an estimate based on the norms of the accessible components of the dislocation density tensor (Figure 26).

A rough order of magnitude approximation can be made based on the misorientation angles between adjacent pixels [79]. This approach was originally applied by Kubin and Mortenson [242] to assess a GND array of screw dislocations based on the misorientation

between neighboring elements. The method is effectively the same as Franks description [156] of a low angle grain boundary as an array of dislocations according to Equation (39).

$$\rho_{GND} = \frac{\theta_m}{ub} \tag{39}$$

Where θ_m is the misorientation between adjacent grains, and u is the step size. While this method was developed based on the assessment of screw dislocations at a twist boundary, a simple tilt boundary can provide the same degree of misorientation with edge dislocations at half the density [243]. A simple parameter, described as the kernel average misorientation can provide a crude estimate for the average misorientation at a single measured point [79].

For the second method for determining the number of GNDs, the lattice misorientations may be more rigorously attributed to the specific, measurable components of the Nye tensor (see Figure 26). El-Dasher et al.[235] showed that the entrywise 1-norm of the dislocation tensor can be used to estimate the overall dislocation density without directly attributing the density to the specific individual types of dislocations according to Equation (38).

$$\rho_{GND}(norm) = \frac{\alpha_{norm}}{b} = \frac{\|\alpha_{ij}\|}{b} \approx \sum_i \sum_j |\alpha_{ij}| \tag{40}$$

where $\|\alpha_{ij}\|$ is a scalar quantity representing the entrywise 1-norm of the dislocation tensor, or the sum of the magnitudes of each *accessible* component of the Nye tensor (i.e. $\|\alpha_{ij}\| = |\alpha_{12}| + |\alpha_{13}| + |\alpha_{21}| + |\alpha_{23}| + |\alpha_{33}|$) . However, there is still considerable error that results from the missing components of the tensor. To account for this difference, it is

common to multiply the result from Equation (40) by a factor to represent the total quantity of GNDs in the inaccessible components of the Nye tensor [244].

$$\rho_{GND}(total) = \frac{\alpha_{total}}{b} = \frac{9}{5}\frac{\|\alpha_{ij}\|}{b} = \frac{9\langle|\alpha_{ij}|\rangle}{b} \tag{41}$$

Where $\langle|\alpha_{ij}|\rangle$ is a scalar quantity that represents the average of the absolute values for all accessible components of the Nye tensor. Several researchers use this method to evaluate the density of dislocations [237, 243, 245]. Ruggles [246] showed that this method was fairly well suited as a general technique for converting the Nye tensor to a scalar measure of the dislocation content.

Angular resolution is the most important concern for measuring dislocation density, as this is the major factor that would prevent EBSD measurements from providing the lower bound threshold of the total dislocation density. The effect of noise is magnified based on the step size chosen for EBSD measurements; for a fixed amount of angular uncertainty, there is a noise threshold where actual density of GNDs cannot be distinguished from the background [247]. This density of spurious dislocations, associated with the lower threshold for measuring GNDs may be described according to Equation (42) [244], which is essentially the same as the measurement of KAM GNDs (Equation (39)).

$$\rho_{sp} = \frac{\theta_R}{ub} \tag{42}$$

where θ_R represents the angular resolution of the measurement. The angular resolution of pattern indexing based on the Hough transform (i.e. conventional EBSD) is often cited to be ~0.5° [248]. In the case of ufg tungsten, measured with a step size of 20 nm, the density of spurious dislocations is approximately $1.59*10^{15}$ m^{-2}. Based on a preliminary analysis of strain in side of the shear band ($\gamma_{SB} = 0.4$), the Ashby prediction for the

dislocation density (Equation (33)) estimates the dislocation density to be $2.51*10^{16}$ m^{-2}, for a grain size of 250 nm. This density of spurious dislocations should not have an effect on the dislocation densities measured inside of a shear band, but it is expected that there will be errors associated with angular resolution in undeformed regions of the sample.

When the threshold GND (i.e. density of spurious dislocations) is close to the measured values for GNDs, it may be important to correct for the spurious dislocations using the concept of a signal to noise ratio that was outlined by Konijnenberg et al. [243]. The signal to noise ratio ($SNR = \left(\rho/\rho_{sp}\right)^2$) can be accounted for in a corrected measurement of the dislocation density.

$$\rho_{GND}(Corrected) = \rho_{GND}\sqrt{SNR} \tag{43}$$

Improving the angular resolution of the EBSD technique is important for accessing the true dislocation density at fine step sizes, particularly in undeformed samples. High angular resolution EBSD (HREBSD), originally introduced by Troost et al. [249] and developed extensively by Wilkinson et al. [80, 232, 241], can be used to improve the angular resolution to ~0.01°, allowing for a significant improvement to the resolution for measuring GNDs.

3.4.1.3. High angular resolution EBSD (HREBSD)

HREBSD uses cross correlation methods to determine the elastic stresses and pattern rotations in comparison to "standard" reference patterns. The reference pattern may be calculated by computational means or acquired in regions of minimal strain (generally based on kernel average misorientations (KAM) or image quality (IQ). The image

correlation technique is used to compare twenty evenly spaced regions of interest (ROI) to the same regions in the reference pattern; a minimum of four regions are required to actually solve for the strain, but the redundant data can help to minimize errors. Each ROI is processed by a fast Fourier transformation (FFT) routine to remove high and low frequency noise from the diffraction patterns. An example of a standard EBSD pattern, the regions of interest used for correlation and the Fourier filtering are shown in Figure 27. The high and low bandpass filters were selected at five and twenty pixels respectively based on the general recommendations described by Jiang et al. [247].

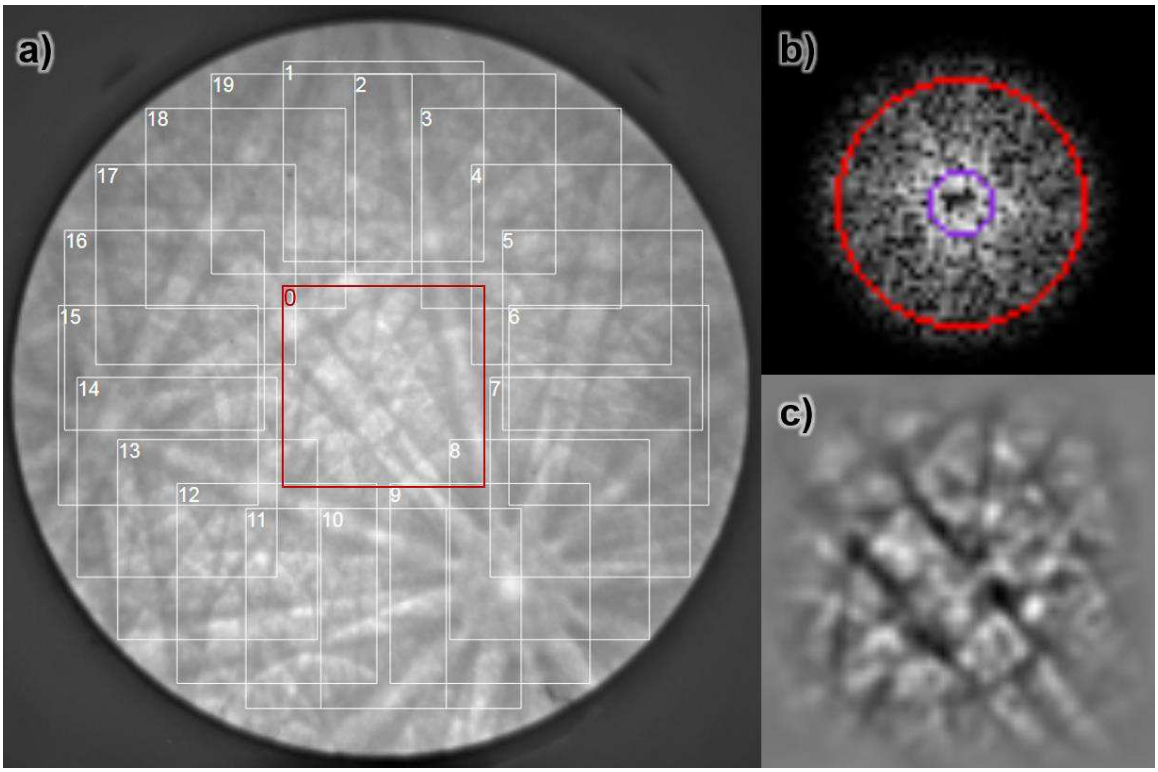

Figure 27 – HREBSD pattern preparation. Part a), shows the twenty overlapping patterns used for cross-correlation. The FFT pattern of the center ROI (0) is shown in b), along with the high, and low frequency band-pass filters employed for image processing, while c), shows the back-transformed image that is used for cross-correlation.

The cross-correlation of ROIs at different positions of the Kikuchi pattern allows for the displacement and elastic strain to be calculated. Although the process of cross-correlation

is computationally expensive compared to the Hough transform for determining orientation, the potential improvements in the resolution of misorientations and GNDs in general are significant. Similar to traditional digital correlation used in strain mapping, the method can provide "sub-pixel" accuracy [218, 250] in correlating between patterns, which allows for a precise accounting of crystal rotations and elastic strains.

An estimation of the strains makes it possible to estimate components of the Nye tensor that are generally considered inaccessible via conventional EBSD (Figure 26). However, the 2D nature of acquisition will still influence the reliability of various components of the elastic strain tensor. Additional improvements over the original algorithm include a "robust" iterative fitting method that can accurately determine large lattice rotations [251]. and a method of "remapping" to account for finite strains [252] instead of the infinitesimal strains utilized in the original Wilkinson, Meaden, and Dingley (WMD) method [232]. Dislocation density was estimated from the plastic strains using an L^1 (least absolute error) optimization to minimize the total energy of dislocations as described by Wilkinson and Randman [241]. The character of dislocations was weighted based on the variation in energy between edge and screw dislocations according to $E_{edge}/E_{screw} = 1/(1-\nu)$, where ν is Poisson's ratio.

For all assessments of GND, dislocations were only considered on {110} type planes [253] and all dislocations had an equivalent magnitude of the Burgers vector (0.274 nm). For conventional EBSD (i.e. using only the Hough transform for indexing) patterns were acquired at a speed of ~ 80-100/s with 5x5 binning in an effort to minimize drift and beam contamination during acquisition. High angular resolution EBSD patterns were acquired at a frame rate of ~2/s with a 2x2 binning of the pattern images. The to assess

the dislocation density of dislocations within the sample, EDAX OIM Analysis software v7.1 [254] was used for analyzing traditionally indexed (Hough transform) orientation maps. The dislocation density was calculated based on kernel average misorientations (KAM GND), solution of the Nye tensor (Nye GND) using ATOM – Analysis Tools for Orientation Maps v2.14 [255]. Additional measurements were performed by HREBSD using CrossCourt 4.25, high angular resolution EBSD software based on the cross correlation function based on the WMD method [232].

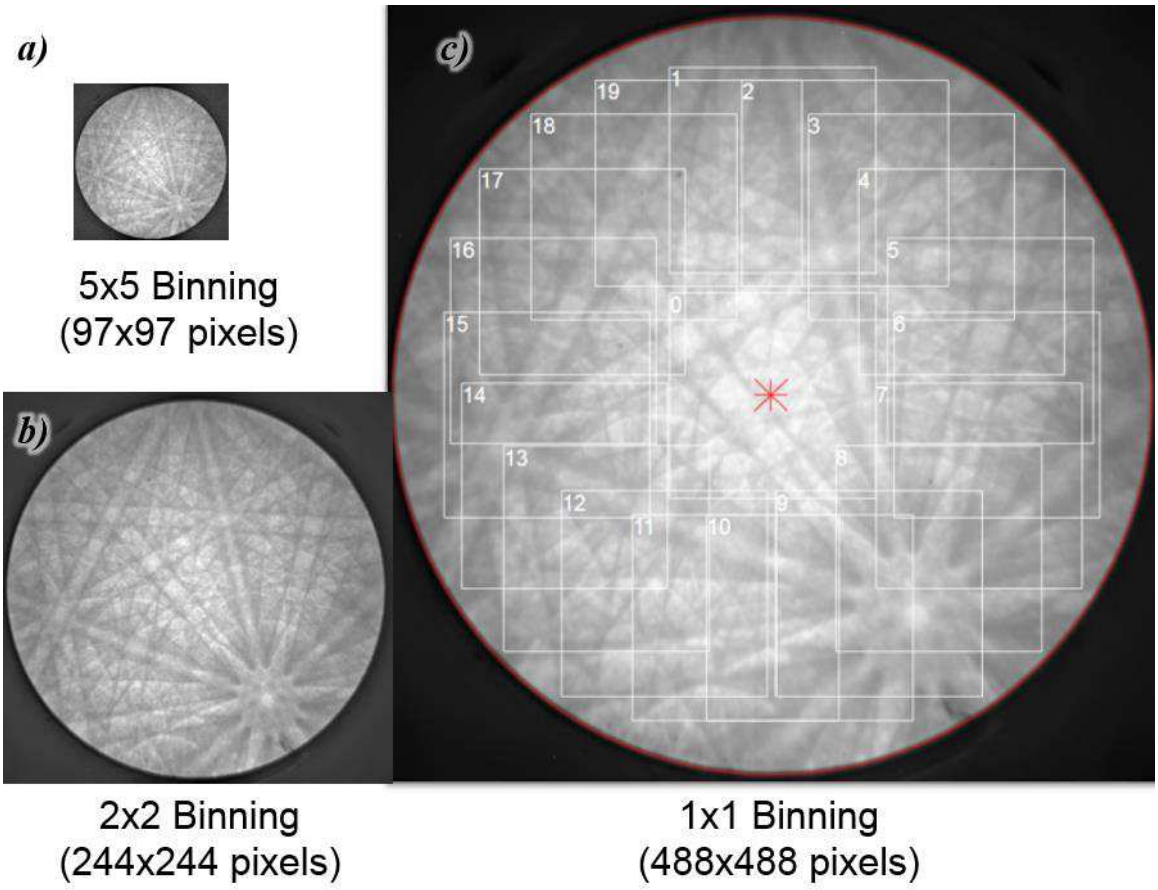

Figure 28 – Tungsten EBSD patterns showing the relative size and quality of patterns acquired at rates of a) ~100/s, b) ~1/s and, c) ~0.25/s. Higher resolution improves angular resolution of indexing for both Hough and cross-correlation (WMD method) analyses. However, long dwell times may lead to drift and carbon deposition. Region c) also shows the regions of interest used in FFT based cross correlation methods.

3.4.2. Transmission electron microscopy (TEM)

Transmission electron microscopy (TEM) samples were prepared using conventional focused ion beam (FIB) lift-out techniques for TEM preparation [256], on a FEI Nano600 dual-beam FIB/SEM . Alternatively, TEM samples of shear bands were prepared by wafering *post-mortem* test specimens to a thickness of ~200µm. Samples were polished on each side to approximately 100µm and thinned to transparency by electropolishing in a Fishione Twin Jet Electropolisher. The electrolyte solution (2wt% NaOH in water) was placed in an ice water bath and polished to perforation. TEM was performed on a JEOL 2100F field emission microscope with 200kV acceleration voltage. Samples were analyzed primarily in bright field and high angular annular dark field modes. Assessment of the dislocations density was performed using scanning transmission electron microscope (STEM) mode using a high angular annular dark field (HAADF) detector. Imaging of dislocations with the HAADF detector improves fidelity by reducing the constraints of the $\vec{g} \cdot \vec{b}$ invisibility criteria [257]. TEM observations helped to validate the dislocation densities, textures, and microstructures that were characterized extensively by EBSD.

CHAPTER 4. RESULTS

Ufg tungsten, synthesized using bottom-up sintering methods, was tested to understand the influence of microstructure and alloying on plastic instabilities and shear band formation. Dozens of powder metallurgical samples were tested by compression at quasi-static and dynamic strain rates to identify the onset of shear band formation. EBSD, TEM, and nanoindentation were used to examine microstructural features that lead to the development of plastic instabilities and shear localization.

4.1. Synthesis of ultrafine grained tungsten and tungsten alloys

In order to demonstrate shear banding behavior in ufg tungsten, an empirical processing study was carried out in collaboration with a number of colleagues at the US Army Research Laboratory. Over 240 individual milling trials were carried out, and hundreds of sintering runs were evaluated. The resulting catalog of over 1,000 samples has a wide range of physical and mechanical properties. In general, these processing studies demonstrated materials with grain sizes as fine as 100nm at a density of 17.4 g/cc (90% of the theoretical density of tungsten). The strengths of these materials ranged from 2.5-4.2 GPa depending on the specific composition and processing conditions. To put this in context, the ECAE samples processed by Wei et al. [36] had a strength of 1.7 GPa, while the "super-strong" tungsten produced by HPT [37] had a maximum strength of 3.1 GPa under quasi-static testing conditions.

This research is focused on the specific mechanisms of shear band formation in ufg tungsten. While the specific details of these processing efforts are beyond the scope of this discussion, the end result of an extensive, albeit largely empirical processing study,

was a reproducible method for processing tungsten to demonstrate shear banding both at quasi-static, and dynamic strain rates. Even unalloyed tungsten, which has a reported ductile to brittle transition temperature above 500K [8], demonstrated sufficient ductility to fail by shear banding at room temperature. Although, fracture does occur along the length of the shear band, the local shear strains observed inside of the band are on order of 0.4 prior to fracture. These materials provided a viable means to test the mechanisms of shear banding observed in ufg BCC metals.

Although grain size is a critical consideration, the goal of this research was to provide tungsten-based materials that reliably demonstrated a high degree of plastic instability and shear banding in a similar fashion to other ufg materials [165, 166]. In order to minimize the occurrence of brittle fracture that tends to result from porosity, higher density materials, greater than 18.3 g/cc (95% of theoretical density), were used for mechanical testing. Sintered tungsten samples with uniform microstructure (e.g. limited macroscopic defects that occur during pressing), and grain sizes of 250-300 nm were able to demonstrate shear banding reliably. With the exception of high strain-rate mechanical testing, all of the materials came from a single sintering run, with multiple (12-15) test specimens cut from the same material.

4.1.1. Unalloyed ultrafine grained tungsten (Unalloyed ufgW)

SEM images of polished and intentionally fractured surfaces in Figure 29, show a highly uniform microstructure that is free from macroscopic processing defects at low magnifications. Higher magnifications show significant porosity; however, pore sizes are fine and evenly distributed throughout the microstructure. The grain size (measured by

EBSD) was 273 ± 101 nm, and density (by the Archimedes method) was 18.6 g/cc (96.2% of theoretical density).

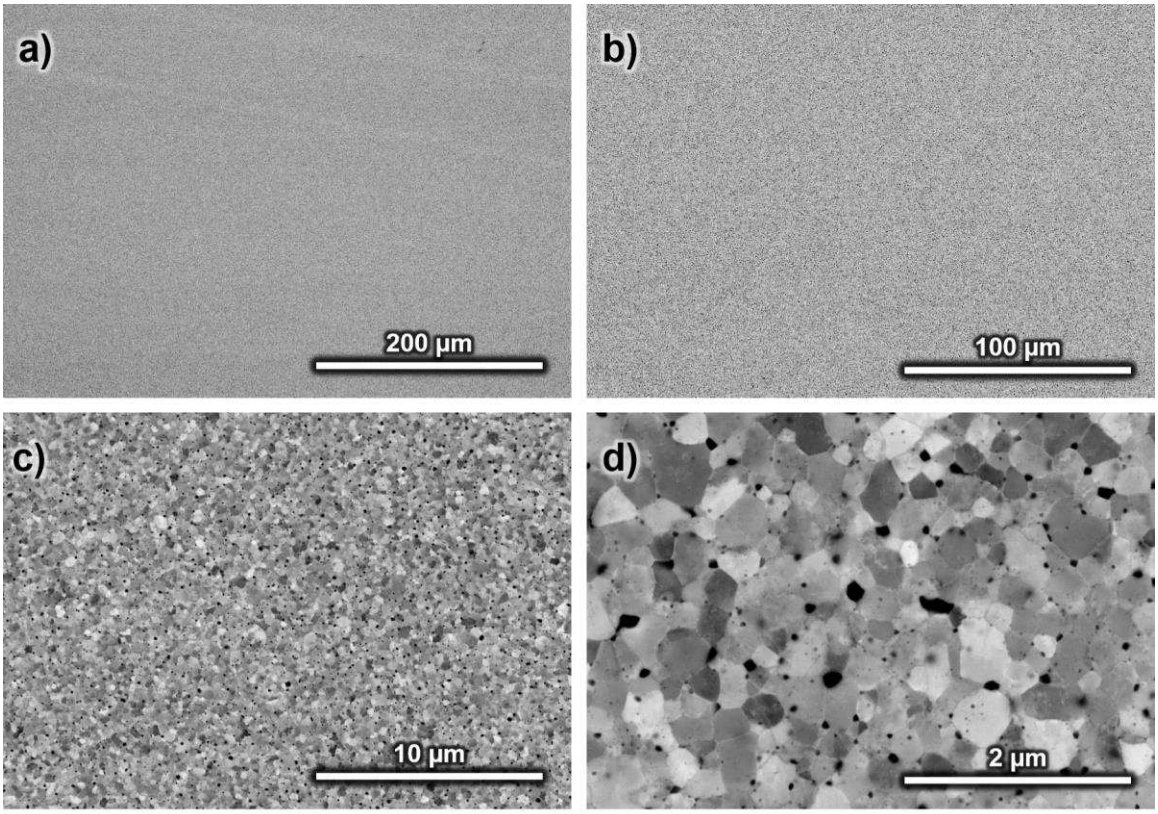

Figure 29 – SEM images of a sintered ufg tungsten (Unalloyed ufgW) used for compression testing. The metallographically polished microstructure was observed in backscatter electron mode.

Unalloyed ufgW samples had a tendency to fail by brittle intergranular fracture. These samples had low ductility and failed catastrophically very soon after the onset of plasticity. In particular, these samples had some difficulty surviving the harsh conditions of ballistic loadings, often fracturing before leaving the gun tube during testing. In order to suppress brittle fracture, boron and rhenium alloy additions were investigated in addition to the nominally pure tungsten samples.

4.1.2. Tungsten doped with boron (ufgW-B)

Boron additions had a significant influence on the fracture behavior of ufg tungsten. Small additions (as low as 0.075 wt%) facilitated a distinct transition from intergranular to transgranular fracture as shown in Figure 30. Although this transition in failure mode has been reported to reduce the ductile to brittle transition temperature of other BCC alloys [258], there was no appreciable increase in the plastic strain to failure for the boron containing samples. Furthermore, boron additions had the tendency of inhibiting densification, resulting in lower overall densities (only 90-92% of theoretical density) after sintering. All of the boron containing samples failed in a completely brittle manner, and showed no signs of shear band formation. Additional details regarding the influence of boron on the microstructure and mechanical behavior of tungsten are provided in the **Error! Reference source not found.**

Figure 30 – Fracture surfaces of a) nominally pure ufg tungsten, showing predominantly intergranular fracture and b) ufg tungsten doped with 0.075 wt% boron, showing a higher propensity for transgranular fracture.

4.1.3. Tungsten rhenium alloys (ufgW-XRe)

Alloying tungsten with rhenium has been shown to significantly improve the room temperature ductility of tungsten [18, 259, 260]. Furthermore, rhenium additions did not

result in any appreciable changes to the densification behavior of ufg tungsten and tungsten-rhenium alloys achieved similar densities and grain sizes to the nominally pure tungsten. The microstructure of an alloy with 5 wt% rhenium (ufgW-5Re) are shown in Figure 31. Although this sample shows several macroscopic defects (unalloyed rhenium inclusions, macroscopic porosity, and non-uniform regions of micro-porosity), the added ductility that resulted from rhenium additions showed a strong resistance to fracture, without affecting the propensity for shear band formation. This particular sample had a grain size of 253 ± 97 nm (by EBSD) a density (by the Archimedes method) was 18.59 g/cc (96.3% of theoretical density). The microstructure was highly representative tungsten rhenium alloys in general, and all of the quasi-static mechanical testing and the shear band characterization studies reported were exclusively from this sample.

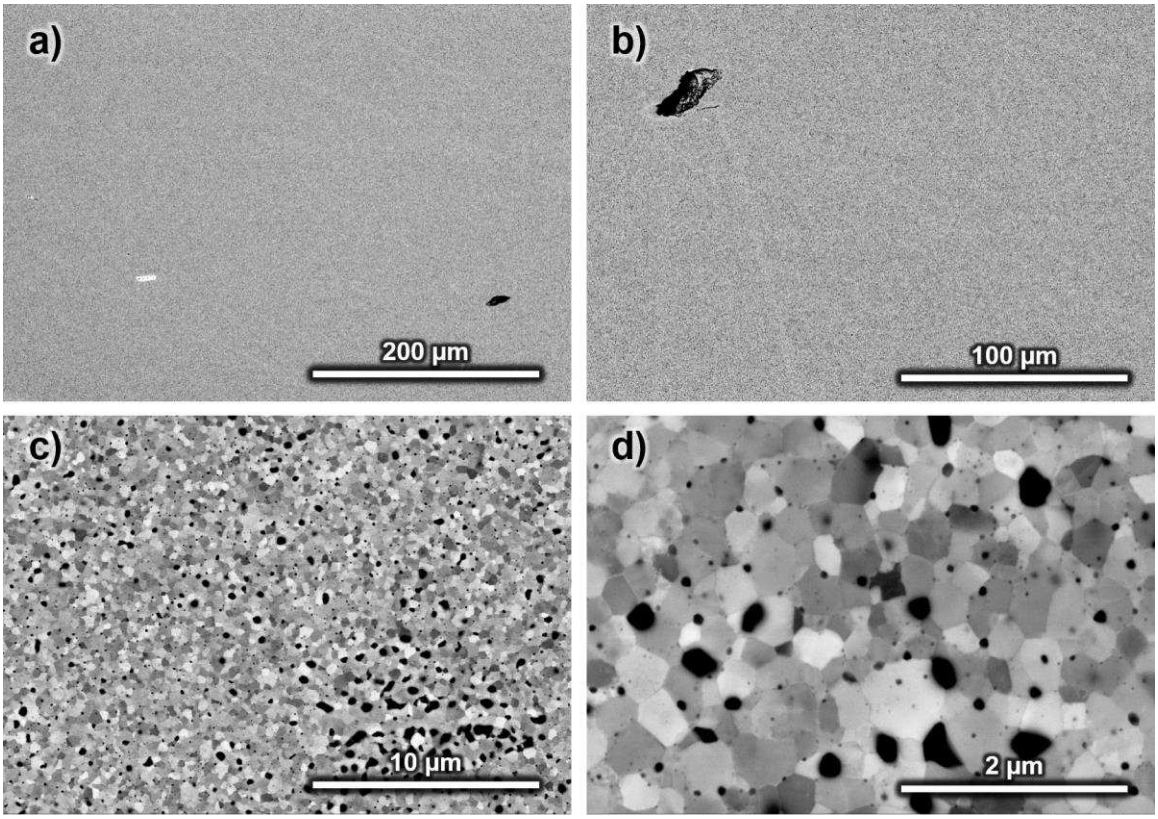

Figure 31 – SEM images of an ufg tungsten alloy with 5 wt% rhenium (ufgW-5Re) used for compression testing. The metallographically polished microstructure observed in backscatter electron mode.

4.2. Mechanical testing

Ductility is a critical, but somewhat counterintuitive, requirement for shear banding. Testing of early sintered ufg samples would often result in fully brittle fracture especially for unalloyed tungsten [53]. Fully brittle behavior is easily identified by the axial fracture, parallel to the loading direction (as opposed to fracture at a 45° angle, which is indicative of a shearing event). This early fracture releases a considerable amount of strain energy and generally precludes shear bands from developing. These observations were similar to some of the early findings of Wei et al. [68]. In many cases, these brittle failures were attributed to with pre-existing defects in the microstructure that could be attributed to specific processing conditions.

Under the appropriate processing conditions, ufg tungsten is not inherently brittle, even in the unalloyed form. These finding have been reported previously by several researchers [31, 82] in the case of tungsten processed by severe plastic deformation. For sintered tungsten, careful control of milling, pressing and sintering parameters can result in a uniform microstructure that can suppress brittle fracture, at least under compressive loading. However, these materials are still not very ductile as a result of the fracture that occurs, immediately after shear banding. Several dozen mechanical tests were performed at quasi-static and dynamic strain rates in order to understand and control this plastic instability, and a representative sample is discussed below.

4.2.1. Quasi-static compression

Initial DIC studies were carried out on un-patterned samples. Although patterning can improve the local resolution of DIC, painting the surface which would interfere with direct observation of the shear bands. Unpainted samples showed the number and thickness of shear bands with higher fidelity, but relying on the native surface features of the samples results in a significant decrease in the strain resolution required for 2D strain maps. Two of the samples were tested to small strain, and two to catastrophic failure by quasi-static compression using digital image correlation. The results of a single large strain compression test of an Unalloyed ufgW sample is shown in Figure 32. Samples showed nearly elastic-perfectly plastic behavior; however, this particular sample shows the modulus of elasticity deviate from ideal behavior as a result of poor DIC tracking. Each of the other three test samples also shear banded. The other sample tested to catastrophic failure, failed early, at less than 1% plastic strain. The sample was pulverized

and generally not recoverable for any useful microscopic analysis. Each of the engineering stress-strain curves of this particular sample showed a steady and continuous decrease in load after yielding, this macroscopic strain softening was observed throughout the plastic region of the test. Ultimately fracture was observed along the direction of the dominant shear bands, accompanied by a catastrophic load-drop. The sample was recovered for microscopic evaluation.

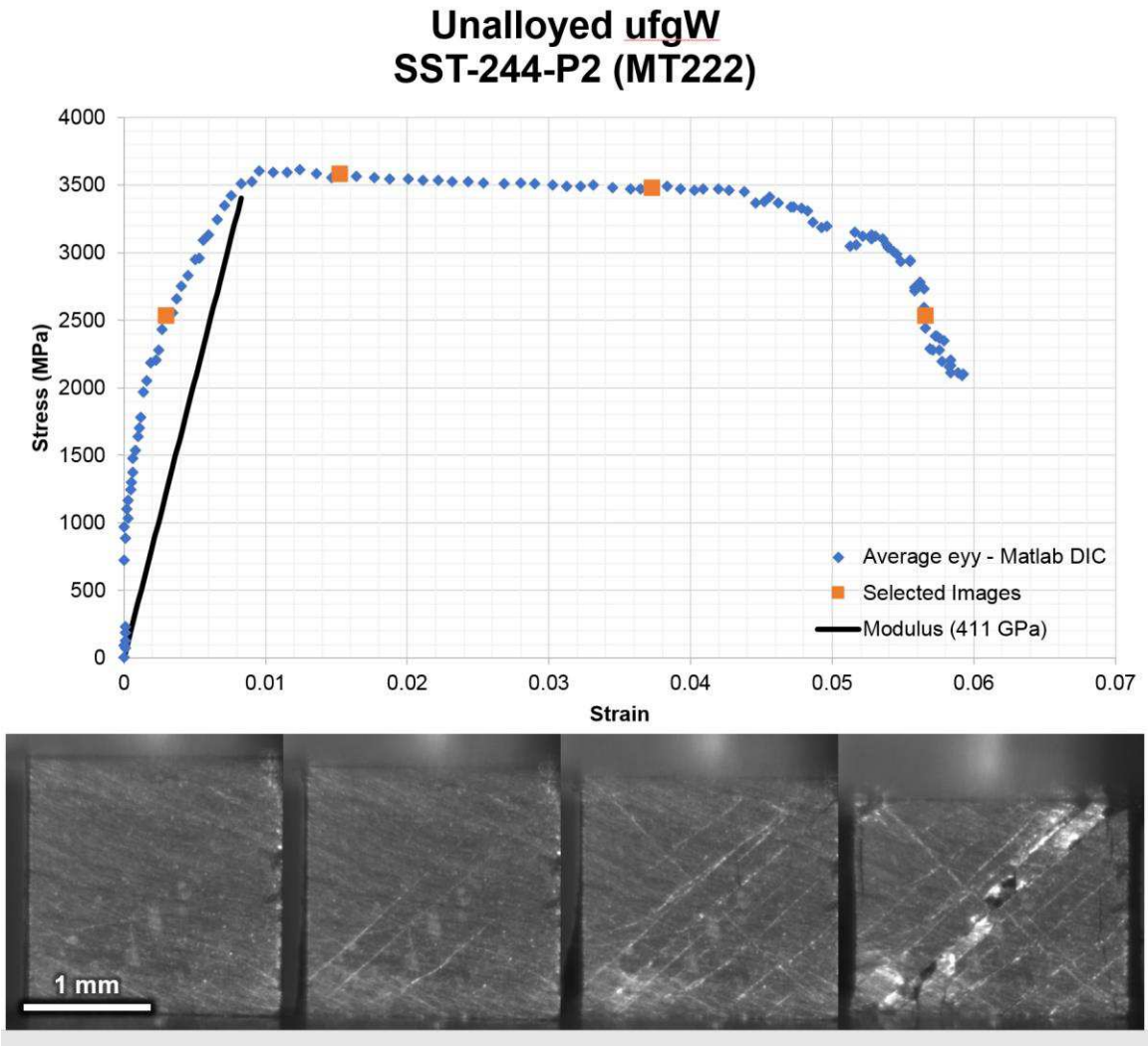

Figure 32 – Compression testing of a standard ufg tungsten (Unalloyed ufgW).

These tests each verified a general observation that shear bands in ufg BCC metals form very quickly after the onset of plasticity. No shear bands were observed during the elastic loading portion of the curves, but they are clearly visible at less than 1% plastic strain. Several fine shear bands initiate early and travel across the length of the specimen. Shear bands initiated at the outside surface, predominantly at the corners, and extended at an angle of approximately 45° from the loading direction (though there is some deviation from the maximum shearing direction). In later images, shear bands are observed to intersect in different regions of the sample. These bands are very narrow (measured to be 8.2 μm) as shown in Figure 33 and do not appear to be impeded by intersecting bands at later stages in deformation. The strain state is highly complex and 3D at these intersection points and it is surprising that fracture is not more prevalent, given the generally brittle nature of tungsten. The amount of strain inside of three separate bands was measured to be 0.38 ± 0.10, and they had uniform thickness within the region measured. However, macroscopic views show significant variations in thickness depending on the region of interest.

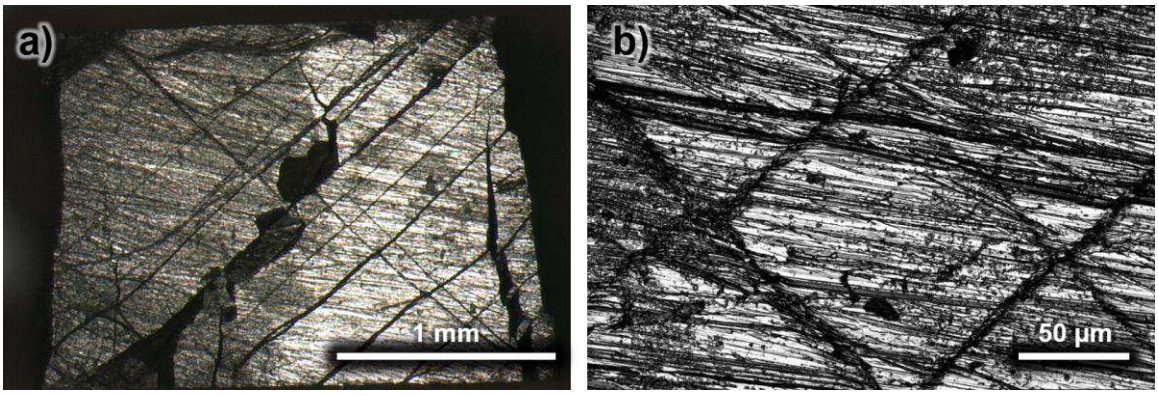

Figure 33 – Images of shear bands in compression tests from Figure 32 taken by a) optical, and b) confocal microscopy. Three of the shear bands in b) were measured to have an average thickness of 8.2 ± 0.4 μm and a shear strain of 0.38 ± 0.10.

Compression tests of the ufg tungsten-rhenium alloy samples (ufgW-5Re) at quasi-static strain rates showed several similarities to the unalloyed ufg tungsten samples. Two samples were tested, and a representative stress-strain curve, shown in Figure 34, also demonstrated nearly elastic-perfectly plastic behavior with shear bands initiating very soon after the onset of plasticity. These curves did show a minor degree of strain hardening; however, this hardening did not prevent several shear bands from forming and propagating across the specimen. The ufgW-5Re sample did not show a load drop, or any evidence of catastrophic failure during the test, and this specimen was also recovered for microscopic analysis.

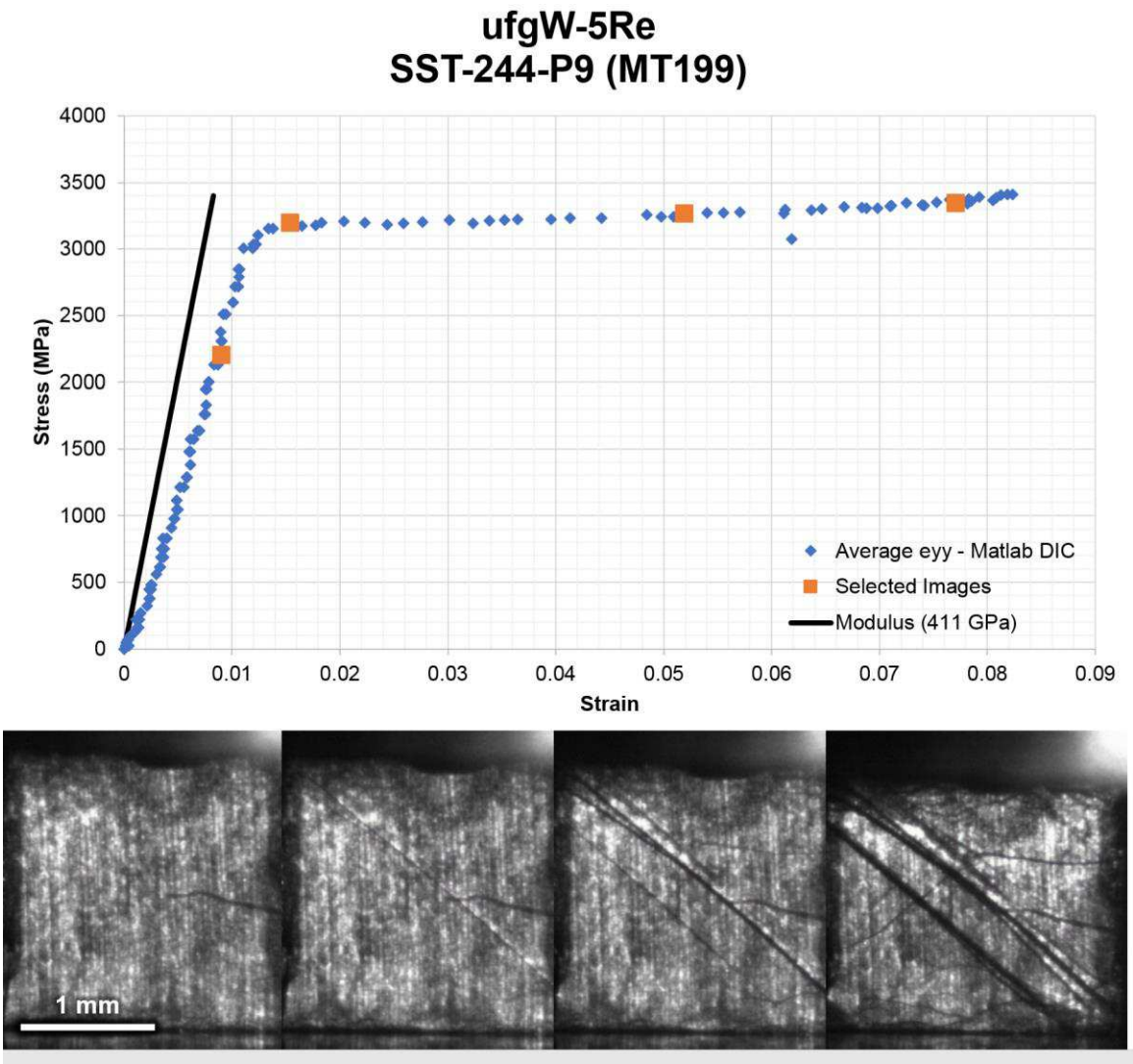

Figure 34 – Compression testing of an ufg tungsten alloy with 5 wt% rhenium (ufgW-5Re).

The morphology of the shear bands appears similar to those in the unalloyed, ufg tungsten (Unalloyed ufgW), except that several of the bands are slightly thicker (upwards of 30 μm) as shown in Figure 35. Several shear bands also show some degree of "out of plane" deformation, which could affect the accuracy of 2D strain analyses, both by DIC and *post-mortem* measurement.

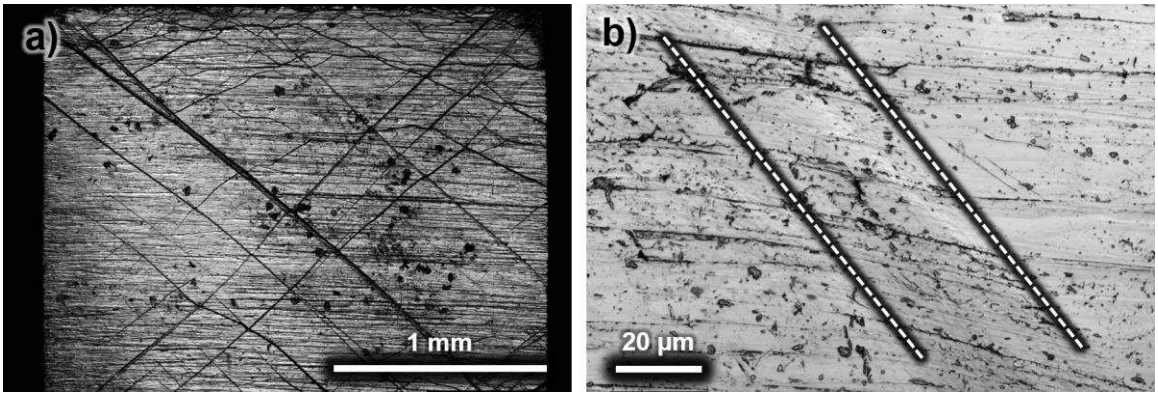

Figure 35 – Confocal microscope images of shear bands from the ufgW-5R alloy (Figure 34). A macroscopic image of the shear bands is shown in a), while b) shows a higher magnification image of a dominant band that initiated from the lower right corner with the shear band highlighted by dashed lines. The shear largest shear band in a) was measured at four points along the length of the band. The thickness of the band measures 34.9±9.1 µm, while the shear strain measures to be 0.20±0.03. The higher resolution image, b) shows a thickness of 33.7±2.7 µm with a strain of 0.12±0.04.

Initial tests showed that ufg tungsten and tungsten alloys demonstrated a strong propensity for shear band formation. While the tungsten rhenium sample showed considerably higher degree of damage tolerance, both samples resisted the brittle axial failure that has been repeatedly observed in compression testing of ufg tungsten. Shear bands in the Unalloyed ufgW sample appear thinner and more diffuse than those propagating the ufgW-5Re sample which exhibited a limited degree of strain hardening. Both of these features may be indicative of the relative plastic instability of each material.

After conducting several preliminary tests describing the extended deformation behavior at large strains and quasi-static rates, additional samples were interrupted at very small strains in order to provide insight to the early stages of shear band formation in ufg tungsten. These used traditional surface patterning techniques (air brush, matte finish, white on black acrylic paint) [261] to improve DIC correlations, particularly at small strains. This patterning prevented direct observation of the shear bands, but the improved

pattern correlation allowed for 2D strain mapping and improved quantification of the strains associated with shear banding. The Lagrange method [262], was chosen for calculating strains (i.e. relative to the initial configuration). Strains were plotted based on the von Mises equivalent strain, because this measure is not dependent on the coordinate system. This allows for a better comparison of strains between shear bands propagating in different directions, or following curved pathways.

The stress strain curve for another Unalloyed ufgW sample is shown in Figure 36. Similar to the results reported in Figure 32, this sample demonstrated nearly elastic-perfectly plastic in interrupted tests; however, the shear banding is not as easily observed during the initial stages of plastic deformation. The lack of observed shear banding behavior may be the result of insufficient resolution that results from averaging over multiple pixels to track displacement, and filtering over several displacements to obtain the strain. The shear band eventually propagates through the entire sample, even at very low global plastic strains (0.4%).

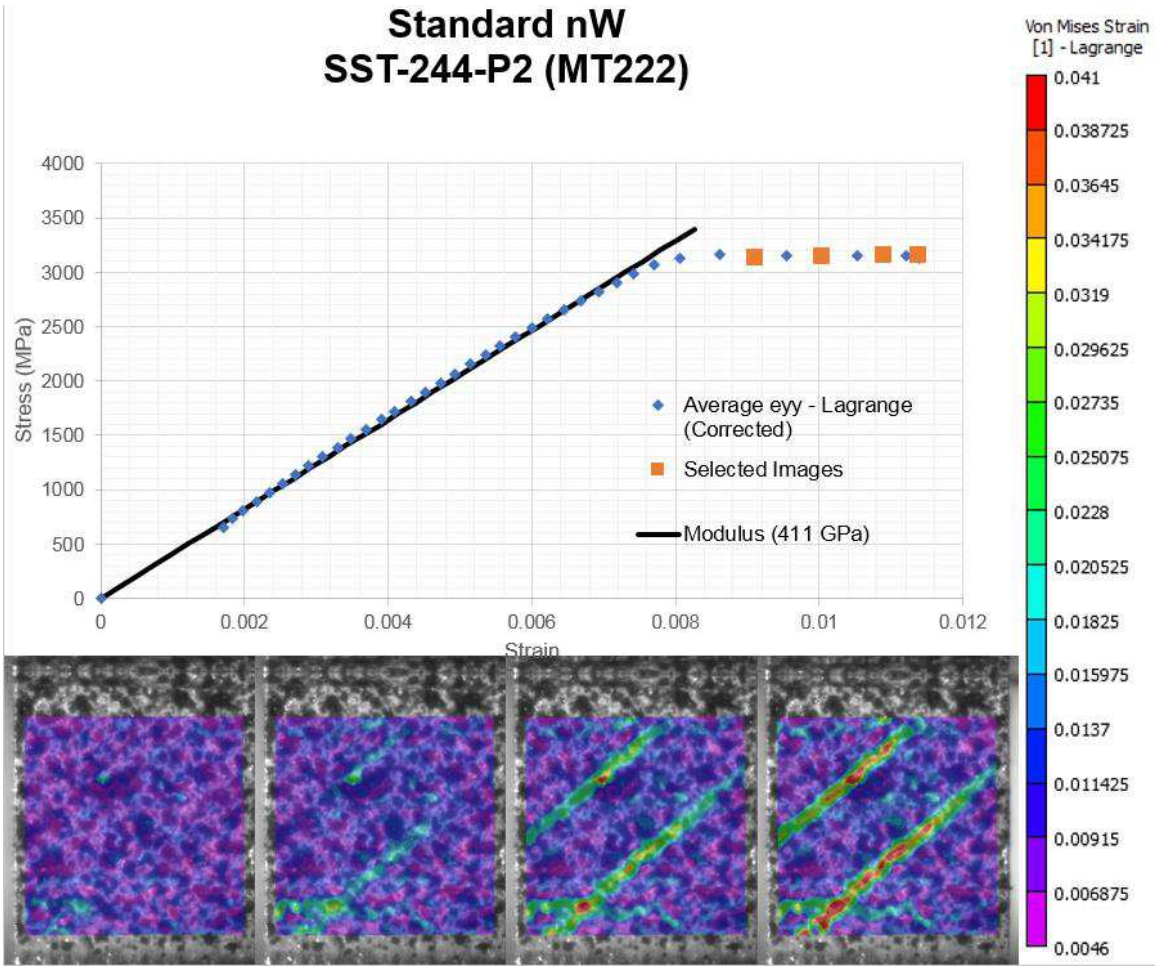

Figure 36 – Stress strain curves for an Unalloyed ufgW sample interrupted at approximately 0.4% plastic strain. An anomalous loading feature was detected (likely the result of debris on the upper punch head); however, this was corrected by tracking the crosshead displacement by DIC and modifying

A similar test was performed to the onset of plastic deformation in a ufgW-5Re sample, shown in Figure 37. The sharpness of the shear band is more apparent than the unalloyed tungsten tested under identical conditions; however, this may be the result of variations in patterning between samples.

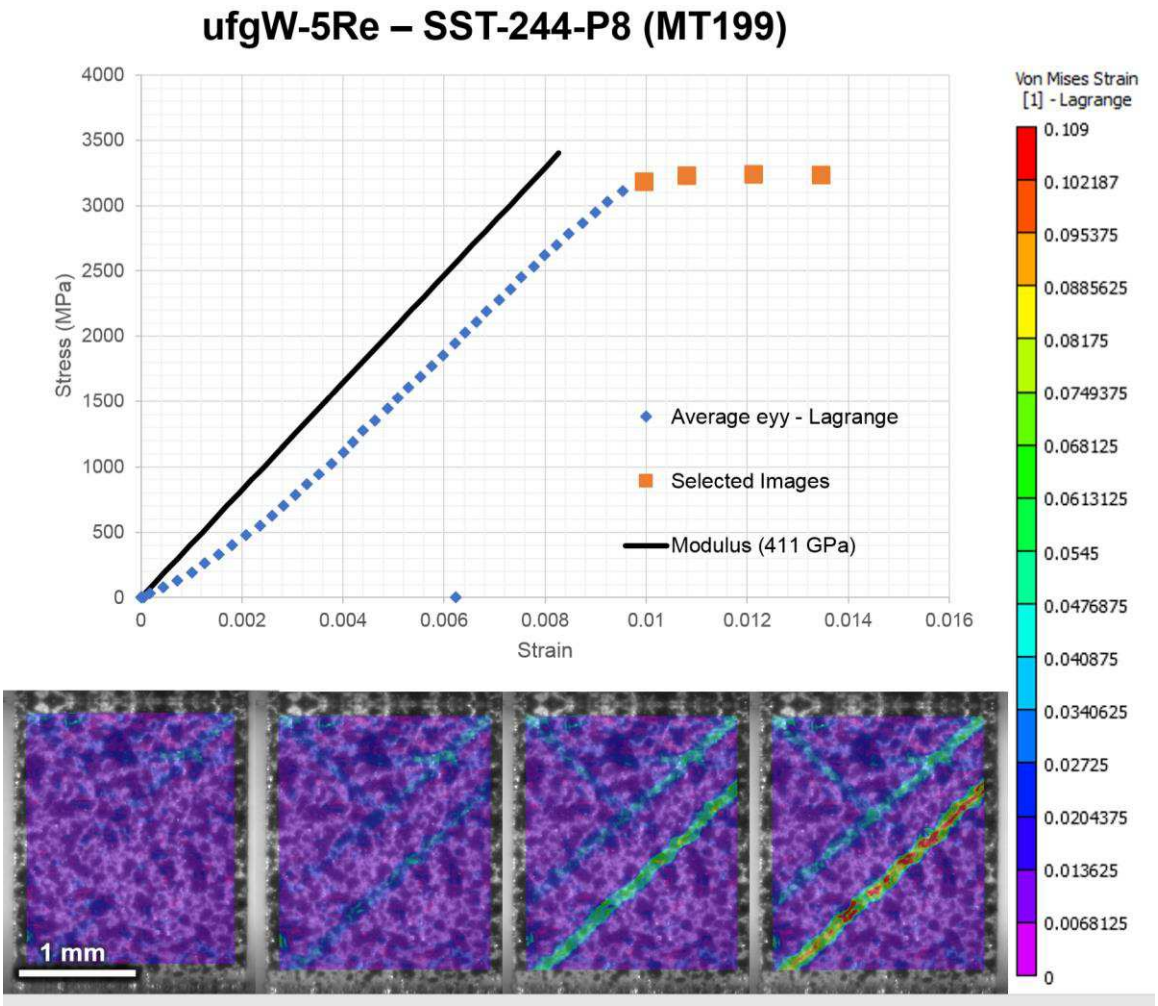

Figure 37 – Digital image correlation of shear banding in a ufgW-5Re alloy tested under quasi-static conditions.

In each of the previous figures (Figure 32-Figure 37) it is clear that the shear band carries the bulk of the plastic strain, while the rest of the region remains largely elastic. However, it is possible that the strain in these regions is simply masked by the relative magnitude of the shear band. In order to verify that the plastic strain is really confined to the band, it is possible to use DIC to measure the strain between bands as shown in Figure 38. The region between shear bands shows a very slight strain increase at low stresses (~500 MPa); however, this region follows the elastic region very closely

thereafter. The total strain observed after unloading is less than 0.15%, which is certainly not considered yielding in an engineering sense.

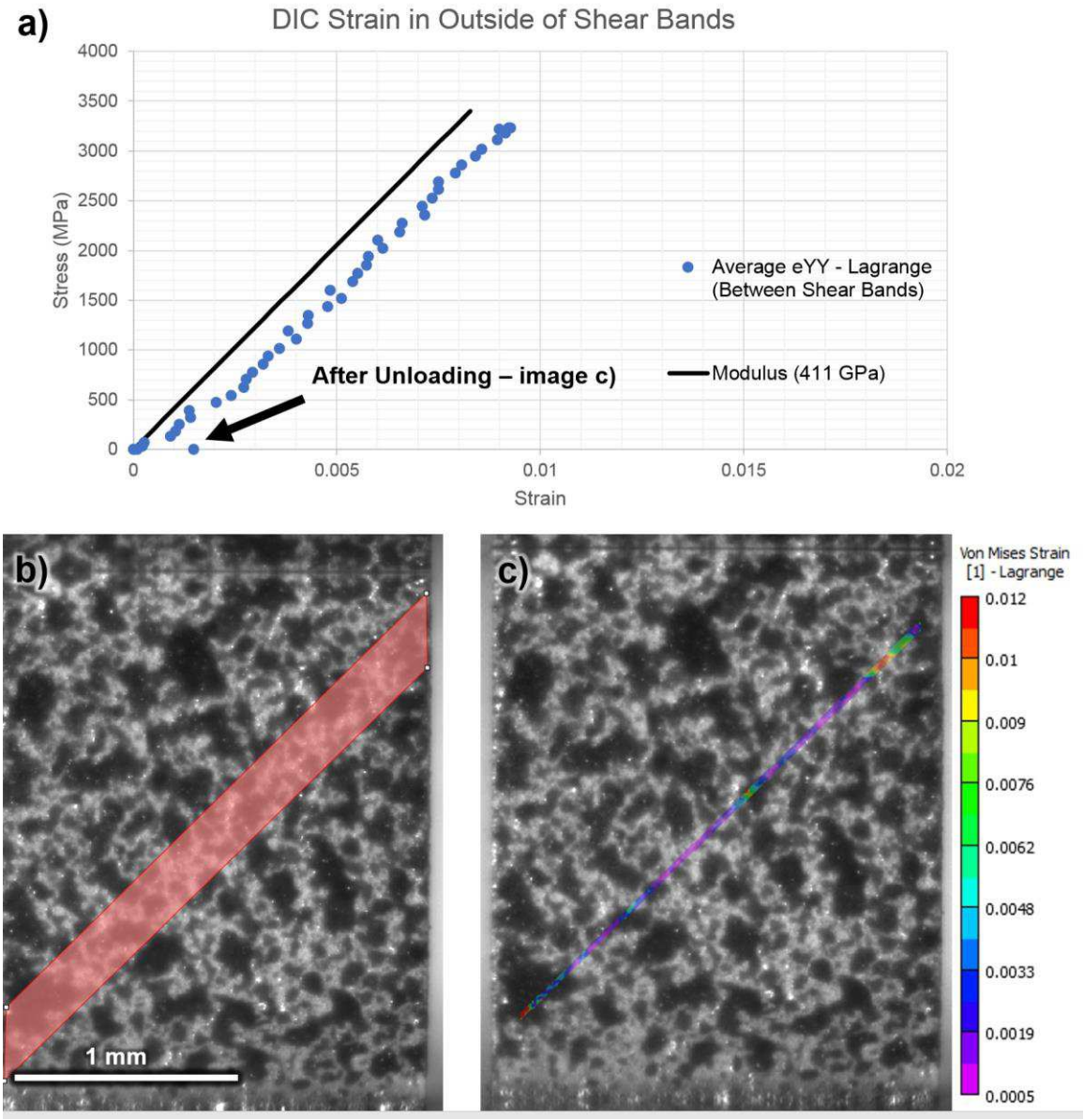

Figure 38 – Stress-strain curves from the region between shear bands in the ufgW-5Re sample as measured by DIC. Loading Modulus = 372 GPa, Unloading Modulus =417 GPa, Plastic Strain = 0.148%

4.2.2. Velocity and temperature of shear bands

The deformation rate is critical to understanding whether a shear band could be adiabatic in nature. Low imposed strain rates allow for temperature to equilibrate, and these are generally accepted to be isothermal. In theory, for a strain localizing material, the strain rate could be considerably higher inside of the shear band, and adiabatic conditions could be observed on a local level. Higher rate DIC (~100FPS), was used to investigate the propagation velocity and local strain rate of a shear band in order to describe limits of deformation rates to determine whether the criterion for adiabaticity is met. The results of these higher frame rate tests are shown for a ufgW-5Re alloy are shown in Figure 39.

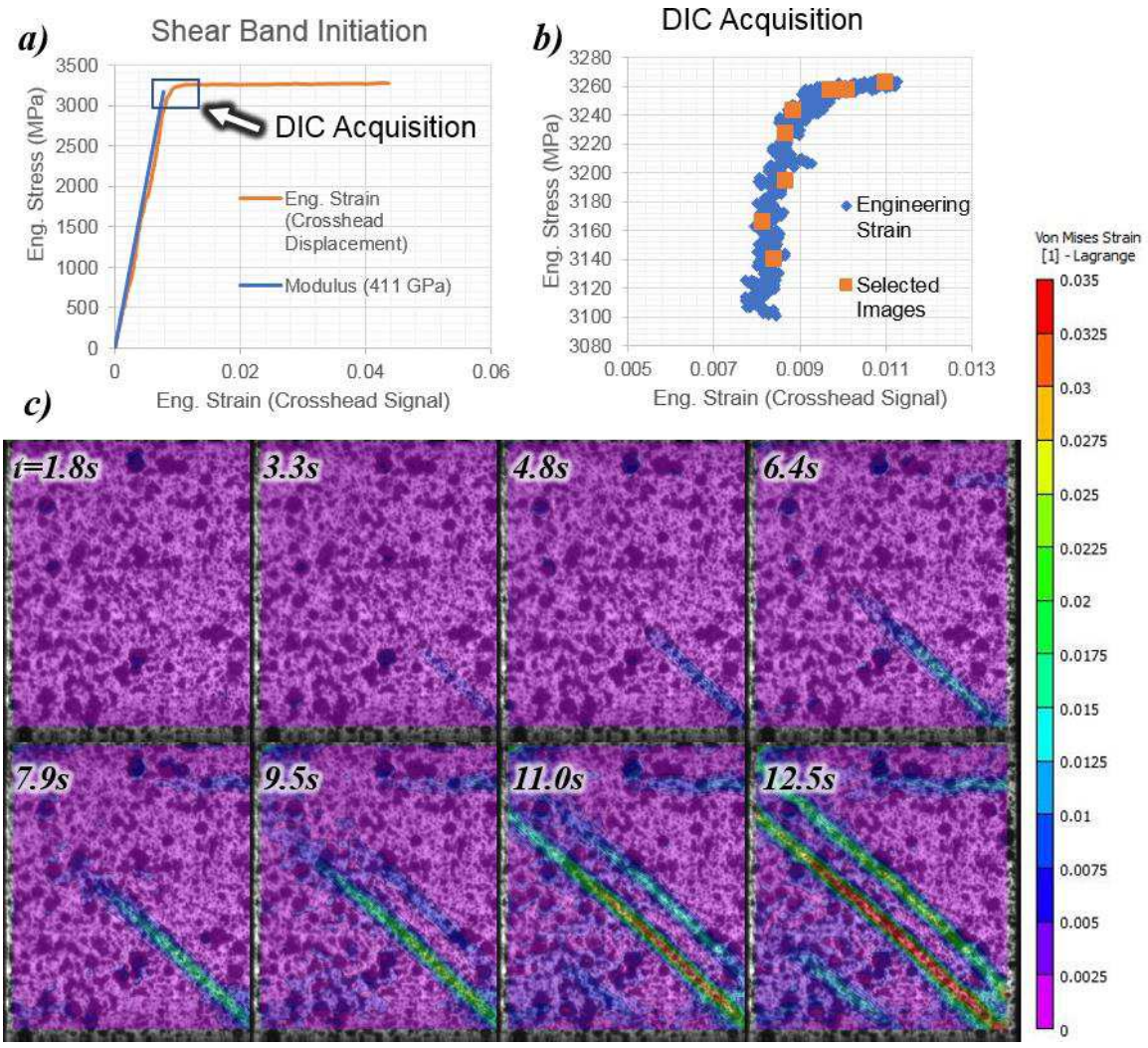

Figure 39 – Higher frame rate (~100 FPS) acquisition of shear band formation in a ufgW-5Re alloy tested under quasi-static conditions.

Over 1,000 images were captured around the yield point, effectively showing the earliest measurable onset of a shear band, and the lengths of the shear bands were measured according to specific strain levels in successive frames. The velocity of the shear band is captured based on the first measurable strain above background. Since this is an indirect measurement of the shear band position based on strain levels, the propagation of higher strain contours indicates strain development inside of the band as the result of: (1) coarsening the thickness of the band, or (2) increasing strain inside of the band, or (3)

some combination thereof. The successively higher strain levels propagate at a higher "effective velocity" than the original band as shown in Figure 40. In general, these velocities are fairly slow in comparison strain data are plotted in terms of the von Mises equivalent strain, it is possible to track the initial formation velocity, in addition to an "effective velocity" for continued levels of deformation.

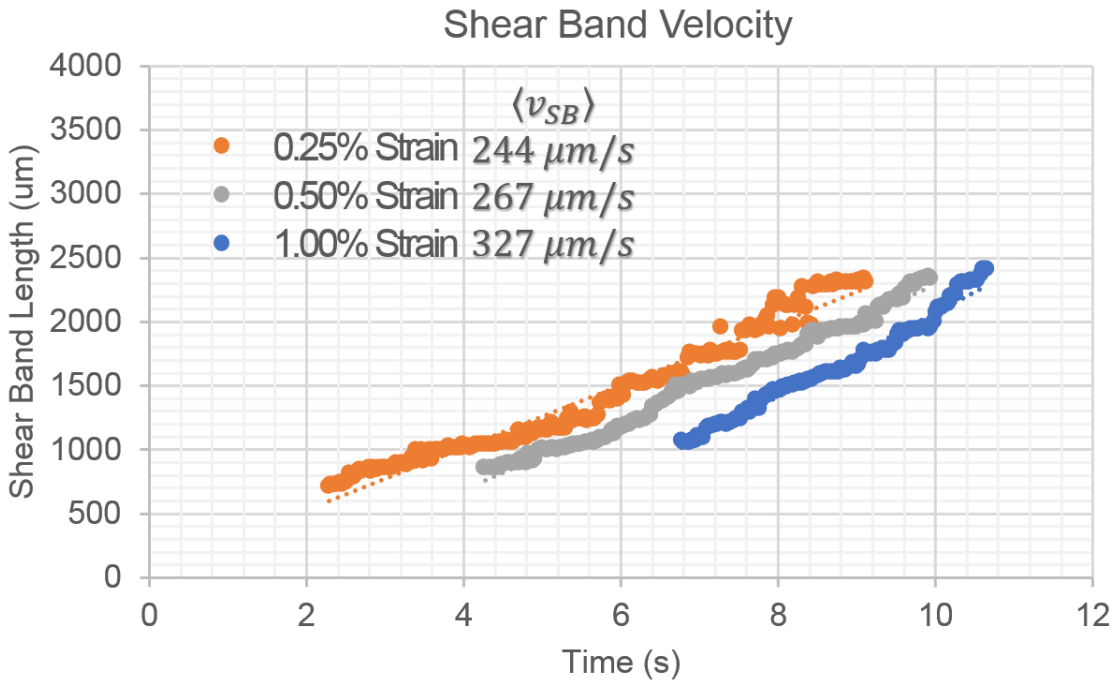

Figure 40 – Shear band velocity <u>at initiation</u>, measured by digital image correlation. The velocity corresponding to a specific strain contour. Shear band velocity tends to increase during the deformation process.

The velocity of a shear band is not solely a function of the prescribed deformation rate, or the mechanical properties of the sample. If strain softening occurs, the velocity of a shear band can be affected by the testing apparatus itself. The load frame acts like a compressed spring, and a frame with a lower effective stiffness stores more energy than a stiff frame. The stiffness of the load frame relative to the sample, affects the strain energy release rate and the propagation velocity of the shear band [121]. In essence, a frame with

a lower stiffness contains more elastic energy at a given load, and will tend to drive the shear bands faster than a stiff frame. The velocity of the shear band may also depend on the number of bands that are propagating at a given time. Despite these external factors, the velocity of a shear band driven at quasi-static strain rates was measured to be less than 1 mm/s. By comparison, the velocity of a shear band in a bulk metallic glass has been estimated to be approximately $0.1c_t$, where c_t is the velocity of a transverse sound wave [263]. In tungsten, this shear band would travel at approximately 289 m/s!

To further validate, the fact that shear bands do not need to be hot in order to propagate, several samples were coated with a fine indium layer via magnetron sputtering. Although these samples did not show any signs of melting the control test showed a similar morphology of indium particles on the surface, even after heating above 300°C, where kinetics favor the formation of an oxide [264]. Figure 41 shows where a shear band propagating out of plane intersected the sample surface, with the compression axis in the vertical direction. Lewandowski and Greer [228] showed surface melting of a tin coating under similar conditions of shear banding in a bulk metallic glass sample.

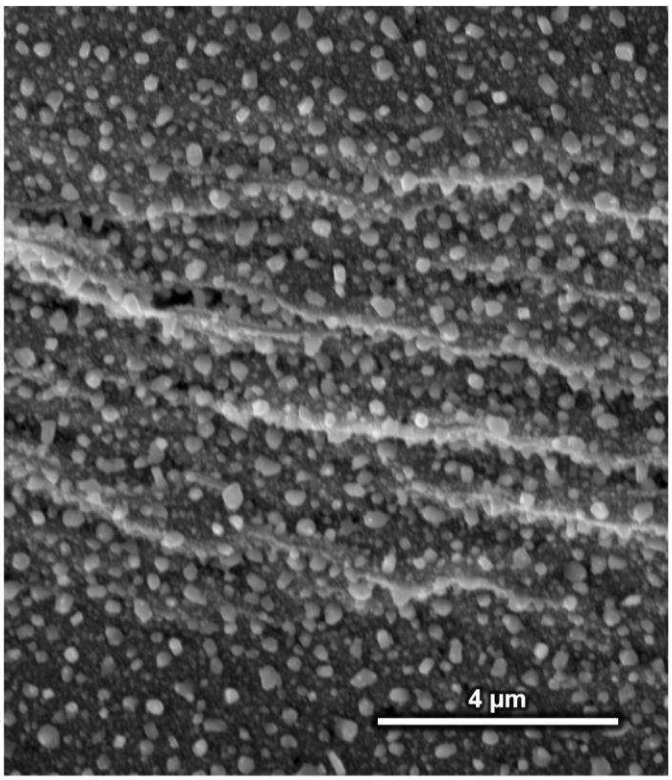

Figure 41 – Shear band formed in a ufgW-5Re alloy that had been sputter coated with a fine (~50nm thick by XRD) indium layer.

Ultimately, the test was deemed inconclusive, and the exact temperature rise was unknown based on the melt technique. However, a lower bound estimate of the temperature can be calculated based on the local strain rates inside of a shear band, and the upper bound may be effectively described based on perfectly adiabatic conditions.

4.2.3. Dynamic compression

Samples tested at high strain rates (~10^3/s) were more likely to fail by brittle fashion than samples tested under quasi-static conditions. Nominally pure tungsten showed an immediate and catastrophic load drop after the onset of yielding. The stress strain curves for three Unalloyed ufgW samples are shown in Figure 42. One sample did show signs of

an unloading portion of the curve; however, the prior load drop was an indication that the sample had already failed in a fully brittle manner.

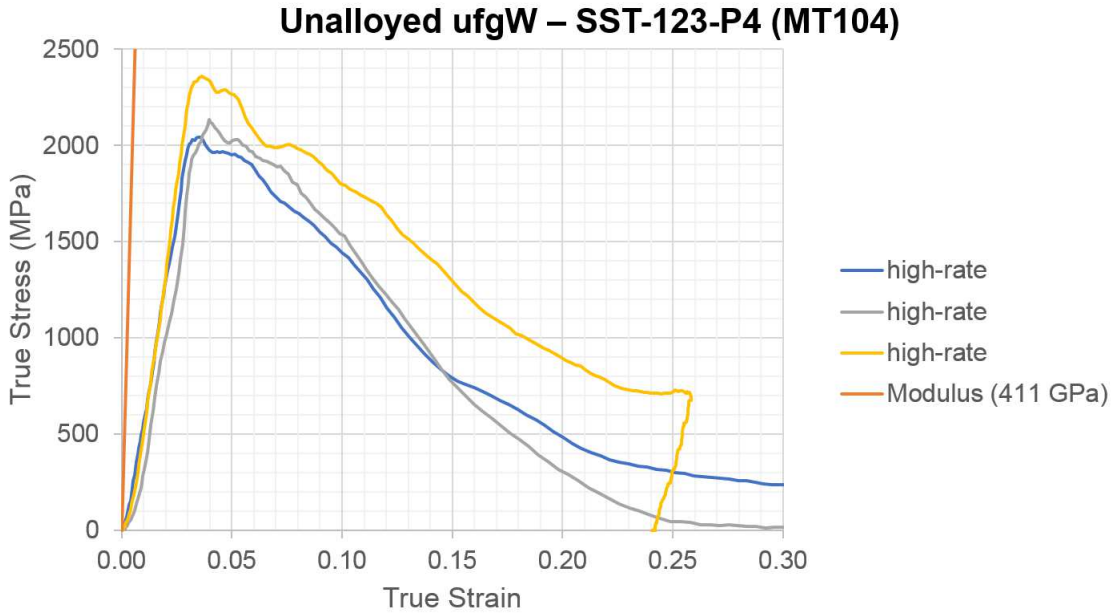

Figure 42 – Split Hopkinson Bar compression, stress-strain curves for unalloyed ufg tungsten. Two samples failed in a brittle manner into a coarse sand, while one sample cracked axially and was recovered for microscopic analysis.

After dynamic testing, some of the larger remnants were recovered for microscopic analysis. Shear bands were not distinguishable at the surface, and fracture surfaces showed that fracture initiated at the outside surface (i.e. not likely a result of internal processing defects). Images of the fracture surfaces are shown in Figure 43 show some signs of transgranular fracture. Although this is generally reported as a positive sign for ductility in tungsten, there was no appreciable ductility, or demonstration of shear banding behavior in any of the Unalloyed ufgW samples.

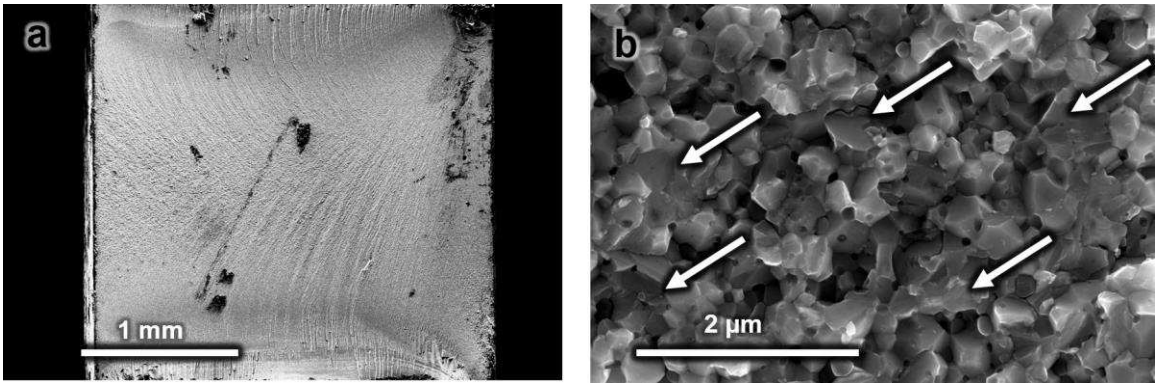

Figure 43 – SEM images of fracture surfaces for an Unalloyed ufgW sample tested at high strain rates. Beach marks in a) show that fracture initiated in the upper right corner of the specimen, at the surface. Arrows in b) show signs of transgranular fracture.

The mechanical testing of ufg tungsten rhenium alloys (ufgW-5Re, ufgW-10Re, and ufgW-25Re) fared better during high-rate testing. Each of these samples showed clear evidence of shear banding; however, the strain localization did not lead to catastrophic failure and elastic unloading was observed. Curves for the ufgW-5Re alloy (Figure 44) showed strain softening throughout the plastic region of the test and several samples were recovered intact.

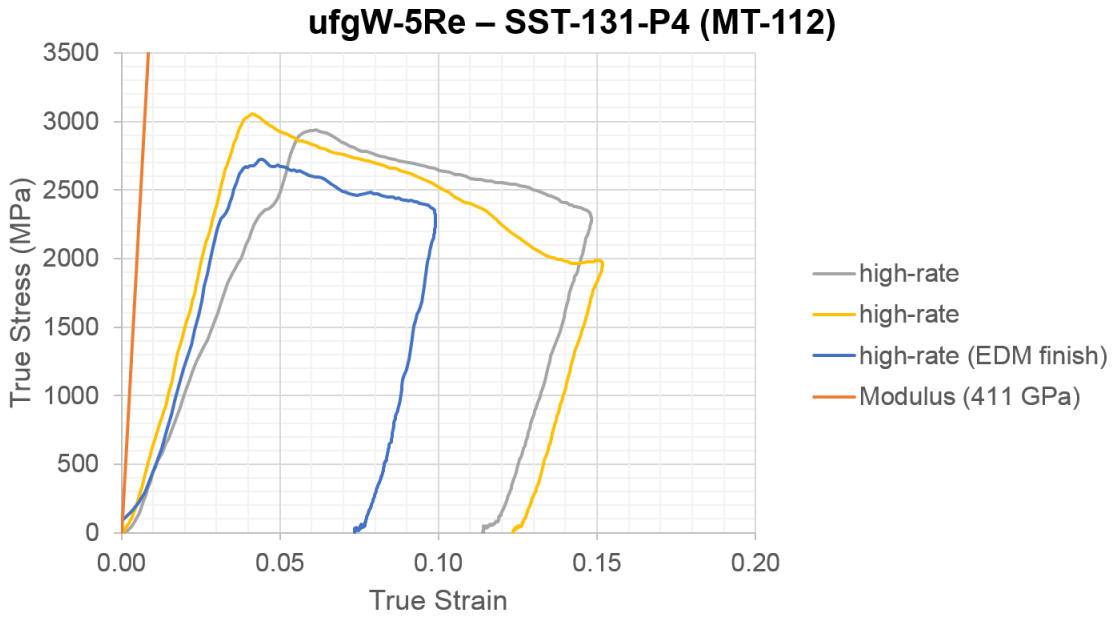

Figure 44 – Dynamic behavior of ufg tungsten with 5wt% rhenium. The material shows shear banding behavior without leading to catastrophic failure, at least over the instrumented portion of the test. Several samples failed in large pieces as the result of the bar rebounding after the instrumented portion of the test.

One of the ufgW-5Re samples (blue curve in Figure 44) was filmed with a high-speed camera during testing. Although the images are of poor resolution, fully formed shear bands can be observed during the later stages of testing. A detailed view of this stress strain curve is shown in Figure 45. The plastic portion of the curve was captured in less than 50 μs, indicating that the conditions of testing were certainly adiabatic. During this time, the shear band is able to propagate through the entire sample, which provides a lower bound for the propagation velocity of the shear band. In high strain rate tests, the propagation velocity of a shear band is at least 57 m/s, over five orders of magnitude faster than the same material tested under quasi-static conditions.

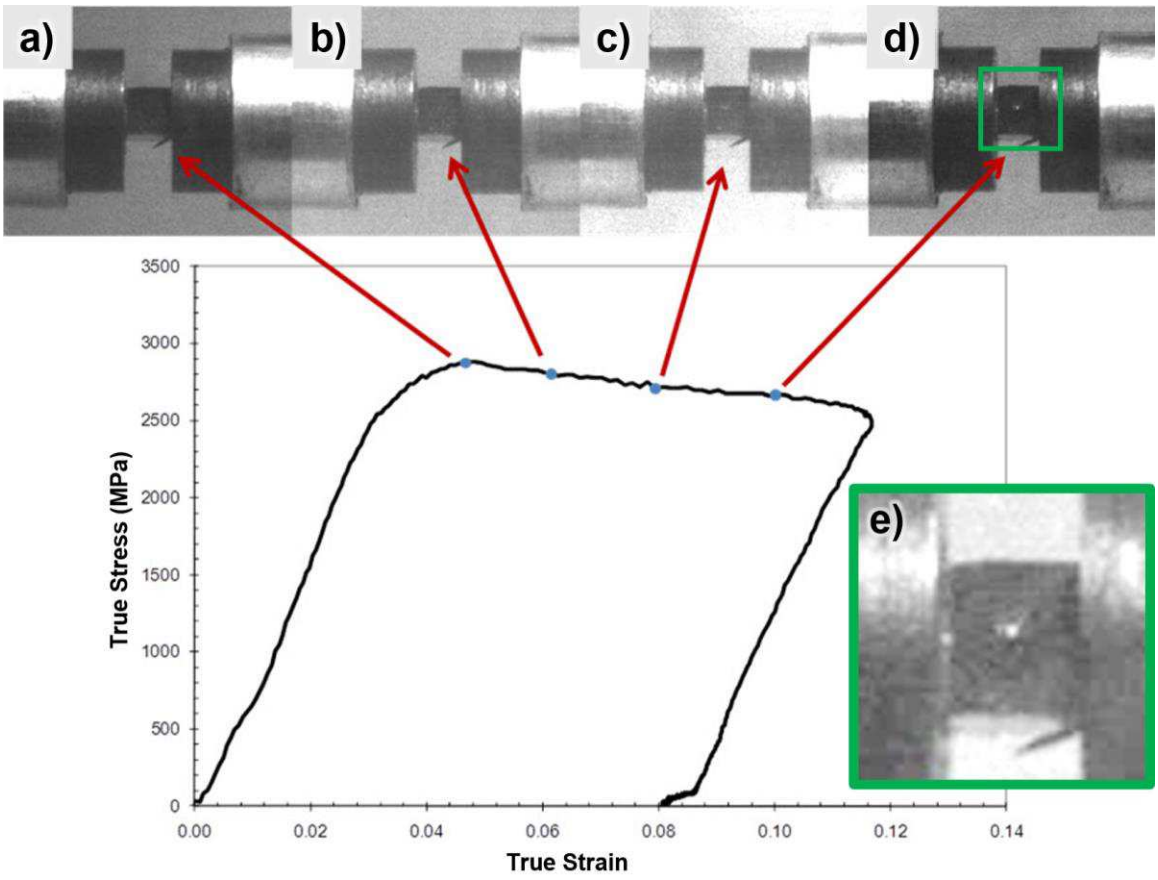

Figure 45 – High speed imaging (~100,000 FPS) of shear band formation in one of the ufgW-5Re samples shown previously. The images show shear bands fully traversing the sample in by image d); however, the contrast and lighting is poor. A shear band is barely discernable in e), a magnified and enhanced image of d).

Shear bands resulting from dynamic testing tend to be thicker and were less likely to meander than those observed during quasi-static testing, as shown in Figure 46. Despite the higher strain rates, the shear strain inside the bands were not significantly different from those measured after quasi-static testing; the strain was slightly lower in dynamic tests, but still within a margin of error of the quasi-static shear band in the same ufgW-5Re alloy. Micro-fractures were observed inside of several bands, and a large axial crack appears to have initiated at the center of the specimen based on the intersection of shear

bands. Although the amount of shear strain was approximately the same as ufgW-5Re samples tested under quasi-static conditions.

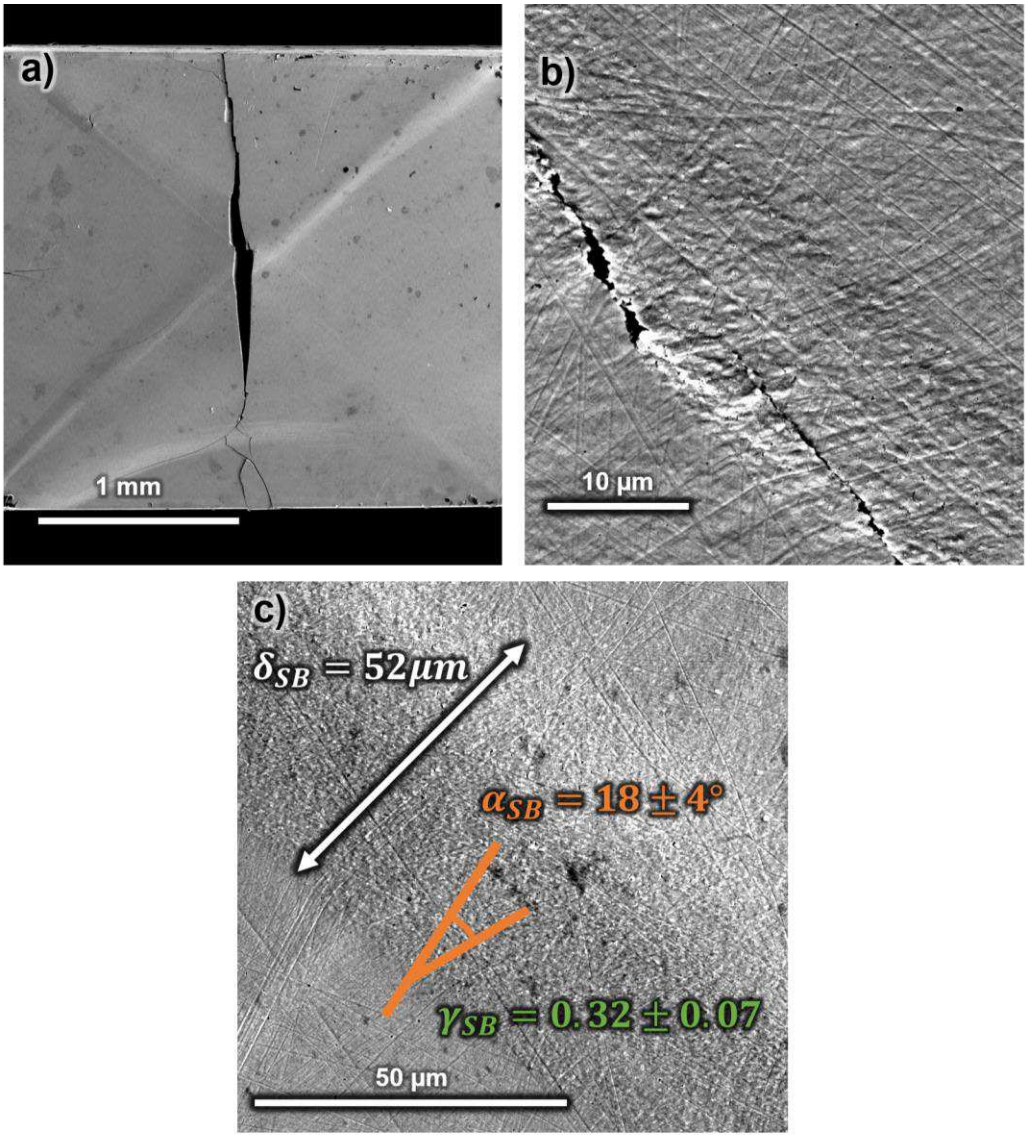

Figure 46 – Shear bands formed during high strain-rate compression in a nW-5Re alloy.

High-speed imaging was also conducted during dynamic testing of an ufgW-10Re sample. Figure 47 shows shear band initiation at early levels of plastic deformation. The results of this test are presented to show the early onset of shear banding, which coincides with the plastic portion of the stress strain curve, even at high strain rates.

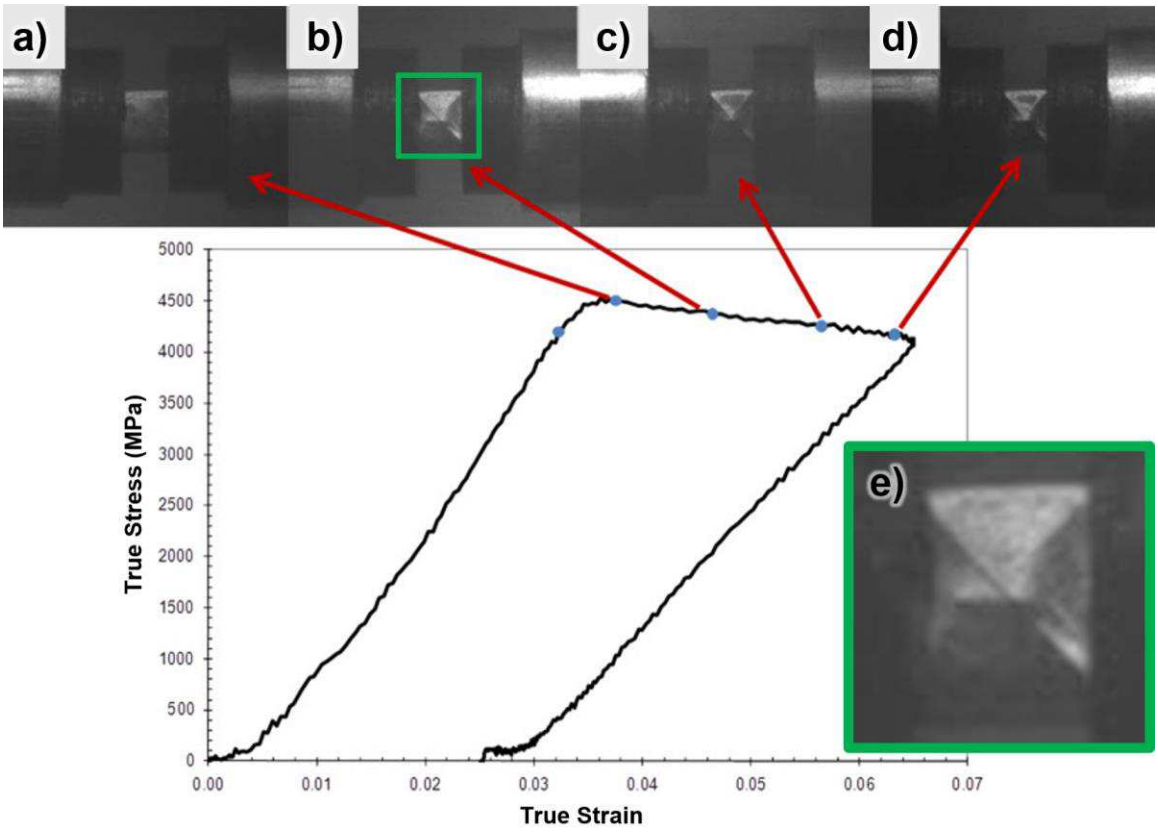

Figure 47 - High speed imaging (~100,000 FPS) of shear band formation in an ufgW-10Re alloy. Strain localization is barely visible in a), and a shear band is fully formed by b). An enhanced, higher magnification image of b) is shown in e).

Alloys with a high rhenium (nW-25Re) content also showed evidence of shear banding; however, the global deformation behavior remained stable. A single sample was loaded three separate times without signs of catastrophic failure as shown in Figure 48. The addition of large amounts of rhenium results in significant improvements to the ductility, and exemplifies the fact that shear banding is not mutually exclusive

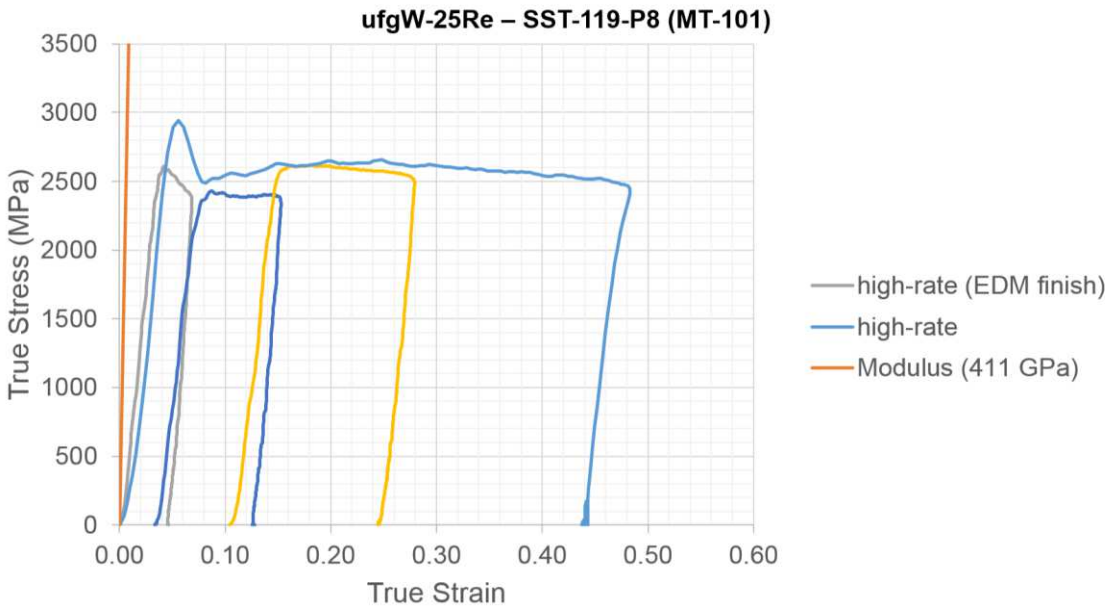

Figure 48 – Tungsten alloyed with large amounts of rhenium show considerable strain without failure in dynamic testing. An initial load drop is clearly visible during the initial stages of deformation, likely coinciding with shear band formation. The stress values level out with additional straining and each of the specimens remained intact after testing.

4.3. Post-mortem characterization

Many of the details of shear band formation and propagation are left in the microstructure, long after the deformation processes have ceased to be active. While there is a wealth of information that can be gathered from *in-situ* measurements (i.e. during shear band formation) the resolution of *ex-situ*, *post-mortem* analysis provides a level of detail that is inaccessible during shear band formation. This *post-mortem* analysis is crucial to understanding the physical processes that lead to instabilities, particularly if a shear band can be captured before the sample is completely pulverized.

4.3.1. Electron backscatter diffraction (EBSD)

The microstructure and dislocation structure of *post-mortem* samples were characterized extensively by EBSD. These orientation maps show a stark contrast in the microstructure

inside and outside of a shear banded region. Inside of a shear band, there is a heavy BCC shearing texture and a slightly elongated grain morphology, which has also been reported in other studies [163, 177]. Inside of a shear band grains show much larger spreads in orientation however, the amount of lattice misorientation between grains is non-uniform. Each of these features describes specific characteristics that can be attributed to deformation based on traditional dislocation mediated plasticity.

The Unalloyed ufgW samples eventually failed by brittle fracture along the length of a shear band, though there was a considerable amount of plastic deformation by way of shear banding prior to catastrophic failure. The structure of these shear bands was investigated by an interrupted compression test similar to that described in Figure 36. The images of the deformed sample used for EBSD analysis are shown in Figure 49.

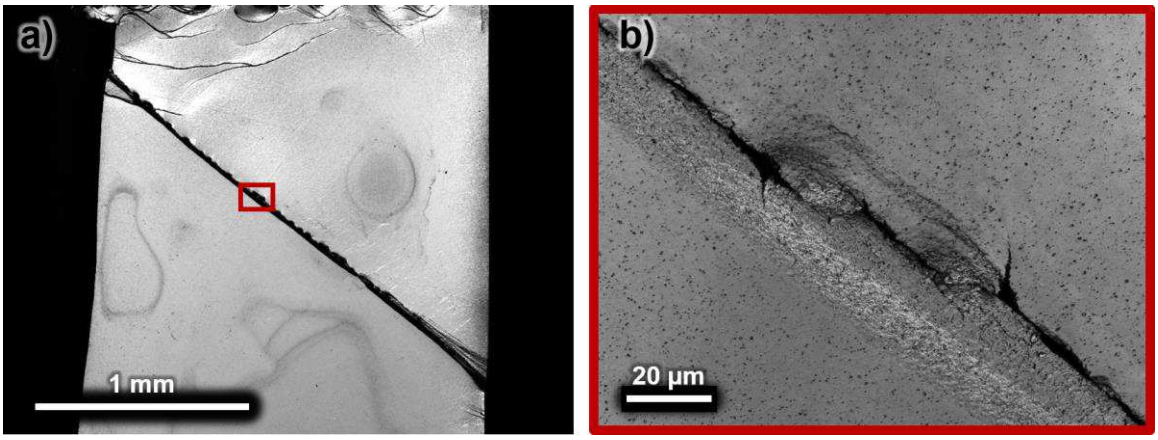

Figure 49 – Microscopic images of a shear band and crack resulting from an interrupted compression test. The width of the shear band was measured to be approximately 25 µm, but strain could not be measured accurately as a result of the limited number of scratches, and the fracture.

This particular compression test was interrupted while deformation by shear banding was transitioning to fracture, but before the material had experienced catastrophic failure. An orientation map of the microstructure across the crack, and the orientation distribution of

this region (represented in terms of pole figures) are shown in Figure 50. An inverse pole figure with overlaid image quality (IPF+IQ) was used to represent the spatial distribution of orientations and pattern quality measured by EBSD. Each individual orientation was plotted on as discrete values, and the orientation of specific planes were represented based on a stereographic projection.

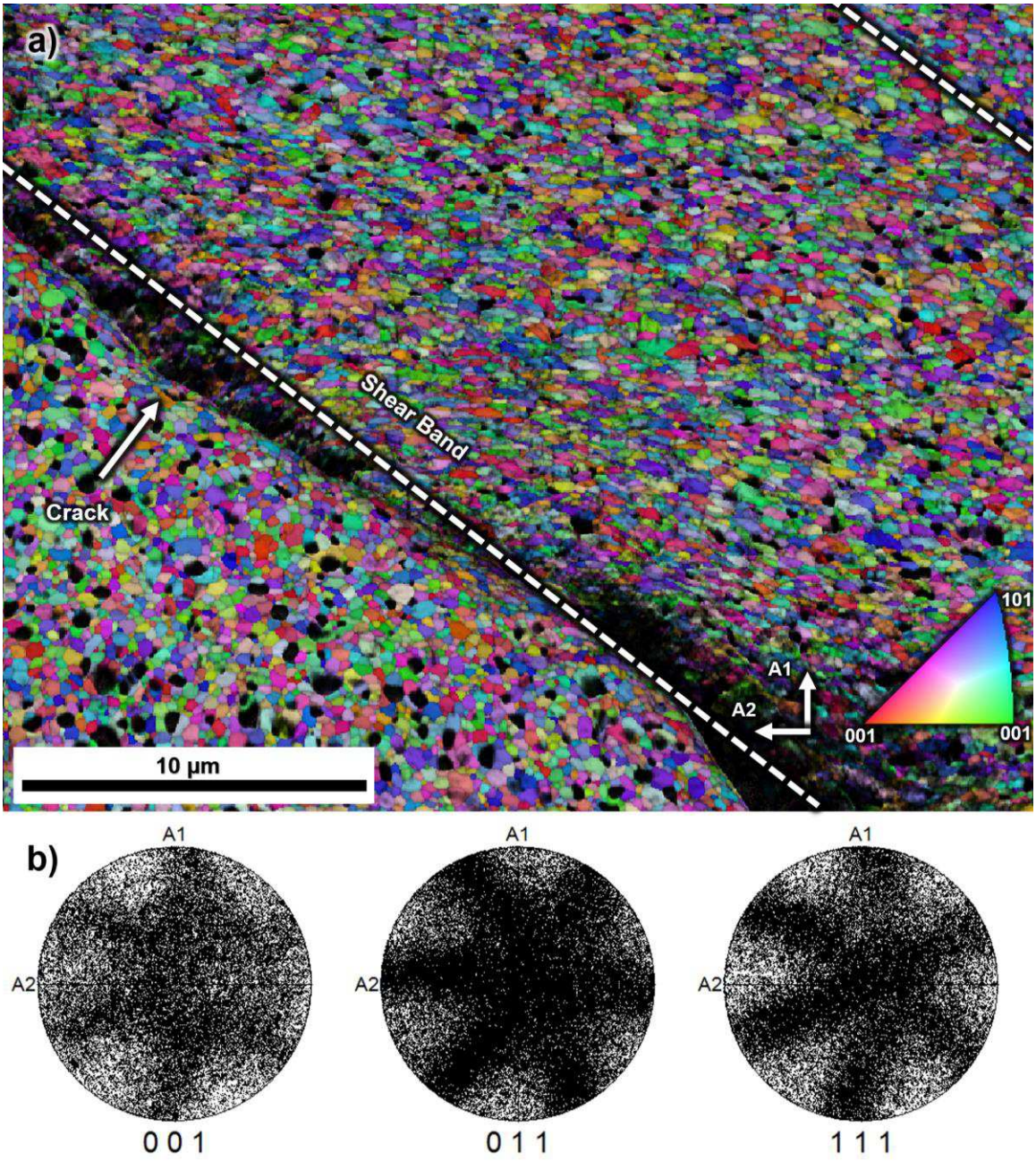

Figure 50 – IPF+IQ map is shown in a) to represent orientation and microstructure of grains across a shear band and crack in a sintered, ufg tungsten sample (Unalloyed ufgW). The frame of reference and corresponding inverse pole figure color legend. The corresponding discrete pole figures, b), show the shearing texture that develops during shear band formation.

The shear band can be further distinguished from the bulk sample based on the orientation spread that is observed within each individual grain. Although, this technique

is sensitive to the individual grain size [81], it provides an effective distinction between the deformed and undeformed regions of the sample. A grain orientation spread (GOS) map, shown in Figure 51. shows that the crack formed at one edge of the shear band and the region on the other side of the crack shows little evidence of deformation.

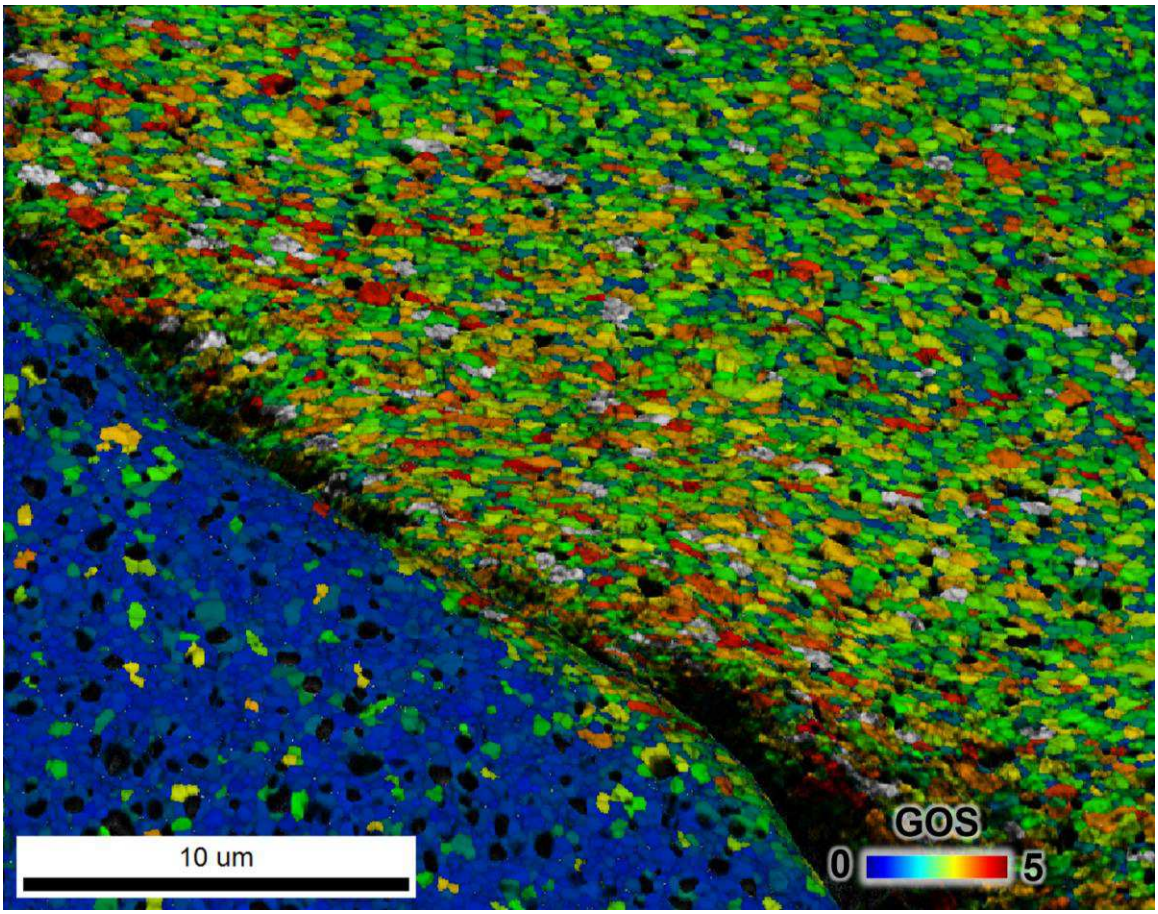

Figure 51 – GOS map of the same region shown in Figure 50.

.

The undeformed region, below the crack, shows a much lower spread in the orientation of individual grains. However, it is also clear that the GOS is not completely uniform within the shear band, with some grains showing significantly larger spreads.

Similar results, aside from fracture, are observed for the microstructure and deformation behavior of an ufgW-5Re alloy. Images of a sample deformed by an interrupted compression test are shown in Figure 52. The macroscopic view, Figure 52 a), shows two

shear bands intersecting in the center of the sample, and several bands that formed out of plane in the bottom portion of the image. The sample had distinct scratches running through the major shear band, and the characteristics of the band were measured in Figure 52 b).

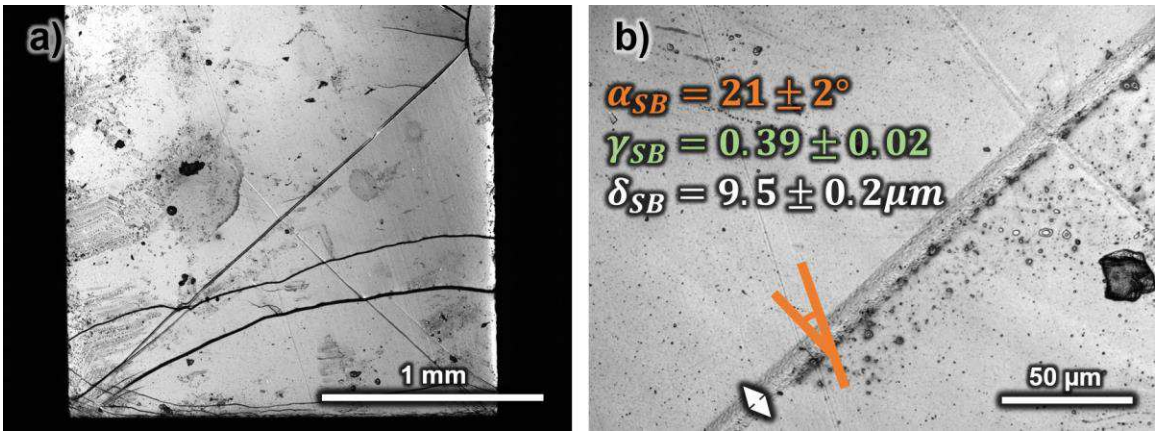

Figure 52 – Confocal microscope images of the surface of a deformed ufgW-5Re alloy deformed in an interrupted quasi-static compression test. The macroscopic image shows two dominant shear bands intersecting at the center of the sample with several out-of-plane shear bands visible in the top region of a). The shear strain ($\gamma_{SB} = 0.4$) and width of the shear band ($\delta_{SB} = 11\mu m$) can be measured directly from b).

The ufgW-5Re samples show heavy texturing and a sharp distinction between deformed and undeformed regions of the sample. An IPF+IQ map of the shear band region and the corresponding discrete pole figures corresponding to the entire image area are shown in Figure 53 .

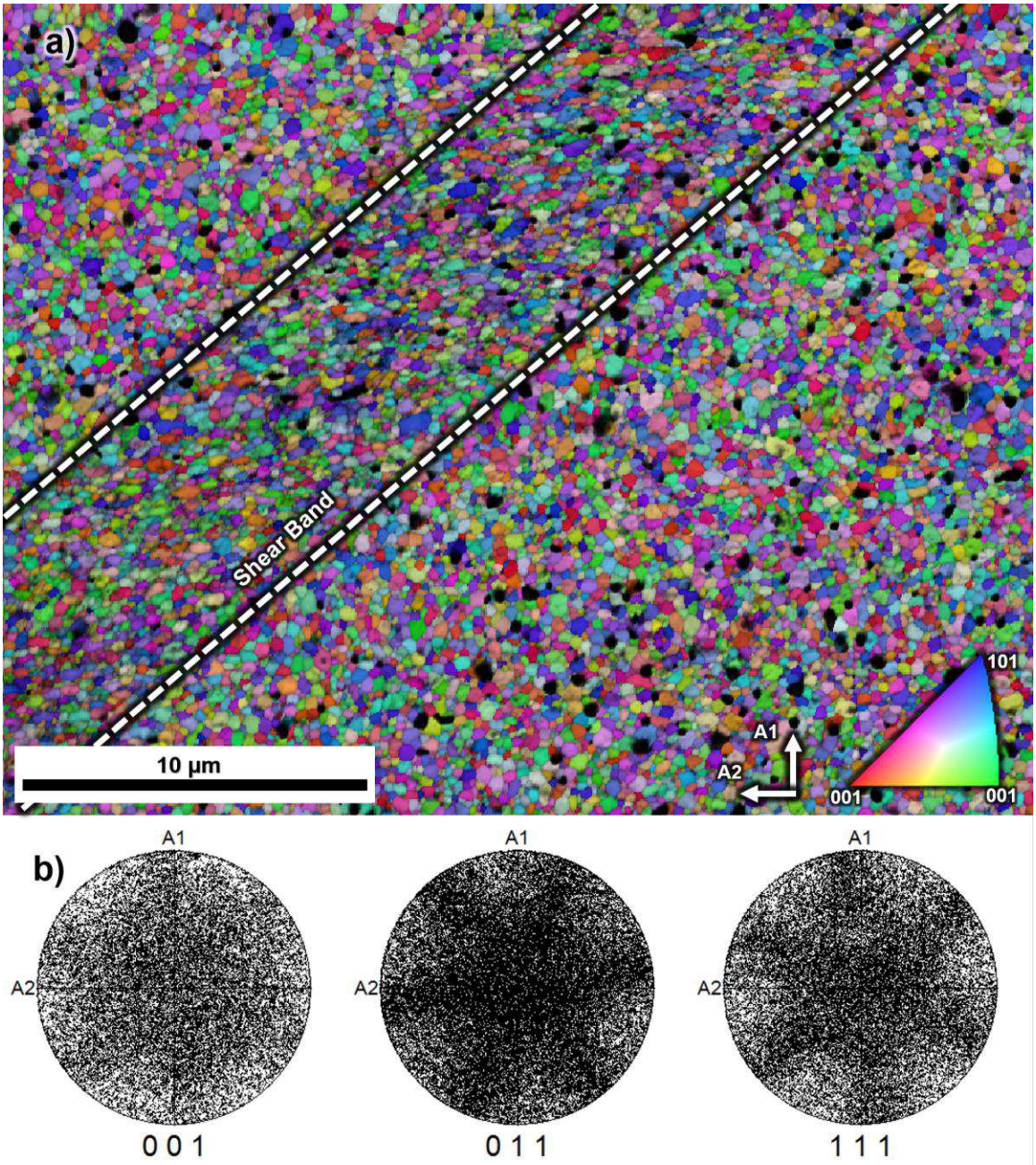

Figure 53 – IPF+IQ map of shear band in ufgW-5Re alloy, and b) corresponding discrete pole figure, highlighting texture development inside of the band. The texture appears less severe as a result of the randomly oriented, undeformed region around the shear band.

Similar to unalloyed tungsten, deformation appears to be heavily constrained within the shear band; however, the magnitude of the grain orientation spread is smaller within the shear band of the ufgW-5Re alloy. The grain orientation spread across the shear banded

region is shown in Figure 54. The thickness of the shear band, measured based on having a GOS>0.5°, was approximately 9.5µm. This value corresponds exactly to the direct measurement from optical microscopy shown in Figure 52.

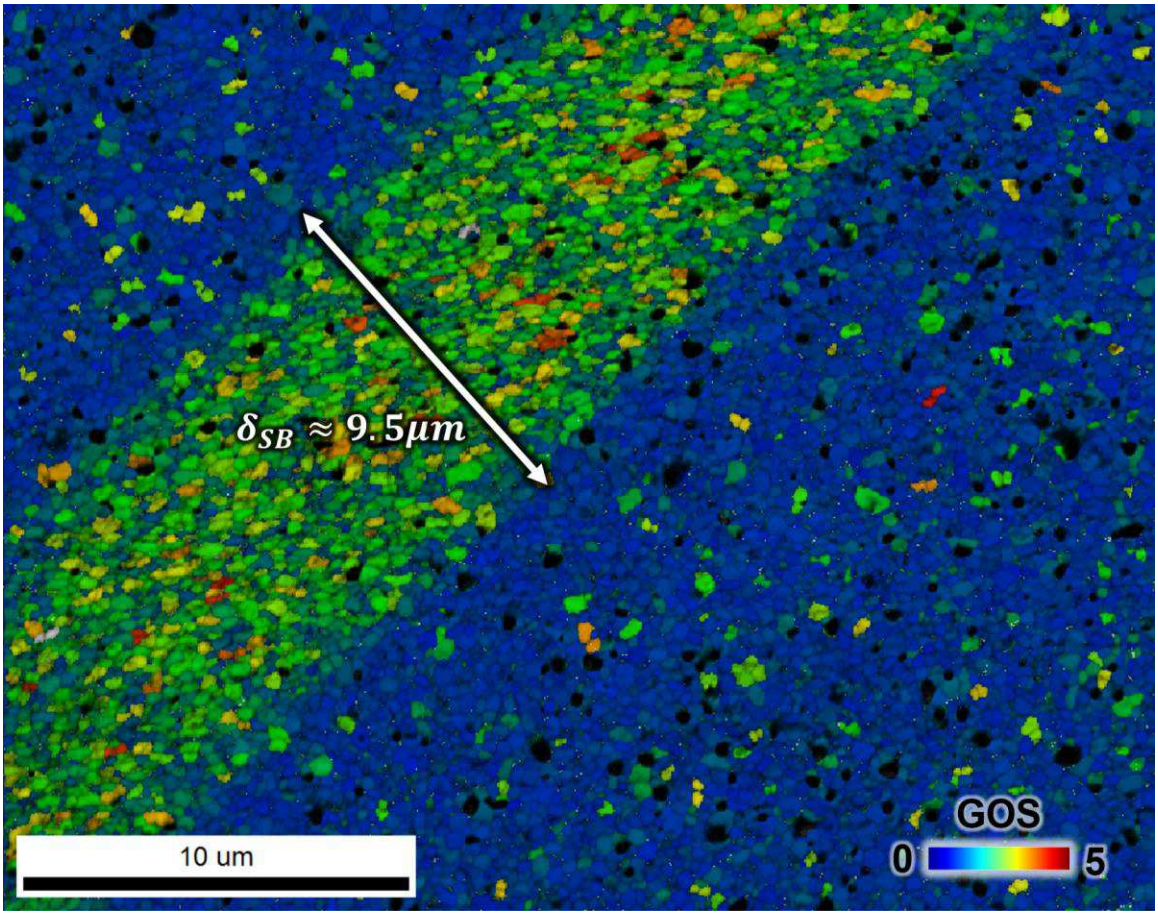

Figure 54 – GOS map, highlighting the boundary of deformation, in a ufgW-5Re sample.

This particular sample shows a secondary shear band that appears to have been intersected by the primary shear band during testing, which impeded further propagation. The obstructed band, shown in Figure 55, can provide an approximation of the shear band thickness during formation. After electropolishing, this region of the shear band was not visible by conventional SEM imaging; however, an EBSD measurement, based on the GOS>0.5, showed the shear band to be approximately 1.46 µm. The shear band thickness

relative to the grain size was approximately 6:1, almost an order of magnitude finer than the relative shear band thickness of 50:1, reported by Jia et al. in ufg and nanocrystalline Fe [165].

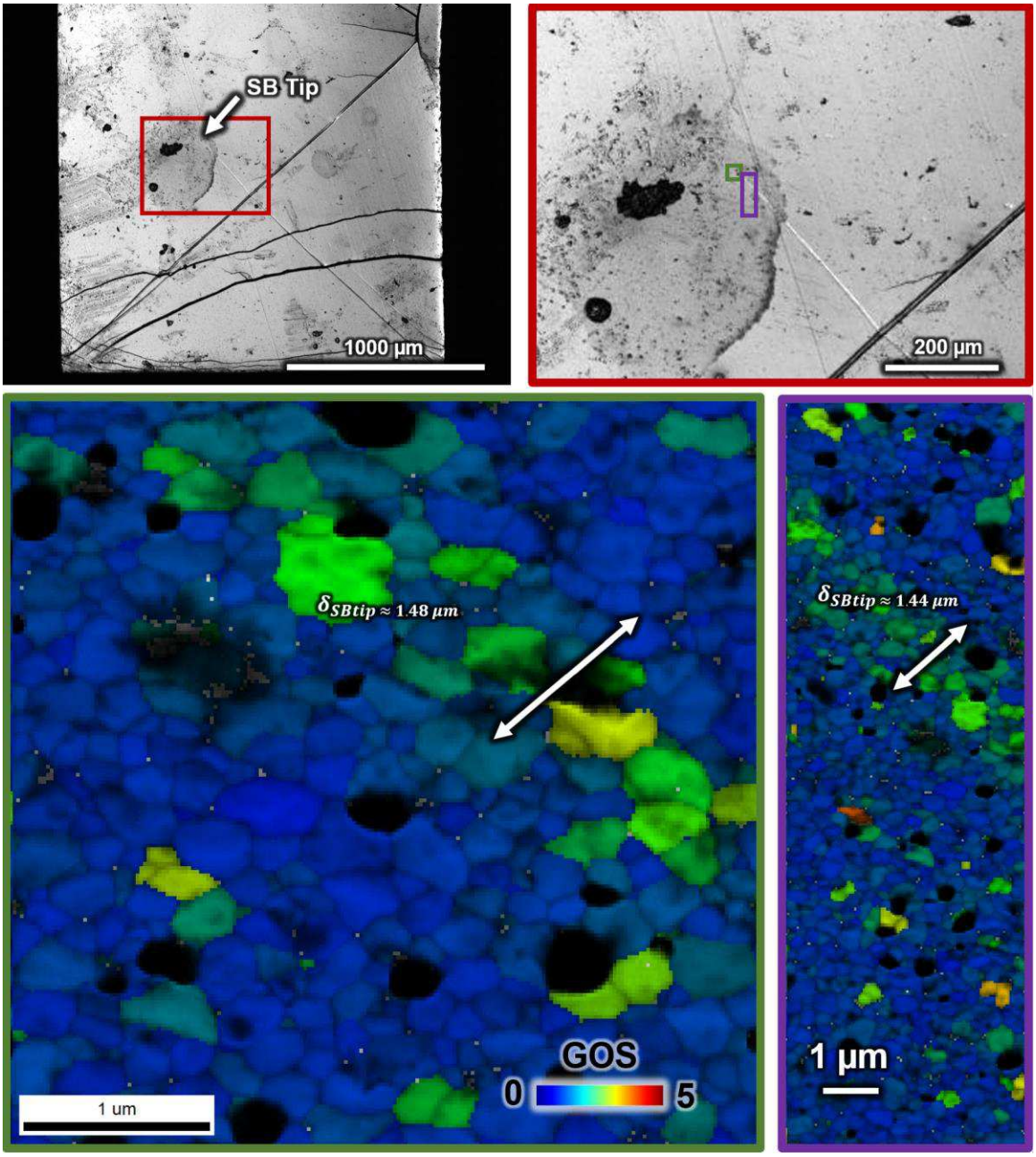

Figure 55 – Thickness measurement near the tip of an interrupted shear band in a ufgW-5Re sample. Areas near the tip of the shear band (top right) were measured by EBSD based on the difference in GOS inside the band.

4.3.1.1. Texture development inside of shear bands

The EBSD characterization of sintered ufg tungsten (Figure 50-Figure 54) shows many similarities between the microstructure inside of shear bands in both the unalloyed and alloyed state. One of the most striking features is the texture that develops inside of the band, however this texture is not unique to ufg metals. The observed texture is exactly what is predicted and observed as a result of shear deformation in other BCC metals [265-267]. Figure 56 a) shows the ideal orientations that are that are expected for deforming BCC metals plotted on a (110) pole figure. Specific "fibres" have been experimentally measured, or modeled based on dislocation mediated plasticity [267]. The deformation fibres, shown as lines in this pole figure correspond to the fact that slip is restricted to {110} type planes and <111> type directions. The specific fibres correspond to orientations where {110} planes in the direction <uvw>, and planes of {hkl} point in the <111> direction.

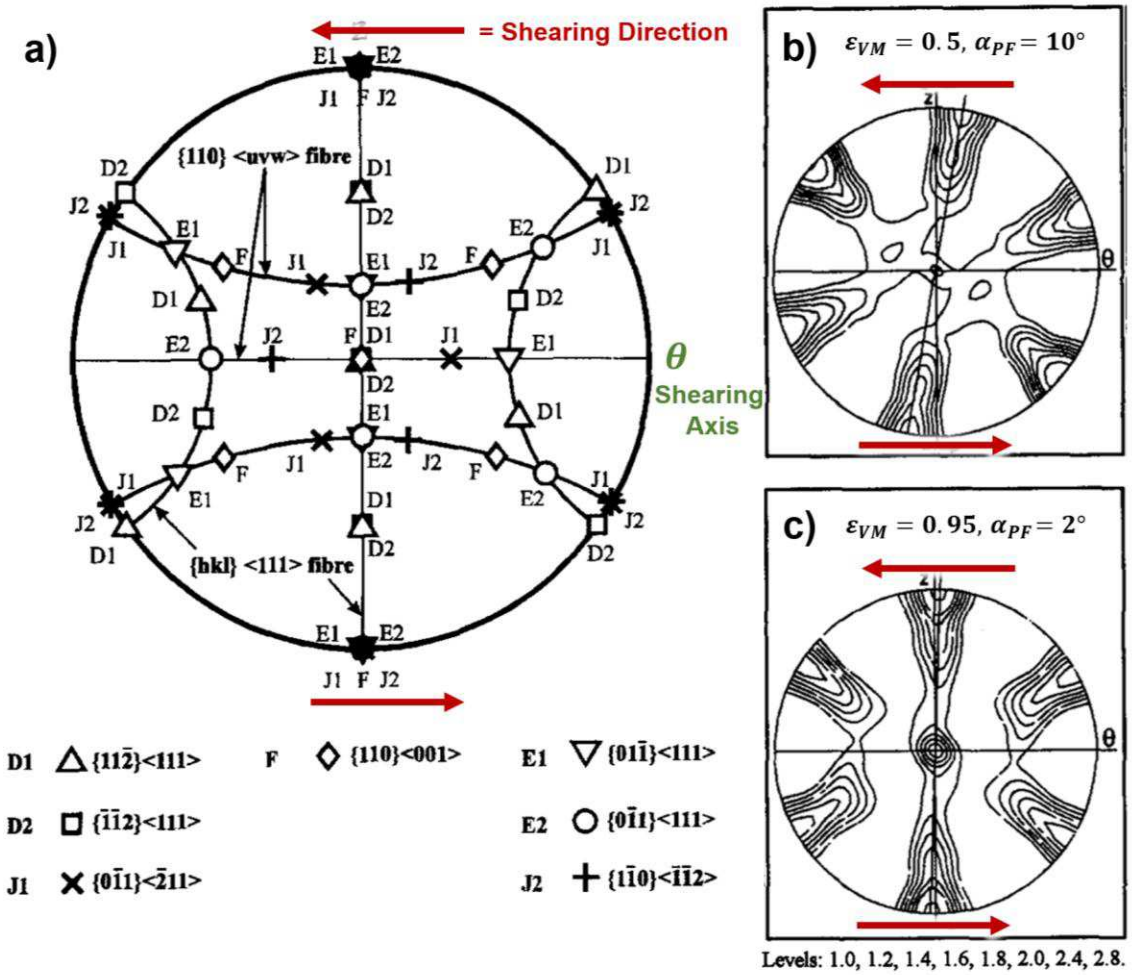

Figure 56 – Shearing textures depicted in {011} type pole figures that result from shear deformation of BCC metals, a) ideal textures observed in torsion experiments for BCC metals. Experimental pole figures for interstitial free steel strained by torsion to a von Mises equivalent strain of 0.5 and 0.95, shown in b), and c) respectively. Used with permission from [265]

The textures observed within shear bands are indistinguishable from the experimental pole figures of [265], especially when accounting for the misorientation (α_{PF}) that results from dislocation mediated plasticity corresponding to simple shear as opposed to pure shear [268]. Rotating the coordinate system of the EBSD dataset shown in Figure 53 by -45 degrees about the A3 axis (out of page) will put the shear band into the same frame of

reference for the deformations imposed in Figure 56. The shearing texture for the W-5Re alloy, shown in Figure 57, is the expected texture for BCC metals deformed by shear.

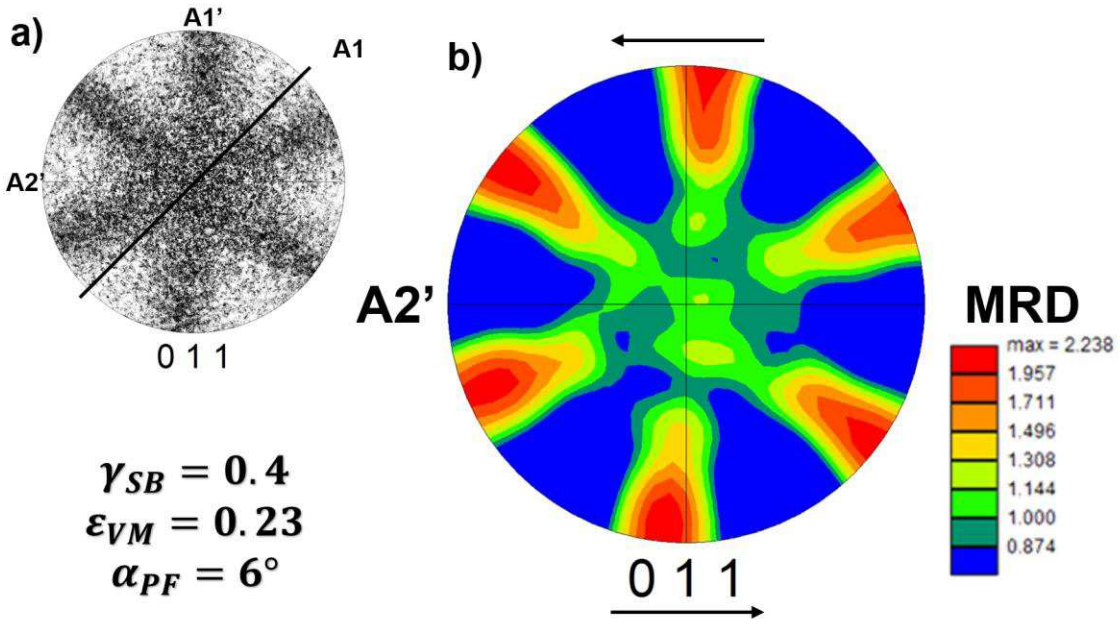

Figure 57 – Pole figures depicting the texture observed inside of the shear band of a ufgW-5Re alloy. The discrete pole figure measured in Figure 53 is rotated 45° counter-clockwise about the A3 axis to coincide with the shearing axis (A2') as shown in part a). The continuous pole figure, b), calculated by fitting a harmonic series expansion (Rank = 15, with 5° full width at half of maximum Gaussian smoothing), Pole figure is plotted in multiples of random distribution (MRD) and shows identical features to the experimental pole figures for sheared BCC iron.

This raises the question of whether the observed textures actually contribute to softening based on the geometric shear banding mechanism. Although the Schmid factor is commonly used to represent hard and soft orientations in a single crystal material. A more suitable model to determine the orientation dependence of strength in a polycrystal is based on an imposed strain according to the Taylor model. A brief derivation of the Taylor model, as applied to EBSD [254], is described in order to understand the

assumptions and limitations of this method. The deformation of a polycrystalline sample generally requires more than one slip system (at least five) to operate within a given grain in order to satisfy the constraints imposed by neighboring grains. For cubic systems, there are many more slip systems than the five required to satisfy an imposed strain and the problem is underdefined. Taylor's analysis [269] uses the concept of minimum work to identify these required slip systems according to Equation (44)

$$\delta W = \sum_{s} \gamma^{(s)} \tau_c^{(s)} = \sum_{i=1}^{3} \sum_{j=1}^{3} \sigma_{ij} \varepsilon_{ij} \tag{44}$$

where δW represents the virtual work that is to be minimized, $\gamma^{(s)}$ is the infinitesimal shear strain associated with dislocation slip for system s, and $\tau_c^{(s)}$ is the critical resolved shear stress. If the critical resolved shear stress is considered to be independent of the slip system ($\tau_c^{(s)} = \tau_C$), and the stresses and strains can be written in terms of the principal components of the strain. Equation (45) may be rewritten as,

$$\delta W = \tau_C \sum_{s} \gamma^{(s)} = |\tilde{\varepsilon_1}|(\sigma_{11} + \lambda\, \sigma_{22} - (1+\lambda)\sigma_{33}) \tag{45}$$

where $|\tilde{\varepsilon_1}|$ is the absolute value of principal component of the strain (it is necessary for all strains to be considered positive in order to describe the total work in the system),

Finally, the Taylor factor may be described based on the sum of all slips required to accommodate a specific deformation. Alternatively, this may be written in terms of the virtual work described in Equation (45).

$$M = \sum_{s} \frac{\gamma^{(s)}}{|\tilde{\varepsilon_1}|} = \frac{\delta W}{|\tilde{\varepsilon_1}|\tau_C} = \frac{|\sigma_{11} + \lambda\, \sigma_{22} - (1+\lambda)\sigma_{33}|}{\tau_C} \tag{46}$$

The Taylor factor is affected by the orientation of the crystal and the imposed strain tensor. A higher value of the Taylor factor in one particular orientation shows that the material requires more virtual work to carry out the imposed deformation (i.e. the material is effectively harder for the imposed strain field). In the case of plastic instabilities, a high Taylor factor developed by strain induced texture would make it more energetically favorable for additional strain to distribute throughout the crystal. In the simple case of compression, the Taylor factor for each orientation may be represented by an inverse pole figure along the loading axis of the material as described in Figure 58.

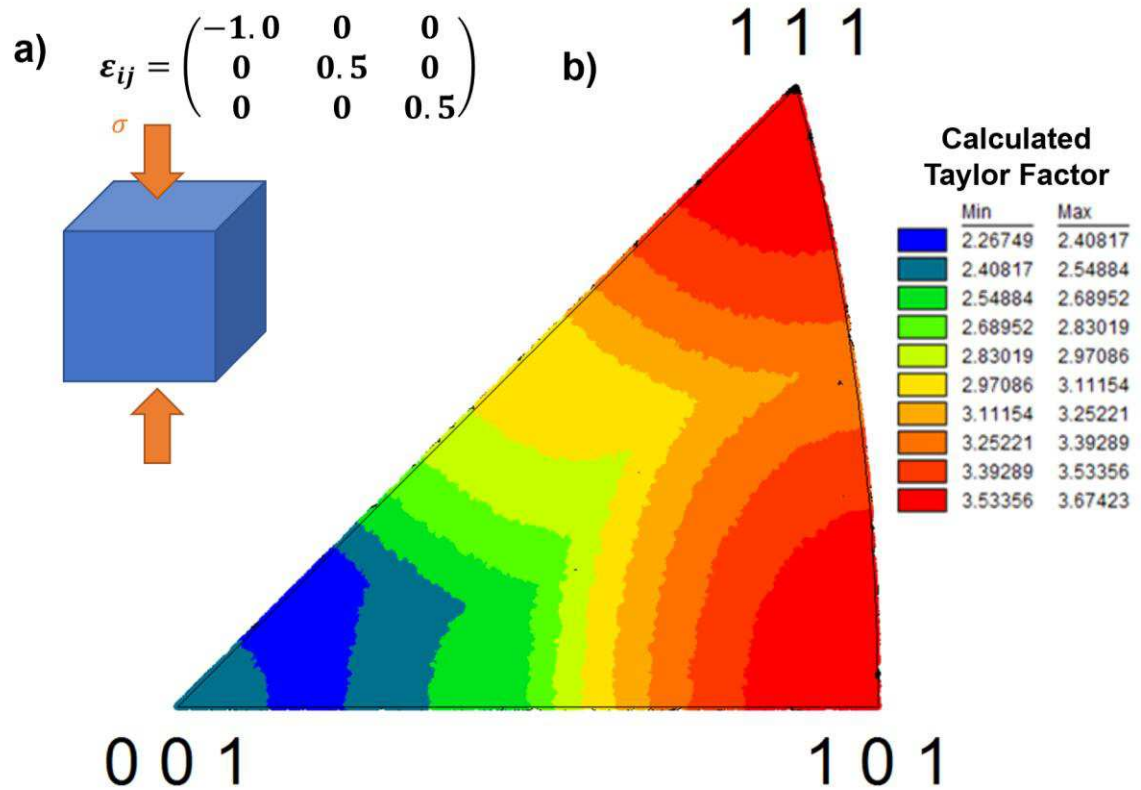

Figure 58 – The orientation dependence of Taylor factors for a BCC metal deformed in compression plotted on an inverse pole figure with respect to the compression axis (A1).

Plotting the observed texture in this frame of reference (i.e. with respect to the compression axis (A1), provides insight to whether the texture developed is truly softer based on the predictions of the Taylor factor. An inverse pole figure showing orientation with respect to the compression axis is shown in Figure 59.

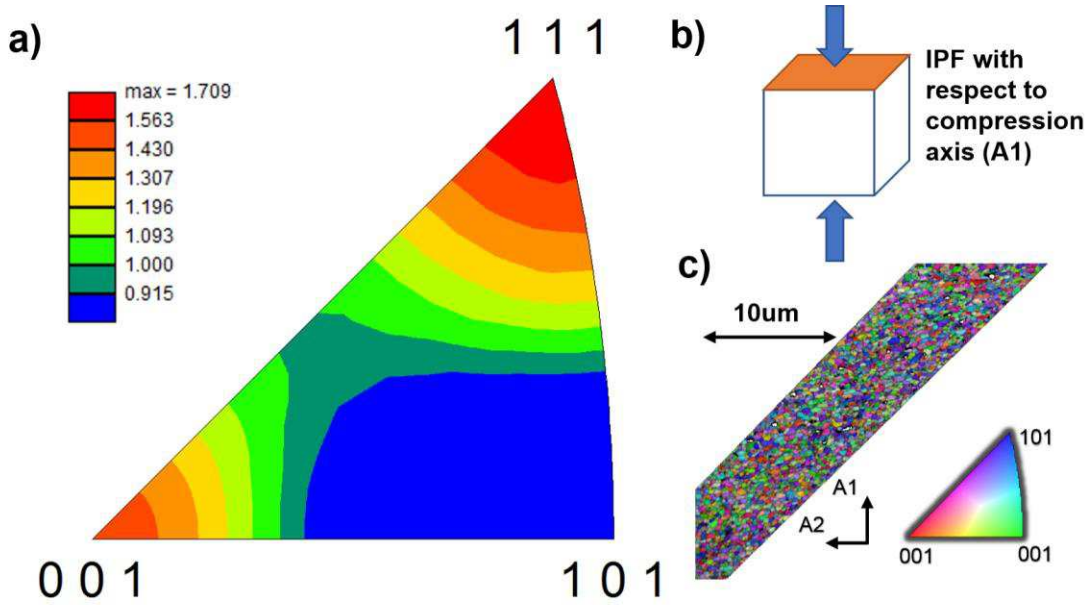

Figure 59 – Texture observed within ufgW-5Re alloy shear bands, plotted in a [100] IPF (with respect to the compression axis, A1. The continuous pole figure, a), was calculated based on the same parameters used in Figure 57. The pole figure shows the orientation with respect to b), the compression axis, for c) a cropped region inside of the shear band.

The texture developed inside of the band shows two dominant orientation relationships with respect to the compression axis, $\{111\} \parallel [100]$, which results in a harder orientation, and $\{001\} \parallel [100]$, which results in a softer orientation according to the calculated Taylor factor in Figure 58. The influence of hard and soft orientations developed inside of a shear band tend to cancel each other out and the net result, based on the average Taylor factor, is that there is no texture-induced softening inside of a shear

band. The EBSD mapping of Taylor factors and the calculated averages are shown in Figure 60.

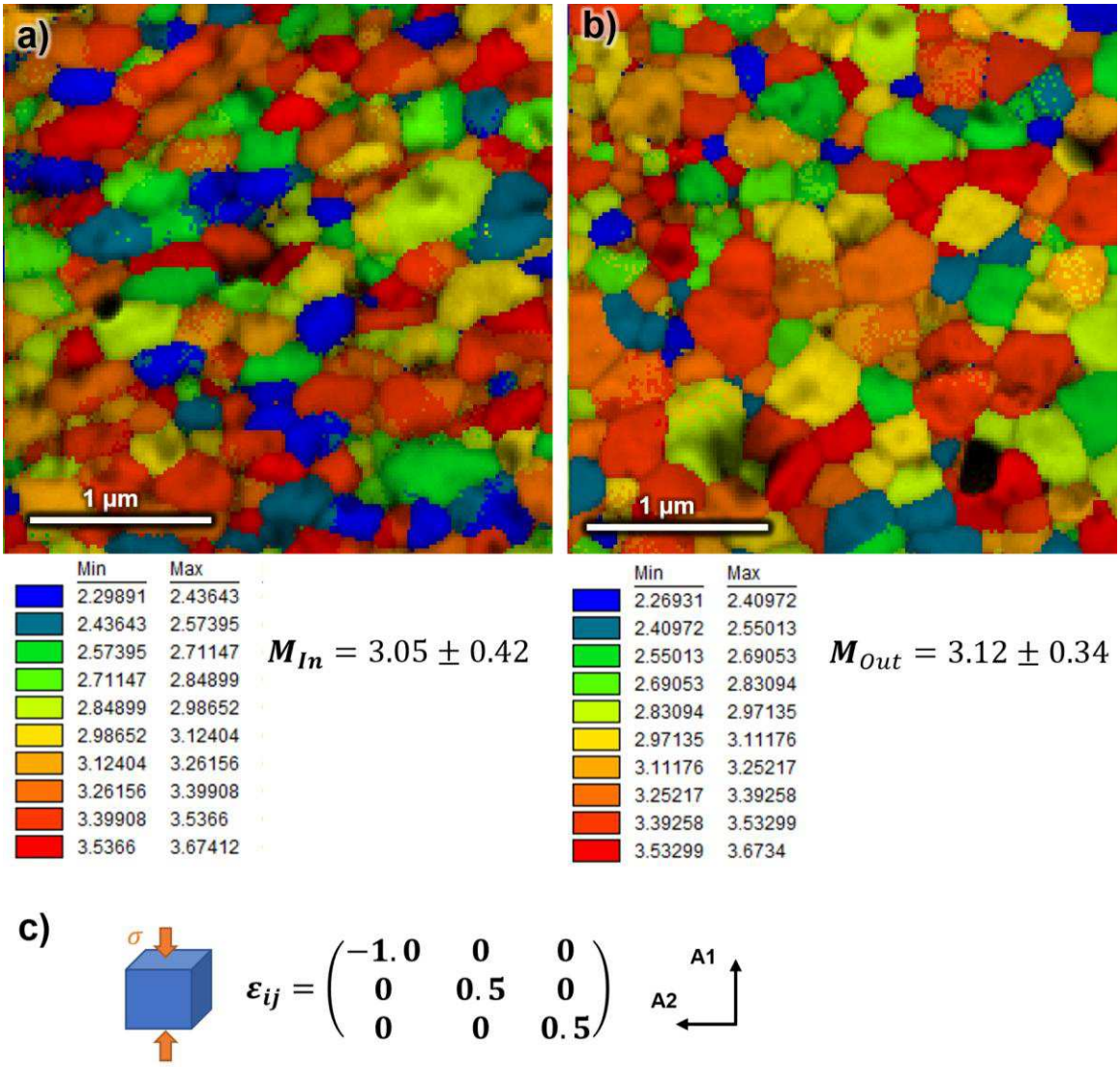

Figure 60 – Calculated Taylor factors for grains, a) inside, and b) outside of a shear band, based on c) the imposed compression strain field.

The texture developed inside of shear bands can be understood based on the conventional textures that develop in BCC metals as a result of dislocation mediated plasticity. According to Taylor factor calculations, deformation leads to the development of both

soft and hard orientations within the shear band, with no statistically relevant effect on the overall strength of the band. While these results do not support the requirement of soft orientations according to the Joshi and Ramesh model for geometric shear banding, the presence of hard and soft orientations within the band could lead to strain incompatibilities that ultimately promote fracture after the texture has developed [270].

4.3.1.2. Dislocation structure inside of shear bands

Another critical aspect to the deformation behavior and plastic stability of ufg tungsten, is the accumulation of dislocations, which occurs over the course of straining the material. It is clear from previous discussions that grains inside of the shear band show much larger distributions in orientation, which should account for a higher dislocation density, but additional analyses may help to quantify the dislocation structure within these bands of deformation.

EBSD offers the unique ability to measure the dislocation density over fairly large regions of the sample, thereby reducing the errors associated with sampling. While there are several methods that are generally applied for describing the dislocation density, a first approximation can be made directly from the average misorientations between neighboring pixels within a grain according to the kernel average misorientation (KAM). Figure 61 shows a comparison between regions inside and outside of a shear band in the Unalloyed ufgW sample.

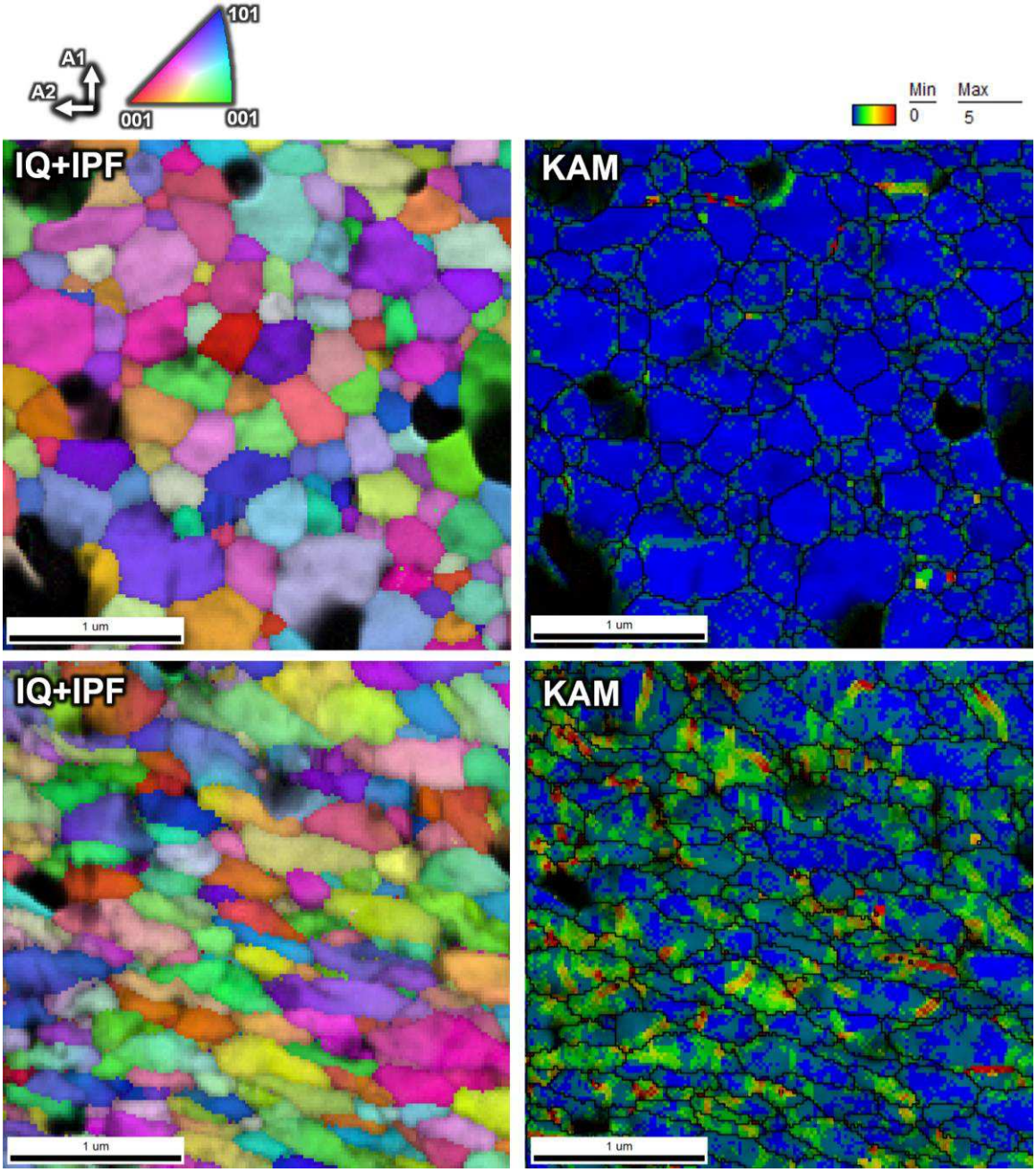

Figure 61 - EBSD maps highlighting the differences in grain structure, morphology and misorientation inside of a shear band. The undeformed region (top) shows highly equiaxed grains and several residual pores within the microstructure. The shear banded region (bottom) shows highly elongated grains with minimal porosity. KAM maps (right) highlight the significant difference in misorientations inside and outside of the shear band.

The total dislocation density was estimated based on Equation (39) and a correction factor for the misorientation was applied (Equation (43)) to reduce the influence of spurious

dislocations (ρ_{sp}). A histogram showing the GND distribution based on misorientations is shown in Figure 62.

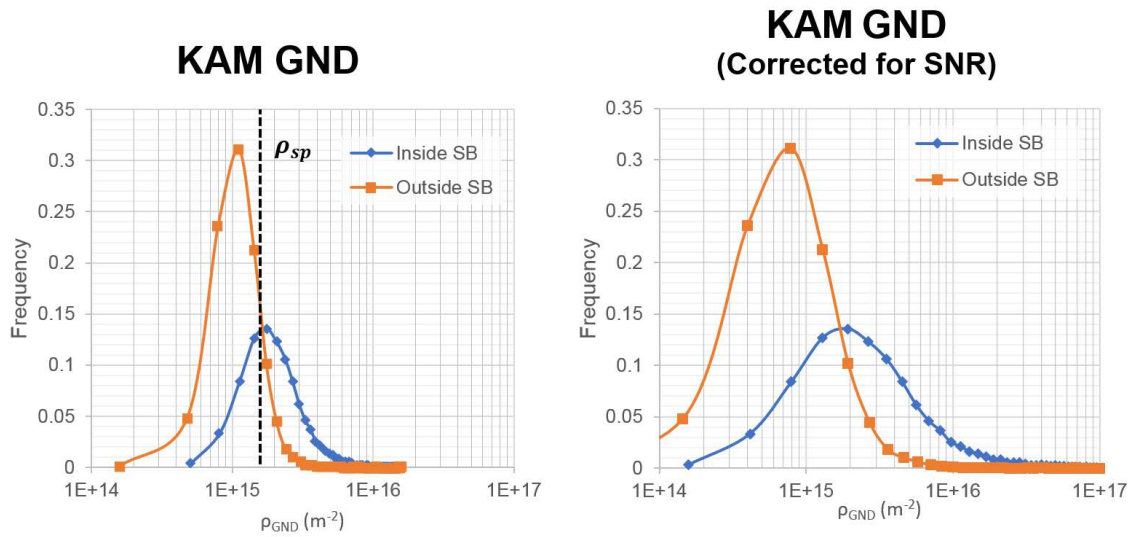

Figure 62 – Distribution of GNDs calculated based on the misorientations (left) and corrected based on the signal to noise ratio of spurious dislocations (right).

Although the required step size (20 nm) and estimated angular resolution ($1.6*10^{15}$ m^{-2}). lead to a very high value for the predicted density of spurious GNDs (ρ_{sp}) [243], it can be seen that the average density of dislocations inside of a shear band ($2.7 \pm 1.5*10^{15}$ m^{-2}), is almost 70% larger than the density spurious dislocations ($1.5*10^{15}$ m^{-2}). However, the density of spurious dislocations is undoubtedly obscuring the dislocation density outside of the shear band ($1.3 \pm 0.5*10^{15}$ m^{-2}), the fact that the dislocation density is lower than the calculated density of spurious dislocations is an indication that the angular resolution is probably closer to 0.4°. There is considerable overlap between the probability distributions; however, further analysis based on the z-test for the difference between means, shows that there is a statistically relevant increase in the mean dislocation density

inside of the shear band (mostly because of the large quantity of data that contribute to these distributions).

Correcting the result for the signal to noise ratio caused by errors in angular resolution, Equation (43), results in dislocation densities of: $6.0 \pm 4.8 * 10^{15}$ m^{-2}, and $1.2 \pm 1.0 * 10^{15}$ m^{-2} inside and outside of the band respectively. The correction factor, based on the signal to noise ratio (SNR), tends to increase the spread between datasets, but it also increases the variance within each sample population. This technique may be useful for visualizing data; however, it does not actually influence our ability to distinguish between dislocation densities inside and outside of the shear band.

A similar estimate of the dislocation density, can be made by assessing the accessible components of the Nye tensor based on Equations (40) and (41). This more rigorous assessment can help account for the complex, 3D nature of lattice curvature and improve our lower-bound estimate of geometrically necessary dislocations. Five of the nine components of the Nye tensor may be solved based on the misorientation of elements measured at the 2D EBSD surface. The magnitude of these individual components provides a true lower bound estimate of the dislocation density based on Equation (40). An additional estimate of the out-of-plane curvature can further increase the lower bound of the dislocation density. This method is discussed in more detail for the ufgW-5Re sample, however the dislocation density distribution plots are shown in Figure 66 to provide a comparison to the KAM GND estimate.

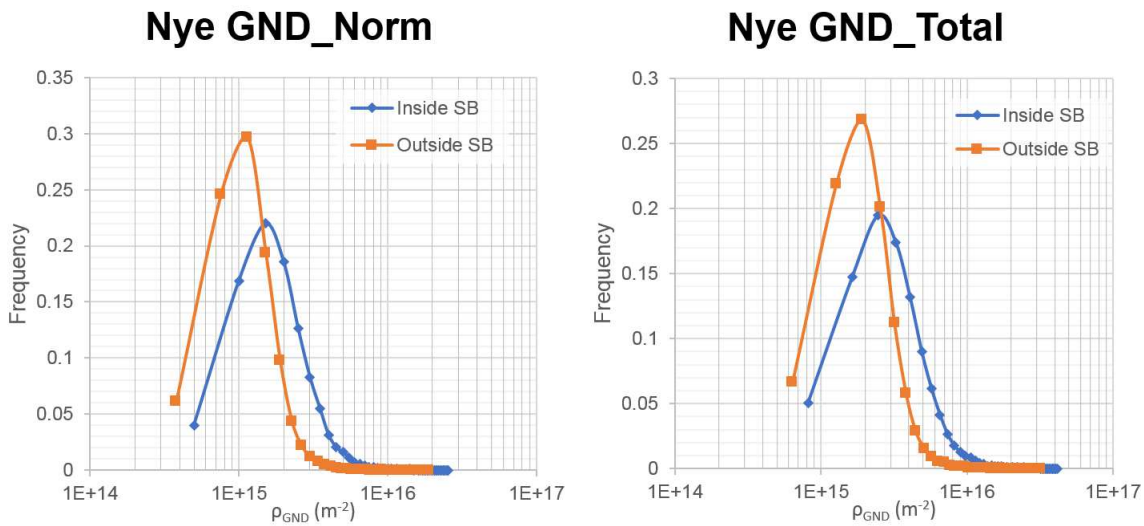

Figure 63 – Distributions of GNDs calculated from the Nye tensor based on the sum of accessible components (left) and with a correction factor applied to account for inaccessible components (right).

The orientation and misorientation maps for the ufgW-5Re sample show strong similarities to the unalloyed tungsten sample; however, the misorientations within the shear banded structure are less severe than observed in the Unalloyed ufgW sample. The uniform nature of the shear band and the known shear strain within the band provide additional insight to the nature of shear banding in ufg materials. Representative EBSD maps of regions inside and outside of the shear band are shown in Figure 64.

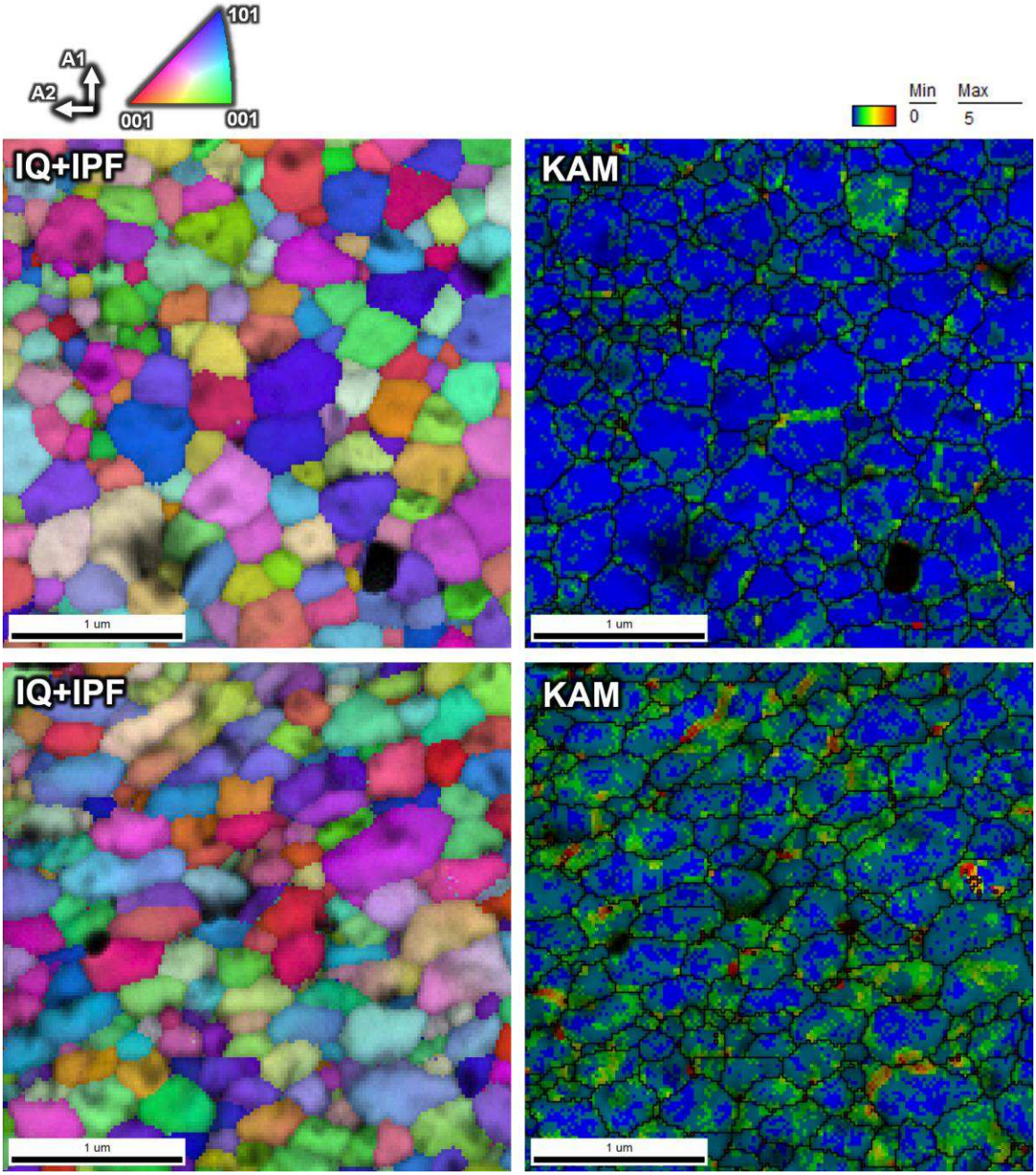

Figure 64 – IPF+IQ and KAM maps for the ufgW-5Re alloy showing deformation outside (top), and inside (bottom), of a shear band.

Similar to the observations in the Unalloyed ufgW sample, the shear band region shows additional misorientations, which may be attributed to GNDs. The density distribution of

GNDs in the ufgW-5Re sample based on the KAM GND approximation are shown in Figure 65.

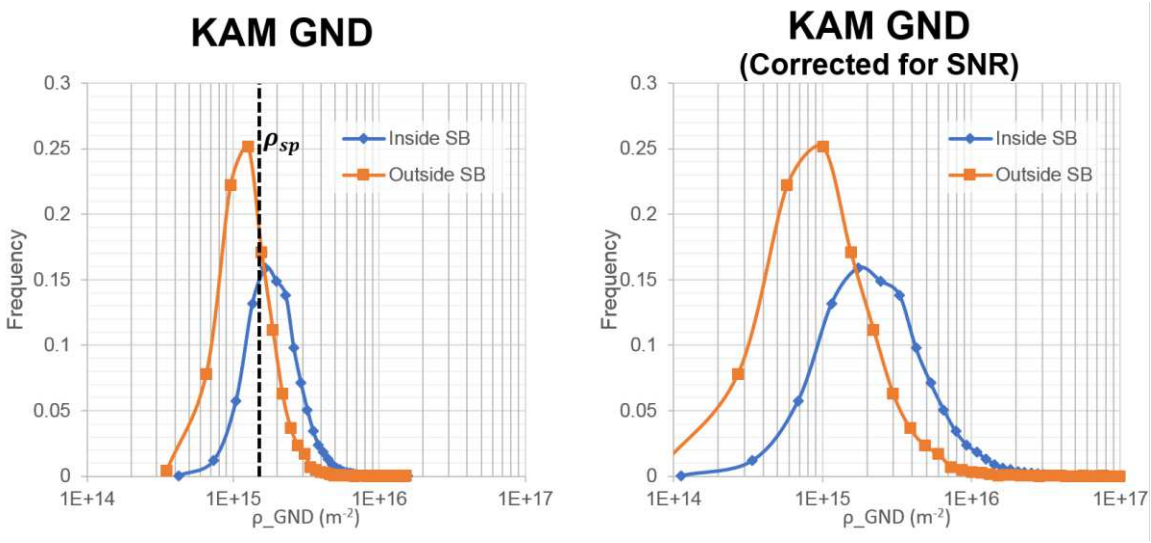

Figure 65 – Histogram of GNDs for the ufgW-5Re alloy sample based on the KAM GND approximation.

The dislocation density was measured to be 2.5±1.0*10^{15} m^{-2} inside of the shear band, and 1.5±0.6*10^{15} m^{-2} outside of the band. Again, the threshold of spurious dislocations masks some of the measured dislocation density below values of ~1.5*10^{-15} m^{-2}, but the average density of dislocations within the shear band is statistically higher than outside of the band. Correcting for the signal to noise based on the angular resolution of EBSD increases the average density inside and outside of the band. The measured dislocation density was 4.2±3.7*10^{15} m^{-2} inside of the band, and 1.7±1.4*10^{15} m^{-2} but there is some concern over whether this correction has any physical meaning. The calculation of accessible components of the Nye tensor is shown in Figure 63. The magnitude of each component (plotted in terms of units of μm^{-1}) varies within the sample, but α_{33} (bottom right) generally shows the largest magnitudes because it is calculated based on in-plane lattice curvatures (see Figure 26).

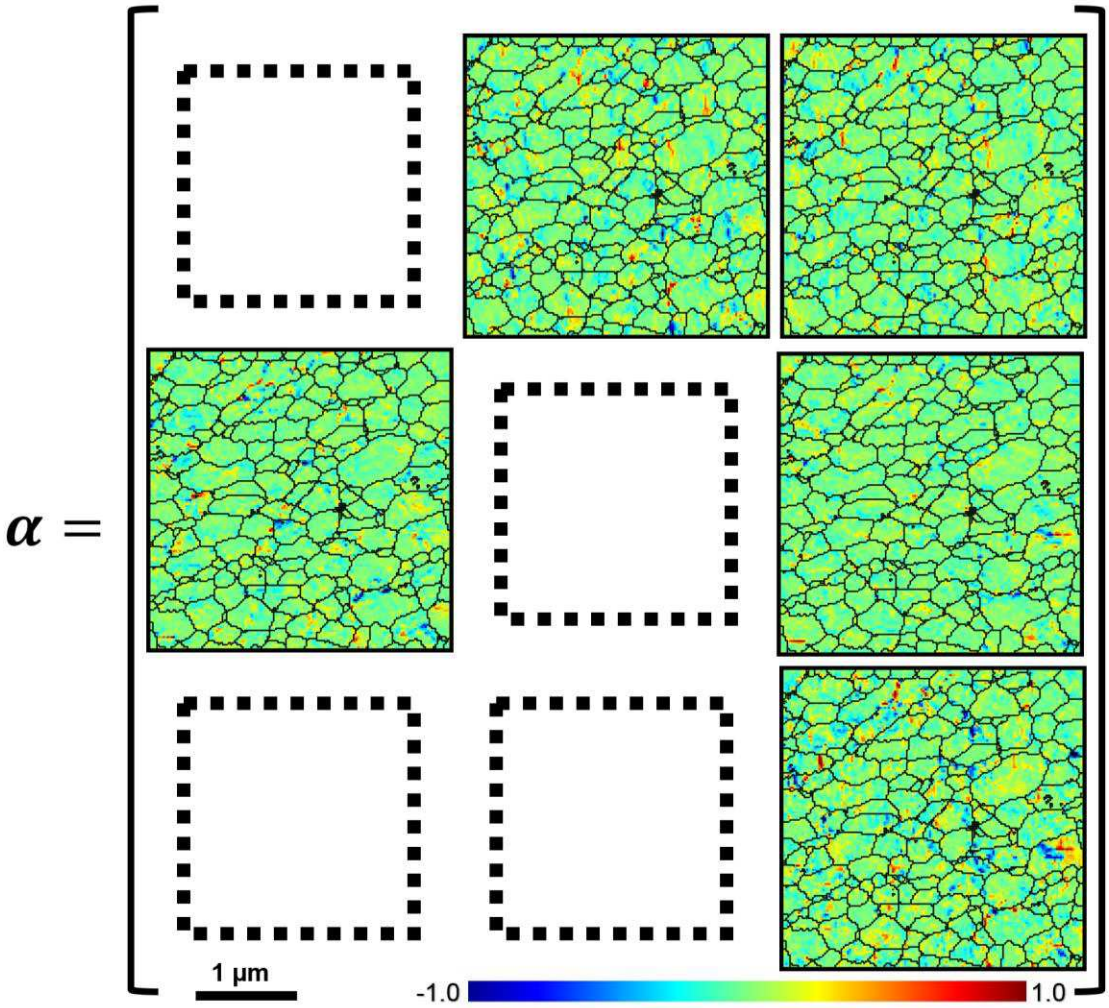

Figure 66 – Individual components of the Nye tensor, which can be used to determine the local density of geometrically necessary dislocations. Note: Units of α_{ij} are presented in μm^{-1}.

The magnitude of the Nye tensor may be calculated as the scalar quantities, α_{norm} and α_{total}, which are proportional to lower bound estimates of the total dislocation density. These quantities are presented in Figure 67. The total dislocation density is calculated based on Equations (40) and (41) ($\rho_{GND} = \alpha/b$).

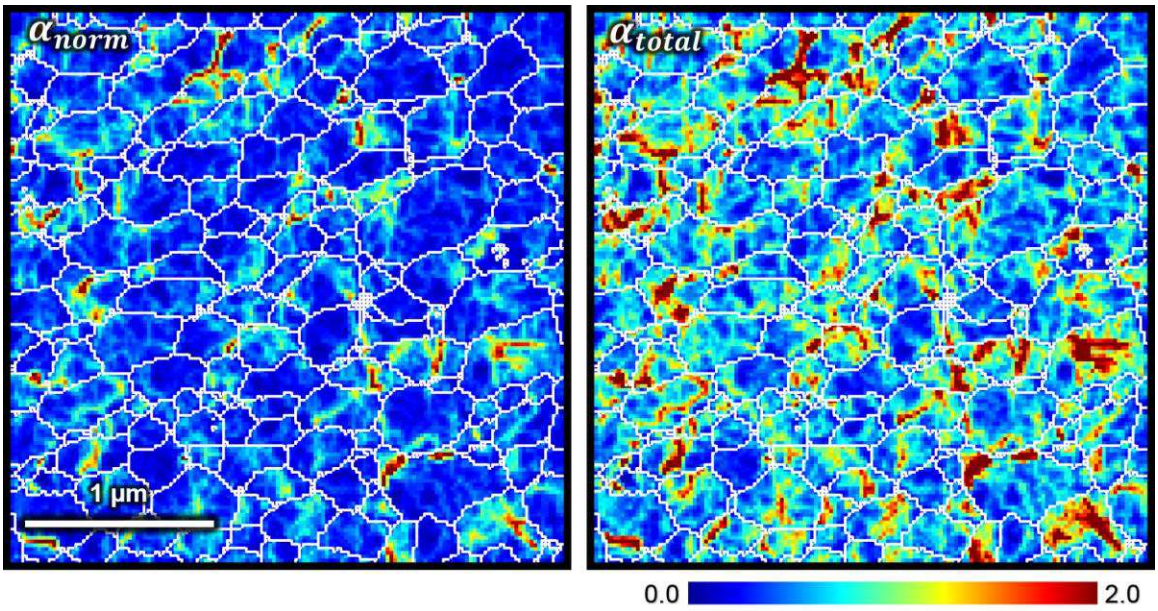

Figure 67 – Scalar magnitude of the Nye tensor, which can be used to calculate the local density of GNDs (units are µm^{-1}).

The total density of GNDs were again plotted as a histogram for direct comparison to the values reported previously. These yield very similar results to the KAM GND for Unalloyed ufgW, as shown in Figure 63, despite the extra rigor involved in actually solving for the Nye tensor. The results of the entrywise norm shows almost the same values as the KAM GND determination. The GND calculated from α_{total} shows an increase compared to the KAM GND calculations, but the same factor could be used to correct KAM misorientations to account for lattice curvatures that occur out-of-plane. The values of the Nye tensors shown in Figure 67 were converted to dislocation densities, and the histogram was plotted in Figure 68.

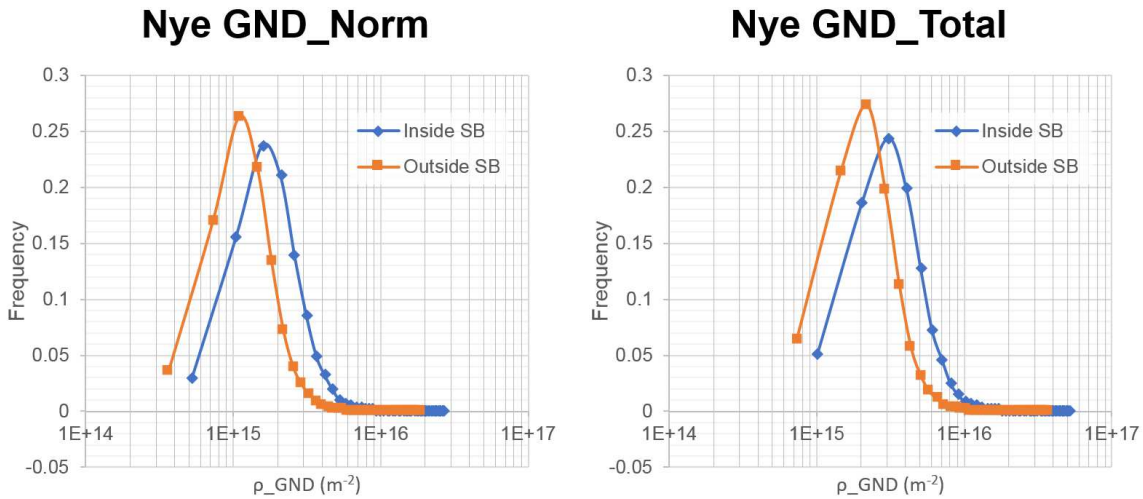

Figure 68 – GNDs calculated based on the Nye tensor for the ufgW-5Re alloy.

As discussed previously, the measurement of GNDs by EBSD is strongly affected by angular resolution and step size. The poor angular resolution of traditional EBSD means that we are probably not capturing the true dislocation density within the undeformed samples. The density of spurious dislocations can be improved by increasing the step size; however, the 200nm grain size of these ufg samples limits the step size that can be used to map lattice curvatures within a grain. Improvements to the angular resolution by HREBSD provides a more effective method for determining the lower-bound threshold of GNDs in ufg materials. Furthermore, the measurement of elastic strains using cross correlation techniques can also allow for an approximation of the four components of the Nye tensor that are inaccessible based on conventional measures of lattice curvature from a 2D sample.

Although there are many technical advantages to cross correlation methods, the technique is not without drawbacks. The requirement for high quality patterns effectively limited the total area that could be scanned. In application, HREBSD for assessing GNDs in ufg tungsten was generally only successful on smaller (1μm x 1μm) regions of the sample.

Performing EBSD on larger scan areas resulted in significant errors from sample contamination, and drift, which led to poor quality maps, even before employing the cross-correlation methods. Reducing the resolution of EBSD patterns led to large errors during pattern correlation and often resulted in larger angular spreads than the original acquisition. Conventional EBSD Images of scan regions in the ufgW-5Re alloy sample are shown in Figure 69.

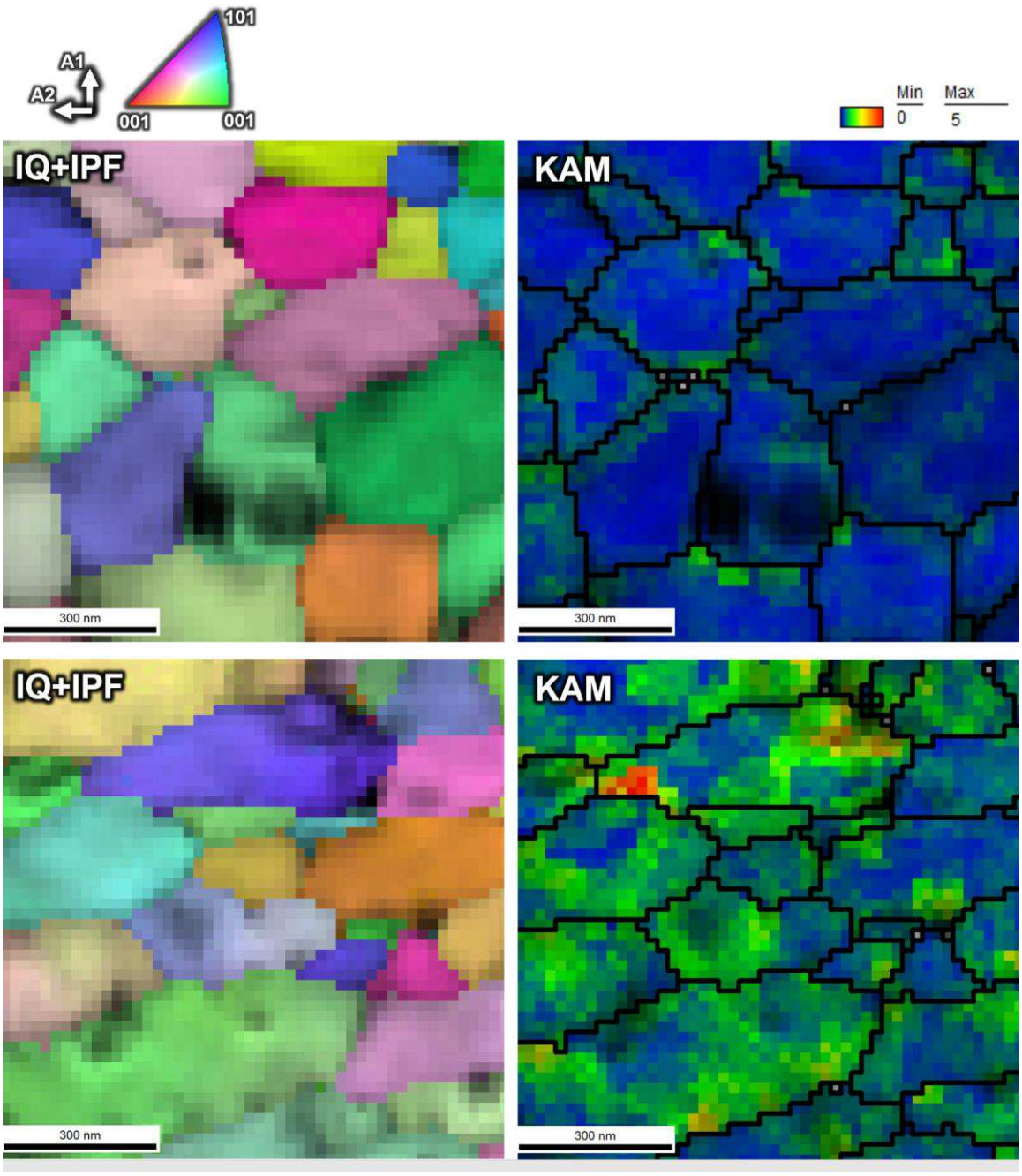

Figure 69 – Conventional EBSD maps of a scan region used for HREBSD. These regions outside (top) and inside (bottom) of a shear band in a ufgW-5Re alloy are directly adjacent to the scans in Figure 64.

The limited viewing area may impose sampling errors; however, these small regions (2250 pixels) contained approximately twenty grains that were suitable for analysis. These regions show similar features to the shear bands analyzed previously; grains are

elongation and show higher degrees of misorientation inside of the shear band. High angular resolution mapping of the undeformed sample showed several regions where the dislocation density approached the values reported for spurious dislocations at an angular resolution of 0.5°. However, there were several regions with dislocation densities that were beyond the lower limit of conventional EBSD. Maps of the total, edge and screw dislocation densities are shown in Figure 70.

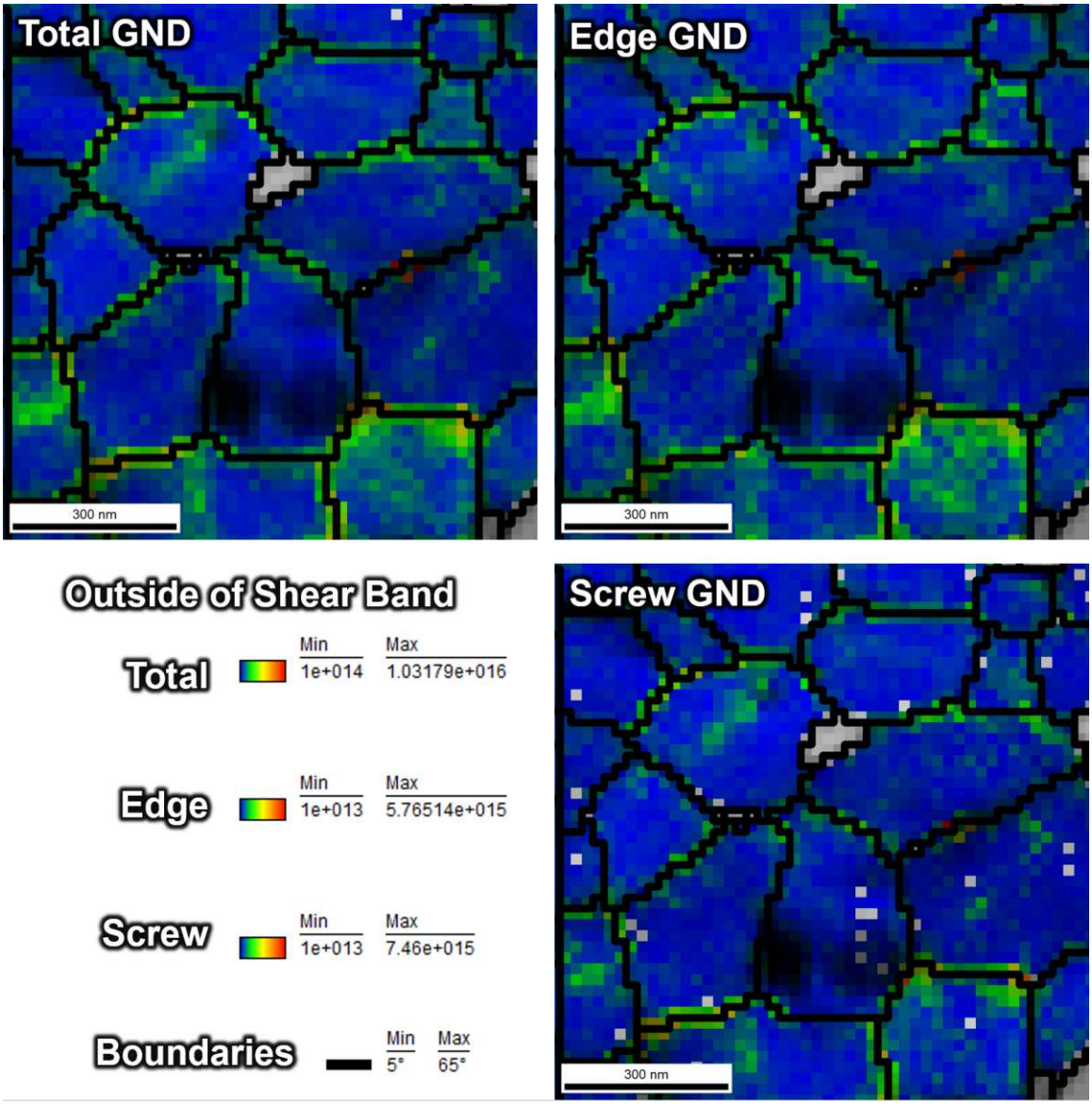

Figure 70 – GND maps of total, edge and screw dislocation densities calculated using cross correlation based HREBSD in an undeformed region of a ufgW-5Re sample.

Similar maps were acquired within the shear banded region as shown in Figure 71. The dislocation density was approximately an order of magnitude higher within the shear band and the dislocation density was plotted on a difference scale from the previous result.

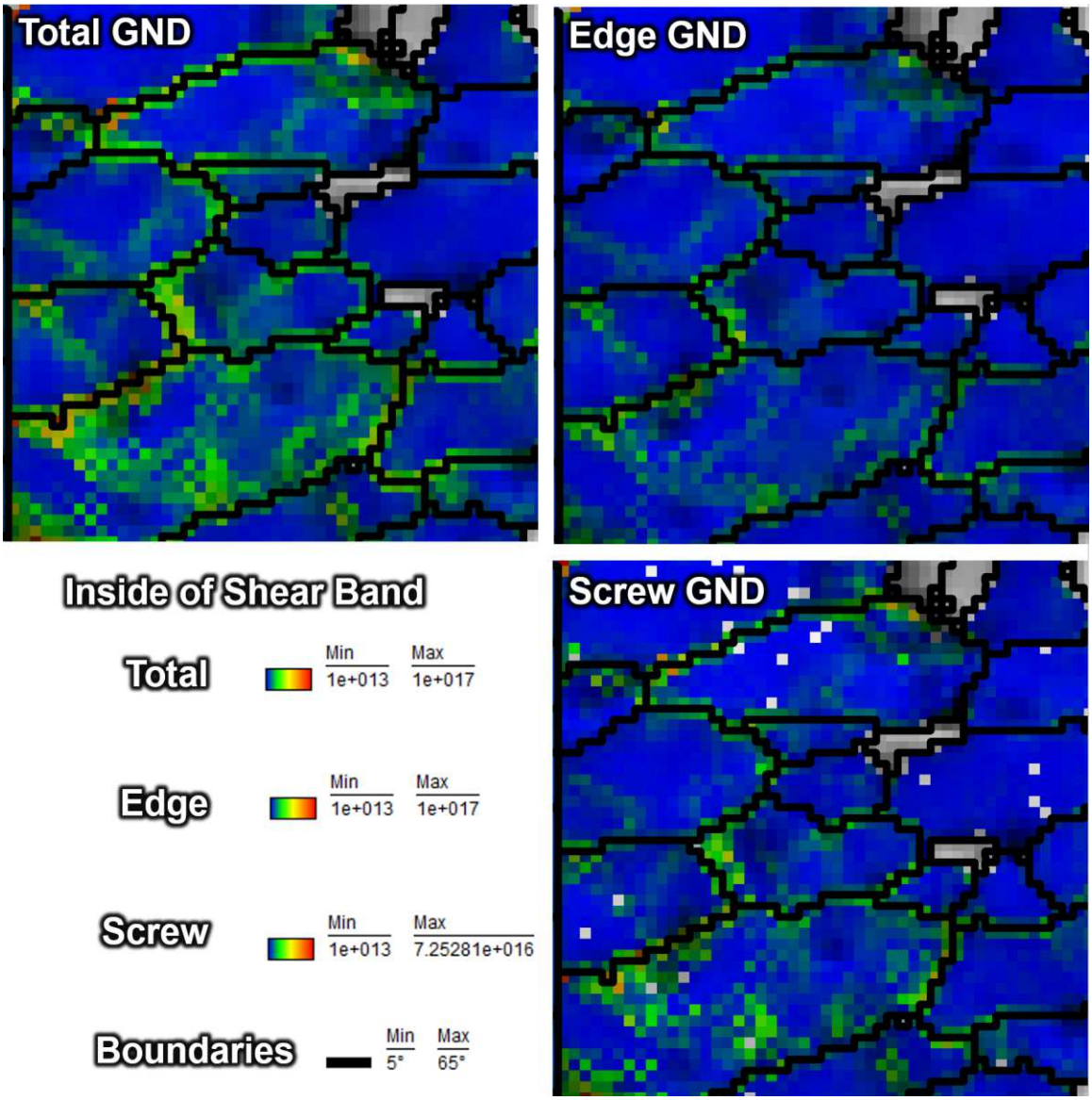

Figure 71 – GND maps of total, edge and screw dislocation densities calculated using cross correlation HREBSD methods. Maps were taken inside of a shear band region that experienced a shear strain of $\gamma \approx 0.4$.

Regions inside of the shear band show a much higher dislocation density in general and there are some grains that show evidence of sub-grain boundary formation and possibly pile-up at grain boundaries. The regions next to grain boundaries are also high in dislocation content for the undeformed sample and this could be an artifact of the measurement technique. There did not appear to be any special insight provided by the

quantities of edge or screw dislocations. The dislocation character is generally important for understanding the state of dislocation mobility; however, HREBSD ascribes dislocation character based on an energy minimization scheme, which does not account for the physical processes that would lead to a predominance of one dislocation in the microstructure. The main goal of the HREBSD method was to help minimize the noise caused by poor angular resolution in order to describe the dislocation structure inside of shear bands more accurately. The calculated dislocation densities inside and outside of shear bands are shown in Figure 72.

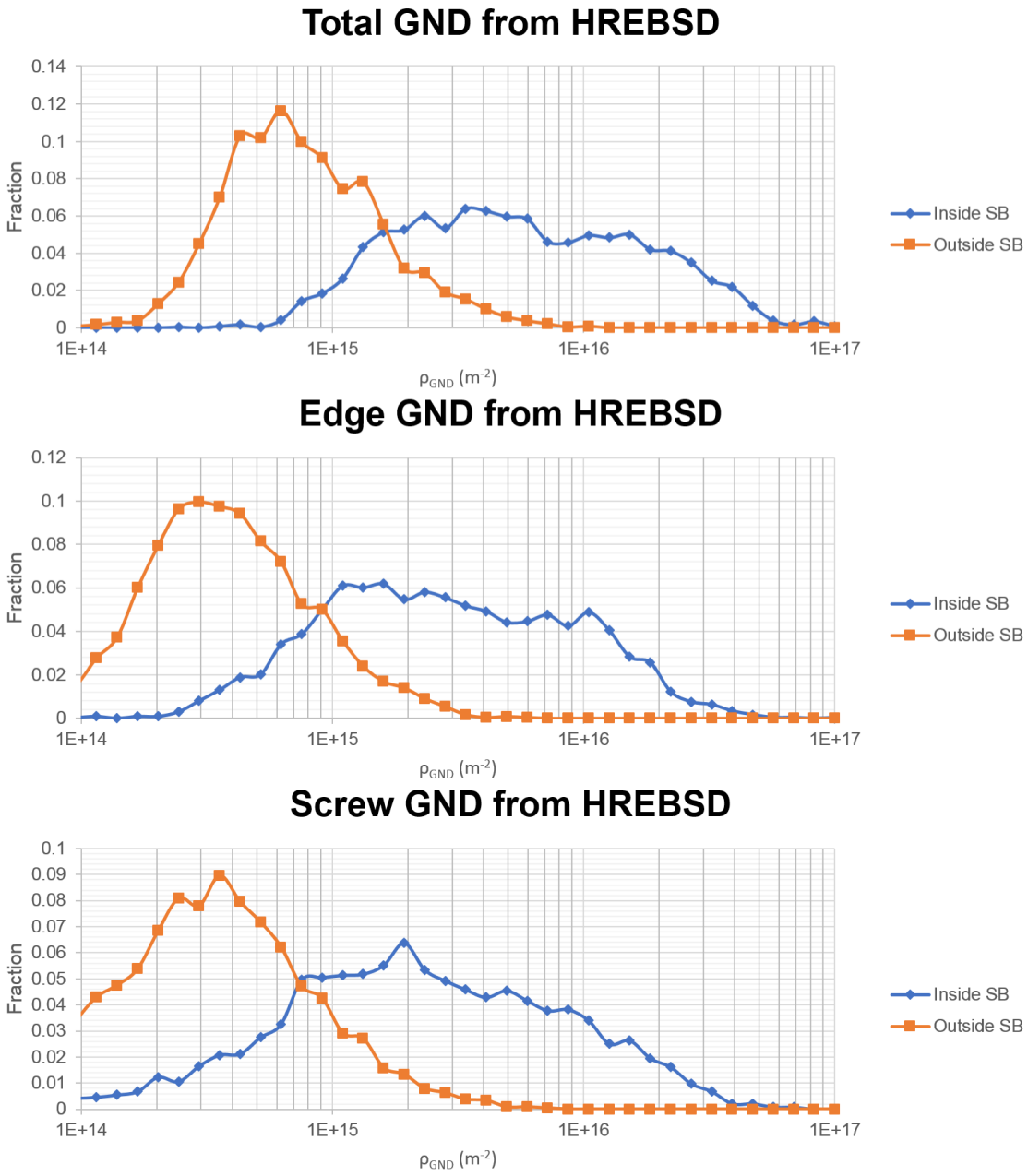

Figure 72 – Probability distribution plots showing the density of geometrically necessary dislocations inside and outside of a shear banded region as calculated from HREBSD.

These results should be taken with a grain of salt, as the method is still under development, and the conditions for measuring dislocation densities in ufg tungsten are

far from ideal for capturing the high-quality patterns that are critical to the accuracy of HREBSD.

The field of continuum dislocation density measurements by EBSD is fairly new and rapidly expanding with regard to our resolved dislocation density distributions. Although the mathematical backbone for these methods were developed by almost seventy years ago [190, 234], recent advancements in that improve the spatial and angular resolution of orientation mapping are allowing these techniques to find practical applications in materials science.

The application of these methods for determining the density of geometrically necessary dislocations in ufg metals has proven moderately successful. The limitations imposed by step size and angular resolution create a significant challenge in describing the density of dislocations beyond a critical threshold. Although there is some question as to whether these methods are accurate enough to measure low dislocation densities in undeformed ufg metals, the deformed microstructure inside of shear band appears to be well suited for these techniques in general. Since these methods are still developing in terms of accuracy and reproducibility, it is important to provide some verification of dislocation density measurements using alternative methods.

4.3.2. Transmission electron microscopy (TEM)

The most widely accepted method for accurately evaluating the density of dislocations in a material is TEM. Although there are many challenges with regard to sampling statistically relevant volumes and introducing defects during specimen preparation, TEM is generally accepted as the gold-standard for measuring dislocation density because of

the accuracy and resolution in comparison to other techniques (e.g. x-ray diffraction, etch pitting, etc.) In order to validate the relatively new and novel methods of assessing geometrically necessary dislocations through EBSD, TEM was performed on several ufg samples to quantify the density of dislocations in as-sintered samples, and within the shear bands of mechanically tested specimens.

The structure of undeformed samples was analyzed by TEM using a FIB lift-out technique. The ufg tungsten samples prepared for this study were all sintered at a temperature of 1400° C, and deformation post-processing was not performed. Based on these processing parameters, dislocations were not expected in any significant quantity in the microstructure. However, STEM imaging showed that approximately half of the sintered grains had dislocations within their microstructure after sintering. An image of the TEM foil, and dislocations within a single grain are shown in Figure 73.

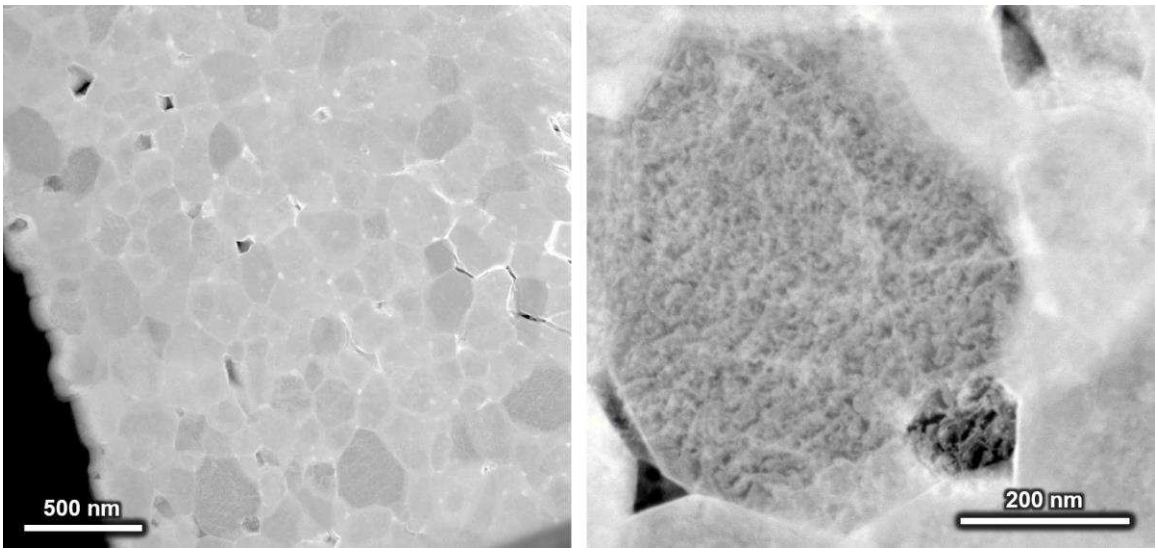

Figure 73 – HAADF TEM images of an Unalloyed ufg W sample after sintering. The lower magnification image (left) shows a number of grains that contain dislocations after sintering. A higher magnification image (right) shows that the dislocations are generally long and straight, though several kinks are observed within the grains.

Although HAADF imaging of dislocations is supposed to provide a more uniform estimate of dislocation content based on the limitations imposed for the $\vec{g} \cdot \vec{b}$ invisibility criteria [257], there were still effective limitations to acquiring large statistics on dislocation content based on contrast. A representative set of five grains were analyzed for dislocation content, details of the dislocation traces used for dislocation and the foil estimate for a single grain are shown in Figure 74.

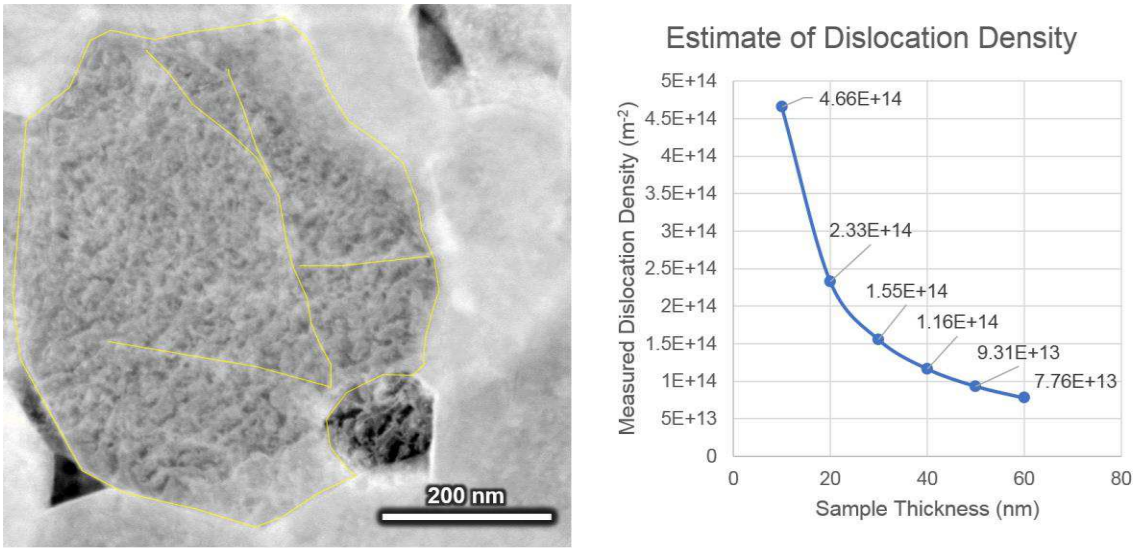

Figure 74 – Dislocation content of a single grain analyzed by TEM using HAADF dark field mode.

The density of dislocations was approximated based on a maximum sample thickness of 40 nm based on previous analysis using the log-ratio method [271] in electron energy loss spectroscopy. The actual thickness of the sample was likely thinner based on the limited electron transparency of tungsten at 200 kV, however, this provides a conservative estimate of the dislocation density measurements.

Several shear banded samples were also analyzed by TEM in order to provide an estimate of the dislocation density inside of shear bands, and within the undeformed regions of the

materials. An image describing the shear band characteristics, and the perforation site of a ufgW-5Re sample tested at quasi-static rates is shown in Figure 75.

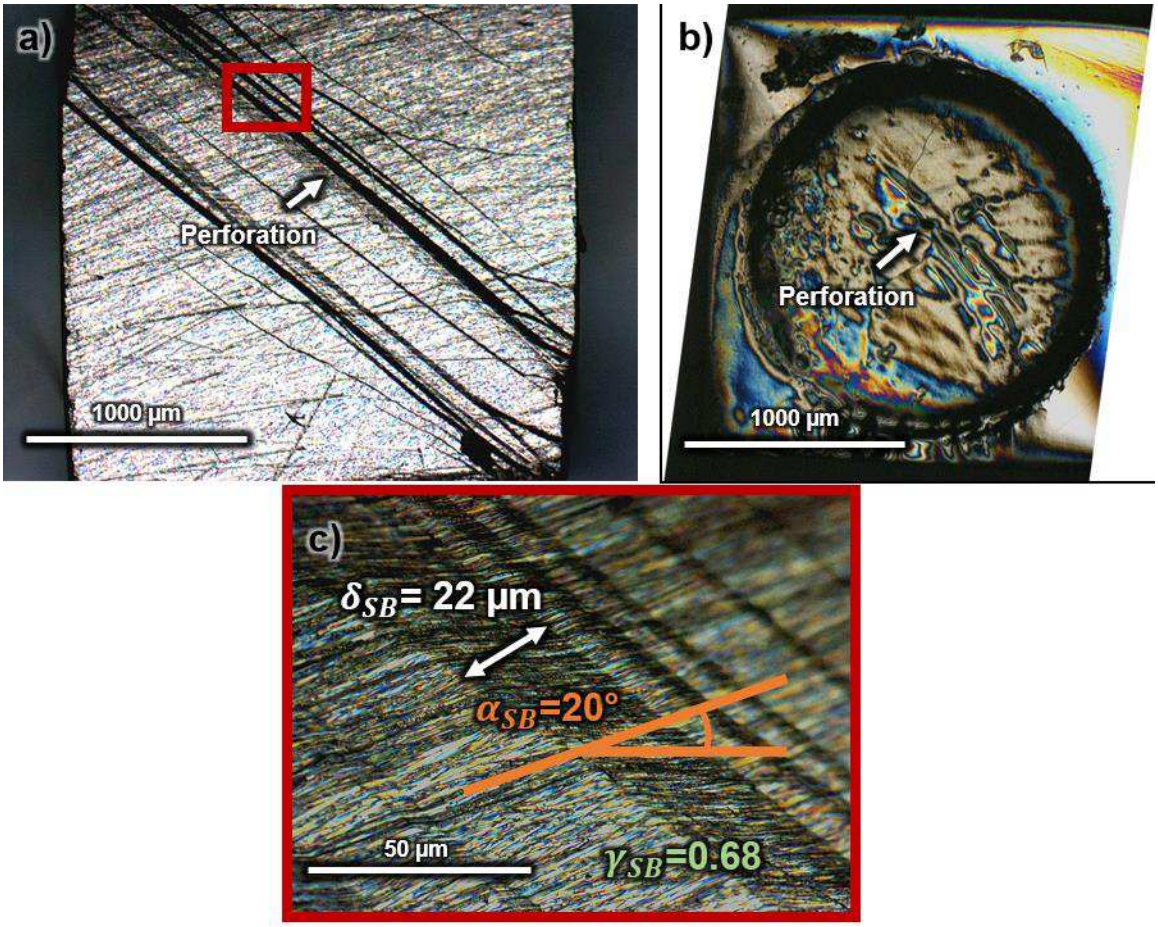

Figure 75 – Image of mechanical test specimen used for TEM analysis (left) and perforation site (inset). Strain characteristics inside of shear band (right).

During electropolishing, the sample perforated at a particular shear band where the strain had been well-characterized after mechanical testing; this particular shear band showed an engineering shear strain of $\gamma_{SB} = 0.39$. The perforation site showed similar microstructural features what was previously observed by EBSD. In particular, the microstructure was heavily elongated in the direction of the shear band, and the sample showed a high degree of texture inside of the band, shown in Figure 76. The texture

appears to be the same shearing texture as reported in Figure 57 based on the 6-fold symmetry of the {110} planes.

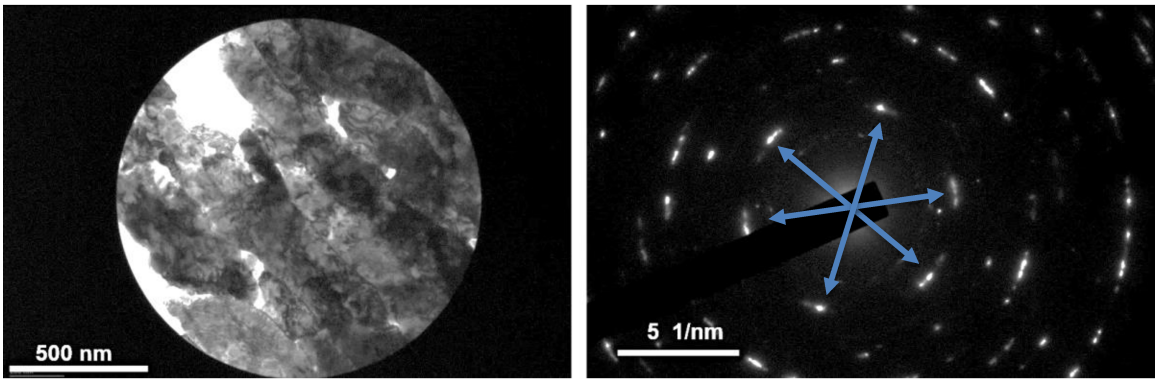

Figure 76 – Bright field TEM image of a shear banded region in a ufgW-5Re alloy (left), and the selected area diffraction pattern (right) corresponding to this area. The diffraction pattern shows a 6-fold symmetry based on the {110} type diffraction peaks, in a fashion similar to the texture observed by EBSD.

The microstructure inside of the shear band showed a high dislocation density that was non-uniformly distributed among grains (similar to observations by EBSD). Dislocations, shown in Figure 77, did not show the long, straight, pure screw character that is traditionally observed in deformed single crystals [272]. In coarse grained samples, screw dislocations have much lower mobility than dislocations with edge character and tend to propagate based on a double kink mechanism at low temperatures [273].

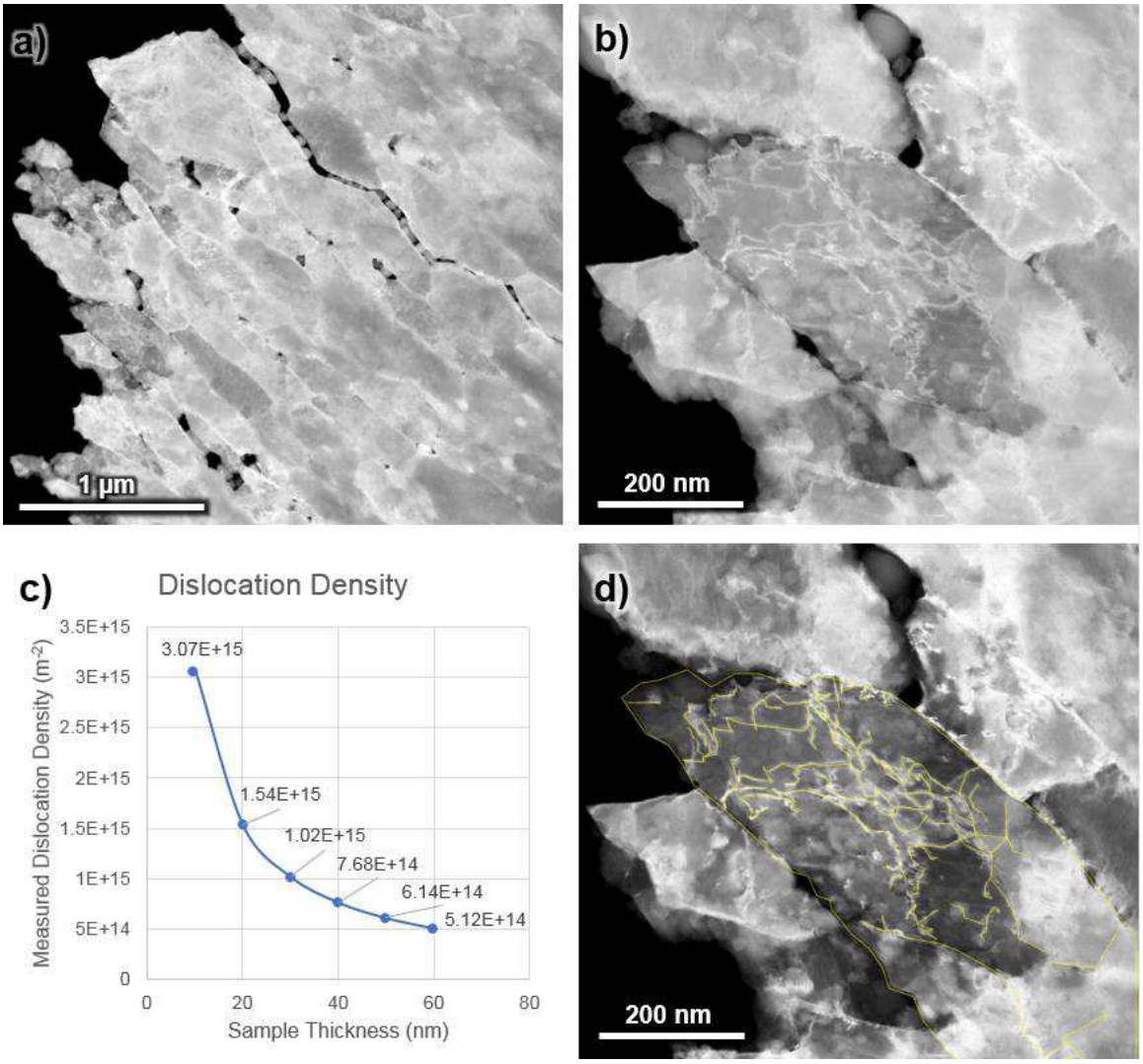

Figure 77 – STEM HAADF images showing a) the elongated grain structure and b) dense dislocation structure inside of a shear band. The dislocation direction varies over the length of the dislocation, indicative of mixed edge and screw character. The dislocation density as a function of film thickness is shown in c) for traced dislocation line lengths d).

This particular grain shows a dislocation density of approximately $7.7*10^{14}$ m^{-2}, though it should be noted that the limited sampling leads to poor statistics over the entirety of the shear band. This feature elucidates the need for alternative methods, such as EBSD, to accurately describe the density of dislocations over much larger regions in the material. The density of dislocations is slightly lower than what was calculated by EBSD methods,

but it fits within a rough order of magnitude in comparison to all of the average dislocation densities measured.

4.3.3. Nanoindentation

A simple and effective method understanding the strain hardening ability inside of a shear band is to test the local properties by nanoindentation after the shear band has formed. Even though shear bands are fairly narrow in ufg metals, the required resolution for positioning the tip and measuring mechanical properties inside of a shear band are well within the capabilities of these instrumented indentation techniques. Figure 78 shows SEM images of several indents that were measured inside and outside of a shear band. A minimum of nine indents were tested in each region of the sample, and two different ufgW-5Re compression tested samples were evaluated.

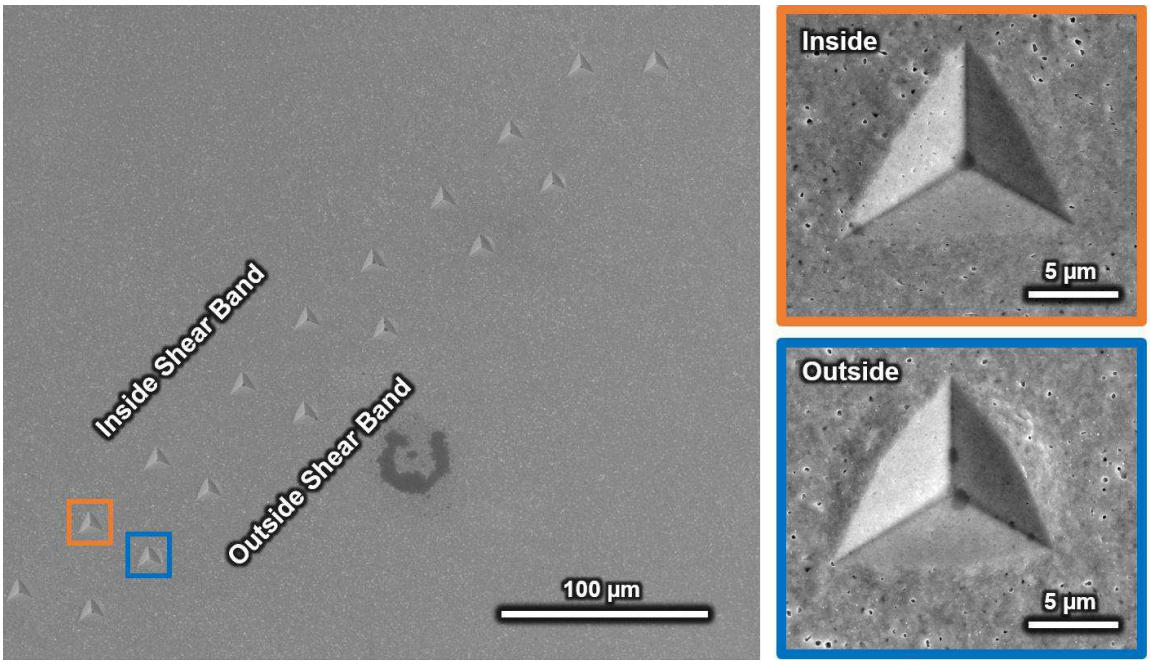

Figure 78 – Nanoindentation tests performed on the ufgW-5Re sample characterized extensively by EBSD.

The indentations outside of the band show rounded edges and pile-ups at the edge of the indent, which have been previously associated with plastic instability bulk metallic glasses [274, 275], nanograined iron [276] and ufg tungsten [53]. However, the indents that are inside the shear band show straight edges without any evidence of a pile-up. The hardness values outside of the shear band are considerably higher over the entire depth of the indent. Figure 79 shows the measured values of hardness for inside and outside of the shear band.

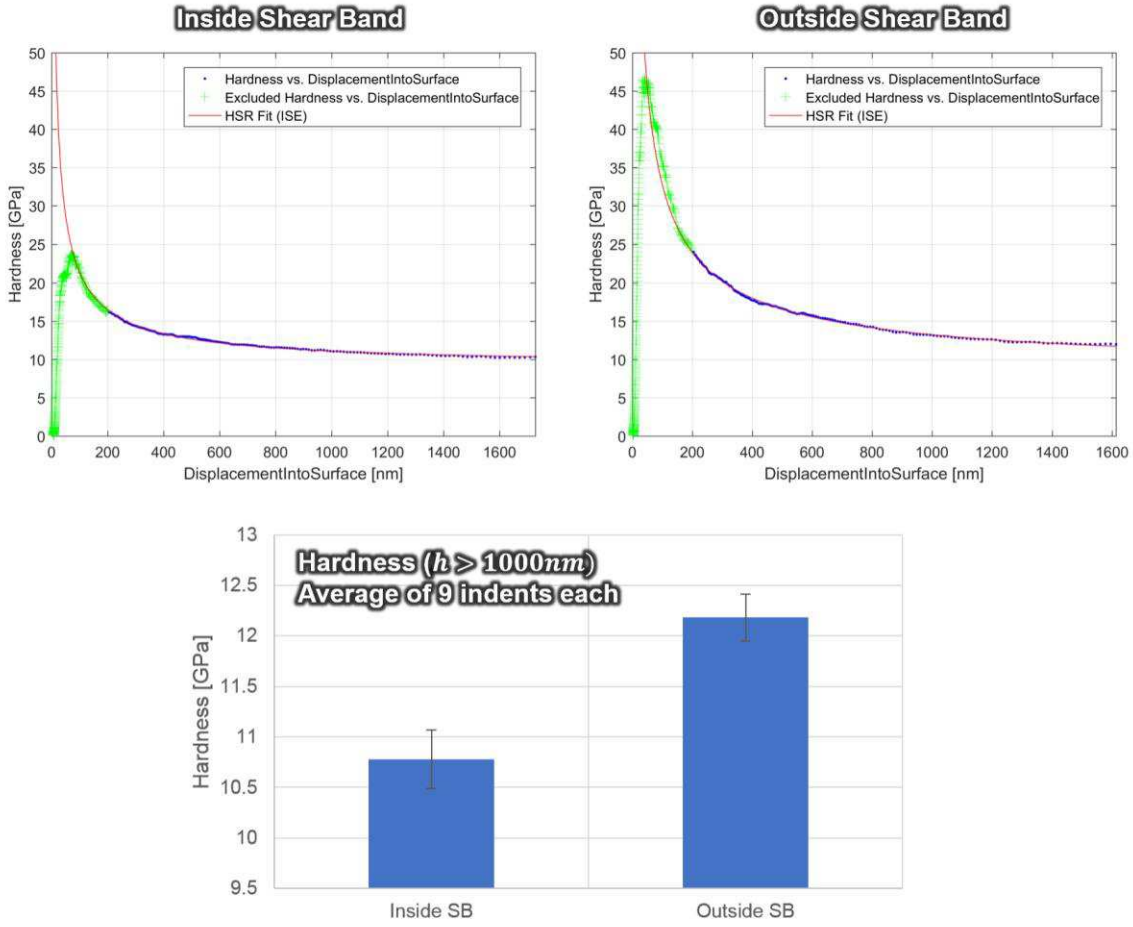

Figure 79 – Representative indents showing the hardness inside (top left) and outside (top right). The undeformed material is considerably stronger over the entire range of the indent. The average hardness, taken at depths greater than 1000nm are also shown (bottom).

The difference in hardness inside and outside of the shear band is highly significant ($\Delta H_{SB} = -1.40 \pm 0.37\ GPa$), and when converted to a yield strength (σ_y) value to the hardness (H) according to the Tabor formula, $\sigma_y = H/3$, the estimated decrease in yield strength is $470 \pm 120\ MPa$. Although there is a significant amount of error in the estimate (and systematic errors in the conversion [277]).

The indentation size effect is apparent at very large depths in tungsten [278], beyond the conventional limits of nanoindentation; however, the size effect may be readily accounted for based on the Nix-Gao equation (Equation (47)) shows that the hardness is a function of indentation depth, based on the concept of geometrically necessary dislocations.

$$H = H_0 \sqrt{1 + \frac{h^*}{h}} \tag{47}$$

The hardness-depth measurements for each indent were modeled according to Equation (47) and the results are shown in Figure 80.

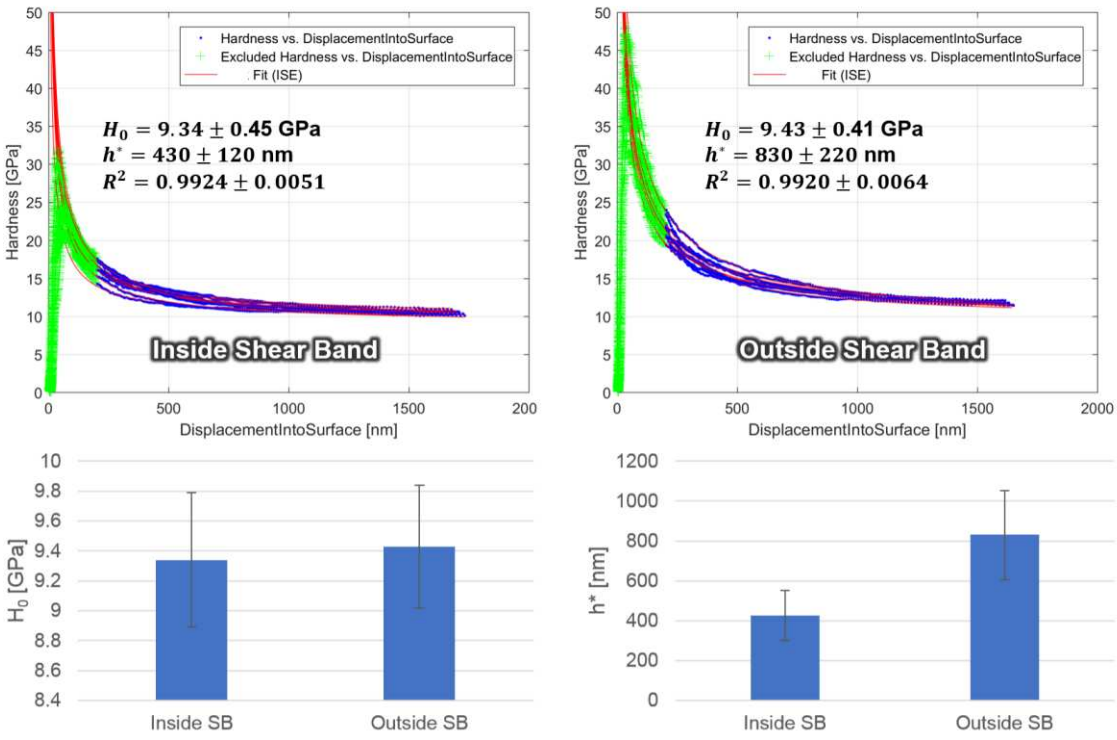

Figure 80 – Overlaid nanoindentation curves of a single ufgW-5Re sample. Each individual hardness curve from nanoindentation inside (top left) and outside (top right) were fitted to the Nix-Gao model.

Although the hardness inside of the shear band is considerably lower than outside, it is observed that these values would converge if the indentation depth is extrapolated beyond the range of the nanoindenter. It appears that the hardness differential at shallow indent depths can be attributed to the difference in h^*, which is a function of the statistically stored dislocations, and not necessarily the geometrically necessary dislocations that dominate behavior at very shallow indent depths. The dislocation structure, beneath the indenter tip has a strong influence on the measured properties inside and outside of a shear band. In a very general sense, this structure can be described according to general descriptions of strain gradient plasticity, which may help to highlight the unusual behavior observed during nanoindentation.

The softer values inside of the indent can directly account for the plastic instabilities associated with ufg tungsten, without relying on the effects of texture or adiabatic heating. It is important to note that this direct evidence of softening was unexpected, based on the significantly higher dislocation densities that were measured inside of shear bands. The hardness and strength of a material are supposed to scale with the square root of dislocation density according to the Taylor hardening equation. This behavior provides the foundation for the strengthening of metals by deformation processing. This observation of softening with increasing dislocation density is unusual; however, these trends have been observed in a number of materials that demonstrate plastic instabilities, and these observations have helped to provide insight to the physical mechanisms of shear banding in ufg tungsten.

CHAPTER 5. DISCUSSION

The results from the previous chapter, namely the observations of shear band during compression testing and detailed characterization of the structure and mechanical properties inside of a shear band provide a detailed picture of what leads to shear band formation in ufg tungsten. These results do not support previously proposed models of adiabatic shear banding, or geometric shear banding. Orientation mapping points to the role of dislocation accumulation in describing shear banding behavior. In ufg metals, the concept of geometrically necessary dislocations has strong implications for saturating strain hardening behavior. In sintered, or annealed metals, the concept of mobile dislocations can play a role in the strain softening of materials. In sintered, or annealed ufg metals, this influence of dislocation mobility is magnified the concept of geometrically necessary dislocations and strain gradient plasticity.

5.1.1. Temperature of shear bands

The ufg materials tested and characterized in this study are inherently susceptible to strain localization and shear banding, even at quasi-static rates. Even though it is absolutely clear that temperature does not play a role in the initiation of plastic instabilities for these materials, it is helpful to quantify the potential influence of temperature as shear bands develop. Furthermore, a thorough understanding of deformation of the adiabatic temperature rise associated with deformation is critical for ballistic applications.

Under adiabatic conditions, since no heat is transferred out of the system, all of the heat of deformation leads to a temperature rise in the material. The specific heat generated

during shear band formation, $Q\ \left[\frac{j}{m^3}\right]$, can be estimated based on the virtual work performed during deformation.

$$Q = \beta \int_0^{\gamma_{SB}} \tau d\gamma \approx \beta \tau \gamma_{SB} \tag{48}$$

where the shear stress (τ), is taken to be half of the yield stress. (β) is the Taylor-Quinney coefficient, which describes the fraction of mechanical energy converted to heat. This coupling term is sensitive to the material, microstructure and strain rate among other factors [279]; however, it is common to prescribe a value of 0.9, which can provide an upper bound approximation [280] for the transfer of plastic energy to heat.

The temperature rise under adiabatic conditions ($\Delta T_{Adiabatic}$), can be approximated as

$$\Delta T_{Adiabatic} = \frac{Q}{\rho C_p} \tag{49}$$

where ρ is the density and $C_p$is the specific heat capacity. This temperature rise is highly sensitive to the strength of the material, and the strain experienced during deformation. The temperature increase under perfectly adiabatic conditions is plotted in Figure 81.

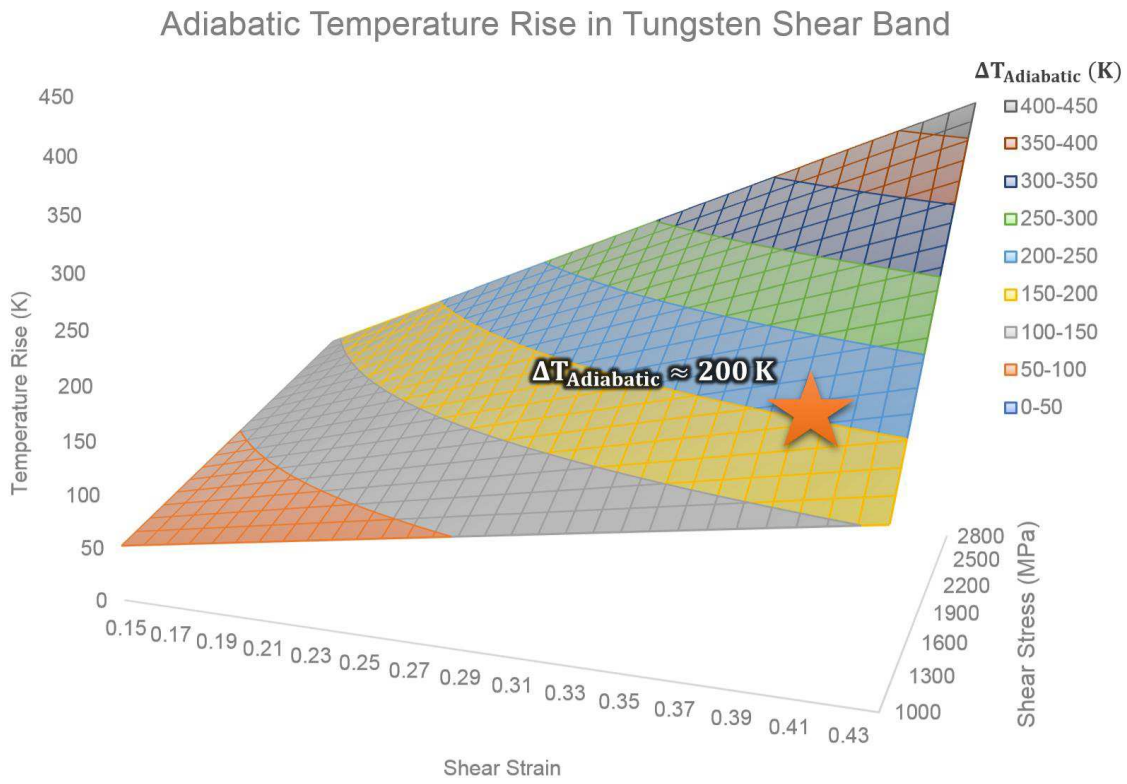

Figure 81 – Adiabatic temperature rise inside of shear band calculated from observations of strain in shear banding ufgW specimens.

From the observed shear strain of 0.4, and the yield strength of 3250 MPa, the estimated temperature rise inside of the shear band is only estimated to be 200°C under perfectly adiabatic conditions.

Estimating the actual temperature rise at the center of a shear band requires accounting for thermal conduction, which reduces the temperature rise associated with plastic deformation. Based on the planar geometry of the shear band, the system can be approximated as a 2D heat source so that the heat transfer problem can be approximated in a form that has been applied to shear bands in bulk metallic glasses [121, 281]. The heat generated inside of the band is modelled as a planar heat source and the temperature

is estimated based heat transfer in a single dimension. The temperature rise at the center of the band can be estimated based on the time required for the deformation to occur.

$$\Delta T_{center} = \frac{H}{\rho C_p \sqrt{\pi \alpha}} \frac{1}{\sqrt{\delta t}} \tag{50}$$

where H $\left[\frac{J}{m^2}\right]$ is the areal density of heat generated inside of the shear band (i.e. $H = Q\delta_{SB}$). The temperature rise associated with shear banding during quasi-static and dynamic mechanical testing is shown in Figure 82. The time in Equation (50), is approximated as the total time for the shear band to traverse the sample. In dynamic tests, the shear bands appear fully formed between frames of high speed imaging ($\Delta t < 10\mu s$). During quasi-static tests, the shear bands travel through the sample within five to twenty seconds; however, the actual velocity of the band depends on several external conditions (load frame stiffness, formation of multiple bands, etc.)

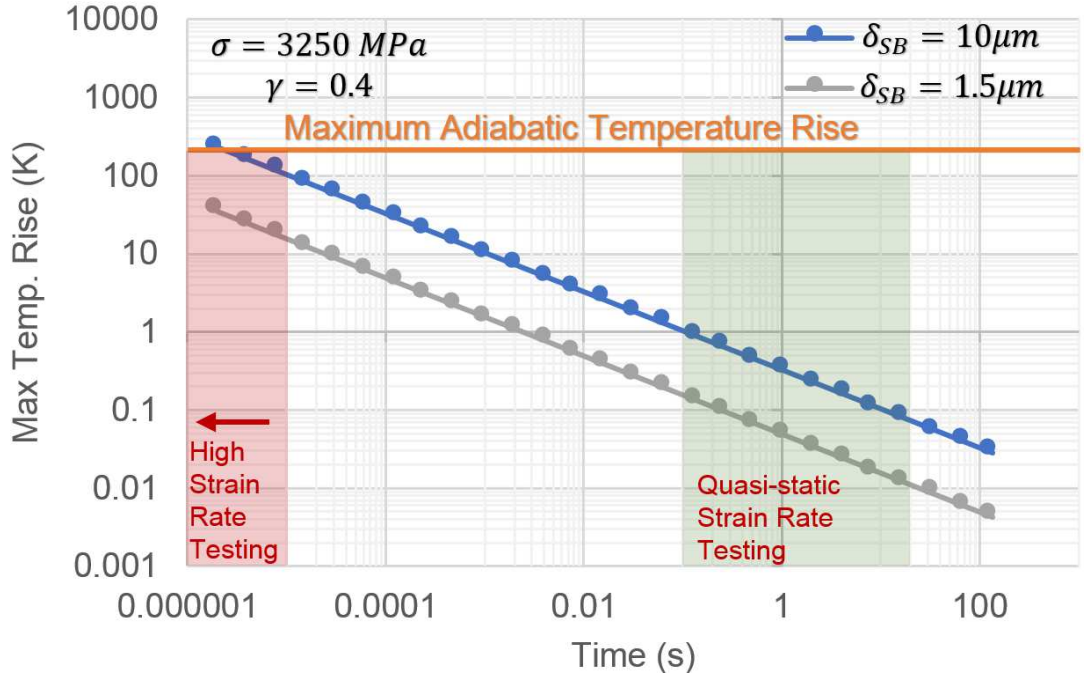

Figure 82 – Calculated temperature rise in a shear band, accounting for heat conduction away from the band.

This heat transfer model provides an effective approximation of the temperature rise as the adiabatic condition is approached. However, this model is not able to capture the actual adiabatic temperature because all of the deformation (and the heat source) is confined by the 2D approximation of the band. However, the approximation appears valid for the low to moderate strain rates imposed by quasi-static deformation, and the temperature rise approaches the adiabatic condition at high strain rates. Based on this analysis, it can be seen that the temperature rise inside of the band is less than 1K under quasi-static conditions. The strain rate where the adiabatic condition is observed is sensitive to the heat generated inside of the band. With a band thickness of ~50μm, and a testing time of ~50μs, it is clear that the shear bands observed under dynamic test conditions met the condition of adiabaticity.

5.1.1. Flow softening behavior of tungsten

The flow softening behavior must be taken into account when describing the susceptibility of a material to adiabatic shear banding. In coarse grained tungsten, the softening influence of temperature is very strong [282, 283] based on the thermally activated mechanisms controlling dislocation motion [273, 284]. The thermal softening behavior of tungsten single crystals as a function of temperature was measured by Brunner [285] as shown in Figure 83.

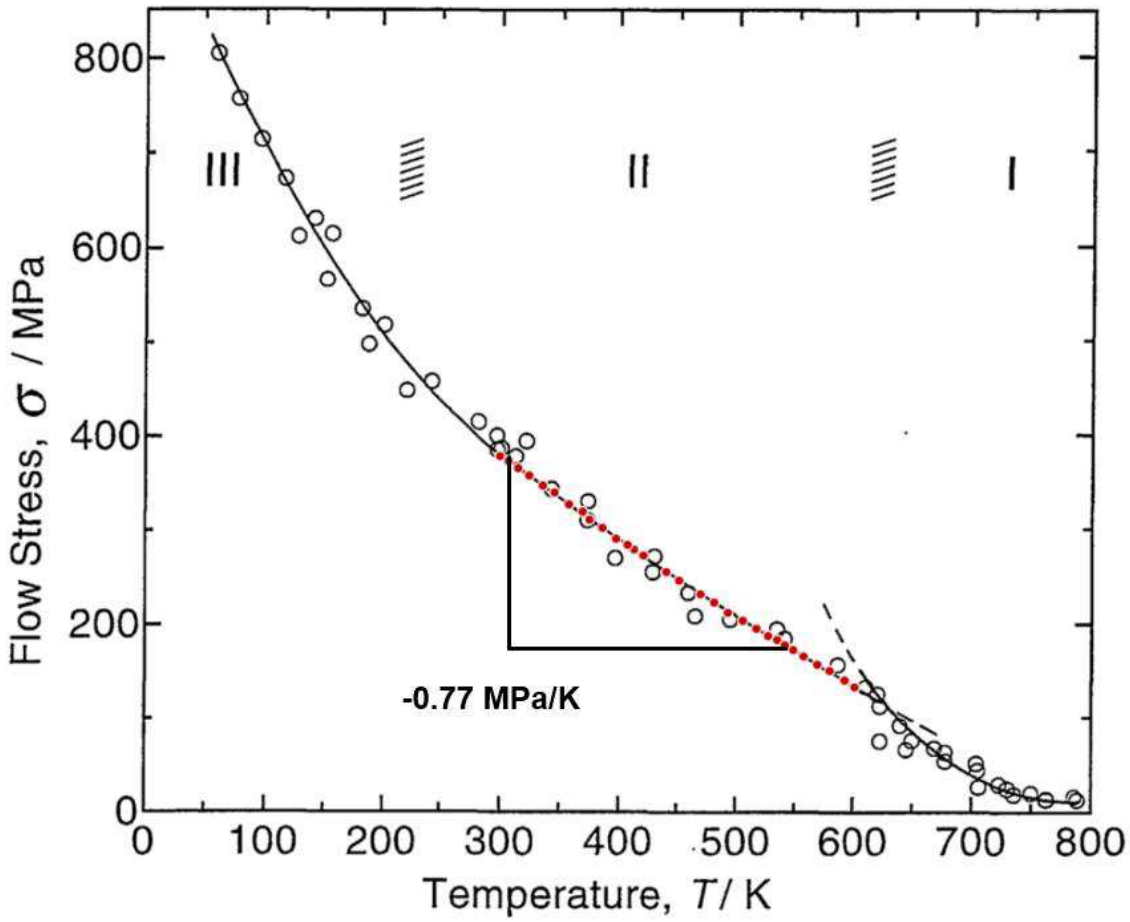

Figure 83 – Measured flow stress of single crystal tungsten over a temperature range of 77-800K. With permission from Brunner [285]. Curve fitting was performed using Web Plot Digitizer [286]

The thermal softening behavior is highly linear over the range of temperatures predicted for shear banding in tungsten. It can be seen that under perfectly adiabatic conditions, the flow stress is reduced by approximately 150MPa. This calculation can be used to provide a more direct comparison between the influence of adiabatic effects and the strain softening phenomenon observed by nanoindentation. The physical reduction in the strength associated with the observed strain softening in sintered ufg tungsten is approximately three times greater than thermal softening effects for the same amount of strain under perfectly adiabatic conditions. This estimate is highly conservative, as the

thermal softening effect will be reduced at very fine grain sizes where there is less of a dependence on screw mobility for describing the deformation behavior of BCC metals in general [287, 288].

Adiabatic shear banding mechanisms must be accounted for when materials are used, or tested in high strain rate environments; however, this does not mean that these are the only mechanisms in play. The microstructure and dislocation structure are also critical descriptors of the strain hardening ability in metals; these factors will have an influence on plastic instability, even if the material is tested under adiabatic conditions. In the most technical sense, any shear band that forms under conditions where heat transfer is effectively stymied can be considered an adiabatic shear band. This description is technically accurate, but not particularly useful, for describing and controlling the root causes of plastic instabilities in ufg metals.

5.2. Geometric shear banding

The strain softening behavior observed in sintered ufg tungsten cannot be explained based on geometric mechanisms. Texture does develop when shear bands form, but these textures are an artifact, not a cause of the highly localized deformation. The texture is not unique; it is the same texture that is generally observed in BCC metals that are subjected to shearing deformations. Finally, this texture does not show signs of being softer than the material surrounding the shear band. Although, there are some interesting implications for fracture, based on the hard and soft orientations developed inside of a shear band.

The specific geometric shear banding model developed by Joshi and Ramesh [72] does not help to describe the shear banding behavior in sintered ufg tungsten. At first glance, this model does describe the several trends related to grain size induced susceptibility to shear banding. In particular, it helps to describe general differences in stability that have been observed for different crystal structures (i.e. FCC vs. BCC). However, the basic rotational accommodation mechanism has not been proven experimentally, and is inconsistent with the results presented in Section 4.3.1.1. In particular, there is no physical reason for a material to preferentially accumulate soft orientations without any consideration of crystal structure.

The formation of texture is driven by the fundamental processes of deformation. For dislocation mediated plasticity, the texture that develops is a natural result of the asymmetric nature of dislocation activity [268]. The rules of dislocation motion are dependent on the crystal structure, and a key finding of this research is that the textures observed inside of a shear band in ufg tungsten are the same as those observed in other BCC metals subjected to shearing. Furthermore, as a first order approximation, these orientations are not harder or softer than the non-textured material (Figure 60).

Finally, according to the original description of geometric shear bands by Asaro [127], a certain amount of strain is required to the rotate and reorient grains before flow softening is observed. In ufg tungsten, a shearing texture is developed inside of shear bands, but this texture is only observed *after* the shear band has formed, and significant straining has occurred. For ufg metals that shear band, the shear band initiates at a very early stage, as shown by the negative strain hardening behavior of iron from Jia et al. [165] in Figure 84. The very early onset of shear banding is a critical finding in our own research as well,

because it does not allow for the incubation strains that are required to develop texture in a material.

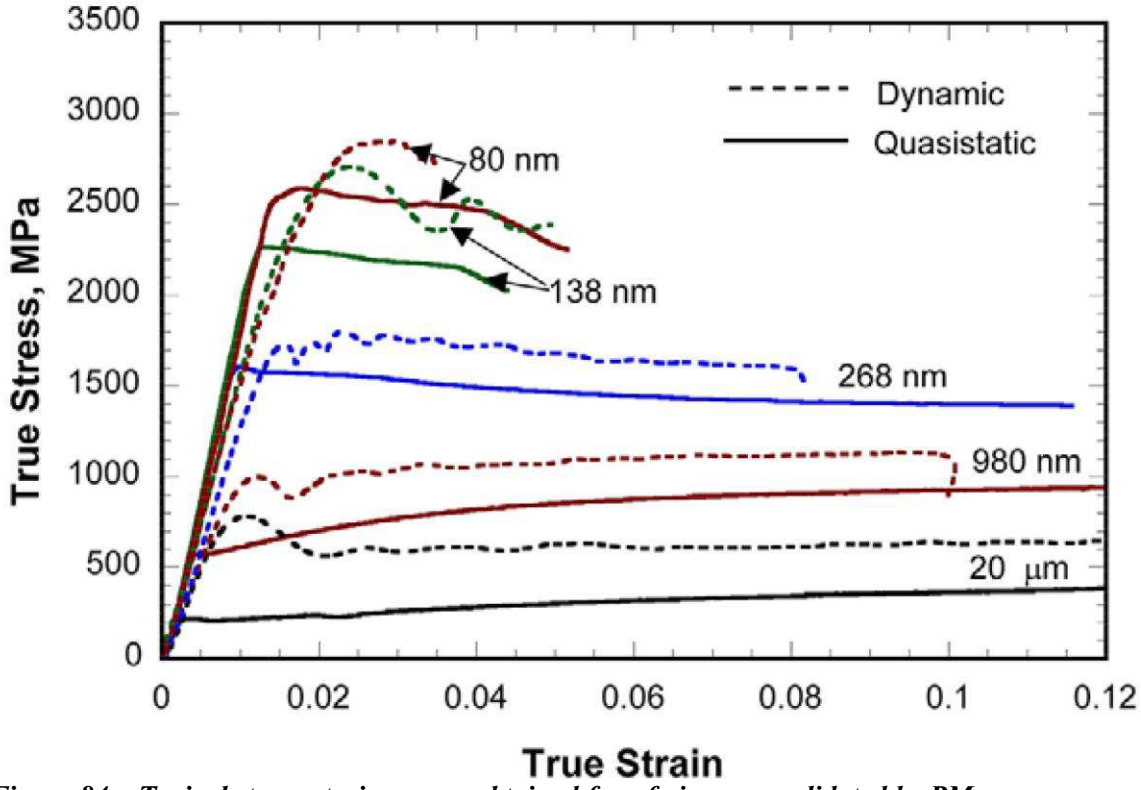

Figure 84 – Typical stress-strain curves obtained for ufg iron consolidated by PM processes under quasi-static ($1–4 \times 10^{-4}$ s^{-1}) and high-strain rate ($3–6 \times 10^{3}$ s^{-1}) uniaxial compression for all of the grain sizes, from [165].

For the stability maps for the Joshi and Ramesh model of geometric shear banding, the strength index, $\mathcal{M}$ from Equation (22), depends only on the difference in shear stresses between hard and soft orientations ($\Delta\tau$), the shear modulus (μ), and the strain rate sensitivity (m). In Figure 85, a plot of the strength index and grain size for various tungsten materials shows that the stability map is fairly good at predicting the susceptibility to shear band formation.

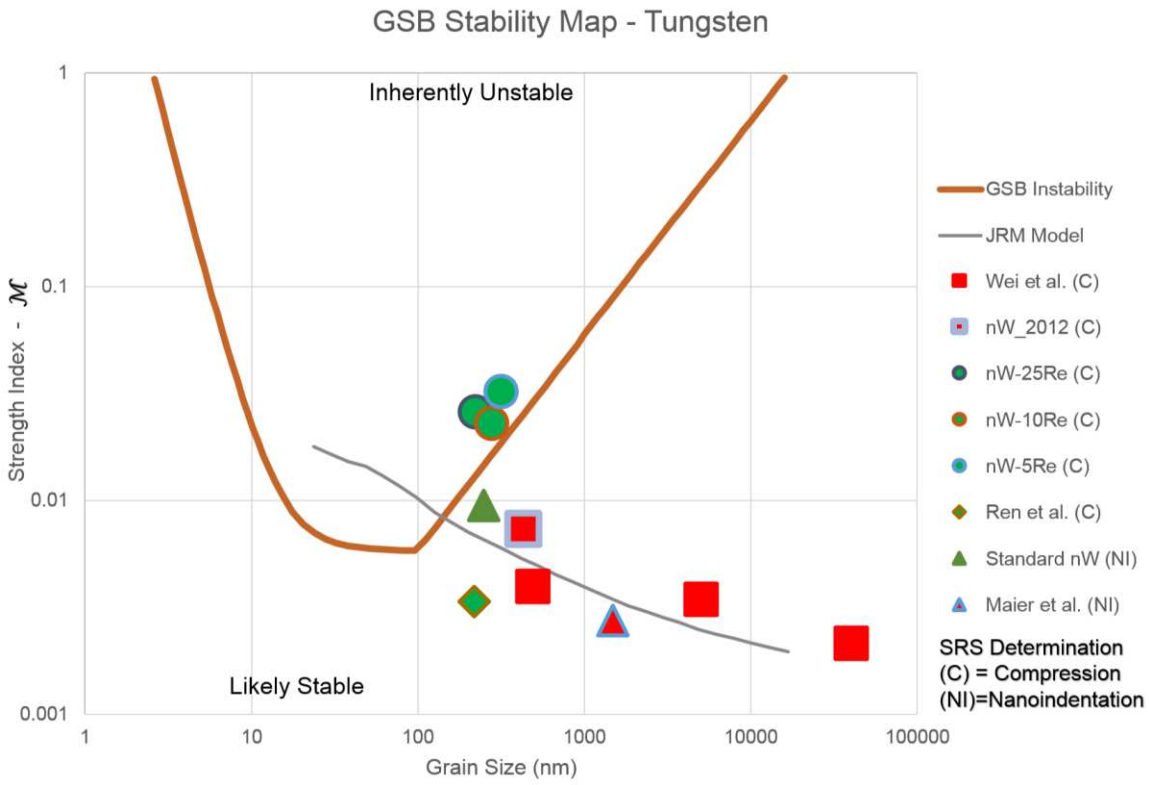

Figure 85 – Susceptibility of tungsten based on the Joshi Ramesh model for geometric shear banding. Samples with a green infill demonstrated shear banding(left), while red sample. Data are from Wei et al. [160], Maier et al. [221], and from material produced by Ren et al. according to [61]. The JRM model [165] shows the expected trend of tungsten based on the relation between grain size and strain rate sensitivity. Nanoindentation was used to measure the strain rate sensitivity of certain samples according to the method of Maier et al. [216].

The strain rate sensitivity of BCC metals has been shown to be a function of grain size according to the JRM model published by Jia et al. [165]. When this relation holds, the stability map (including the strength index) is only a function of grain size (shown by the JRM Model line). Indeed, grain size appears to be the controlling factor for describing the stability of tungsten. Samples with a higher strain rate sensitivity (as a result of a very wide grain size distribution), even though the average grain size was comparable to our own unalloyed ufgW, demonstrate shear banding, while samples with a lower strain rate sensitivity (because of rhenium additions) also show the same localization behavior. It

can be seen that grain size is the controlling factor for whether plastic instabilities develop, not the strength index.

5.3. Limitations to strain hardening in ultrafine grained tungsten

When grain sizes approach the lower limits of the ultrafine grain regime, there are significant implications for the dislocations that are required to accommodate strain in the lattice. The concept of strain gradient plasticity effectively accounts for the confining effects of grain boundaries, allowing for a prediction of the density of mobile dislocations for a given strain. These models provide insight into the limitations in strain hardening observed in ufg materials. In particular, SGP models account for the high dislocation densities that are necessary to deform ufg metals.

One of the main staples of metallurgical practice is the relation between the dislocation density and the strength of a material. While the derivation is largely empirical, the Taylor hardening model (Equation (24)), which relates the flow stress to dislocation density ($\sigma_f \propto \sqrt{\rho}$) provides a sound explanation for the work hardening behavior of metals. According to the most conservative EBSD estimates, the dislocation density inside of the shear band is almost twice as large as the dislocation density in the undeformed sample, and there should be a corresponding *increase* in the flow stress. Although the Taylor model does not account for this directly, it is necessary to consider the number of mobile dislocations and their implications for the deformability of the material.

The density of *mobile* dislocations (ρ_m) required to deform a material at a specific strain rate can be described according to the Orowan equation [289].

$$\dot{\gamma} = \rho_m b \bar{v} \tag{51}$$

where $\dot{\gamma}$ is the shear strain rate, and $\bar{v}$ is the average velocity of the dislocations. Instead of relying on the strain rate to estimate the density of mobile dislocations, it is possible to estimate ρ_m based on the total strain, and the average distance traveled by a dislocation over the course of the straining experiment Equation (51) [289].

$$\gamma = \rho_m b \bar{x} \tag{52}$$

where $\bar{x}$ is the average distance traveled by each dislocation. The grain size effectively provides an upper bound for this slip distance. This rough calculation that does not account for crystal structure, slip direction, dislocation multiplication, and many other factors governing the accounting process for dislocations to accommodate a prescribed deformation. However, the confining influence of grain boundaries increases the number of dislocations considerably. The required number of dislocations to produce a shear strain of 0.4 in a material with 250 nm grain size (i.e. $\bar{x}$) is approximately $5.8*10^{15}$ m^{-2}. This simple model only accounts for the confinement of slip in the shearing direction.

Using Ashby's method of describing geometrically necessary dislocations still does not account for the underlying crystallographic effects (as described by Arsenlis and Parks [240]), but it does provide another lower bound estimate for the number of dislocations required to accommodate the strain inside of an ultrafine grain. Figure 86 presents the geometrically necessary dislocations predicted as a function of grain size and shear strain.

These plots, based on Equation (33) are similar to the ones previously presented in Figure 21, and relate more directly to the topic at hand.

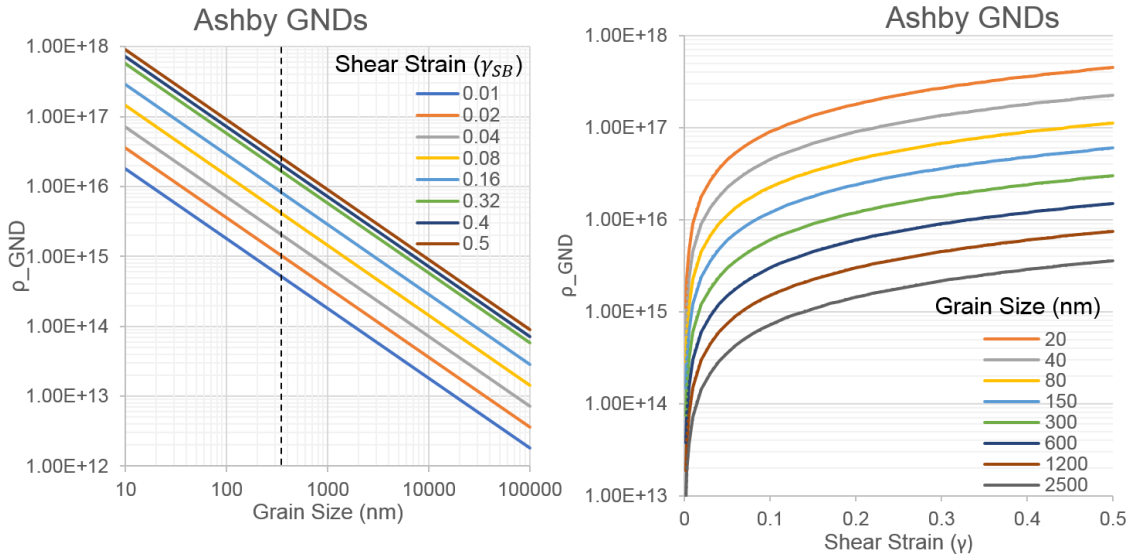

Figure 86 – Description of geometrically necessary dislocations required to accommodate deformation.

The required dislocation density to accommodate a shear strain of 0.4 with a grain size of 250 nm, is estimated to be $2.5*10^{16}$ m^{-2}. This independent derivation provides a factor two difference compared to the result of Equation (52). This density is much larger than the dislocation densities measured by EBSD or TEM, and very close to the theoretical limit of dislocations that can be accommodated in a lattice [290]. In fact, only the dislocation density estimated by HREBSD comes close to this value. This discrepancy can be accounted for by addressing the subtle differences between the dislocations associated with Ashby's concept of GNDs and the measurement of the Nye tensor based on lattice curvature.

Although Ashby [74] relies heavily on Nye's concept [190] of a tensor property to describe the continuous distribution of dislocations. There is a subtle difference that

accounts for a difference between the measured and predicted values of dislocation density. Ashby's concept of GNDs is based on the number of *mobile* dislocations that are required to accommodate deformation. In the case of the simple bending experiment (Figure 18), all of these dislocations are geometrically required to stay in the lattice in order to accommodate the prescribed strain gradient. However, in the more general sense, Ashby predicts the number of GNDs based on the initial and final state, this is akin to describing the number of *mobile* dislocations that are required from the modified Orowan equation (Equation (52)). This treatment does not stipulate that the dislocations have to accumulate in the lattice. By contrast, the Nye tensor, and the EBSD measurement of dislocations accounts for only the dislocations that contribute to lattice curvature at the time of measurement.

Dislocations can annihilate, based on dislocation-dislocation interactions, or be absorbed into grain boundaries which would result in a gradient in misorientation angles between grains. An example of this is shown in Figure 87, where the misorientation between grains can vary by more than five degrees. These results indicate that a significant fraction of the dislocations are so close to the grain boundary that they are not measured in the total GND calculation; alternatively, these dislocations have actually been incorporated into the grain boundary.

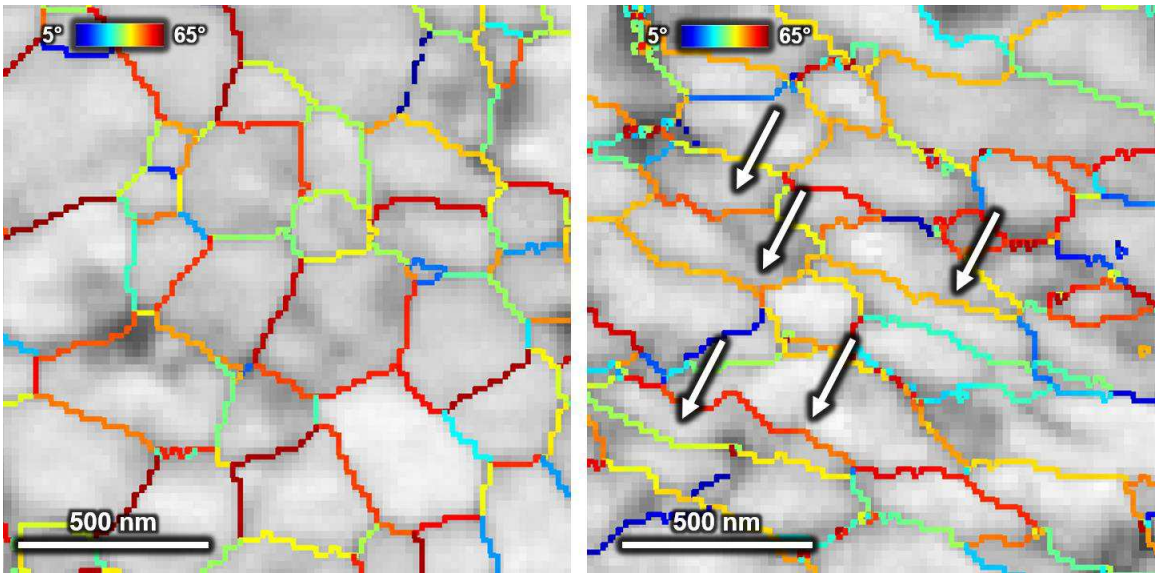

Figure 87 – Misorientation angle between grains outside (left) and inside (right) of a shear band. EBSD data is from a magnified region of the unalloyed ufgW sample described in Figure 61.

The critical observation is that the required number of dislocations to accommodate the strain inside of a shear band is tremendous. Even at low strains (~1%) the required number of dislocations is $5.84*10^{14}$ m^{-2}. This value is late into the stages of work hardening (Stage III Figure 21), and corresponds to the region where work hardening is exhausted [291]. The general hardening behavior, divided into stages based on the work hardening parameter is shown in Figure 88.

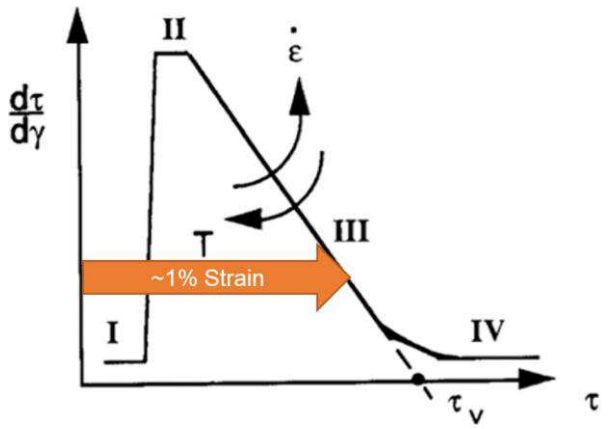

Figure 88 – Stages of work hardening, strain rate and temperature have a particularly large impact on the hardening behavior in stage III of deformation. From Rollett and Kocks [291].

5.4. Effects of dislocation mobility on strain softening behavior

So far, the general description of strain gradient plasticity provides a viable mechanism for the very low work hardening behavior of ufg metals in general. This trend is highly general for a number of materials with ultrafine grain sizes [113, 116, 155, 292] However, it is clear from nanoindentation results that the plastic instabilities that lead to shear banding are the direct result of a highly significant *softening* behavior. The reduced hardness inside of shear bands, and the associated decrease in flow stress in that region provide a direct mechanism for the plastic instabilities and shear banding that is observed in BCC metals with a sintered ufg microstructure.

The key to this softening behavior relies on the concept of mobile dislocations in the lattice. When the number of dislocations required to accommodate even 1% strain is higher than the number of dislocations in the lattice, the predicted dislocation density indicates that strain hardening should be completely exhausted. Furthermore, even though TEM analysis of sintered ufg tungsten has been shown moderate dislocation densities, the material is *effectively* starved of the dislocations required for plastic deformation. This is

subtly different from the Greer-Nix model of dislocation starvation [293], which has been used to explain the extremely high strengths of nanopillars as the result of an extremely limited dislocation content. In sintered ufg tungsten, the material is only starved of dislocations based on the extensive number of mobile dislocations required for deformation.

This is certainly the case based on Ashby GND calculations, and the degree of starvation becomes more severe as the grain size decreases. When the starvation condition is present, the material must nucleate and move new dislocations [293] instead of relying on the movement and multiplication of existing dislocations. Most of the reports of dislocation starvation have been used to account for the increased strength of single crystal nanopillars, and bursts of strain activity as the diameter decreases. In a polycrystalline material, the effects will be slightly different. Modelling studies have shown that these "low source density" materials are likely to exhibit an upper yield point phenomenon [294].

The shear banding associated with ultrafine grain sizes, and well-annealed microstructures, is not restricted to ufg tungsten and iron samples. Strain localizations have also been reported in a number of "well-annealed" microstructures including ufg aluminum [295, 296], annealed HPT copper [297], and extruded and annealed aluminum-nickel [298]. These specific cases of ufg FCC materials shear banding are not expected based on geometric mechanisms or the effects of grain size leading to a reduced strain rate sensitivity [113]. In many cases, this has also been associated with a yield point phenomenon (e.g. reported by Tsuji et al. in ufg 1100 series Al and interstitial free (IF) Fe [296]), and even attributed to the formation of *Lüders-like* bands.

The dislocation structure of ufg metals can vary significantly based on the processing conditions employed to make them. In retrospect, observations of shear banding at quasi-static rates were in materials that had experienced a high temperature consolidation step (e.g. hot pressing [165]). By contrast, deformation processed materials showed stable deformation at quasi-static rates, only failing by shear banding when tested at high strain rates [36, 68, 169]. Furthermore, an upper yield point phenomenon was detected in annealed ECAE iron; however, this was attributed to impurities [169] and a more traditional Lüders mechanism.

5.5. Differences from traditional Lüders band mechanisms

The shear bands observed in sintered ufg metals show a number of strong similarities to Lüders bands, based on the rapid increase in mobile dislocations leading to the localization of plastic strains. The traditional Lüders mechanism is based on increasing the density of mobile dislocations by unpinning them from a "solute atmosphere," or other point defects in the material. The *Lüders-like* shear banding mechanism, observed in annealed ufg metals, shows a large increase in mobile dislocations based on strain gradient plasticity. Grain size plays a critical role because of the number of dislocations that are required to deform to a given strain based on grain boundary confinement and the mechanism of strain gradient plasticity. The characteristic strain that is observed in a Lüders band depends on the rate of work hardening after yield [299]. The poor work-hardening ability of ufg materials contributes to the extensive strain observed inside of the shear band; however, this cannot account for the difference in strength between the deformed, and undeformed microstructures.

This mechanism can be distinguished from more traditional Lüders bands that result from dislocation interactions with point defects for a variety of reasons. First, if there are point defects present in the sintered material, they would be also be present in sintered coarse-grained tungsten with larger grain sizes. However, these coarser grained materials do not show the same propensity for shear band formation [53]. Second, IF steels are not susceptible to Lüders band formation at coarse grain sizes [128], but annealed ufg samples localize in a manner similar to ufg tungsten [296]. Finally, if point defects were responsible for dislocation pinning, FCC metals (e.g. Cu and Al), which show a lower propensity for point defects [295-297] (and traditional Lüders band formation) would not localize. This *Lüders-like* mechanism is prevalent in materials that require at least an order of magnitude more dislocations than the starting microstructure has available to accommodate even moderate amounts of deformation (~1% strain). This mechanism should apply in a general sense, regardless of crystal structure or the susceptibility to forming point defects.

The previously described models of shear banding, based on adiabatic, and geometric mechanisms, cannot account for the shear banding behavior observed in ufg tungsten tested under quasi-static conditions. The deformation behavior in these materials has been shown to be the result of dislocation mediated plasticity, and the plastic instabilities that develop in these materials may also be understood based on dislocation behavior. The concept of strain gradient plasticity has been used in a very general sense to describe the relationship between grain size and density of geometrically necessary dislocations, which distinguishes the behavior of ufg tungsten from a coarse-grained material.

Ultimately, shear banding can be explained by a strain softening behavior that is driven, not by temperature or texture, but by the mobility of dislocations in the lattice.

CHAPTER 6. SUMMARY, CONCLUSIONS, and FUTURE WORK

Based on careful control of processing and microstructure, ufg tungsten has been developed to demonstrate shear banding under both quasi-static, and high rate loads. A detailed analysis of these shear bands has provided tremendous insight into the mechanisms that lead to plastic instabilities and shear banding in ufg metals. These insights provide a detailed picture of the mechanism of shear banding, which is not driven by the commonly attributed influence of temperature or texture. These new understandings provide a number of opportunities to improve the performance and reliability of tungsten in ballistic applications. Furthermore, these findings may also support efforts to stabilize deformation, and improve the ductility of tungsten in a number of other extreme engineering environments.

In general, the shear bands observed in ufg tungsten have been attributed to a *Lüders-like* phenomenon based on the dislocation structure, propagation velocity, and the relative stability of the bands. These are different from the traditional Lüders bands described by Cottrell and Bilby [133], where solute atmospheres trap dislocations and a yield point phenomenon is observed as they break away and become mobile. However, the strain softening behavior and plastic instability can be attributed to similar increases in the density of mobile dislocations. Other localization models, specifically thermal and geometric softening, cannot account for the early onset of shear band formation and the relative softening of the band.

Thermal effects may play a role in the morphology and persistence of the band at high strain rates, but the adiabatic temperature rise becomes an important factor only after the band has formed. Likewise, it is impossible to ignore the effects of deformation texture in

shear band development, but these textures are not present at the time of initiation. Also, the texture that develops is a traditional BCC shearing texture, which does not show signs of being harder or softer than the surrounding matrix. Finally, the strain rate sensitivity is certainly a mitigating factor in the overall plastic instability, but this does not appear to be the main factor controlling the *formation* of shear bands.

The shear bands observed in sintered ufg tungsten show a number of similarities to Lüders bands, particularly the observed dependence of plastic instabilities on the mobile dislocation content. This correlation means that we can rely on a decades of metallurgical processing knowledge to control shear band initiation. From an industrial standpoint, the processing parameters for suppressing inhomogeneous yielding have been developed into a common practice. Various methods of controlled deformation processing methods [128] have been shown to minimize the upper yield-point phenomenon. These provide a number of viable mechanisms for tuning instability based on the needs for ductility at quasi-static strain rates without inhibiting shear band formation at ballistic rates.

6.1. Future research

Although the results of this study have been fairly effective in dispelling some theories and establishing a viable mechanism for shear band formation in sintered ufg tungsten, there are several aspects where additional research would shore up these results and improve our understandings of plastic instabilities and shear banding in ufg metals.

The *Lüders-like* mechanism of shear banding is heavily dependent on the initial density of dislocations, their mobility, and the density of dislocations required to accommodate deformation. Additional TEM investigations of this dislocation density before and after

deformation would help to shed light on the details of dislocation mobility as it applies to shear band formation. Furthermore, improved detection of geometrically necessary dislocations by EBSD and HREBSD would be useful for describing the behavior of dislocations en masse, with continuum-based dislocation theories. However, this depends on improving the angular resolution of orientation imaging microscopy.

The influence of point defects on yield point phenomena is well reported for traditional Lüders bands. Although there is clear evidence that shear banding observed in well annealed ufg metals is distinctly different from this traditional Lüders bands, it is possible to study and quantify the effects of point defects using positron annihilation [300], and internal friction [301] measurements.

Additional information regarding the dislocation character would also be helpful in describing the deformation behavior of ufg tungsten. There is a large discrepancy in the mobility of edge and screw dislocations at room temperature. Research from Cheng et al. [287, 288] have shown that the propensity of edge and mixed dislocations in the deformed microstructure provide the mechanism for observations of reduced strain rate sensitivity and improved ductility in BCC metals in general. These new findings are highly illuminating, but they do not provide the description of what physical mechanism leads to the relative decrease in screw dislocations in the first place. TEM using weak beam, dark field mode, would help to measure the dislocation character explicitly, and establish the specific dislocation reactions to account for this dislocation structure. Also, novel techniques like electron channeling contrast imaging can help to establish dislocation orientation and character explicitly, while also providing results that are

comparable to EBSD in terms of the continuum, approach for assessing dislocation density [302].

Additional improvements in the fidelity of strain maps, based on digital image correlation, would be easily attainable based on improved patterning techniques. Higher resolution images would clearly help to answer several basic questions about shear band formation: (1) What is the local strain that is required for initiation? (2) Does the shear band reach a characteristic strain before growing in width in a manner described in most Lüders band phenomena?

The formation mechanisms could also be assessed with greater fidelity by controlling the strain energy release rate in a method used by Han et al. [303]. Increasing the effective stiffness of the load frame by using a deformable support ring could help to identify stability limits for inherently unstable materials. If these stability limits do not exist, the method would provide improved control over shear band formation and propagation. This could be used to improve the effective temporal resolution for observing shear banding, and minimize the influence of strain-rate variations on shear band formation.

One of the most important issues to be studied is related to the shear banding that is observed in ufg BCC metals that are prepared by severe plastic deformation. These materials do show a propensity for strain localization if the grain size is fine enough, and the concept of dislocation starvation certainly does not apply. Bulk ufg tungsten produced by high pressure torsion also presents an instability, even at quasi-static strain rates. Figure 89 shows a *post-mortem* image of failure by shear banding. Even though the test

was sub-scale, the material is expected to exhibit bulk shear banding behavior. However, the detailed mechanism of this of this instability is not clear.

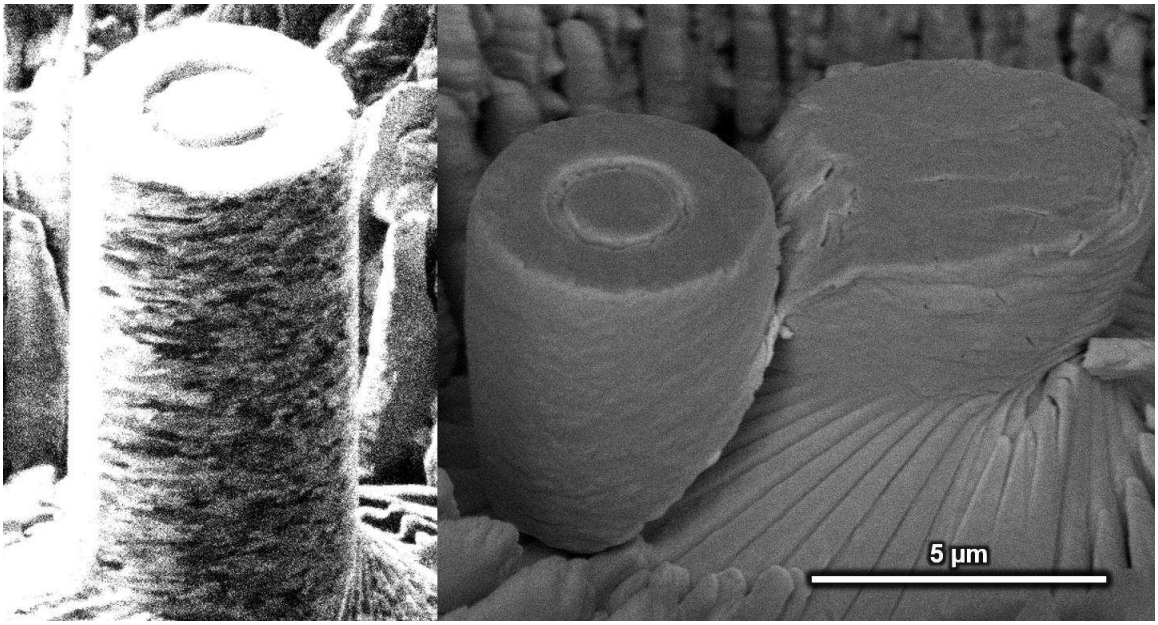

Figure 89 – Shear banding behavior in a 5 µm diameter pillar of HPT processed tungsten tested by micropillar compression [163]. Courtesy of Jonathan Ligda, US Army Research Lab.

Promoting shear banding and plastic instability in tungsten is a primary concern for making reliable and effective munitions for military applications. However, the more difficult problem, which affects the viability of tungsten in extreme engineering environments, is the limited room temperature ductility. Although, rhenium additions are very effective in ductilizing tungsten, these are not viable for most industrial applications. One important result of this research was the observation that ufg tungsten can exhibit extensive plasticity, albeit unstable plasticity, without directly resulting in brittle fracture. Furthermore, indentation tests show that initially unstable deformation (i.e. pile-ups) becomes more uniform as a result of deformation. However, these positive signs for plasticity in compression and indentation are a long way off from demonstrating

meaningful ductility in tension. A considerable effort should be applied to making the deformation behavior of ufg metals more stable. Hopefully this research has provided a useful antithesis for those endeavors.

Bibliography

[1] S.G. Caldwell, H. Kestler, N. Reheis, Secondary Operations and Quality Control for Refractory Metal Powders, ASM International, Materials Park, OH, 2015.
[2] R.K. Barnhart, Barnhart Concise Dictionary of Etymology, HarperCollins1995.
[3] Refractory Metals (Mo, Nb, Re, Ta, W), ASM Handbooks Online: ASM Desk Editions and General References, ASM International, Materials Park, OH, 2013.
[4] M. Bauccio, ASM metals reference book, ASM international1993.
[5] CES Edupack Granta Design Limited, Cambridge, UK, 2016.
[6] E. Lassner, W.D. Schubert, Tungsten: Properties, chemistry, technology of the element, alloys, and chemical compounds, Kluwer Academic and Plenum Publishers, New York, 1999.
[7] A.P. Valintine, D. Hull, Effect of temperature on the brittle fracture of polycrystalline tungsten, Journal of the Less Common Metals 17(4) (1969) 353-361.
[8] S.W.H. Yih, C.T. Wang, Tungsten: Sources, Metallurgy, Properties and Applications, Plenum Publishing Corporation1979.
[9] M. Rieth, A. Hoffmann, Influence of microstructure and notch fabrication on impact bending properties of tungsten materials, International Journal of Refractory Metals and Hard Materials 28(6) (2010) 679-686.
[10] A. Giannattasio, Z. Yao, E. Tarleton, S.G. Roberts, Brittle–ductile transitions in polycrystalline tungsten, Philosophical Magazine 90(30) (2010) 3947-3959.
[11] P. Schade, 100years of doped tungsten wire, International Journal of Refractory Metals and Hard Materials 28(6) (2010) 648-660.
[12] W.D. Coolidge, Ductile tungsten, 249th Meeting of the American Institute of Electrical Engineers, A.I.E.E., New York, 1910, pp. 961--965.
[13] W.D. Coolidge, Tungsten and method of making the same for use as filaments of incandescent electric lamps and for other purposes, General Electric Company, United States, 1913, p. 10.
[14] D. Terentyev, J. Riesch, S. Lebediev, A. Bakaeva, J.W. Coenen, Mechanical properties of as-fabricated and 2300 °C annealed tungsten wire tested up to 600 °C, International Journal of Refractory Metals and Hard Materials 66 (2017) 127-134.
[15] W.D. Klopp, W.R. Witzke, Mechanical properties and recrystallization behavior of electron-beam-melted tungsten compared with arc-melted tungsten, NASA Technical Note, NASA, Washington D. C. , 1966.
[16] K. Farrell, A.C. Schaffhauser, J.O. Stiegler, Recrystallization, grain growth and the ductile-brittle transition in tungsten sheet, Journal of the Less Common Metals 13 (1967) 15.
[17] G. Geach, J. Hughes, Plansee Proceedings, (1956).
[18] R.I. Jaffee, C.T. Sims, The effect of rhenium on the fabricability and ductility of molybdenum and tungsten, Battelle Memorial Institute, 1958.
[19] P.L. Raffo, Yielding and fracture in tungsten and tungsten-rhenium alloys, Journal of the Less Common Metals 17 (1969) 17.
[20] R.P. Simpson, Solid Solution Softening (Rhenium Ductilizing Effect and Bubble Strengthening in Tungsten-Rhenium Alloys), Air Force Materials Laboratory, 1973.
[21] L. Romaner, C. Ambrosch-Draxl, R. Pippan, Effect of Rhenium on the Dislocation Core Structure in Tungsten, Physical Review Letters 104(19) (2010).

[22] D. Cereceda Señas, Multiscale Modeling of the plastic behaviour in single crystal tungsten: from atomistic to crystal plasticity simulations, Escuela Tecnica Superior de Ingenieros Industriales, Universidad Politecnica de Madrid, Madrid,, 2015.
[23] K. Srivastava, R. Gröger, D. Weygand, P. Gumbsch, Dislocation motion in tungsten: Atomistic input to discrete dislocation simulations, International Journal of Plasticity 47 (2013) 126-142.
[24] C.R. Weinberger, C.C. Battaile, T.E. Buchheit, E.A. Holm, Incorporating atomistic data of lattice friction into BCC crystal plasticity models, International Journal of Plasticity 37 (2012) 16-30.
[25] G.E. Dieter, D.J. Bacon, Mechanical metallurgy, McGraw-hill New York1986.
[26] W. Cai, V.V. Bulatov, J. Chang, J. Li, S. Yip, Dislocation core effects on mobility, Elsevier, Amsterdam2004.
[27] G. Taylor, Thermally-activated deformation of BCC metals and alloys, Progress in materials science 36 (1992) 29-61.
[28] C. St. John, The brittle-to-ductile transition in pre-cleaved silicon single crystals, Philosophical Magazine 32(6) (1975) 1193-1212.
[29] P.B. Hirsch, S.G. Roberts, The brittle-ductile transition in silicon, Philosophical Magazine A 64(1) (1991) 55-80.
[30] W.D. Klopp, Review of ductilizing of group VIA elements by rhenium and other solutes, DTIC Document, 1968.
[31] A.A.N. Németh, J. Reiser, D.E.J. Armstrong, M. Rieth, The nature of the brittle-to-ductile transition of ultra fine grained tungsten (W) foil, International Journal of Refractory Metals and Hard Materials 50 (2015) 9-15.
[32] A.S.M. Argon, S.R., Fracture of Tungsten Single Crystals at Low Temperatures, Acta Metallurgica 14 (1966).
[33] D. Brunner, V. Glebovsky, Analysis of flow-stress measurements of high-purity tungsten single crystals, Materials Letters 44(3–4) (2000) 144-152.
[34] J. Reiser, J. Hoffmann, U. Jäntsch, M. Klimenkov, S. Bonk, C. Bonnekoh, M. Rieth, A. Hoffmann, T. Mrotzek, Ductilisation of tungsten (W): On the shift of the brittle-to-ductile transition (BDT) to lower temperatures through cold rolling, International Journal of Refractory Metals and Hard Materials 54 (2016) 351-369.
[35] J. Reiser, S. Wurster, J. Hoffmann, S. Bonk, C. Bonnekoh, D. Kiener, R. Pippan, A. Hoffmann, M. Rieth, Ductilisation of tungsten (W) through cold-rolling: R-curve behaviour, International Journal of Refractory Metals and Hard Materials 58 (2016) 22-33.
[36] Q. Wei, K.T. Ramesh, E. Ma, L.J. Kesckes, R.J. Dowding, V.U. Kazykhanov, R.Z. Valiev, Plastic flow localization in bulk tungsten with ultrafine microstructure, Applied Physics Letters 86(10) (2005) 101907.
[37] Q. Wei, H. Zhang, B. Schuster, K. Ramesh, R. Valiev, L. Kecskes, R. Dowding, L. Magness, K. Cho, Microstructure and mechanical properties of super-strong nanocrystalline tungsten processed by high-pressure torsion, Acta Materialia 54(15) (2006) 4079-4089.
[38] R. Matera, G. Federici, Design requirements for plasma facing materials in ITER, Journal of Nuclear Materials 233 (1996) 17-25.
[39] M. Rieth, S.L. Dudarev, S.M. Gonzalez de Vicente, J. Aktaa, T. Ahlgren, S. Antusch, D.E.J. Armstrong, M. Balden, N. Baluc, M.F. Barthe, W.W. Basuki, M. Battabyal, C.S. Becquart, D. Blagoeva, H. Boldyryeva, J. Brinkmann, M. Celino, L. Ciupinski, J.B. Correia, A. De Backer, C. Domain, E. Gaganidze, C. García-Rosales, J. Gibson, M.R. Gilbert, S. Giusepponi, B. Gludovatz, H. Greuner, K. Heinola, T. Höschen, A. Hoffmann, N. Holstein, F. Koch, W. Krauss, H. Li, S. Lindig, J. Linke, C. Linsmeier, P. López-Ruiz, H. Maier, J. Matejicek, T.P. Mishra, M. Muhammed, A. Muñoz,

M. Muzyk, K. Nordlund, D. Nguyen-Manh, J. Opschoor, N. Ordás, T. Palacios, G. Pintsuk, R. Pippan, J. Reiser, J. Riesch, S.G. Roberts, L. Romaner, M. Rosiński, M. Sanchez, W. Schulmeyer, H. Traxler, A. Ureña, J.G. van der Laan, L. Veleva, S. Wahlberg, M. Walter, T. Weber, T. Weitkamp, S. Wurster, M.A. Yar, J.H. You, A. Zivelonghi, Recent progress in research on tungsten materials for nuclear fusion applications in Europe, Journal of Nuclear Materials 432(1–3) (2013) 482-500.
[40] E.L. Olcott, J.D. Batchelor, Failure mechanisms in dense tungsten alloy rocket nozzles, Journal of Spacecraft and Rockets 1(6) (1964) 635-642.
[41] L. Marshall, G. Corpening, R. Sherrill, A Chief Engineer's View of the NASA X-43A Scramjet Flight Test, AIAA/CIRA 13th International Space Planes and Hypersonics Systems and Technologies Conference, American Institute of Aeronautics and Astronautics, 2005.
[42] T. Leonhardt, Properties of tungsten-rhenium and tungsten-rhenium with hafnium carbide, JOM Journal of the Minerals, Metals and Materials Society 61(7) (2009) 68-71.
[43] M. Eff, B. Thompson, S.S. Babu, T. Leonhardt, Establishing W-based Friction Stir Welding Tool Life for Thick Section Steel Applications, Friction Stir Welding and Processing VII (2013) 107-116.
[44] L. Magness, Properties and Performance of KE Penetrator Materials, in: A. Bose, R.J. Dowding (Eds.), Tungsten & Tungsten Alloys--1992, MPIF, Princeton, NJ, 1992.
[45] L. Magness, A phenomenological investigation of the behavior of high density metals under the high pressure, high strain rate loading environment of ballistic impact, Materials Science and Engineering Johns Hopkins, Baltimore, MD, 1992.
[46] L.S. Magness, High strain rate deformation behaviors of kinetic energy penetrator materials during ballistic impact, Mechanics of materials 17(2) (1994) 147-154.
[47] M.A. McDiarmid, S. Engelhardt, M. Oliver, P. Gucer, P.D. Wilson, R. Kane, M. Kabat, B. Kaup, L. Anderson, D. Hoover, L. Brown, B. Handwerger, R.J. Albertini, D. Jacobson-Kram, C.D. Thorne, K.S. Squibb, Health effects of depleted uranium on exposed Gulf War veterans: a 10-year follow-up, J Toxicol Environ Health A 67(4) (2004) 277-96.
[48] L.S. Magness, W.A. Leonard, D. Kapoor, M. Chung, J. Trogolo, The Performance and Deformation Behavior of Oriented Columnar-Grained Tungsten Polycrystalline Penetrators, (May) (1998).
[49] J. Liu, S. Li, A. Fan, H. Sun, Effect of fibrous orientation on dynamic mechanical properties and susceptibility to adiabatic shear band of tungsten heavy alloy fabricated through hot-hydrostatic extrusion, Materials Science and Engineering: A 487(1-2) (2008) 235-242.
[50] W.J. Bruchey Jr., R.N. Herring, P.W. Kingman, E.J. Horwath, Deformation mechanisms in tungsten single crystals in ballistic experiments, US Army Research Laboratory, 1993, p. 36.
[51] W.J. Bruchey, E.J. Horwath, W. Rowe, The effect of crystallographic orientation on the performance of single crystal tungsten subscale penetrators, Final Report, Mar. 1989-Mar. 1990 Army Research Lab., Aberdeen Proving Ground, MD. 1 (1993).
[52] H. Li, G. Subhash, L.J. Kecskes, R.J. Dowding, Mechanical behavior of tungsten preform reinforced bulk metallic glass composites, Materials Science and Engineering: A 403(1-2) (2005) 134-143.
[53] B. Butler, E. Klier, D. Casem, A. Dwivedi, M. Gallagher, J. Hays, Demonstration of Shear Localization in Ultrafine Grained Tungsten Alloys via Powder Metallurgy Processing Route, DTIC Document, 2012.
[54] K. Cho, L. Kecskes, R. Dowding, B. Schuster, Q. Wei, R.Z. Valiev, Nanocrystalline and Ultra-Fine Grained Tungsten for Kinetic Energy Penetrator and Warhead Liner Applications, DTIC Document, 2007.

[55] L.J. Kecskes, K.C. Cho, R.J. Dowding, B.E. Schuster, R.Z. Valiev, Q. Wei, Grain size engineering of bcc refractory metals: Top-down and bottom-up--Application to tungsten, Materials Science and Engineering: A 467(1-2) (2007) 33-43.
[56] S.N. Mathaudhu, A.J. deRosset, K.T. Hartwig, L.J. Kecskes, Microstructures and recrystallization behavior of severely hot-deformed tungsten, Materials Science and Engineering: A 503(1-2) (2009) 28-31.
[57] Q. Wei, B.E. Schuster, S.N. Mathaudhu, K.T. Hartwig, L.J. Kecskes, R.J. Dowding, K.T. Ramesh, Dynamic behaviors of body-centered cubic metals with ultrafine grained and nanocrystalline microstructures, Materials Science and Engineering: A 493(1-2) (2008) 58-64.
[58] B.E. Schuster, J.P. Ligda, Z.L. Pan, Q. Wei, Nanocrystalline refractory metals for extreme condition applications, JOM 63(12) (2011) 27--31.
[59] A.V. Ganeev, R.K. Islamgaliev, R.Z. Valiev, Refinement of tungsten microstructure upon severe plastic deformation, The Physics of Metals and Metallography 115(2) (2014) 139-145.
[60] Y. Estrin, A. Vinogradov, Extreme grain refinement by severe plastic deformation: A wealth of challenging science, Acta Materialia 61(3) (2013) 782-817.
[61] C. Ren, Z.Z. Fang, H. Zhang, M. Koopman, The study on low temperature sintering of nano-tungsten powders, International Journal of Refractory Metals and Hard Materials 61 (2016) 273-278.
[62] T. Hao, Z.Q. Fan, T. Zhang, G.N. Luo, X.P. Wang, C.S. Liu, Q.F. Fang, Strength and ductility improvement of ultrafine-grained tungsten produced by equal-channel angular pressing, Journal of Nuclear Materials 455(1-3) (2014) 595-599.
[63] H. Wang, Z.Z. Fang, K.S. Hwang, H. Zhang, D. Siddle, Sinter-ability of nanocrystalline tungsten powder, International Journal of Refractory Metals and Hard Materials 28(2) (2010) 312-316.
[64] Z.Z. Fang, H. Wang, Densification and grain growth during sintering of nanosized particles, International Materials Reviews 53(6) (2008) 326-352.
[65] J. Paramore, Z. Fang, H. Zhang, X. Wang, D. Siddle, K. Cho, Production of nanocrystalline tungsten using ultra-high-pressure rapid hot consolidation (UPRC), Advances in Powder Metallurgy and Particulate Materials 2 (2007) 08.
[66] L. Magness, L. Kecskes, M. Chung, D. Kapoor, F. Biancianello, S. Ridder, Behavior and performance of amorphous and nanocrystalline metals in ballistic impacts, 19th International Symposium on Ballistics (7–11 May 2001, Interlaken, Switzerland), 2001, pp. 1183-1189.
[67] Z.C. Cordero, E.L. Huskins, M. Park, S. Livers, M. Frary, B.E. Schuster, C.A. Schuh, Powder-Route Synthesis and Mechanical Testing of Ultrafine Grain Tungsten Alloys, Metallurgical and Materials Transactions A 45(8) (2014) 3609-3618.
[68] Q. Wei, T. Jiao, K. Ramesh, E. Ma, L. Kecskes, L. Magness, R. Dowding, V. Kazykhanov, R. Valiev, Mechanical behavior and dynamic failure of high-strength ultrafine grained tungsten under uniaxial compression, Acta Materialia 54 (2006) 11.
[69] B. Dodd, Y. Bai, Adiabatic shear localization: frontiers and advances, Elsevier2012.
[70] C. Zener, J. Hollomon, Effect of strain rate upon plastic flow of steel, Journal of Applied physics 15(1) (1944) 22-32.
[71] S.P. Joshi, K.T. Ramesh, Stability Map for Nanocrystalline and Amorphous Materials, Physical Review Letters 101(2) (2008).
[72] S.P. Joshi, K.T. Ramesh, Rotational diffusion and grain size dependent shear instability in nanostructured materials, Acta Materialia 56(2) (2008) 282-291.
[73] S.P. Joshi, K.T. Ramesh, Grain size dependent shear instabilities in body-centered and face-centered cubic materials, Materials Science and Engineering: A 493(1-2) (2008) 65-70.

[74] M. Ashby, The deformation of plastically non-homogeneous materials, Philosophical Magazine 21(170) (1970) 399-424.
[75] D. Cereceda, M. Diehl, F. Roters, D. Raabe, J.M. Perlado, J. Marian, Unraveling the temperature dependence of the yield strength in single-crystal tungsten using atomistically-informed crystal plasticity calculations, International Journal of Plasticity (2015).
[76] K. Srivastava, Atomistically-informed discrete dislocation dynamics modeling of plastic flow in body-centered cubic metals, Karlsruher Institut fur Technologie, 2014.
[77] M. Chen, E. Ma, K. Hemker, Mechanical behavior of nanocrystalline metals, in: Y. Gogotsi (Ed.), Nanomaterials Handbook, CRC Press, Boca Raton, FL, 2006.
[78] N. Fleck, G. Muller, M. Ashby, J. Hutchinson, Strain gradient plasticity: theory and experiment, Acta Metallurgica et Materialia 42(2) (1994) 475-487.
[79] M. Calcagnotto, D. Ponge, E. Demir, D. Raabe, Orientation gradients and geometrically necessary dislocations in ultrafine grained dual-phase steels studied by 2D and 3D EBSD, Materials Science and Engineering: A 527(10–11) (2010) 2738-2746.
[80] A.J. Wilkinson, T.B. Britton, Strains, planes, and EBSD in materials science, Materials Today 15(9) (2012) 366-376.
[81] S.I. Wright, M.M. Nowell, D.P. Field, A review of strain analysis using electron backscatter diffraction, Microsc Microanal 17(3) (2011) 316-29.
[82] J. Reiser, J. Hoffmann, U. Jäntsch, M. Klimenkov, S. Bonk, C. Bonnekoh, A. Hoffmann, T. Mrotzek, M. Rieth, Ductilisation of tungsten (W): On the increase of strength AND room-temperature tensile ductility through cold-rolling, International Journal of Refractory Metals and Hard Materials 64 (2017) 261-278.
[83] <Thermoviscoplastic response of polycrystalline tungsten in compression - Ramesh 1999 MSE A.pdf>.
[84] K.T. Ramesh, Nanomaterials: Mechanics and Mechanisms, Nanomaterials, Springer2009, p. 343.
[85] R.G. Hasenbein, Wear and Erosion in Large Caliber Gun Barrels, DTIC Document, 2004.
[86] R.N. Jones, H.P. Hitchcock, D.R. Villegas, Interior Ballistics of Guns, in: U. Army (Ed.) Washington DC, 1965.
[87] R. Davitt, P, Comparison of the advantages and disagvantages of depleted uanium and tungsten alloy as penetrator materials, Tank Ammo Section Report No. 107, US Army Armament Research and Development Command, 1980.
[88] W. Lanz, W. Odermatt, Penetration limits of conventional large caliber anti tank guns/kinetic energy projectiles, Proc. of the 13th International Symposium on Ballistics, Stockholm, Sweden, 1992.
[89] D. Lodge, A. Dilkes, Use of an Instrumented 120MM Projectile for Obtaining In-Bore Gun Dynamics Data, DTIC Document, 2001.
[90] J. Mescall, Materials Issues in Computer Simulations of Penetration Mechanics, Computational Aspects of Penetration Mechanics, Springer1983, pp. 47-62.
[91] V. Alekseevskii, Penetration of a rod into a target at high velocity, Combustion, Explosion, and Shock Waves 2(2) (1966) 63-66.
[92] A. Tate, A theory for the deceleration of long rods after impact, Journal of the Mechanics and Physics of Solids 15(6) (1967) 387-399.
[93] K.H. Eckelmeyer, S.G. Caldwell, Depleted Uranium and Uranium Alloys, 2013 ed., ASM International, Materials Park, OH, 2013.
[94] N.H. Harley, E.C. Foulkes, L.H. Hilborne, A. Hudson, C.R. Anthony, A Review of the Scientific Literature As It Pertains to Gulf War Illnesses. Volume 7 Depleted Uranium, DTIC Document, 1999.

[95] S. Handley-Sidhu, M.J. Keith-Roach, J.R. Lloyd, D.J. Vaughan, A review of the environmental corrosion, fate and bioavailability of munitions grade depleted uranium, Science of the total environment 408(23) (2010) 5690-5700.
[96] K.H. Eckelmeyer, S.G. Caldwell, Tungsten and Tungsten Heavy Alloys, ASM Handbooks Online: ASM Desk Editions and General References, ASM International, Materials Park, OH, 2013.
[97] P.L. Raffo, W.D. Klopp, W.R. Witzke, Mechanical Properties of Arc-Melted and Electron-Beam-Melted Tungsten-Base Alloys, NASA Technical Note, Washington D.C., 1965, p. 23.
[98] P.J. Fink, J.L. Miller, D.G. Konitzer, Rhenium reduction—alloy design using an economically strategic element, JOM 62(1) (2010) 55-57.
[99] Y.-J. Hu, M.R. Fellinger, B.G. Bulter, Y. Wang, K.A. Darling, L.J. Kecskes, D.R. Trinkle, Z.-K. Liu, Solute-induced solid-solution softening and hardening in bcc tungsten, Acta Materialia 141(Supplement C) (2017) 304-316.
[100] Y.-J. Hu, S.-L. Shang, Y. Wang, K.A. Darling, B.G. Butler, L.J. Kecskes, Z.-K. Liu, Effects of alloying elements and temperature on the elastic properties of W-based alloys by first-principles calculations, Journal of Alloys and Compounds 671 (2016) 267-275.
[101] K.H. Eckelmeyer, S.G. Caldwell, Very High Density Metals, Metals Handbook: Desk Edition, ASM International, Materials Park, OH, 1998, pp. 691–695.
[102] F. Cardarelli, Materials handbook: a concise desktop reference, Springer Science & Business Media2008.
[103] Hardness Conversions for Steels, ASM Handbooks Online: ASM Desk Editions and General References, ASM International, Materials Park, OH, 2000, pp. 282-287.
[104] U.S.G. Survey, Mineral Commodity Summaries 2017, US Geological Survey, 2017.
[105] L. Magness, D. Kapoor, R. Dowding, Novel Flow-Softening and Flow-Anisotropy Approaches to Developing Improved Tungsten Kinetic Energy Penetrator Materials, Materials and Manufacturing Processes 10(3) (1995) 531-540.
[106] L.S. Magness, T.G. Farrand, Deformation behavior and its relationship to the penetration performance of high-density kinetic energy penetrator materials, Proceedings of the 1990 Army Science Conference, Durham, NC, 1990, pp. 149-165.
[107] R. Seydel, Practical bifurcation and stability analysis, Springer Science & Business Media2009.
[108] ASTM_International, Standard Test Methods for Tension Testing of Metallic Materials, E8/E8M-15a, West Conshohocken, PA 19428-2959. United States, 2015.
[109] S.D. Antolovich, R.W. Armstrong, Plastic strain localization in metals: origins and consequences, Progress in Materials Science 59(Supplement C) (2014) 1-160.
[110] A. Considère, Use of the iron and steel in buildings, Ann Des Ponts Chaussees 9 (1885) 574-575.
[111] H.J. Kleemola, M.A. Nieminen, On the strain-hardening parameters of metals, Metallurgical Transactions 5(8) (1974) 1863-1866.
[112] E. Hart, Theory of the tensile test, Acta Metallurgica 15(2) (1967) 351-355.
[113] K. Ramesh, Mechanical Failure Processes in Nanomaterials, Nanomaterials: mechanics and mechanisms, Springer Verlag2009.
[114] A. Molinari, R.J. Clifton, Analytical Characterization of Shear Localization in Thermoviscoplastic Materials, Journal of Applied Mechanics 54(4) (1987) 806-812.
[115] T.W. Wright, The physics and mathematics of adiabatic shear bands, Cambridge University Press2002.

[116] I.S. Yasnikov, A. Vinogradov, Y. Estrin, Revisiting the Considère criterion from the viewpoint of dislocation theory fundamentals, Scripta Materialia 76(Supplement C) (2014) 37-40.
[117] N. Perez, Introduction to fracture mechanics, Fracture Mechanics, Springer2017, pp. 53-77.
[118] J. Li, Behavior and properties of shear bands, Polymer Engineering & Science 24(10) (1984) 750-760.
[119] A. Poliakov, H. Herrmann, Self‐organized criticality of plastic shear bands in rocks, Geophysical Research Letters 21(19) (1994) 2143-2146.
[120] P. Schall, M. van Hecke, Shear bands in matter with granularity, Annual Review of Fluid Mechanics 42 (2010).
[121] A. Greer, Y. Cheng, E. Ma, Shear bands in metallic glasses, Materials Science and Engineering: R: Reports 74(4) (2013) 71-132.
[122] B.E. Hobbs, A. Ord, Plastic instabilities: Implications for the origin of intermediate and deep focus earthquakes, Journal of Geophysical Research: Solid Earth 93(B9) (1988) 10521-10540.
[123] M.-A. Fardin, T. Ober, C. Gay, G. Grégoire, G. McKinley, S. Lerouge, Potential “ways of thinking” about the shear-banding phenomenon, Soft Matter 8(4) (2012) 910-922.
[124] J. Lins, H. Sandim, H.-J. Kestenbach, D. Raabe, K. Vecchio, A microstructural investigation of adiabatic shear bands in an interstitial free steel, Materials Science and Engineering: A 457(1) (2007) 205-218.
[125] M. Kuroda, V. Tvergaard, Effects of texture on shear band formation in plane strain tension/compression and bending, International Journal of Plasticity 23(2) (2007) 244-272.
[126] L. Anand, S.R. Kalidindi, The process of shear band formation in plane strain compression of fcc metals: Effects of crystallographic texture, Mechanics of Materials 17(2) (1994) 223-243.
[127] R.J. Asaro, Geometrical effects in the inhomogeneous deformation of ductile single crystals, Acta Metallurgica 27(3) (1979) 445-453.
[128] E. Hall, Yield point phenomena in metals and alloys, Springer Science & Business Media2012.
[129] A.H. Cottrell, LXXXVI. A note on the Portevin-Le Chatelier effect, The London, Edinburgh, and Dublin Philosophical Magazine and Journal of Science 44(355) (1953) 829-832.
[130] Y. Estrin, L.P. Kubin, Plastic instabilities: phenomenology and theory, Materials Science and Engineering: A 137(Supplement C) (1991) 125-134.
[131] T. Byun, N. Hashimoto, Strain localization in irradiated materials, Nuclear Engineering and technology 38(7) (2006) 619.
[132] T.D. de la Rubia, H.M. Zbib, T.A. Khraishi, B.D. Wirth, M. Victoria, M.J. Caturla, Multiscale modelling of plastic flow localization in irradiated materials, Nature 406(6798) (2000) 871-874.
[133] A.H. Cottrell, B.A. Bilby, Dislocation Theory of Yielding and Strain Ageing of Iron, Proceedings of the Physical Society. Section A 62(1) (1949) 49.
[134] H. Neuhäuser, A. Hampel, Observation of lüders bands in single crystals, Scripta Metallurgica et Materialia 29(9) (1993) 1151-1157.
[135] M.H. Tresca, On further applications of the flow of solids, Journal of the Franklin Institute 106(6) (1878) 396-404.
[136] W. Johnson, Henri Tresca as the originator of adiabatic heat lines, International Journal of Mechanical Sciences 29(5) (1987) 301-310.
[137] R. DeHoff, Thermodynamics in materials science, CRC Press2006.
[138] R. Batra, Effect of material parameters on the initiation and growth of adiabatic shear bands, International journal of solids and structures 23(10) (1987) 1435-1446.

[139] R. Batra, C. Kim, Analysis of shear banding in twelve materials, International journal of plasticity 8(4) (1992) 425-452.
[140] M. Staker, The relation between adiabatic shear instability strain and material properties, Acta metallurgica 29(4) (1981) 683-689.
[141] Y. Bai, C. Cheng, S. Yu, On evolution of thermo-plastic shear band, Acta Mechanica Sinica 2(1) (1986) 1.
[142] B. Dodd, Y. Bai, Width of adiabatic shear bands formed under combined stresses, Materials science and technology 5(6) (1989) 557-559.
[143] J.F.C. Lins, H.R.Z. Sandim, H.J. Kestenbach, D. Raabe, K.S. Vecchio, A microstructural investigation of adiabatic shear bands in an interstitial free steel, Materials Science and Engineering: A 457(1-2) (2007) 205-218.
[144] A. Molinari, C. Musquar, G. Sutter, Adiabatic shear banding in high speed machining of Ti–6Al–4V: experiments and modeling, International journal of Plasticity 18(4) (2002) 443-459.
[145] P. Longère, A. Dragon, X. Deprince, Numerical study of impact penetration shearing employing finite strain viscoplasticity model incorporating adiabatic shear banding, Journal of Engineering Materials and Technology 131(1) (2009) 011105.
[146] M.L. a, K.T. Ramesh, The thermoviscoplastic response of polycrystalline tungsten in compression, Materials Science and Engineering: A 276(1-2) (2000) 9--21.
[147] T. Dümmer, J. Lasalvia, G. Ravichandran, M. Meyers, Effect of strain rate on plastic flow and failure in polycrystalline tungsten, Acta Materialia 46(17) (1998) 6267-6290.
[148] S. Pappu, S. Sen, L.E. Murr, D. Kapoor, L.S. Magness, Deformation twins in oriented, columnar-grained tungsten rod ballistic penetrators, Materials Science and Engineering: A 298(1-2) (2001) 144--157.
[149] J.C. Li, Mechanical properties of nanocrystalline materials, CRC Press2011.
[150] E. Hall, The deformation and ageing of mild steel: III discussion of results, Proceedings of the Physical Society. Section B 64 (1951) 747.
[151] N. Petch, The cleavage strength of polycrystals, J. Iron Steel Inst 174(1) (1953) 25–28.
[152] J.D. Eshelby, F.C. Frank, F.R.N. Nabarro, XLI. The equilibrium of linear arrays of dislocations, The London, Edinburgh, and Dublin Philosophical Magazine and Journal of Science 42(327) (1951) 351-364.
[153] J.C.M. Li, The interaction of parallel edge dislocations with a simple tilt dislocation wall, Acta Metallurgica 8(5) (1960) 296-311.
[154] J. Li, Y. Chou, The role of dislocations in the flow stress grain size relationships, Metallurgical and Materials Transactions 1(5) (1970) 1145-1159.
[155] M.A. Meyers, A. Mishra, D.J. Benson, Mechanical properties of nanocrystalline materials, Progress in Materials Science 51(4) (2006) 427-556.
[156] D. Hull, D.J. Bacon, Introduction to dislocations, Elsevier2011.
[157] Y. Wang, M. Chen, F. Zhou, E. Ma, High tensile ductility in a nanostructured metal, Nature 419(6910) (2002) 912-915.
[158] E. Ma, Instabilities and ductility of nanocrystalline and ultrafine-grained metals, Scripta Materialia 49(7) (2003) 663-668.
[159] A. Vinogradov, Mechanical Properties of Ultrafine-Grained Metals: New Challenges and Perspectives, Advanced Engineering Materials 17(12) (2015) 1710-1722.
[160] Q. Wei, Strain rate effects in the ultrafine grain and nanocrystalline regimes—influence on some constitutive responses, Journal of materials science 42(5) (2007) 1709-1727.
[161] Q. Wei, S. Cheng, K. Ramesh, E. Ma, Effect of nanocrystalline and ultrafine grain sizes on the strain rate sensitivity and activation volume: fcc versus bcc metals, Materials Science and Engineering: A 381(1) (2004) 71-79.

[162] D.S. Gianola, D.H. Warner, J.F. Molinari, K.J. Hemker, Increased strain rate sensitivity due to stress-coupled grain growth in nanocrystalline Al, Scripta Materialia 55(7) (2006) 649-652.
[163] J.P. Ligda, Effects of Grain Size on the Quasi-Static Mechanical Properties of Ultrafine-Grained and Nanocrystalline Tantalum, Nanoscale Science, University of North Carolina at Charlotte, Charlotte, 2013, p. 221.
[164] J.P. Ligda, B.E. Schuster, Q. Wei, Transition in the deformation mode of nanocrystalline tantalum processed by high-pressure torsion, Scripta Materialia 67(3) (2012) 253-256.
[165] D. Jia, K.T. Ramesh, E. Ma, Effects of nanocrystalline and ultrafine grain sizes on constitutive behavior and shear bands in iron, Acta Materialia 51(12) (2003) 3495-3509.
[166] D. Jia, K.T. Ramesh, E. Ma, Failure mode and dynamic behavior of nanophase iron under compression, Scripta Materialia 42(1) (2000) 73-78.
[167] B. Butler, T. Sano, J. Ligda, Deformation behavior of ultrafine grained tungsten from powder metallurgy processes TMS 2016, TMS, Nashville, TN, 2016.
[168] K. Cho, L. Kecskes, R. Dowding, B. Schuster, Q. Wei, R. Valiev, Nanocrystalline and Ultra-Fine Grained Tungsten for Kinetic Energy Penetrator and Warhead Liner Applications, (2007).
[169] Q. Wei, L. Kecskes, T. Jiao, K.T. Hartwig, K.T. Ramesh, E. Ma, Adiabatic shear banding in ultrafine-grained Fe processed by severe plastic deformation, Acta Materialia 52(7) (2004) 1859-1869.
[170] T. Malow, C.C. Koch, P. Miraglia, K.L. Murty, Compressive mechanical behavior of nanocrystalline Fe investigated with an automated ball indentation technique, Materials Science and Engineering: A 252(1) (1998) 36-43.
[171] J.E. Carsley, A. Fisher, W.W. Milligan, E.C. Aifantis, Mechanical behavior of a bulk nanostructured iron alloy, Metallurgical and Materials Transactions A 29(9) (1998) 2261-2271.
[172] P.G. Sanders, C.J. Youngdahl, J.R. Weertman, The strength of nanocrystalline metals with and without flaws, Materials Science and Engineering: A 234–236 (1997) 77-82.
[173] K.T. Ramesh, Mechanical Failure Processes in Nanomaterials, Nanomaterials: mechanics and mechanisms, Springer Verlag2009.
[174] Q. Wei, D. Jia, K. Ramesh, E. Ma, Evolution and microstructure of shear bands in nanostructured Fe, Applied Physics Letters 81 (2002) 1240.
[175] A. Marchand, J. Duffy, An experimental study of the formation process of adiabatic shear bands in a structural steel, Journal of the Mechanics and Physics of Solids 36(3) (1988) 251-283.
[176] Q. Wei, L. Kecskes, K. Ramesh, Effect of low-temperature rolling on the propensity to adiabatic shear banding of commercial purity tungsten, Materials Science and Engineering: A 578 (2013) 394-401.
[177] Q. Wei, D. Jia, K.T. Ramesh, E. Ma, Evolution and microstructure of shear bands in nanostructured Fe, Applied Physics Letters 81(7) (2002) 1240.
[178] Q. Wei, S. Cheng, K.T. Ramesh, E. Ma, Effect of nanocrystalline and ultrafine grain sizes on the strain rate sensitivity and activation volume: fcc versus bcc metals, Materials Science and Engineering: A 381(1-2) (2004) 71-79.
[179] A.S. Khan, S. Huang, Continuum theory of plasticity, John Wiley & Sons1995.
[180] M. Barney, G. Campbell, J. Stolken, A. Schwartz, J. Plitzko, W. King, J. Morris, Experimental assessment of gradient plasticity, Lawrence Livermore National Lab., CA (US), Presented at Materials Research Society Fall 2000 Meeting, Boston, MA, November 27-December 1,2000, 2000, p. 9.
[181] M.F. Ashby, S. Bahk, J. Bevk, D. Turnbull, The influence of a dispersion of particles on the sintering of metal powders and wires, Progress in Materials Science 25(1) (1980) 1-34.

[182] E. Demir, D. Raabe, N. Zaafarani, S. Zaefferer, Investigation of the indentation size effect through the measurement of the geometrically necessary dislocations beneath small indents of different depths using EBSD tomography, Acta Materialia 57(2) (2009) 559-569.
[183] O. Kraft, P.A. Gruber, R. Mönig, D. Weygand, Plasticity in Confined Dimensions, Annual Review of Materials Research 40(1) (2010) 293-317.
[184] W.D. Nix, H. Gao, Indentation size effects in crystalline materials: A law for strain gradient plasticity, Journal of the Mechanics and Physics of Solids 46(3) (1998) 411-425.
[185] R. Maaß, S. Van Petegem, D. Ma, J. Zimmermann, D. Grolimund, F. Roters, H. Van Swygenhoven, D. Raabe, Smaller is stronger: The effect of strain hardening, Acta Materialia 57(20) (2009) 5996-6005.
[186] S.R. Agnew, B.R. Elliott, C.J. Youngdahl, K.J. Hemker, J.R. Weertman, Microstructure and mechanical behavior of nanocrystalline metals, Materials Science and Engineering: A 285(1–2) (2000) 391-396.
[187] G.M. Pharr, E.G. Herbert, Y. Gao, The indentation size effect: a critical examination of experimental observations and mechanistic interpretations, Annual Review of Materials Research 40 (2010) 271-292.
[188] D.S. Gianola, C. Eberl, Micro- and nanoscale tensile testing of materials, JOM 61(3) (2009) 24-35.
[189] Z.C. Cordero, B.E. Knight, C.A. Schuh, Six decades of the Hall–Petch effect – a survey of grain-size strengthening studies on pure metals, International Materials Reviews 61(8) (2016) 495-512.
[190] J.F. Nye, Some geometrical relations in dislocated crystals, Acta Metallurgica 1(2) (1953) 153-162.
[191] E.C. Aifantis, The physics of plastic deformation, International Journal of Plasticity 3(3) (1987) 211-247.
[192] N. Fleck, J. Hutchinson, Strain gradient plasticity, Advances in applied mechanics 33 (1997) 296-361.
[193] Y. Estrin, A. Molotnikov, C.H.J. Davies, R. Lapovok, Strain gradient plasticity modelling of high-pressure torsion, Journal of the Mechanics and Physics of Solids 56(4) (2008) 1186-1202.
[194] G. Voyiadjis, D. Faghihi, C. Zhang, Analytical and Experimental Determination of Rate- and Temperature-Dependent Length Scales Using Nanoindentation Experiments, Journal of Nanomechanics and Micromechanics 1(1) (2011) 24-40.
[195] X. Zhang, K. Aifantis, Interpreting the internal length scale in strain gradient plasticity, Rev. Adv. Mater. Sci 41(1) (2015) 72-83.
[196] R.K. Abu Al-Rub, G.Z. Voyiadjis, Analytical and experimental determination of the material intrinsic length scale of strain gradient plasticity theory from micro- and nano-indentation experiments, International Journal of Plasticity 20(6) (2004) 1139-1182.
[197] A. Arsenlis, D. M. Parks, R. Becker, V. V. Bulatov, On the evolution of crystallographic dislocation density in non-homogeneously deforming crystals, Journal of the Mechanics and Physics of Solids 52(6) (2004) 1213-1246.
[198] S. Basinski, Z. Basinski, Recrystallization, Grain Growth and Textures, Am. Soc. Metals, Metals Park, OH (1966) 26.
[199] E.C. Aifantis, On the microstructural origin of certain inelastic models, ASME J. Eng. Mater. Technol 106(4) (1984) 326-330.
[200] N. Fleck, J. Hutchinson, A reformulation of strain gradient plasticity, Journal of the Mechanics and Physics of Solids 49(10) (2001) 2245-2271.
[201] N.A. Fleck, J.W. Hutchinson, J.R. Willis, Guidelines for Constructing Strain Gradient Plasticity Theories, Journal of Applied Mechanics 82(7) (2015) 071002-071002-10.

[202] N.A. Fleck, J.R. Willis, A mathematical basis for strain-gradient plasticity theory—Part I: Scalar plastic multiplier, Journal of the Mechanics and Physics of Solids 57(1) (2009) 161-177.
[203] A.G. Evans, J.W. Hutchinson, A critical assessment of theories of strain gradient plasticity, Acta Materialia 57(5) (2009) 1675-1688.
[204] D. Korn, A. Morsch, R. Birringer, W. Arnold, H. Gleiter, Measurements of the elastic constants, the specific heat and the entropy of grain boundaries by means of ultra-fine grained materials, Le Journal de Physique Colloques 49(C5) (1988) C5-769-C5-779.
[205] P.G. Sanders, J.A. Eastman, J.R. Weertman, Elastic and tensile behavior of nanocrystalline copper and palladium, Acta Materialia 45(10) (1997) 4019-4025.
[206] B. Butler, E. Klier, M. Kelly, M. Gallagher, Thermal Stability of Milled Nanocrystalline Tungsten Powders, DTIC Document, 2011.
[207] G.L. Krasko, Site Competition Effect of Impurities and Grain Boundary Stability in Iron and Tungsten, US Army Research Laboratory, 1994.
[208] G.L. Krasko, Effect of impurities on the electronic structure of grain boundaries and intergranular cohesion in iron and tungsten, Materials Science and Engineering: A 234-236 (1997) 1071--1074.
[209] R.L. Smialek, G.L. Webb, T.E. Mitchell, Solid solution softening in BCC metal alloys, Scripta Metallurgica 4(1) (1970) 33-37.
[210] C. Eberl, R. Thompson, D. Gianola, W. Sharpe Jr, K. Hemker, Digital image correlation and tracking, MatLabCentral, Mathworks file exchange server, 2006.
[211] F. Hild, S. Roux, Digital image correlation: from displacement measurement to identification of elastic properties–a review, Strain 42(2) (2006) 69-80.
[212] P. Bing, Q. Kemao, X. Huimin, A. Anand, Two-dimensional digital image correlation for in-plane displacement and strain measurement: a review, Measurement Science and Technology 20(6) (2009) 062001.
[213] G. Pharr, W. Oliver, Measurement of thin film mechanical properties using nanoindentation, Mrs Bulletin 17(07) (1992) 28-33.
[214] X. Li, B. Bhushan, A review of nanoindentation continuous stiffness measurement technique and its applications, Materials Characterization 48(1) (2002) 11-36.
[215] D.A. Lucca, K. Herrmann, M.J. Klopfstein, Nanoindentation: Measuring methods and applications, CIRP Annals - Manufacturing Technology 59(2) (2010) 803-819.
[216] V. Maier, K. Durst, J. Mueller, B. Backes, H.W. Höppel, M. Göken, Nanoindentation strain-rate jump tests for determining the local strain-rate sensitivity in nanocrystalline Ni and ultrafine-grained Al, Journal of Materials Research 26(11) (2011) 1421-1430.
[217] H. Kolsky, An Investigation of the Mechanical Properties of Materials at very High Rates of Loading, Proceedings of the Physical Society. Section B 62(11) (1949) 676.
[218] M.A. Sutton, J.J. Orteu, H. Schreier, Image correlation for shape, motion and deformation measurements: basic concepts, theory and applications, Springer Science & Business Media2009.
[219] P. Zhou, K.E. Goodson, Subpixel displacement and deformation gradient measurement using digital image/speckle correlation (DISC), OPTICE 40(8) (2001) 1613-1620.
[220] W.C. Oliver, G.M. Pharr, An improved technique for determining hardness and elastic modulus using load and displacement sensing indentation experiments, Journal of Materials Research 7(6) (1992) 1564-1583.
[221] V. Maier, C. Schunk, M. Göken, K. Durst, Microstructure-dependent deformation behaviour of bcc-metals – indentation size effect and strain rate sensitivity, Philosophical Magazine 95(16-18) (2015) 1766-1779.

[222] J. Alkorta, J.M. Martínez-Esnaola, J. Gil Sevillano, Critical examination of strain-rate sensitivity measurement by nanoindentation methods: Application to severely deformed niobium, Acta Materialia 56(4) (2008) 884-893.
[223] Metallography and Microstructures of Refractory Metals and Alloys, ASM Handbooks Online: ASM Desk Editions and General References, ASM International, Materials Park, OH, 2004, pp. p. 877–888.
[224] W.S. Rasband, ImageJ National Institutes of Health, USA, p. Java based image analysis software.
[225] C.A. Schneider, W.S. Rasband, K.W. Eliceiri, NIH Image to ImageJ: 25 years of image analysis, Nature Methods 9 (2012) 671.
[226] Y.Q. Cheng, Z. Han, Y. Li, E. Ma, Cold versus hot shear banding in bulk metallic glass, Physical Review B 80(13) (2009).
[227] L. Wang, Shear-Band Formation and Thermal Activation in Metallic Glasses, University of Tenessee, Knoxville, 2011.
[228] J.J. Lewandowski, A.L. Greer, Temperature rise at shear bands in metallic glasses, Nature Materials 5(1) (2005) 15-18.
[229] A.J. Schwartz, M. Kumar, B.L. Adams, D.P. Field, Electron backscatter diffraction in materials science, Springer2009.
[230] O. Engler, V. Randle, Introduction to texture analysis: macrotexture, microtexture, and orientation mapping, CRC press2009.
[231] F.J. Humphreys, Review Grain and subgrain characterisation by electron backscatter diffraction, Journal of Materials Science 36(16) (2001) 3833-3854.
[232] A.J. Wilkinson, G. Meaden, D.J. Dingley, High-resolution elastic strain measurement from electron backscatter diffraction patterns: New levels of sensitivity, Ultramicroscopy 106(4–5) (2006) 307-313.
[233] a. E Kroner, K.H. Anthony, Dislocations and Disclinations in Material Structures: The Basic Topological Concepts, Annual Review of Materials Science 5(1) (1975) 43-72.
[234] E. Kroner, General continuum theory of dislocations and proper stresses, Arch. Rat. Mech. Anal (1960) 273-334.
[235] B.S. El-Dasher, B.L. Adams, A.D. Rollett, Viewpoint: experimental recovery of geometrically necessary dislocation density in polycrystals, Scripta Materialia 48(2) (2003) 141-145.
[236] S. Sun, B.L. Adams, W.E. King, Observations of lattice curvature near the interface of a deformed aluminium bicrystal, Philosophical Magazine A 80(1) (2000) 9-25.
[237] W. Pantleon, Resolving the geometrically necessary dislocation content by conventional electron backscattering diffraction, Scripta Materialia 58(11) (2008) 994-997.
[238] D.P. Field, K.R. Magid, I.N. Mastorakos, J.N. Florando, D.H. Lassila, J.W. Morris, Mesoscale strain measurement in deformed crystals: A comparison of X-ray microdiffraction with electron backscatter diffraction, Philosophical Magazine 90(11) (2010) 1451-1464.
[239] T.J. Ruggles, T.M. Rampton, A. Khosravani, D.T. Fullwood, The effect of length scale on the determination of geometrically necessary dislocations via EBSD continuum dislocation microscopy, Ultramicroscopy 164(Supplement C) (2016) 1-10.
[240] A. Arsenlis, D. Parks, Crystallographic aspects of geometrically-necessary and statistically-stored dislocation density, Acta materialia 47(5) (1999) 1597-1611.
[241] A.J. Wilkinson, D. Randman, Determination of elastic strain fields and geometrically necessary dislocation distributions near nanoindents using electron back scatter diffraction, Philosophical magazine 90(9) (2010) 1159-1177.
[242] L. Kubin, A. Mortensen, Geometrically necessary dislocations and strain-gradient plasticity: a few critical issues, Scripta materialia 48(2) (2003) 119-125.

[243] P.J. Konijnenberg, S. Zaefferer, D. Raabe, Assessment of geometrically necessary dislocation levels derived by 3D EBSD, Acta Materialia 99 (2015) 402-414.
[244] B.L. Adams, J. Kacher, EBSD-based microscopy: Resolution of dislocation density, Computers, Materials, & Continua 14(3) (2010) 185-196.
[245] B. Beausir, C. Fressengeas, Disclination densities from EBSD orientation mapping, International Journal of Solids and Structures 50(1) (2013) 137-146.
[246] T.J. Ruggles, Characterization of Geometrically Necessary Dislocation Content with EBSD-Based Continuum Dislocation Microscopy, Department of Mechanical Engineering, Brigham Young University, Provo, Utah, 2015, p. 83.
[247] J. Jiang, T.B. Britton, A.J. Wilkinson, Measurement of geometrically necessary dislocation density with high resolution electron backscatter diffraction: Effects of detector binning and step size, Ultramicroscopy 125 (2013) 1-9.
[248] S.I. Wright, M.M. Nowell, D.P. Field, A review of strain analysis using electron backscatter diffraction, Microscopy and microanalysis 17(3) (2011) 316-329.
[249] K. Troost, P. Van der Sluis, D. Gravesteijn, Microscale elastic‐strain determination by backscatter Kikuchi diffraction in the scanning electron microscope, Applied Physics Letters 62(10) (1993) 1110-1112.
[250] J. Quinta Da Fonseca, P.M. Mummery, P.J. Withers, Full-field strain mapping by optical correlation of micrographs acquired during deformation, Journal of Microscopy 218(1) (2005) 9-21.
[251] T.B. Britton, A.J. Wilkinson, Measurement of residual elastic strain and lattice rotations with high resolution electron backscatter diffraction, Ultramicroscopy 111(8) (2011) 1395-1404.
[252] T.B. Britton, A.J. Wilkinson, High resolution electron backscatter diffraction measurements of elastic strain variations in the presence of larger lattice rotations, Ultramicroscopy 114 (2012) 82-95.
[253] C.R. Weinberger, B.L. Boyce, C.C. Battaile, Slip planes in bcc transition metals, International Materials Reviews 58(5) (2013) 296-314.
[254] EDAX OIM Analysis, AMETEX - Materials Analysis Division, Sandy, Utah, 2014, p. Software for Orientation Imaging Microscopy.
[255] B. Beausir, J. Fundenberger, ATOM - Analysis Tools for Orientation Maps, Université de Lorraine, Metz, 2015.
[256] L.A. Giannuzzi, J.L. Drown, S.R. Brown, R.B. Irwin, F.A. Stevie, Applications of the FIB lift-out technique for TEM specimen preparation, Microscopy Research and Technique 41(4) (1998) 285-290.
[257] P.J. Phillips, M.C. Brandes, M.J. Mills, M. De Graef, Diffraction contrast STEM of dislocations: Imaging and simulations, Ultramicroscopy 111(9) (2011) 1483-1487.
[258] M.K. Miller, E.A. Kenik, M.S. Mousa, K.F. Russell, A.J. Bryhan, Improvement in the ductility of molybdenum alloys due to grain boundary segregation, Scripta Materialia 46(4) (2002) 299-303.
[259] <The effect of rhenium on the fabricability and ductility of molybdenum and tungsten.pdf>.
[260] M. Garfinkle, W.R. Witzke, W.D. Klopp, Superplasticity in Tungsten--Rhenium Alloys., NASA, 1968.
[261] C. Solutions, Testing Guide, Vic-2D v6, Correlated Solutions, Inc.
[262] R. Asaro, V. Lubarda, Mechanics of solids and materials, Cambridge University Press2006.
[263] D.B. Miracle, A. Concustell, Y. Zhang, A.R. Yavari, A.L. Greer, Shear bands in metallic glasses: Size effects on thermal profiles, Acta Materialia 59(7) (2011) 2831-2840.

[264] H. Schoeller, J. Cho, Oxidation and reduction behavior of pure indium, Journal of Materials Research 24(2) (2011) 386-393.
[265] J. Baczynski, J.J. Jonas, Texture development during the torsion testing of α-iron and two IF steels, Acta Materialia 44(11) (1996) 4273-4288.
[266] R. Williams, Shear textures in copper, brass, aluminum, iron, and zirconium, Trans. Met. Soc. AIME 224 (1962).
[267] S. Li, I.J. Beyerlein, M.A.M. Bourke, Texture formation during equal channel angular extrusion of fcc and bcc materials: comparison with simple shear, Materials Science and Engineering: A 394(1) (2005) 66-77.
[268] U.F. Kocks, C.N. Tomé, H.-R. Wenk, Texture and anisotropy: preferred orientations in polycrystals and their effect on materials properties, Cambridge university press2000.
[269] G.I. Taylor, Plastic Strain in Metals, Journal of the Institute of Metals (62) (1938) 307-324.
[270] S.I. Wright, D.P. Field, Recent studies of local texture and its influence on failure, Materials Science and Engineering: A 257(1) (1998) 165-170.
[271] T. Malis, S.C. Cheng, R.F. Egerton, EELS log-ratio technique for specimen-thickness measurement in the TEM, Journal of Electron Microscopy Technique 8(2) (1988) 193-200.
[272] J.R. Stephens, Dislocation structures in single-crystal tungsten and tungsten alloys, Metallurgical and Materials Transactions 1(5) (1970) 1293-1301.
[273] A. Seeger, The kink picture of dislocation mobility and dislocation-point-defect interactions, Le Journal de Physique Colloques 42(C5) (1981) C5-201-C5-228.
[274] W.J. Wright, R. Saha, W.D. Nix, Deformation mechanisms of the Zr40Ti14Ni10Cu12Be24 bulk metallic glass, Materials Transactions 42(4) (2001) 642-649.
[275] C.E. Packard, C.A. Schuh, Initiation of shear bands near a stress concentration in metallic glass, Acta Materialia 55(16) (2007) 5348-5358.
[276] T.R. Malow, C.C. Koch, P.Q. Miraglia, K.L. Murty, Compressive mechanical behavior of nanocrystalline Fe investigated with an automated ball indentation technique, Materials Science and Engineering: A 252(1) (1998) 36-43.
[277] P. Zhang, S.X. Li, Z.F. Zhang, General relationship between strength and hardness, Materials Science and Engineering: A 529 (2011) 62-73.
[278] N.A. Stelmashenko, M.G. Walls, L.M. Brown, Y.V. Milman, Microindentations on W and Mo oriented single crystals: An STM study, Acta Metallurgica et Materialia 41(10) (1993) 2855-2865.
[279] J.J. Mason, A.J. Rosakis, G. Ravichandran, On the strain and strain rate dependence of the fraction of plastic work converted to heat: an experimental study using high speed infrared detectors and the Kolsky bar, Mechanics of Materials 17(2) (1994) 135-145.
[280] D. Rittel, L.H. Zhang, S. Osovski, The dependence of the Taylor–Quinney coefficient on the dynamic loading mode, Journal of the Mechanics and Physics of Solids 107(Supplement C) (2017) 96-114.
[281] W.J. Wright, R.B. Schwarz, W.D. Nix, Localized heating during serrated plastic flow in bulk metallic glasses, Materials Science and Engineering: A 319-321(Supplement C) (2001) 229-232.
[282] A. Lennon, K. Ramesh, The thermoviscoplastic response of polycrystalline tungsten in compression, Materials Science & Engineering A 276(1-2) (2000) 9-21.
[283] A.M. Lennon, Rate-dependent thermomechanical behavior and shear localization in a BCC metal Mechanical Engineering, Johns Hopkins University, Baltimore, Maryland, 1998.
[284] A. Seeger, Peierls barriers, kinks, and flow stress: Recent progress: Dedicated to Professor Dr. Haël Mughrabi on the occasion of his 65th birthday, Zeitschrift für Metallkunde 93(8) (2002) 760-777.
[285] D. Brunner, Comparison of flow-stress measurements on high-purity tungsten single crystals with the kink-pair theory, Materials Transactions 41(1) (2000) 9.

[286] A. Rohatgi, WebPlotDigitizer, 2017.
[287] G.M. Cheng, W.W. Jian, W.Z. Xu, H. Yuan, P.C. Millett, Y.T. Zhu, Grain Size Effect on Deformation Mechanisms of Nanocrystalline bcc Metals, Materials Research Letters 1(1) (2013) 26--31.
[288] G.M. Cheng, W.Z. Xu, W.W. Jian, H. Yuan, M.H. Tsai, Y.T. Zhu, Y.F. Zhang, P.C. Millett, Dislocations with edge components in nanocrystalline bcc Mo, Journal of Materials Research 28(13) (2013) 1820-1826.
[289] D. Rodney, J. Bonneville, 16 - Dislocations A2 - Laughlin, David E, in: K. Hono (Ed.), Physical Metallurgy (Fifth Edition), Elsevier, Oxford, 2014, pp. 1591-1680.
[290] R.M.J. Cotterill, Does dislocation density have a natural limit?, Physics Letters A 60(1) (1977) 61-62.
[291] A.D. Rollett, U. Kocks, A review of the stages of work hardening, Solid State Phenomena, Trans Tech Publ, 1993, pp. 1-18.
[292] R. Song, D. Ponge, D. Raabe, J.G. Speer, D.K. Matlock, Overview of processing, microstructure and mechanical properties of ultrafine grained bcc steels, Materials Science and Engineering: A 441(1–2) (2006) 1-17.
[293] J.R. Greer, W.D. Nix, Nanoscale gold pillars strengthened through dislocation starvation, Physical Review B 73(24) (2006) 245410.
[294] D.S. Balint, V. Deshpande, A. Needleman, E. Van der Giessen, Size effects in uniaxial deformation of single and polycrystals: a discrete dislocation plasticity analysis, Modelling and Simulation in Materials Science and Engineering 14(3) (2006) 409.
[295] P. Sun, E. Cerreta, G. Gray, J. Bingert, The effect of grain size, strain rate, and temperature on the mechanical behavior of commercial purity aluminum, Metallurgical and Materials Transactions A 37(10) (2006) 2983-2994.
[296] N. Tsuji, Y. Ito, Y. Saito, Y. Minamino, Strength and ductility of ultrafine grained aluminum and iron produced by ARB and annealing, Scripta Materialia 47(12) (2002) 893-899.
[297] Y.Z. Tian, S. Gao, L.J. Zhao, S. Lu, R. Pippan, Z.F. Zhang, N. Tsuji, Remarkable transitions of yield behavior and Lüders deformation in pure Cu by changing grain sizes, Scripta Materialia 142(Supplement C) (2018) 88-91.
[298] D.J. Lloyd, L.R. Morris, Luders band deformation in a fine grained aluminium alloy, Acta Metallurgica 25(8) (1977) 857-861.
[299] N. Tsuchida, Y. Tomota, K. Nagai, K. Fukaura, A simple relationship between Lüders elongation and work-hardening rate at lower yield stress, Scripta Materialia 54(1) (2006) 57-60.
[300] A. Seeger, The study of defects in crystals by positron annihilation, Applied physics 4(3) (1974) 183-199.
[301] M.S. Blanter, I. Golovin, H. Neuhauser, H. Sinning, Internal friction in metallic materials, A Handbook., Springer Verlag, Berlin, 2007.
[302] B.E. Dunlap, T.J. Ruggles, D.T. Fullwood, B. Jackson, M.A. Crimp, Comparison of dislocation characterization by electron channeling contrast imaging and cross-correlation electron backscattered diffraction, Ultramicroscopy 184(Part A) (2018) 125-133.
[303] Z. Han, Y. Li, H.J. Gao, Effect of frame stiffness on the deformation behavior of bulk metallic glass, Journal of Materials Research 25(10) (2011) 1958-1962.

Vita

Brady G. Butler was born on March 6, 1984 in Salt Lake City, Utah to parents Glenn L. and Janet H. Butler. Brady studied Metallurgical Engineering at the University of Utah, where he graduated as valedictorian of the College of Mines and Earth Sciences, with a Bachelor of Science degree in 2006. He continued his studies at the University of Utah, under the guidance of Professor Z. Zak Fang. Brady received a Master of Science degree in Metallurgical Engineering in 2008, with a research topic describing the "Preparation of Complex Lithium-Based Hydrogen Storage Materials Using a High Temperature Vapor Phase Reactor." In the Summer of 2008, Brady joined Booz Allen Hamilton as a research engineer, contracted to the U.S. Army Research Laboratory, and in October of 2010, he became a federal research engineer at the laboratory. In 2013, Brady resumed graduate studies, in pursuit of a PhD in Materials Science and Engineering at Johns Hopkins University, under the guidance of Professor Kevin J. Hemker